Transient Transport Experiments in the CDX-U Spherical Torus

Tobin Leo Munsat

A DISSERTATION
PRESENTED TO THE FACULTY
OF PRINCETON UNIVERSITY
IN CANDIDACY FOR THE DEGREE
OF DOCTOR OF PHILOSOPHY

RECOMMENDED FOR ACCEPTANCE
BY THE DEPARTMENT OF
ASTROPHYSICAL SCIENCES

January, 2001

© Copyright 2001 by Tobin Leo Munsat.
All rights reserved.

To Mom, Dad, Mei

Abstract

Electron transport has been measured in CDX-U using two separate perturbative techniques. Gas modulation at the plasma edge introduces cold-pulses which propagate towards the plasma center, providing time-of-flight information leading to a determination of χ_e as a function of radius. Sawteeth at the q=1 radius (r/a$\sim$0.15) induce heat-pulses which propagate outward towards the plasma edge, providing a complementary time-of-flight based χ_e profile measurement. This work represents the first localized measurement of χ_e in a spherical torus.

It is found that $\chi_e = 1 - 2$ m^2/s in the plasma core (r/a $< 1/3$), increasing by an order of magnitude or more outside of this region. Furthermore, the χ_e profile exhibits a sharp transition near r/a=1/3, indicating a possible transport barrier. Spectral and profile analyses of the soft x-ray, scanning interferometer, and edge probe data show no evidence of a significant magnetic island in the high χ_e region.

In support of the electron transport experiments, a multichannel Thomson scattering system has been designed and constructed, providing the first electron profile information in CDX-U. The edge cold-pulse experiments make extensive use of the EBW electron temperature diagnostic, the sawtooth heat-pulse measurements are made with the soft x-ray array, and χ_e profiles are compared with T_e and n_e profiles from the Thomson scattering system.

Acknowledgments

From the moment I met Bill Hooke, good things started happening. He has always been so generous with his attention and wisdom, and he is at the top of the list of the *many* people that I am indebted to.

Dick Majeski and Masa Ono deserve extra special mention for taking on the responsibility of being my thesis advisors. Their guidance and daily help has been invaluable, and working with them has been a pleasure.

Although Dick and Masa have been my official advisors, I have unofficially recruited an entire "advising team" over the course of this work. Benoit LeBlanc and Phil Efthimion in particular have gone far beyond the call of duty in donating their time and knowledge to the cause. Eric Fredrickson and Ed Synakowski have also been most patient and helpful whenever I knock on their door and astound them with the giant holes in my knowledge. I am also lucky to have Sam Cohen right down the hall, to constantly offer new perspectives on work and life.

Franco Paoletti has spent many a late evening battling EFIT with me, and the CDX-U EFIT effort would have been hopeless without his help.

There's not much I can say about Jim Taylor that hasn't been said before, since he has been an integral part of so many experimental efforts at PPPL and helped so many students over the years. Not only can he fix any problem that you throw at him, but no matter how lousy your day is going you'll feel better about life after a couple of minutes in Jim's company.

One of the best parts of grad school is the time spent with the other students, and the ones in this program have been great. I was lucky to get the timing just right to see Jon go through his graduate work, to see how it's supposed to be done. Troy, Scott, Dan, Jef, Adam, Jill, Brent – I hope we keep crossing paths for years to come. Also, no mention of the students would be complete without

an acknowledgment of Barbara Sarfaty, den mother and advocate for us all. Even when we drive her batty (most of the time, actually) she is always looking out for us. It's hard to imagine a better person to have on your side.

It seems silly to even bring up my family, because it is beyond obvious how much they've done for me. My brother Steve has been the one that I've looked up to for my whole life, and he hasn't steered me wrong yet.

Although I already put her on the dedication page, Mei deserves another mention here. She's the best.

Contents

Abstract **v**

Acknowledgments **vii**

1 Introduction **1**

1.1 Fusion Energy 3

1.1.1 Fusion Reactions 3

1.1.2 Thermonuclear Fusion 3

1.2 The Tokamak 5

1.3 The Spherical Torus 7

1.4 Thesis Outline 8

2 The CDX-U Spherical Torus **11**

2.1 Vessel and Plasma Dimensions 12

2.2 Typical Plasma Parameters 13

2.3 Power Systems 15

2.3.1 Ohmic Heating System 15

2.3.2 Toroidal and Poloidal Field Coil Power Systems 21

2.3.3 RF Heating System 23

2.4 Diagnostics 24

2.4.1 Plasma Current Rogowski Coil 24

2.4.2 Poloidal Mirnov Coils 24

2.4.3 ψ Loops 28

2.4.4 Microwave Interferometer 28

2.4.5 Multipoint Thomson Scattering 32

2.4.6 Electron Bernstein Wave Temperature Diagnostic 32
2.4.7 Triple Langmuir Probe 38
2.4.8 AXUV diode and Bolometer Array 41
2.4.9 Soft X-ray Array 43
2.4.10 Multilayer Mirror Array 44
2.4.11 Fast Visible Camera 44
2.5 Data Acquisition and Storage 44
2.5.1 Tokamak Control and Data Acquisition 45
2.5.2 File Storage 50

3 The CDX-U Multichannel Thomson Scattering System 55
3.1 Introduction 56
3.2 The TVTS Ruby Laser System 62
3.2.1 Beam Path and Optics 62
3.2.2 Control Electronics 72
3.2.3 Multi-Pulse Calculations 74
3.3 Light Collection 81
3.3.1 Collecting Lens 82
3.3.2 Fiber-Optic Bundles 85
3.3.3 Viewing Dump 90
3.3.4 High-Dispersion Spectrometer 92
3.3.5 Intensified CCD Camera 101
3.3.6 Laser Timing Jitter 102
3.4 Calibration 104
3.4.1 Spectral Calibration of Spectrometer 105
3.4.2 Determination of ICCD Quantum-Efficiency 107
3.4.3 Whiteplate Calibration of Collection Optics and Detector . . 108
3.4.4 Full System Calibration Using Raman Scattering 111
3.5 System Performance Calculations 117
3.5.1 Statistical Error Bars 118

4 Determination of χ_e Using Temperature Perturbations 125
4.1 Introduction 125
4.1.1 Transport in Spherical Tori 127

4.1.2 Perturbation Experiments to Measure χ_e 129
4.2 Cold-Pulse Experiments Using Edge Gas-Puffing 132
4.2.1 Experimental Setup 132
4.2.2 Modeling of Edge Perturbations 135
4.2.3 Experimental Results 137
4.3 Heat-Pulse Experiments Using Sawteeth 144
4.3.1 Experimental Setup 144
4.3.2 Modeling of Sawtooth Perturbations 145
4.3.3 Experimental Results 149
4.4 Comparison With Neoclassical Estimates and Scaling Laws 160
4.5 Conclusions 163

5 Conclusions and Future Work **165**
5.1 Electron transport in ST's 165
5.2 TVTS system 166

Bibliography **169**

List of Figures

1.1 Reaction rates for fusion fuels 4
1.2 Historical progress of the Lawson triple product 6

2.1 Diagram of CDX-U cross-section 14
2.2 Typical CDX-U waveforms 16
2.3 Circuit diagram of ohmic system version 1 17
2.4 Current waveform from ohmic system version 1 17
2.5 Loop voltage waveform from ohmic system version 1 18
2.6 Circuit diagram of ohmic system version 2 19
2.7 Current waveform from ohmic system version 2 20
2.8 Loop voltage waveform from ohmic system version 2 21
2.9 CDX-U poloidal field coil geometry 22
2.10 Modeled response of Mirnov loops 26
2.11 Magnetic fluctuations observed with Mirnov array 27
2.12 Typical EFIT equilibrium 29
2.13 Interferometer waveforms 31
2.14 Interferometer inversion results 33
2.15 Characteristic frequencies in CDX-U 36
2.16 EBW radiometer schematic 37
2.17 Triple probe biasing and metering circuit 39
2.18 Diagram of triple probe tip 41
2.19 CDX-U bolometer array 42
2.20 CDX-U soft x-ray array 43
2.21 CDX-U multilayer mirror array 45
2.22 Schematic of CDX-U control system 46

3.1 Scattering geometry from single moving particle 57
3.2 Scattering geometry indicating scattering angle relative to wave polarization direction 59
3.3 Cutaway view of CDX-U vessel and TVTS system 62
3.4 TVTS laser window flange, full view 63
3.5 TVTS laser window, cross-sectional view 63
3.6 TVTS coverage in CDX-U 65
3.7 TVTS laser optical table layout 66
3.8 TVTS laser beam layout 67
3.9 TVTS laser Gaussian-beam trace 68
3.10 TVTS laser triggering layout 72
3.11 TVTS Pockels cell driver circuit 73
3.12 TVTS Pockels cell optoisolator circuit 74
3.13 Modeled behavior of TVTS laser cavity with single pulse 79
3.14 Modeled behavior of TVTS laser cavity with multiple pulses 80
3.15 TVTS collection lens layout 83
3.16 TVTS collection lens, closeup 83
3.17 Collection lens spot-size analysis 84
3.18 Plastic fiber-optic bundles 87
3.19 Attenuation spectrum of Bicron BCF-98 plastic optical fiber 88
3.20 TVTS fiber bundle holder 89
3.21 TVTS viewing dump, top view 90
3.22 TVTS viewing dump, as seen from collecting optics 91
3.23 Transmission spectrum of holographic notch-filter 93
3.24 Holographic transmission grating for TVTS spectrometer 94
3.25 Spectrometer x(out) vs. z(in), straight slit 97
3.26 Spectrometer x(out) vs. z(in), curved slit 98
3.27 Curved entrance-slit for TVTS spectrometer 99
3.28 Spectrometer dispersion vs. λ 100
3.29 Spectral calibration of TVTS spectrometer 106
3.30 Quantum-Efficiency Verification of ICCD 109
3.31 Whiteplate response at CCD 110
3.32 Relative Intensity of Raman Scattering Lines in N_2 114

3.33 Relative Intensity of Raman Scattering Lines in H_2 114
3.34 Comparison of measured and expected Raman scattering signals . . 116
3.35 Typical CDX-U T_e and n_e profiles 122
3.36 Typical CDX-U T_e and n_e profiles 123

4.1 Measurement of χ from steady-state and perturbative methods . . . 131
4.2 Experimental setup for CDX-U coldpulse experiments 133
4.3 Representative waveforms for CDX-U coldpulse experiments 136
4.4 Modeled trajectory of $\tilde{T}_e$ peak from edge to center 138
4.5 Comparison of χ_e model with data from fast-scanning EBW radiometer 140
4.6 Comparison of χ_e model with data from EBW radiometer and triple probe 142
4.7 Comparison of χ_e model with data from one fixed and one variable-frequency EBW radiometer 143
4.8 Layout of SXR array with CDX-U flux surfaces 145
4.9 Typical sawtooth traces on SXR array 146
4.10 Modeled evolution of δ-function temperature perturbation 148
4.11 SXR array data from propagating heat-pulse 150
4.12 Heat-pulse trajectory, with quadratic best-fit to central points . . . 151
4.13 Comparison of χ_e behavior with electron profiles 153
4.14 SXR fluctuation levels vs. minor radius 155
4.15 SXR fluctuation spectra in the distinct confinement regions 156
4.16 Interferometer fluctuation levels and spectra vs. minor radius 158
4.17 Fluctuation spectra from triple-probe 159
4.18 Neoclassical estimate of χ_e in CDX-U 161
4.19 χ_e scalings for CDX-U 162

List of Tables

1.1 Overview of World Energy Resources 2
1.2 Fusion Reactions 3

2.1 CDX-U vacuum chamber and plasma dimensions 13
2.2 Typical CDX-U plasma parameters 13
2.3 Ohmic heating circuit version 1 parameters 15
2.4 Ohmic heating circuit version 2 parameters 18
2.5 CDX-U poloidal field coil locations 22
2.6 Poloidal Field Electrical Characteristics 23
2.7 Location and orientation of B_θ loops 25
2.8 ψ loops locations 30
2.9 Layout of the CDX-U diagnostic channels 48
2.10 Layout of the CDX-U diagnostic channels, crates 2 and 3 49
2.11 Digitization rates and recording windows for all CDX-U diagnostics 50
2.12 Data directories and file suffixes for all CDX-U datafile types 51
2.13 CDX-U datafile format 53

3.1 TVTS laser beam path and Gaussian-beam trace values 70
3.2 TVTS capacitor information 72
3.3 Parameters used in the multi-pulsed Q-switch simulation 77
3.4 TVTS collection lens specifications 82
3.5 TVTS collection lens specifications 86
3.6 Holographic spectrometer specifications 94
3.7 DG-535 delay generator settings for TVTS ICCD control 102
3.8 WinView software settings for TVTS ICCD control 103
3.9 Emission Lines for Spectrometer Calibration 105

Chapter 1

Introduction

Energy demand in the next century and beyond will be determined by both industrial development and world population growth. Though the most technologically advanced countries (U.S., Japan, Europe) presently account for the bulk of the world energy consumption, rapid industrial development combined with continuing population increase in the remainder of the world will account for most of the energy consumption increase.

Predictions of future energy needs vary greatly, but one can make some general statements based on the trends of the more developed countries. The United States presently consumes ∼300 GJ/yr per person, the European Community consumes ∼150 GJ/yr per person, and the world average is ∼75 GJ/yr per person. An increase in world consumption to levels of only half of present U.S. consumption (as predicted in several studies, [Edmonds and Reilly, 1985; Holdren, 1990; Johannson *et al.*, 1992; Houghton *et al.*, 1990]) will mean a doubling of overall energy demand. Additionally, as the proportion of electricity use within total energy consumption increases, a doubling of total energy use may lead to a tripling or more of electricity demand.

Table 1.1 (from [Livingston *et al.*, 1982]) compares the known reserves of several energy sources using *present* world energy consumption levels, demonstrating the expected lifetime of each quantity. Increased energy demand will commensurately shorten these estimates. Though there is a possibility that additional reserves may be discovered, the potential benefit of the successful development of fusion as an energy source is obvious.

Energy Source	**Estimated Resources ($\times 10^{18}$ J)**	**Est. Lifetime**
Coal	122,000	407 years
Oil	12,810	43 years
Natural Gas	10,200	34 years
Uranium	1,760	5.9 years
Lithium (D-T fusion reactions)		
Land	1×10^{7}	30,000 years
Oceans	1×10^{10}	$3\text{x}10^{7}$ years

Table 1.1: Known reserves of several energy sources, with lifetimes based on present world energy consumption of 3×10^{20} J/yr.

A second major factor to consider when comparing possible energy sources is that of environmental impact. Presently, over 75% of the world energy supply comes from fossil fuels (oil, coal, natural gas) [Livingston *et al.*, 1982], the burning of which contributes to environmental problems on several levels. Acute air pollution, particularly in urban areas, is aggravated by the particulates emitted from the burning of fossil fuels. Regional smogs from the interaction of hydrocarbons and nitrogen oxides lead to crop damage, forest damage, and public health risk. Globally, CO_2 emission from the burning of fossil fuels is the largest contributor to the buildup of "greenhouse gases" in the atmosphere [J.P. Holdren, 1997].

Though fusion does produce radioactive waste products, estimates of "integrated biological hazard potentials" and "annualized intruder hazard potentials" , show fusion to have 200 to 10,000 times less waste-management based radioactivity hazard than fission, primarily based on the lower level of radioactivity and the shorter half-life of fusion waste products [Holdren, 1991].

Finally, one needs to consider the potential hazards associated with accidents. Because fusion plants only have a few minutes worth of fuel in the reactor system at any given time (as opposed to fission plants, which have several years' worth of fuel in the reactor chamber at a time), the possibility of a nuclear "meltdown" does not exist in a fusion reactor. Catastrophic failure in a fusion-reactor setting would result in the burning plasma simply ceasing to burn.

Renewable energy sources such as hydroelectric power, geothermal energy, windpower, and solar energy may all contribute to the future energy supply, and indeed

all of these provide an energy source with similar advantages as fusion. Unfortunately none of these have the potential to supply enough energy to meet the needs of the growing population, due ultimately to land-use limitations. That said, it is important to develop all of these as part of the the future "portfolio" of energy sources. Fusion energy could potentially provide the optimum combination of a virtually inexhaustable source, low environmental impact, safety, and low land use.

1.1 Fusion Energy

1.1.1 Fusion Reactions

If a deuterium nucleus collides with a tritium nucleus with enough energy to overcome the electrostatic repulsion, a fusion reaction will occur, releasing a helium nucleus and a neutron (see table 1.2). The mass of the products will be slightly less than that of the initial constituents, and the mass difference m will be released as kinetic energy of the products, by the familiar relationship $E = mc^2$. The energy released is great enough that just 1 kg of fuel would provide 10^8 kWH of energy, or enough to run a 1 GWe power plant for a day.

D+D	$\xrightarrow[50\%]{}$	T(1.01 MeV)	+	p(3.02 MeV)
	$\xrightarrow[50\%]{}$	He^3(0.82 MeV)	+	n(2.45 MeV)
D+T	$\longrightarrow$	He^4(3.5 MeV)	+	n(14.1 MeV)
D+He^3	$\longrightarrow$	He^4(3.6 MeV)	+	p(14.7 MeV)

Table 1.2: Fusion reactions with the highest collision cross-sections [Huba, 1994]

1.1.2 Thermonuclear Fusion

The coulomb repulsion of the nuclei is nontrivial, though, and the primary challenge in harnessing fusion energy is to provide an environment where the fuel nuclei have enough energy to overcome it. In a thermonuclear reactor, the fuel is heated up to extremely high temperatures, so that the typical thermal energy of the nuclei is sufficient to induce fusion reactions. As the energy of the nuclei increases, the likelihood of any collision to produce a fusion reaction increases, but at the same

time the likelihood of having a collision decreases, so that there exists an optimum temperature to maximize the fusion reactivity. Figure 1.1 demonstrates the reaction rates for three fusion fuel combinations as a function of temperature. The D-T fuel provides the highest reactivity at the lowest temperature (maximum at T∼60 keV), and thus the D-T fuel will likely be the first fuel used in a working fusion reactor.

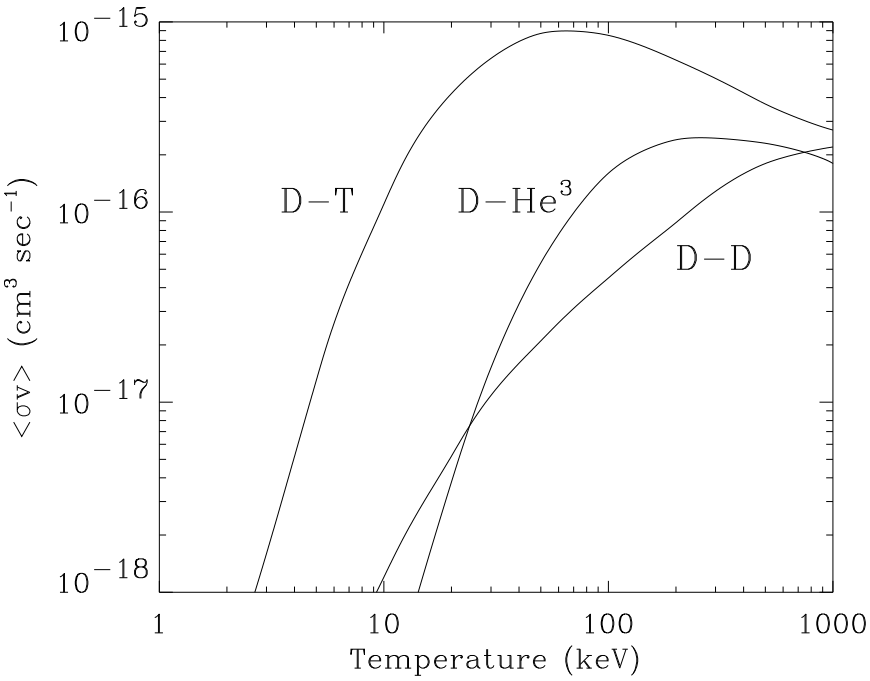

Figure 1.1: Reaction rates as a function of temperature for the three most reactive fusion fuels.

In addition to maximizing the fusion reaction rate through temperature optimization, the reaction rate can be increased through an increase in density. Quite simply, higher particle density translates into higher probability for collisions.

The third factor contributing to fusion reaction rate is that of confinement. In order to attain a sufficient probability of fusion-producing collisions, the particles must be held in the reactor system before they lose their energy. This characteristic time is referred to as the energy confinement time, or τ_E.

In order to produce a useful fusion power plant, the total power produced must exceed the power expended in maintaining the plasma conditions. The ratio of fusion power out to power in is commonly called Q, with $Q = 1$ signifying "scientific breakeven". One can notice that in the D-T reaction (fig. 1.2, third line), 80% of

the fusion energy is given to the neutron, and 20% is given to the He^4 (due simply to conservation of momentum). In a magnetic confinement scheme the neutron will be unconfined due to its neutral charge, and it will be possible (with some finite efficiency) to harness this energy. The energy in the He^4 nucleus, though, will be confined in the device, and can serve to re-heat the plasma. If the He^4 energy becomes sufficient to maintain the plasma temperature, the plasma can reach a self-sustaining "burn". Because of the energy distribution of the fusion products, Q must exceed 5 to reach burn conditions. Even more stringent is the requirement to produce an economic, self-sustaining fusion reactor, for which Q must greatly exceed 5 (∼50-100).

A useful figure of merit for a plasma confinement device based on power balance considerations is the product $n\,T\,\tau_E$, also referred to as the Lawson triple-product [Lawson, 1957]. The ignition requirement for a fusion reactor is given by the Lawson criterion,

$$n\,T\,\tau_E > 5 \times 10^{21}\ \mathrm{m}^{-3}\,\mathrm{s\,keV} \tag{1.1}$$

Progress in fusion energy development can be measured by the progress of the Lawson triple product through recent history, shown in fig. 1.2. Although values sufficient to satisfy the Lawson criterion of n, T, and τ_E, have all been separately achieved, they have not been achieved simultaneously. Progress has been remarkably steady, though, and it is widely believed that the next large magnetic confinement device will achieve at least scientific breakeven.

1.2 The Tokamak

The two primary methods for confining hot plasmas are inertial confinement and magnetic confinement. In the inertial confinement scheme, small pellets of fuel are struck with intense laser light from all sides, causing the pellet shell to explode. The corresponding implosion of the fuel within the cell causes the fuel to reach extremely high pressures and temperatures, for very brief periods. The energy from this miniature nuclear explosion would then be harnessed.

The subject of this thesis falls within the other scheme, magnetic confinement.

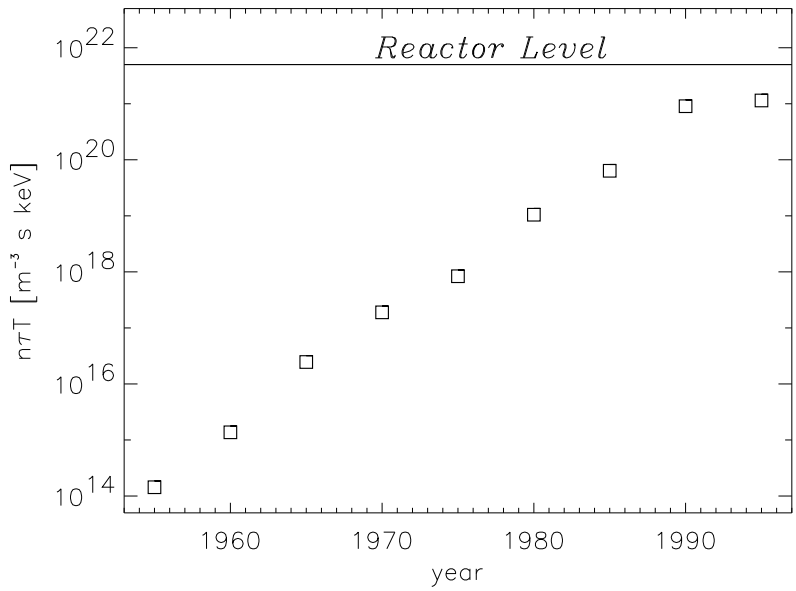

Figure 1.2: The progress in fusion development can be measured by the exponential increase in the Lawson triple-product $n\tau_E T$ over time [Wesson, 1997].

In this method, the plasma is also brought to very high temperatures and densities (though orders of magnitude less than in inertial-confinement fusion), but is confined in steady-state.

By far the most successful magnetic confinement scheme to date is the Tokamak, originally devised in the U.S.S.R. in the late 1950's [Sakharov and Tamm, 1959]. Early results included the achievement of $T_e \sim 1$ keV and $n\tau \sim 10^{18}$ m^{-3} s on the T-3 tokamak at the Kurchatov institute in Moscow [Peacock *et al.*, 1969]. Later advances included the injection of neutral beams and the introduction of divertors, leading to dramatic increase in temperature and confinement. Tokamaks presently hold the world record for temperature, confinement time, and fusion power, most recently exemplified on the JET tokamak, which reached $nT\tau_E \sim 10^{21}$ m^{-3} s keV with Q $\sim$ 95% in a deuterium-tritium plasma [Keilhacker *et al.*, 1999]. Indeed, fig. 1.2 is essentially a plot of tokamak progress over the past 50 years.

1.3 The Spherical Torus

In a D-T fusion reactor, the total fusion power produced is given by

$$P_f = E_F \int n_D n_T \langle \sigma v \rangle_{DT} dV$$

where E_F is the power per reaction (17.6 MeV), n_D and n_T are the ion densities, and $\langle \sigma v \rangle_{DT}$ is the reaction rate (see fig. 1.1). Ignoring the volume integration for the moment, it is useful to recast this equation into a more separable form, using the definition of plasma beta,

$$\beta = \frac{\text{plasma pressure}}{\text{magnetic pressure}} = \frac{nT}{\frac{B^2}{2\,\mu_0}}$$

where n is the total ion density. Defining N_D and N_T as the deuterium and tritium fractions, so that $n_D n_T = N_D N_T (\frac{n^2}{4})$, we can express the fusion power as

$$P_f = (N_D N_T) \left(\frac{B^4}{16 \mu_0^2} \right) \left(\beta^2 \right) \left(\frac{\langle \sigma v \rangle_{DT} E_F}{T^2} \right) \tag{1.2}$$

The first term is maximized simply by using a 50:50 mix of deuterium and tritium fuel. The second term demonstrates the dependence on magnetic field, which is usually the primary driver of reactor cost. The third factor is highly configuration-dependent, depending on a multitude of geometrical and plasma physics factors. This will be discussed in some detail in the following section. The fourth factor, nearly constant since $\langle \sigma v \rangle_{DT} \sim T^2$ in the region of interest to fusion reactors, is dependent on the physics of the nuclear reactions used. Clearly the way towards a successful fusion reactor is to find a configuration that can simultaneously provide high magnetic field and high β, maximizing the second and third terms of the fusion power equation.

Equation 1.2, while providing a start towards identifying the key parameters involved in reactor scaling, neglects the important limitations on β imposed by magnetohydrodynamic (MHD) stability. Additionally, a tokamak fusion reactor will need to run in steady-state, precluding the use of ohmic current drive and imposing the requirement for steady current-drive. Since radio-frequency current drive has limited efficiency, configurations which maximize the fraction of "bootstrap"

(pressure-driven) current are favorable.

An approach that appears to answer all of these demands is the low-aspect-ratio tokamak, or spherical torus (ST) [Peng and Strickler, 1986; Stambaugh *et al.*, 1998]. In the ST approach, the device is made as compact as possible by removing all non-essential elements from the inboard side, leaving only the inner legs of the toroidal field coils and an ohmic-heating solenoid. More advanced designs may remove the ohmic heating solenoid as well. In this configuration, the aspect ratio ($A = R/a$) is reduced to 1.5 or less, which turns out to provide several advantageous features.

Though the minimization of copper cross-section in the center-stack necessarily limits the achievable toroidal field in an ST, the low aspect ratio and high natural elongation ($\kappa \sim 1.5$ or more) leads to β values that are an order of magnitude higher than in conventional tokamaks. Ideal MHD stability studies have found stable equilibria with β of 45% at $A = 1.4$ [Menard *et al.*, 1997], and the START ST has achieved $\beta \sim 30\%$ in the laboratory [Gryaznevich *et al.*, 1998; Gates *et al.*, 1998].

ST's may also provide extremely high bootstrap fraction, an essential feature of a steady-state reactor. Bootstrap fractions of 99%, predicted in the ideal MHD study of [Menard *et al.*, 1997], could eliminate the need for an ohmic solenoid altogether. With self-driven current fractions this high, the remaining current drive could be provided by radio-frequency techniques.

Transport in ST's may also prove to be better than that in conventional tokamaks. Microinstability studies have predicted that as A falls below $\sim$1.5, the toroidal drift mode and the MHD ballooning mode are both stabilized, primarily due to the reduction of "bad" magnetic curvature at low aspect ratio [Rewoldt *et al.*, 1996].

1.4 Thesis Outline

This thesis is comprised of three main sections. Chapter 2 introduces the CDX-U spherical torus, including the upgrades to the power systems and diagnostics that were necessary to perform the transport study, and were performed as part of this work. Chapter 3 covers the design, construction, and operation of the multichannel

Thomson scattering system, necessary to provide electron temperature and density profiles, also performed as part of this thesis. Chapter 4 describes a set of transport experiments which were used to measure χ_e profiles in CDX-U. Following these three primary sections, chapter 5 includes major conclusions and directions for future work.

Chapter 2

The CDX-U Spherical Torus

The Current-Drive Experiment Upgrade (CDX-U) was proposed in 1988 to explore DC helicity injection in a low aspect-ratio toroidal geometry [Ono and The CDX Group, 1988]. Through 1993, this method was developed as a possible long-pulse or steady-state current drive technique [Ono *et al.*, 1987; Darrow, 1988; Darrow *et al.*, 1990; Ono *et al.*, 1992]. Following the helicity injection experiments, the formation of a tokamak with 2.4 kA driven entirely by pressure driven bootstrap currents was demonstrated [Forest *et al.*, 1992; Forest, 1992; Forest *et al.*, 1994]. Formation of 10 kA tokamak plasmas using DC helicity injection was later demonstrated [Hwang, 1993], and anomalous current diffusion in the fully bootstrap-current driven configuration was observed [Hwang *et al.*, 1996].

In 1992-1993 CDX-U underwent a major upgrade, with the introduction of a new center-stack [Jones, 1992] to provide ohmic-heating capability. Ohmic start-up efficiency, the q(a) limit, and the dependence of resistive MHD on q(a) in plasmas of aspect-ratio of 1.6 were investigated [Jones, 1995]. Investigation of H-mode inducement through the injection of ECH-heated, ripple-trapped electrons was performed in [Choe, 1996; Choe *et al.*, 1996; Choe *et al.*, 1998].

In 1998 CDX-U underwent a second major upgrade, which included the introduction of DC power supplies, the rearrangement of the entire capacitor inventory to the ohmic power system, and an overhaul of the data acquisition hardware and software systems. Additionally, a separate control room was developed, allowing remote operation of the experiment and all diagnostics from outside the test-cell.

This upgrade resulted in a longer and more reproducible plasma, as well as providing improvements to stored data reliability and usability. Some aspects of this upgrade will be described below.

Diagnostic development, both for general tokamak applications and for specialized low-aspect ratio applications, has been a continuing effort on CDX-U. A novel density fluctuation diagnostic using tangential phase-contrast imaging was developed in [Lo, 1997; Lo *et al.*, 1995], capable of measuring the radial wavenumber of core sawtooth activity and broadband density fluctuations ($k_\perp \rho_i \approx 0.4$) consistent with predictions based on nonlinear electrostatic turbulence models. Additionally, CDX-U has enjoyed a long-standing collaboration with the Johns Hopkins University spectroscopy group, which has developed several spectroscopic diagnostics including a tomographic soft x-ray system using filtered diodes, and a tomographic array of finely-tuned multilayer mirrors [Stutman *et al.*, 1996; Stutman *et al.*, 1997b; Stutman *et al.*, 1997a].

In recent years, CDX-U has turned towards RF work, with the development of a high-harmonic fast-wave (HHFW) heating system [Menard, 1998]. This work demonstrated the first heating results using HHFW [Menard *et al.*, 1999; Stutman *et al.*, 1999], a primary candidate for both heating and current drive in the high β plasmas produced in low aspect-ratio tokamaks. Most recently, CDX has become involved in studies of plasma-edge interactions, particularly with the development of lithium plasma-limiting surfaces.

2.1 Vessel and Plasma Dimensions

In 1996 the CDX-U vacuum vessel was upgraded from aluminum to stainless steel. The inner radius was increased from 61 cm to 70.2 cm to accommodate the HHFW antenna, and the number of o-rings was reduced. Metal-gasket sealed con-flat flanges were used wherever possible, a notable exception being the large top and bottom seals which join the top and bottom flanges to the outer vessel wall. The design and details of the new vessel is included in [Menard, 1998]. An overview of the vessel and plasma dimensions is presented in table 2.1, and a schematic drawing of the CDX-U cross-section is presented in figure 2.1, showing the basic vessel dimensions as well as selected in-vessel components.

Parameter	Value
Vessel cylinder outer radius	71.1 cm
Vessel cylinder inner radius	70.2 cm
Vessel cylinder height (H)	89.9 cm
Vessel volume	1.37 m^3
Center column outer radius	9.4 cm
Center column limiter outer radius	11.0 cm
Top and bottom limiter inner height	±37.3 cm
Antenna limiter inner radius	56.0 cm
Plasma geometric center radius (R_0)	33.5 cm
Plasma minor radius (a)	22.5 cm
Plasma aspect ratio ($A=R_0/a$)	1.5
Plasma half-height (b)	35-38 cm
Plasma elongation (κ=b/a)	1.55-1.7
Plasma triangularity	0.2-0.4

Table 2.1: CDX-U vacuum chamber and plasma dimensions

The plasma outer boundary is defined by both the boron nitride antenna limiter and the boron carbide (B_4C) outer rail limiter, which was constructed to match the antenna limiter boundary at two tangent points. The plasma height is limited by the top and bottom rail limiter set, which contains a pair of B_4C limiters at one toroidal location. The plasma is often compressed below this limit by the poloidal shaping coils.

2.2 Typical Plasma Parameters

Typical CDX-U plasma parameters are outlined in table 2.2, and waveforms are presented in figure 2.2.

Parameter	Description	Value
B_T	Toroidal field	2300 Gauss
$n_e(0)$	Central electron density	4×10^{19} m^{-3}
$T_e(0)$	Central electron temperature	100 eV
$I_P(0)$	Plasma current	70 kA

Table 2.2: Typical CDX-U plasma parameters

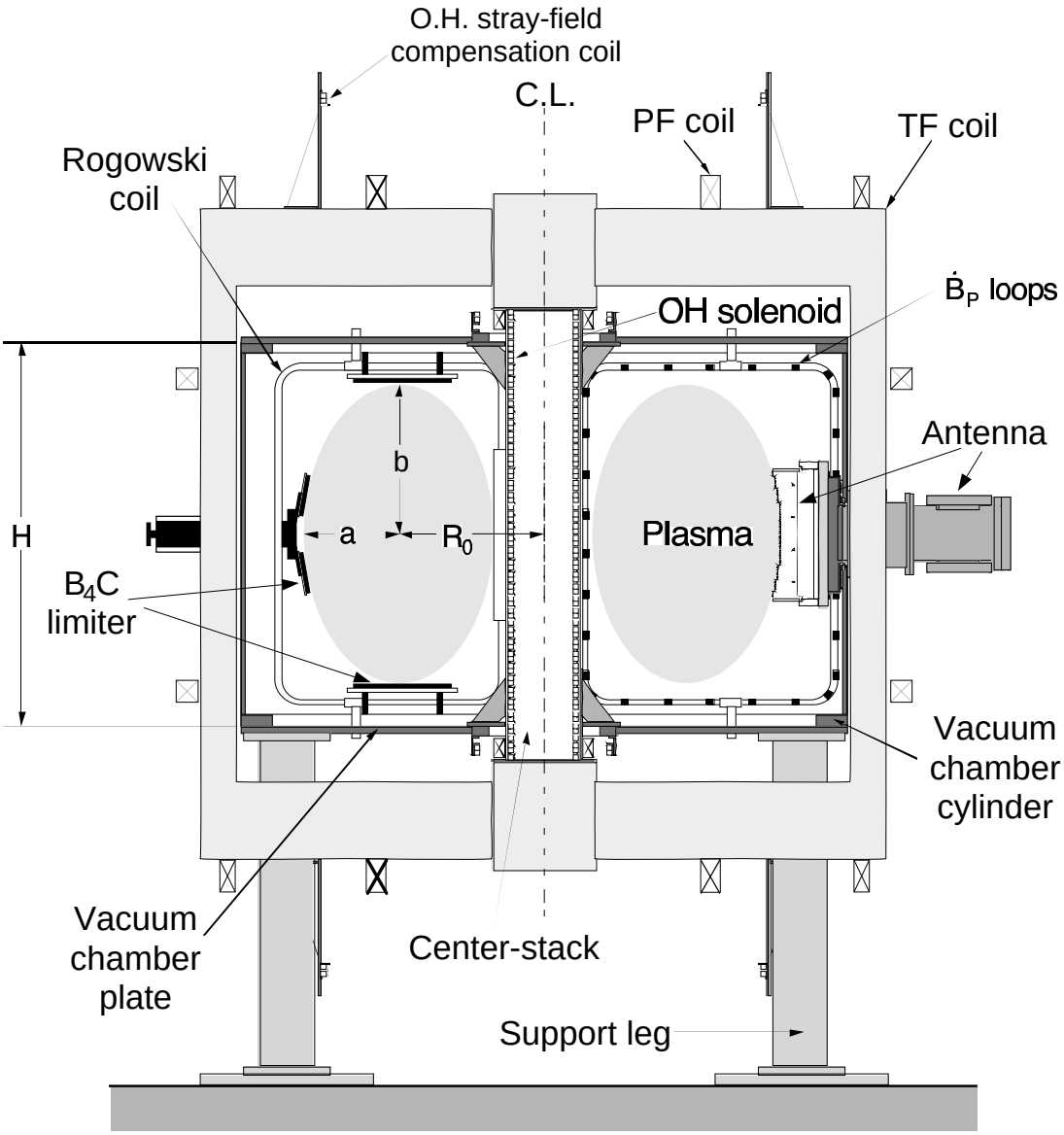

Figure 2.1: Drawing of the CDX-U cross-section showing center column, vacuum chamber cylinder, vacuum chamber plates, magnetic field coils, magnetic diagnostics, rail limiters, and HHFW antenna.

The toroidal field ramps up over ∼200 ms, at which time the ohmic-solenoid capacitor banks are fired (see section 2.3.1). Despite a dropping loop voltage, the current and density are quite flat from t=219 to 223.7 ms. An internal reconnection event (IRE) occurs at t=223.7 ms, which is evident on all waveforms. The plasma is terminated at t=228.0 ms, at which time V_{loop}=-1.3 V. The P_{rad} signal is measured by a single wideband diode with a vertical viewing chord at R=34.2 cm (see section 2.4.8). It is therefore only a rough guide of the relative radiated power. The single viewing chord also makes this diode susceptible to changes in the plasma radial position, so that the precipitous drop in the signal at the IRE may be interpreted as a sudden radial shift of the plasma.

2.3 Power Systems

2.3.1 Ohmic Heating System

Through April 2000, the ohmic heating solenoid was powered by a two-stage capacitor bank system, schematically shown in figure 2.3, hereafter referred to as "version 1" of the ohmic heating system. Values of the circuit components are listed in table 2.3.

Element	**Values**		
C1	C=73 mF	V=1000 V	E=36.5 kJ
C2	C=330 mF	V=700 V	E=80.8 kJ
L_{OH}	L=113 μH	R=5 mΩ	

Table 2.3: Ohmic heating circuit version 1 parameters

At t=200 ms (after the toroidal field ramps up to its full value), SCR1 is fired, allowing current from capacitor bank C1 to flow through the ohmic solenoid. Once C1 is completely discharged (at t∼216 ms) SCR2 is fired and C2 is discharged, carrying current in the opposite direction through the solenoid.

The solenoid current waveform and resultant loop voltage are presented in figures 2.4 and 2.5. These figures were produced with the PSPICE circuit modeling package, but the actual waveforms are indistinguishable from the modeled data.

In May of 2000, a revised ohmic circuit (hereafter referred to as "version 2") was installed to improve the loop voltage evolution in an attempt to improve the plasma

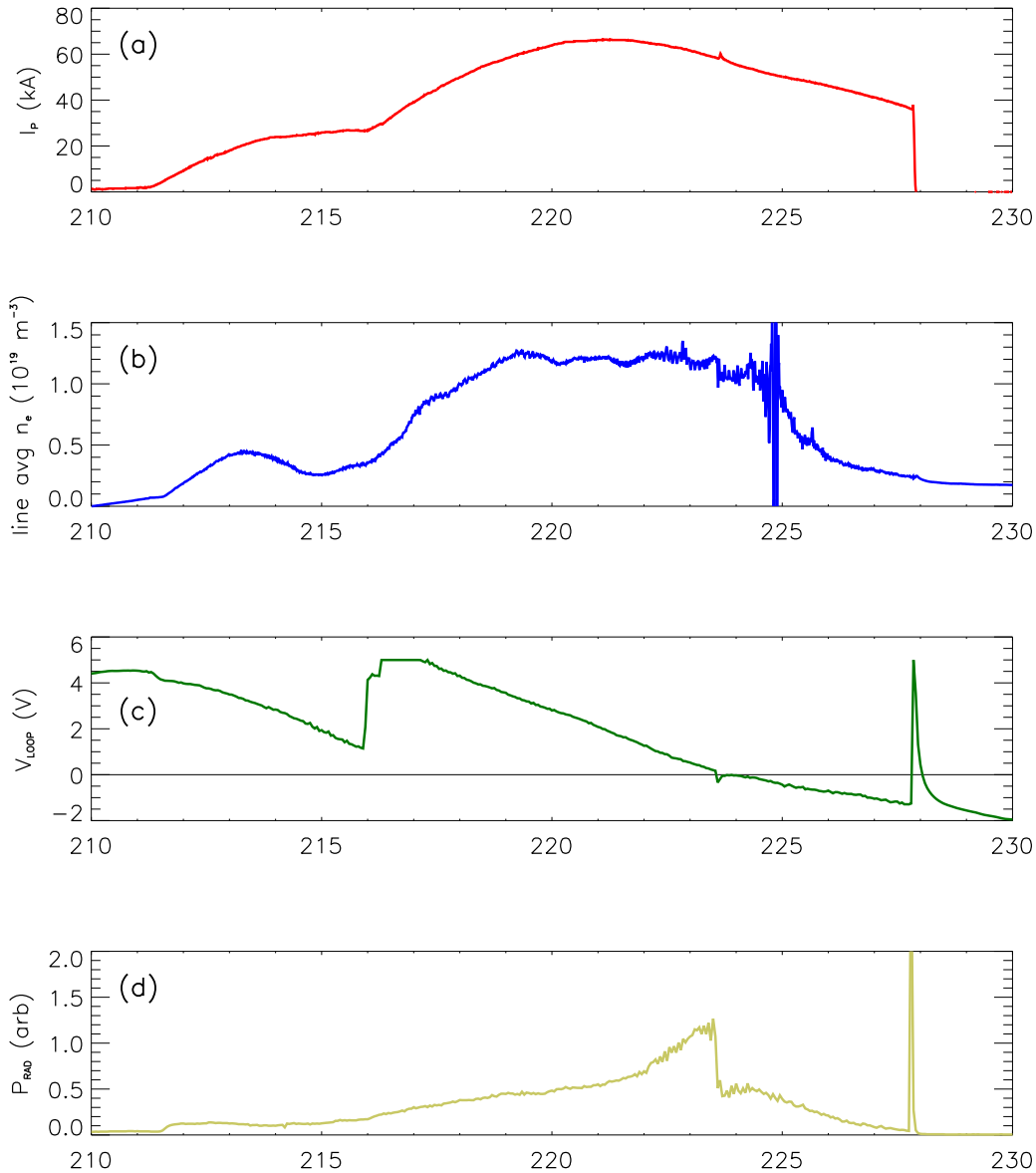

Figure 2.2: Waveforms for a typical CDX-U discharge. The toroidal field ramps up over ∼200 ms, at which time the ohmic-solenoid capacitor banks are fired. Despite a dropping loop voltage, the current and density are quite flat from t=219 to 223.7 ms. An IRE occurs at t=223.7 ms, which is evident on all waveforms. The plasma is terminated at t=228.0 ms, when V_{loop}=-1.3 V.

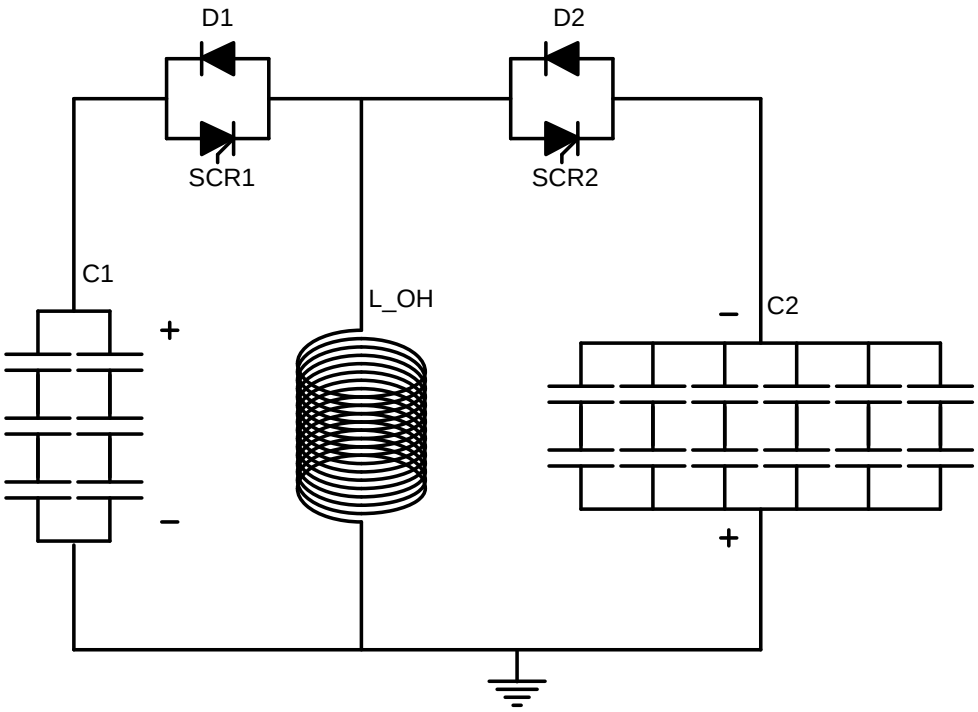

Figure 2.3: Circuit diagram of ohmic system version 1

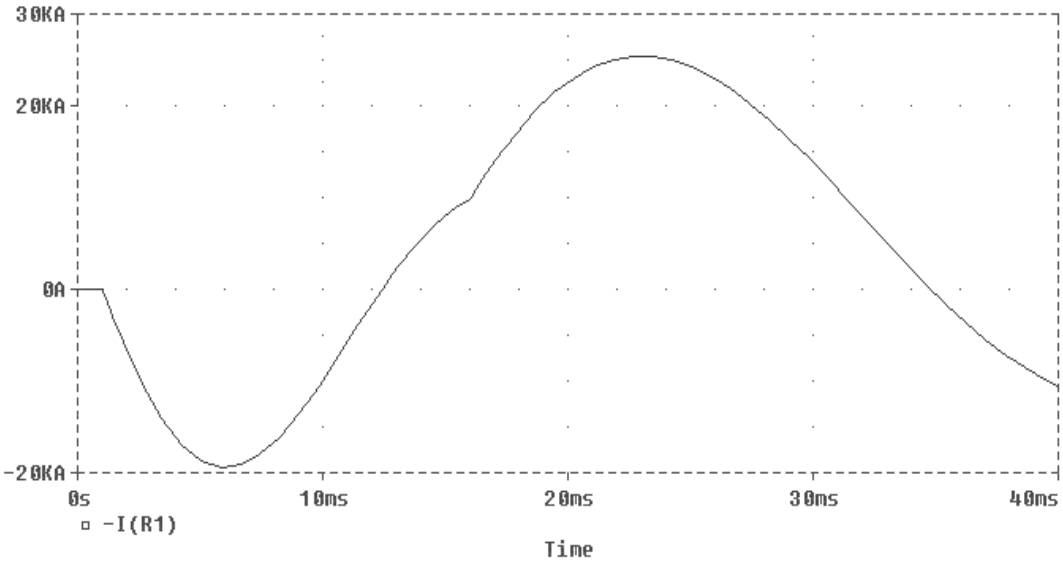

Figure 2.4: Current waveform from ohmic system version 1

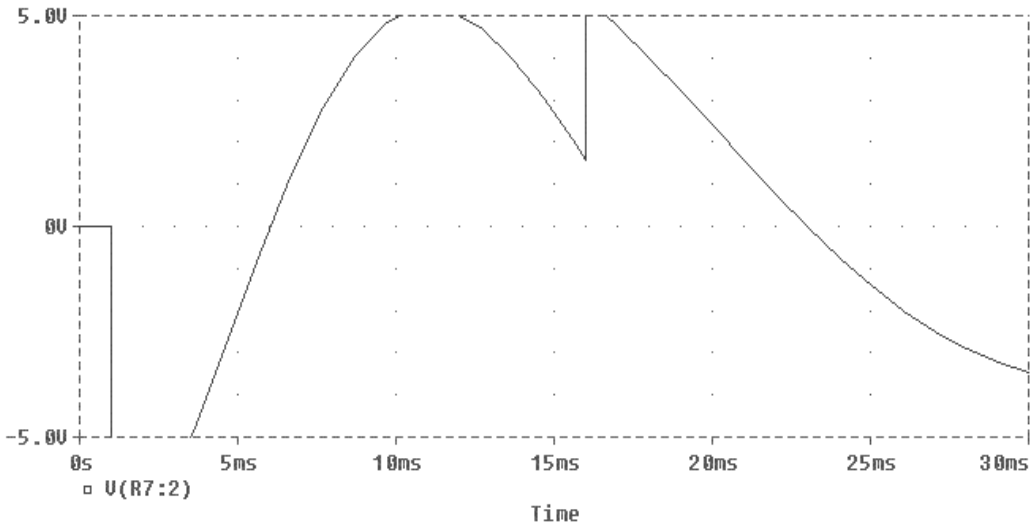

Figure 2.5: Loop voltage waveform from ohmic system version 1

Element	**Values**		
C1	C=73 mF	V=1000 V	E=36.5 kJ
C2	C=220 mF	V=1050 V	E=121.2 kJ
L_{OH}	L=113 μH	R=5 mΩ	
L_{Q3}	L=179 μH	R=1.5 mΩ	

Table 2.4: Ohmic heating circuit version 2 parameters

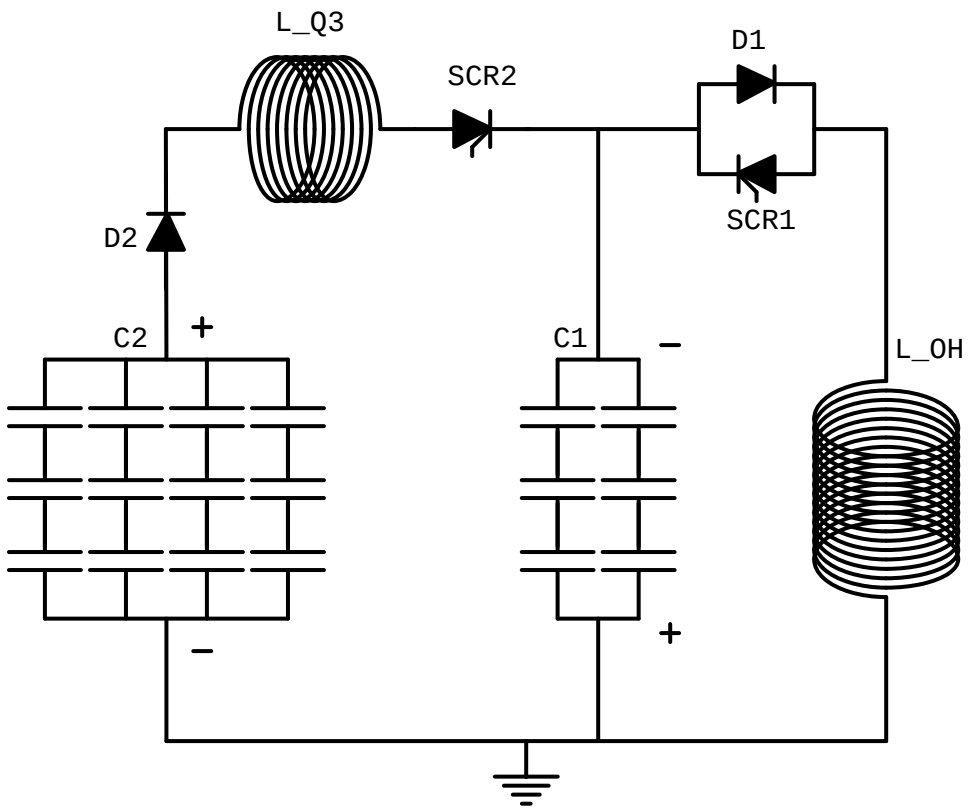

Figure 2.6: Circuit diagram of ohmic system version 2

current formation. This upgrade included a rearrangement of the capacitor bank configuration, as well as the addition of an inductive choke into the OH2 portion. The inductor used consists of a set of three PPPL Q-3 coils connected in parallel, spaced 7.5 inches apart in a bracket mount. A schematic of the version 2 ohmic system is presented in figure 2.6, and values of the circuit components are listed in table 2.4.

C1 is fired through SCR1 at t=200 ms, driving current through the solenoid, just as in the version 1 design. It was advantageous to keep the OH1 stage identical during the ohmic circuit upgrade, so as to minimize the effort developing plasma startup waveforms. At t=214 ms, SCR2 is fired, opening C2 to the inductors Q3 and L_{OH}. Because of the high inductance of Q3, the Q3 contribution to I_{OH} is limited for several ms. After t$\sim$15 ms, C1 has completely discharged, and I_{OH} is supplied entirely from C2. Near the end of the current rampup, at t $\sim$22 ms, the ring-through of C1 supplies some positive current to L_{OH}, which acts to keep V_{loop} at nearly 2 V for several ms. The solenoid current waveform and resultant loop voltage are presented in figures 2.7 and 2.8. As with figures 2.4 and 2.5, these figures were produced with the PSPICE circuit modeling package, but the actual waveforms are indistinguishable from the modeled data.

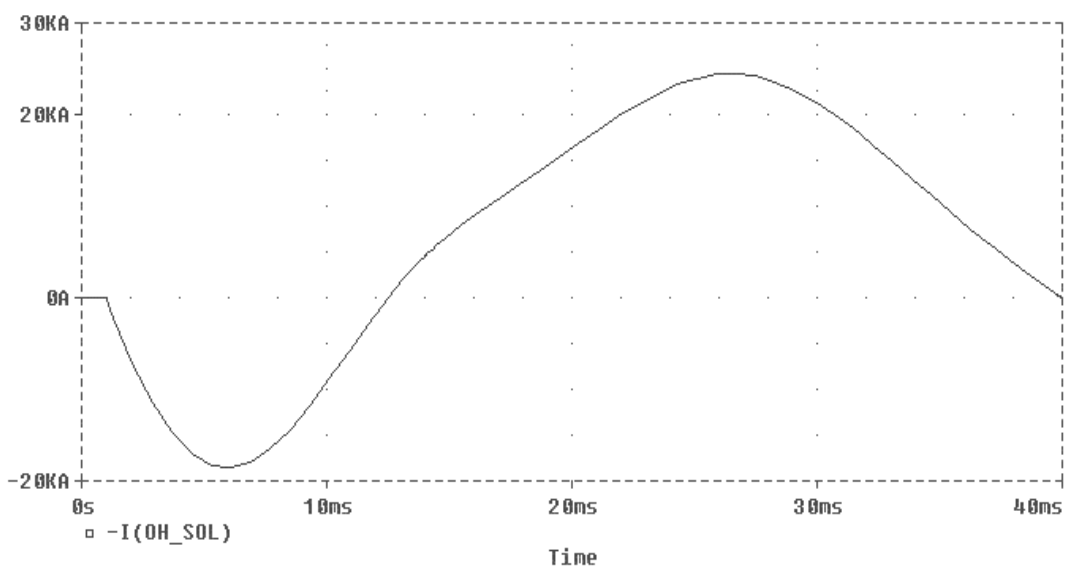

Figure 2.7: Current waveform from ohmic system version 2

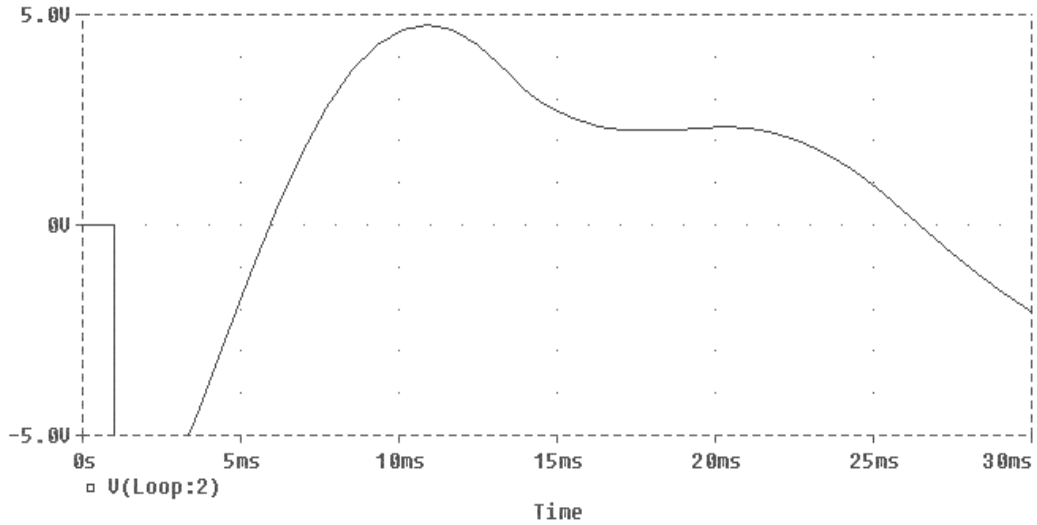

Figure 2.8: Loop voltage waveform from ohmic system version 2

The current through the ohmic solenoid is measured with a Rogowski coil consisting of Kapton-coated windings around a flexible 32-inch long, 3/16 inch diameter plastic tube. The windings are wound ∼75 per inch, and the measured inductance of this coil is 620 μH. The signal is sent to a PDX model E1605-2 integrator and timing module, set to 10 ms integration time. The output of the Rogowski coil and integrator combination was calibrated in February 1999 to be 0.023 V/kA, or 43.5 kA/V.

2.3.2 Toroidal and Poloidal Field Coil Power Systems

The CDX-U poloidal field set includes four pairs of coils, color coded for easy reference. This set includes a vertical field coil pair (blue), top/bottom shaping field coils (orange), a null-field coil (yellow), and a coil pair (green) to correct for the fringe fields at the ends of the ohmic solenoid, which are exacerbated by strong eddy currents induced in the thick steel inner flange ring on the upper and lower vessel flanges. The coil locations are listed in table 2.5, and shown schematically in figure 2.9.

The green coil is powered by a fast capacitor bank, so that the current waveform roughly matches the loop voltage waveform from the ohmic circuit, which drives

Coil	Color	R(cm)	Z(cm)	W(cm)	H(cm)
Vertical	Blue	83.3	±36.0	3.0	3.8
Shaping	Orange	39.9	±84.0	3.0	6.7
OH Correction	Green	10.9	±48.6	3.7	7.4
Null Field	Yellow	70.3	±79.2	2.2	4.4

Table 2.5: CDX-U poloidal field coil locations

the flange eddy currents that the green coil is meant to cancel. The yellow coil is also driven by a fast capacitor bank, and is oriented to oppose the blue coils in order to form a null vertical field during the plasma startup phase.

The blue, orange, and toroidal field coils are individually powered by a set of Robicon power supplies originally used as the shaping field supplies for the PBX-M tokamak. A summary of the coil electrical characteristics and power supplies is presented in table 2.6.

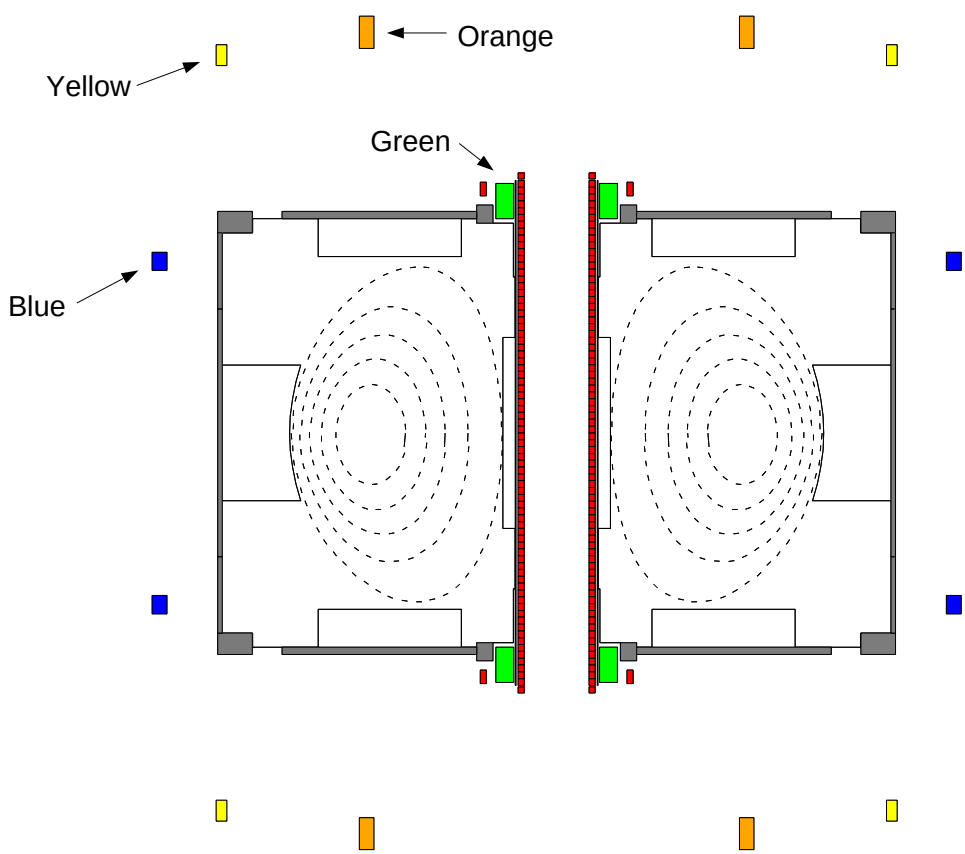

Figure 2.9: CDX-U poloidal field coil geometry

Coil	Color	turns	L (μH)	R (mΩ)	Power source
Toroidal		128	5600	154	500 V, 20 kA Robicon PS
Vertical	Blue	15	603	31	300 V, 5 kA Robicon PS
Shaping	Orange	19	520	25	300 V, 5 kA Robicon PS
OH Correction	Green	51	300	24	660 V, 22 mF cap bank
Null Field	Yellow	2	13.5	2.5	580 V, 50 mF cap bank

Table 2.6: Poloidal Field Electrical Characteristics

2.3.3 RF Heating System

CDX-U is equipped with a 12 MHz high-harmonic fast-wave (HHFW) RF heating system capable of delivering $\sim$ 200 kW of RF power. The majority of this system was developed as part of [Menard, 1998], with the subsequent addition of the final high-power amplification stage. A brief overview is presented here.

The HHFW system is composed of a 12 MHz signal generator and multi-stage amplification system, a pair of impedance matching networks, and a two-strap rotatable antenna.

The amplification stage consists of a Wavetek tunable signal generator, which produces $\sim$ 10 mW. This signal is fed through a 19 dB attenuator chain, then through an Amplifier Research model 100L119 amplifier, which amplifies the signal to $\sim$200 W. The signal is further amplified through a Henry Radio model 5K amplifier, bringing the power to $\sim$ 1 kW, and through a final power amplifier custom built at PPPL, bringing the signal to $\sim$200 kW.

The final output is then fed to a pair of impedance matching networks. The impedance of each strap is 50 Ω, and each strap is located at the end of a 20 m flexible RG-214 transmission line (characteristic impedance of 50 Ω). The strap impedance is nearly entirely inductive, though, necessitating the impedance matching networks to convert the antenna strap impedance to a real 50 Ω load.

The RF antenna is mounted on a rotatable vacuum seal, to provide flexibility in matching the antenna angle to the field-line pitch at the plasma edge. The curvature of the straps was designed to match a spherical plasma boundary (a good approximation in CDX-U), so that the curvature match is maintained at any strap angle. Faraday shields provide a semi-transparent ground plane between the straps and the antenna, and boron-nitride shielding on the antenna sides matches

the curvature of the boron-carbide outer limiter, to protect the antenna from plasma flow along the magnetic field lines (see fig. 2.1).

2.4 Diagnostics

2.4.1 Plasma Current Rogowski Coil

Plasma current is measured with a Rogowski coil placed inside the vacuum vessel, which encircles the plasma cross-section. The coil consists of two halves, with independent signal leads for each half-coil. The layout is shown schematically in figure 2.1. To find the net enclosed current, the signal from the two halves must be effectively subtracted from each other. This is done in practice by reversing the polarity of one of the signals with a short length of twin-axial cable with the leads switched, and the two signals are then fed to a summing integrator. The integrator used is a PPPL model E1939, with time constant set to 1 ms. The Rogowski coil and integrator combination were calibrated in March 1999 to be 0.0059 V/kA, or 169 kA/V.

2.4.2 Poloidal Mirnov Coils

CDX-U is equipped with an array of 30 poloidal magnetic pickup loops, mounted in a thin-walled stainless-steel tube encircling the plasma cross-section (see figure 2.1). The location and orientation of the probes is listed in table 2.7.

The Mirnov loop array was recalibrated in March 2000. A series of calibration shots were taken wherein each of the upper and lower Blue coils and the upper and lower Orange coils were fired individually, and the response of the Mirnov array was recorded. The response was then compared to the modeled magnetic field at each loop location, taking into account the orientation of the loop. The calibration factors complete the equation

$$\vec{B} \cdot \vec{l}\,[tesla] = B_{SIG}\,[V \cdot s] \;\times\; F_{CAL}\,\left[\frac{tesla}{V \cdot s}\right] \tag{2.1}$$

where $\vec{B}$ is the actual field at the Mirnov loop location, $\vec{l}$ is the loop orientation, B_{SIG} is the measured loop signal, and F_{CAL} is the calibration factor. F_{CAL} for each

Coil (old name)	**R (cm)**	**Z (cm)**	θ
Mag 01 (I3)	20	42	180
Mag 02 (I2)	30	42	180
Mag 03 (I1)	40	42	180
Mag 04 (O1)	50	42	180
Mag 05 (O2)	60	42	180
Mag 06 (O3)	65	39.5	135
Mag 07 (O4)	68	35	90
Mag 08 (O5)	68	25	90
Mag 09 (O6)	68	15	90
Mag 10 (O7)	68	5	90
Mag 11 (O8)	68	-5	90
Mag 12 (O9)	68	-15	90
Mag 13 (O10)	68	-25	90
Mag 14 (O11)	68	-35	90
Mag 15 (O12)	65	-39.5	45
Mag 16 (O13)	60	-42	0
Mag 17 (O14)	50	-42	0
Mag 18 (I16)	40	-42	0
Mag 19 (I15)	30	-42	0
Mag 20 (I14)	20	-42	0
Mag 21 (I13)	15	-39.5	-45
Mag 22 (I12)	11	-35	-90
Mag 23 (I11)	11	-25	-90
Mag 24 (I10)	11	-15	-90
Mag 25 (I9)	11	-5	-90
Mag 26 (I8)	11	5	-90
Mag 27 (I7)	11	15	-90
Mag 28 (I6)	11	25	-90
Mag 29 (I5)	11	35	-90
Mag 30 (I4)	15	39.5	-135

Table 2.7: Location and orientation of B_θ loops, with θ measured counter-clockwise from the positive R direction.

loop is determined by

$$F_{CAL}\ \left[\frac{tesla}{V \cdot s}\right] = \frac{B_{CALC}\ \left[\frac{Tesla}{kA \cdot turn}\right] \times I_{COIL}\ [kA \cdot turn]}{B_{SIG}\ [V \cdot s]} \tag{2.2}$$

where B_{CALC} is the modeled field. A plot of B_{CALC} for each coil in response to each of the Blue and Orange coils is shown in figure 2.10. In practice, the calibration factor for each loop was determined by the calibration shot using the coil which produced the highest absolute response, i.e. Orange-upper was used to calibrate loops 1-4, Blue-upper for loops 5-10, etc.

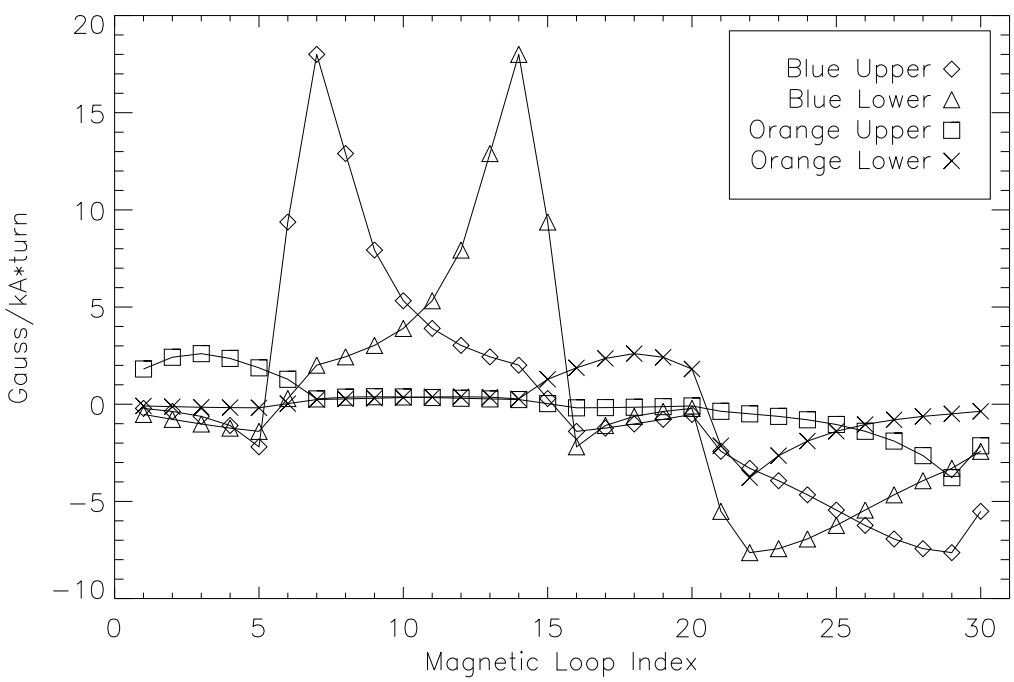

Figure 2.10: Modeled response of the CDX-U Mirnov loop set to each of the poloidal field coils fired individually. The coil producing the highest absolute response was used for calibration of each loop (i.e. Orange Upper was used to calibrate loops 1-4, Blue Upper for loops 5-10, etc.).

The Mirnov loop array is normally digitized at 250 kHz, and has been regularly used to observe edge MHD activity, and to assist in the development of plasma startup waveforms. An image of the typical response of the Mirnov array to edge

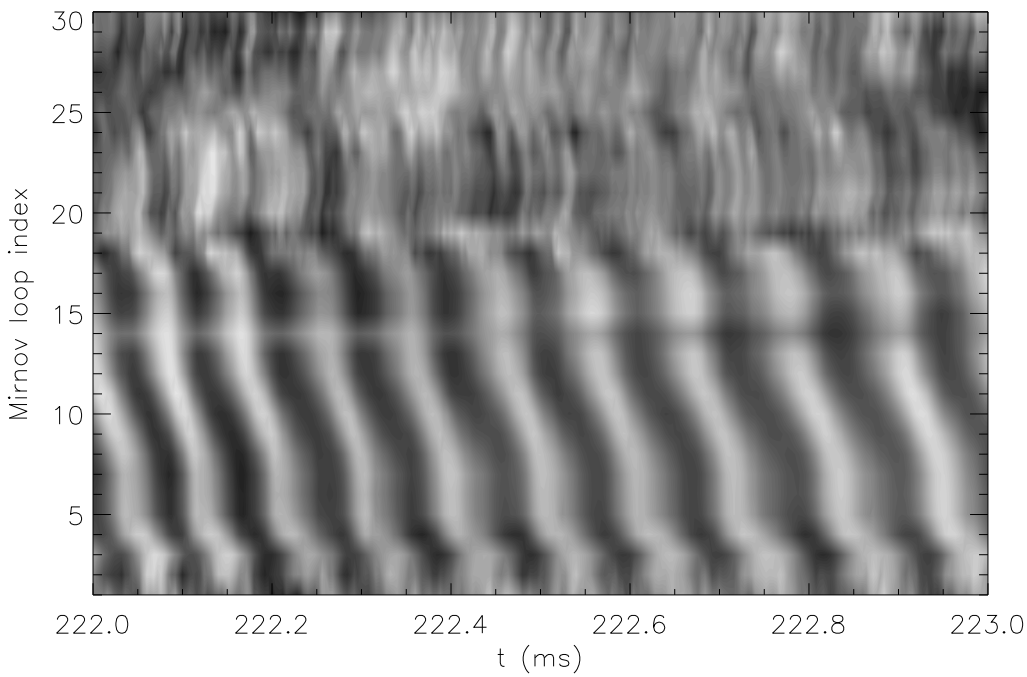

Figure 2.11: Typical response of the Mirnov array to edge MHD activity. A dominant m=2, n=1 mode (∼10 kHz) is visible on the entire array, as well as a higher frequency (∼40 kHz) mode visible on the inboard loops (indices 20-30).

MHD activity is shown in figure 2.11. A dominant m=2, n=1 mode (∼10 kHz) is visible on the entire array, as well as a higher frequency (∼40 kHz) mode visible on the inboard loops (indices 20-30).

The magnetics data is also used in an ongoing effort to produce equilibrium reconstructions using the EFIT code, but results from this effort have proven difficult to obtain. The ramping rates of the coil and plasma currents in CDX-U are relatively fast compared to the vessel-current damping time, particularly in the thick steel rings at the upper and lower vessel flanges. Because of this, large eddy currents are produced which are present during the entire plasma discharge. Though it has been possible to accommodate these eddy currents with correction coils and discharge programming to provide effective plasma startup and control, this effect introduces large, poorly diagnosed responses in the magnetic signals. These effects are exacerbated by the placement of the Mirnov loops, which is in many cases closer to the vessel wall than to the plasma current.

Despite this limitation, EFIT and JSOLVER have both been used to produce MHD equilibria using constraints provided by the other plasma diagnostics, such as the total plasma current, toroidal field, the plasma shape, and the location of the q=1 and q=2 magnetic surfaces. An example of a typical equilibrium is shown in figure 2.12.

2.4.3 ψ Loops

A set of 11 poloidal flux loops is mounted on the center-stack to measure loop voltage, which can be time integrated to provide a measure of poloidal flux (ψ). The midplane loop is used for the V_{loop} measurement, and all signals are digitized and integrated to provide 11 ψ measurements. The location of the ψ loops is listed in table 2.8.

2.4.4 Microwave Interferometer

CDX-U is equipped with a single-channel 140 GHz microwave interferometer, mounted on a moving stage which provides the capability of radial shot-to-shot scans. The beamline is vertical through the plasma, directed through windows at the top and bottom of the vacuum vessel. The entire microwave system including steering

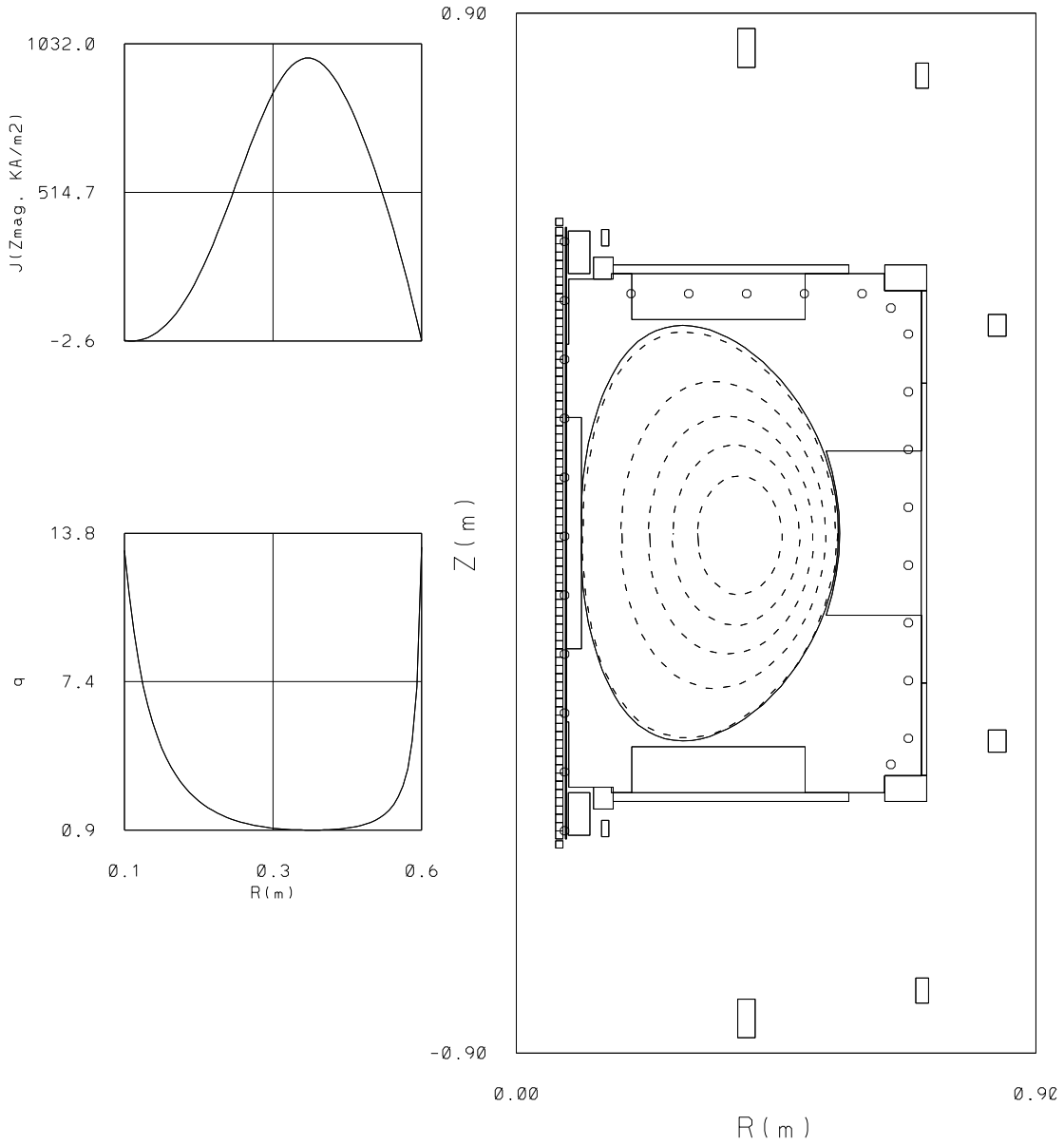

Figure 2.12: Typical EFIT equilibrium, produced *without* the use of the Mirnov array, due to large errors introduced by vessel eddy-currents. The equilibrium is constrained by other plasma properties such as total plasma current, toroidal field, plasma shape, and location of q=1 and q=2 magnetic surfaces.

Loop index	R (cm)	Z (cm)
$\psi 01$	8.5	51.0
$\psi 02$	8.5	40.8
$\psi 03$	8.5	30.6
$\psi 04$	8.5	20.4
$\psi 05$	8.5	10.2
$\psi 06$	8.5	0.0
$\psi 07$	8.5	-10.2
$\psi 08$	8.5	-20.4
$\psi 09$	8.5	-30.6
$\psi 10$	8.5	-40.8
$\psi 11$	8.5	-51.0

Table 2.8: Location of ψ loops mounted on the CDX-U center-stack. Loop $\psi 06$ is used for V_{loop} measurements.

mirrors is mounted on a remotely-controllable moving stage which provides major-radial coverage of 34- 58 cm. The hardware was constructed in 1989, and is described in [Forest *et al.*, 1990]. Remote scanning capability and the modified Abel-inversion data analysis routines were developed as part of this thesis.

The plasma and reference output signals are connected to an amplitude and phase detector, and the phase detector output signal is digitized for subsequent analysis. The plasma interferometer output phase difference is described in [Hutchinson, 1987] and satisfies the relation

$$\Delta\phi = \frac{\lambda}{m_e c^2} \frac{e^2}{4\pi\epsilon_0} \int n_e dl \tag{2.3}$$

For 140 GHz microwaves, $\lambda = 2.14$ mm, and $\frac{\lambda}{m_e c^2}\frac{e^2}{4\pi\epsilon_0} \approx 6 \times 10^{-18}$ m^2. Each change of $\Delta\phi = 2\pi$ is visible on the phase detector output as one fringe, so that the total line-integrated electron density is given by

$$\int \mathrm{n_e dl} \approx 1 \times 10^{18}\ \mathrm{m}^{-2} \text{ per fringe.} \tag{2.4}$$

A plot of the interferometer output for a typical shot is shown in figure 2.13, both in raw form (a) and after the application of a fringe-counting routine (b).

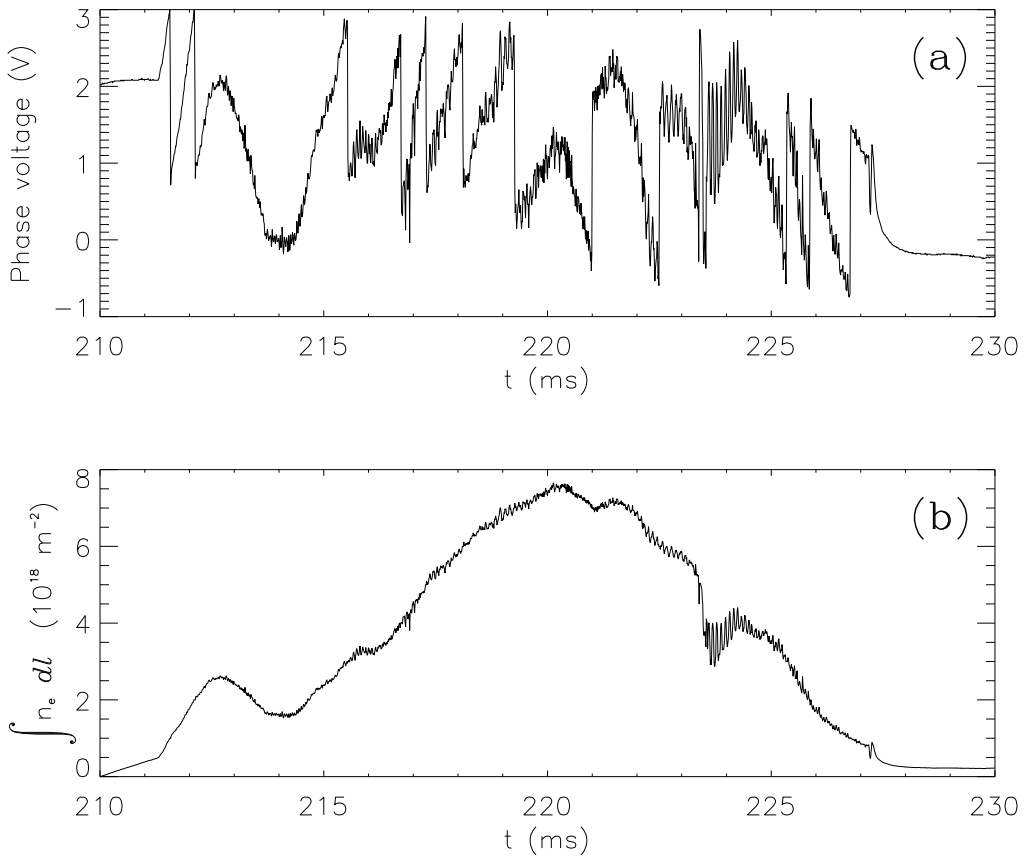

Figure 2.13: Interferometer output for a typical shot, both in raw form (a) and after the application of a fringe-counting routine (b).

The remote movement control of the inteferometer, coupled with the reproducibility of the CDX-U plasma, allows for shot-to-shot density scans covering slightly more than half of the major-radial plasma extent. An modified Abel-inversion routine is used to derive a radial n_e profile from the line-integrated data. The method is to first take a parameterized model density profile (as a function of normalized flux-function) and map it onto physical space, using the four global parameters R_0, a, κ (elongation), and δ (triangularity). The model density profile is then used to produce a set of model line-integrated signals corresponding to the locations of the experimental data points. Typically data points are taken from R=35 cm to R=60 cm in 2.5 cm increments. The parameters of the model density profile are then adjusted until a best fit is reached between the modeled and experimental line-integrated data.

Figure 2.14 shows modeled and experimental profiles for a typical CDX-U plasma. Figure 2.14a is a best-fit hollow model profile taken at t=214.0 ms, showing the early plasma formation at the edge and an outward-shifted plasma center due to an imbalance in the plasma current and the vertical field. Figure 2.14b shows the resulting line-integrated signals from the model (solid line) and measured data (squares). Figures 2.14c and 2.14d correspond to similar data for the same shot, but at t=219.0 ms, by which time the density has fully evolved to a peaked profile.

2.4.5 Multipoint Thomson Scattering

A major portion of this thesis work is the design and construction of a multi-point Thomson scattering diagnostic for electron temperature and density profiles. The system is fully described in chapter 3.

2.4.6 Electron Bernstein Wave Temperature Diagnostic

A new electron temperature diagnostic is under development on CDX-U which is a variation on the conventional electron cyclotron emission technique [Efthimion *et al.*, 1999b; Taylor *et al.*, 2001]. Though the development of this diagnostic is not explicitly part of this thesis work, early data from the EBW system is an important part of these transport studies, particularly the cold-pulse experiments described in chapter 4. An overview of the EBW system is provided here.

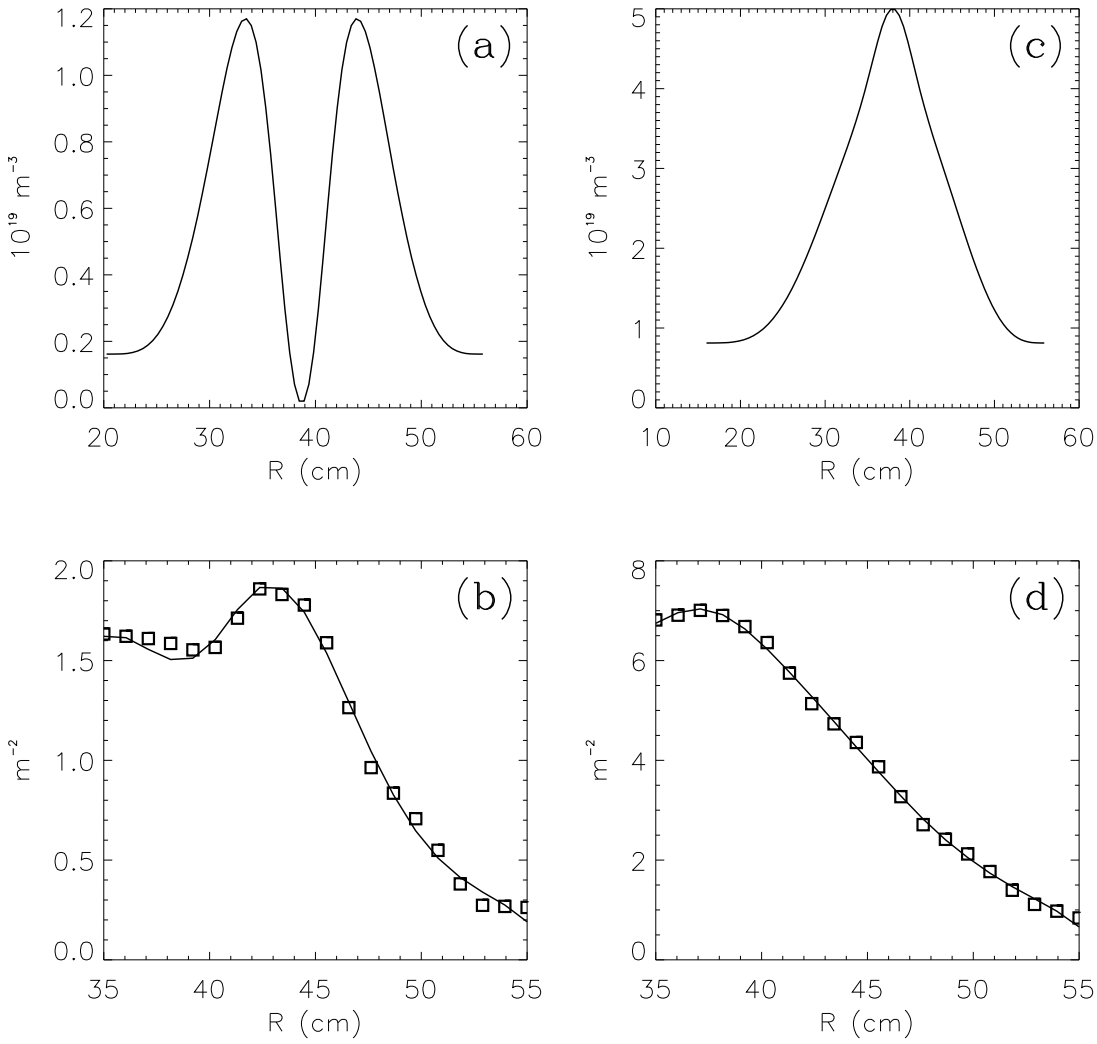

Figure 2.14: (a) Best-fit hollow model density profile taken at t=214.0 ms, showing early plasma formation at edge and outward-shifted plasma center due to imbalance in plasma current and vertical field; (b) Resulting line-integrated signals from model (solid line) and measurements (squares); (c,d) Similar data for peaked density profile taken at t=219.0 ms, showing fully evolved density profile.

Conventional tokamaks have used the emission of electron-cyclotron waves (ECE) at the plasma edge as a means of measuring the electron temperature over extended plasma volumes [Hutchinson, 1987]. At each point in a volume of magnetically confined plasma, electrons are gyrating at a characteristic frequency $\Omega_e = \frac{E \cdot B}{m_e \cdot c}$. Electromagnetic waves at integer harmonics of this frequency are emitted locally and propagate through the plasma, allowing detection at the edge. Since $\Omega_e \propto B$, and the total magnetic field magnitude varies approximately as 1/R (the deviation from 1/R coming from the poloidal-field component), a range of frequencies for detection can be chosen to correspond to a range of locations in the plasma.

If the plasma is locally "optically thick" ($\tau > 2$) to waves at the emission frequency, the emission intensity is that of a blackbody at the electron temperature, $I(\omega) = \frac{\omega^2 T_e(R)}{8\pi^3 c^2}$ (Rayleigh-Jeans law). Calibrated measurement of the emission intensity can thus provide a localized measurement of electron temperature.

Many magnetically confined plasmas, including ST's, cannot use this technique because of accessibility or wave-damping limitations. In ST's, the plasma pressure is high compared to the magnetic field, or, equivalently, $\omega_p \gg \Omega_e$, where the plasma frequency $\omega_p = \sqrt{\frac{n_e e^2}{m_e \epsilon_0}}$. Because of this, the emission does not propagate to the edge, preventing detection. Additionally, the requirement of optical thickness $\tau > 2$ to satisfy the blackbody condition in practice limits conventional ECE diagnostics to plasmas with $T_e > 1$ keV.

Early ECE measurements on PLT [Hosea *et al.*, 1977] were explained as electron Bernstein waves (EBW) emitting at blackbody levels, propagating to the upper-hybrid layer, and mode-converting to extraordinary mode emission.

From the electrostatic dispersion relation for a collisionless hot plasma (see [Bekefi, 1966; Stix, 1962]), the real and imaginary wavenumber for propagation perpendicular to the magnetic field can be calculated:

$$Re(k_\perp) \approx \left(\frac{4}{\sqrt{\pi}}\right)^{1/3} \left(\frac{\Omega_e}{v_{te}}\right) \left(\frac{{\omega_{pe}}^2}{\omega^2 - (\Omega_e - \Delta\Omega_e)^2}\right)^{1/3} \tag{2.5}$$

$$Im(k_\perp) \approx \frac{A\,\sqrt{\pi}\,{\omega_{pe}}^2\,{\Omega_e}^2}{Re(k_\perp^2)\,v_{te}^3} \tag{2.6}$$

where $\Delta\Omega_e = \frac{\Omega_e {v_{te}}^2}{c^2}$, v_{te} is the electron thermal velocity, and $A = F(\omega, \Omega_e, T_e)$ is defined in [Bornatici *et al.*, 1983].

The wave propagation can be calculated from $Re(k_\perp)$, and the optical thickness τ can be calculated from $Im(k_\perp)$. In CDX-U, $\tau \sim 300$ for the fundamental cyclotron frequency, which easily satisfies the blackbody condition $\tau > 2$. Accessibility can be achieved using a scenario in which the EBW propagates to the upper hybrid layer and mode converts to an electromagnetic extraordinary mode, which either propagates out of the plasma or tunnels through a narrow cutoff layer and mode converts to an ordinary mode which propagates out of the plasma. The first scheme (X-mode detection) has been studied in [Wu *et al.*, 1996] and the second scheme (O-mode detection) was used in the W7-X stellarator for EBW detection [Laqua and Hartfuss, 1998] and also in the reverse direction to achieve heating ([Laqua *et al.*, 1997]). A map of relevant frequencies as a function of position is shown in figure 2.15. Included are the upper and lower X-mode cutoff frequencies f_R and f_L, the upper-hybrid frequency f_{UH}, the plasma frequency f_{pe}, and the first three harmonics of the electron cyclotron frequency f_{ce} $\left(= \frac{\Omega_e}{2\pi}\right)$. Also shown is the frequency range of the heterodyne radiometer, described below.

The heterodyne radiometer system is shown in figure 2.16. Both a wide angle spiral antenna (AEL Colmar ASO-1503A) and a narrower angle ridged waveguide antenna have been used on CDX-U, mounted on a quartz window oriented radially, facing the center-stack. The antenna output is sent to a second harmonic mixer, where it is mixed with a local oscillator signal provided by a sweepable 2-4 GHz signal generator. The mixer output is amplified and filtered in a double sideband intermediate frequency section, and then rectified by a video detector and amplified for final output.

One of the main difficulties in the development of the EBW system as a temperature diagnostic has been the uncertainty in the density profile, particularly at the edge where the cutoff thickness is critically dependent on the density gradient scale length. Indeed, interpretation of the EBW data must not ignore the possibility that the intensity of the detected EBW signal depends on edge parameters only, and is only marginally affected by the core conditions, if at all. The coldpulse experiments described in chapter 4 demonstrate that the intensity of the EBW signals does indeed depend on the core conditions, and that even in the absence of

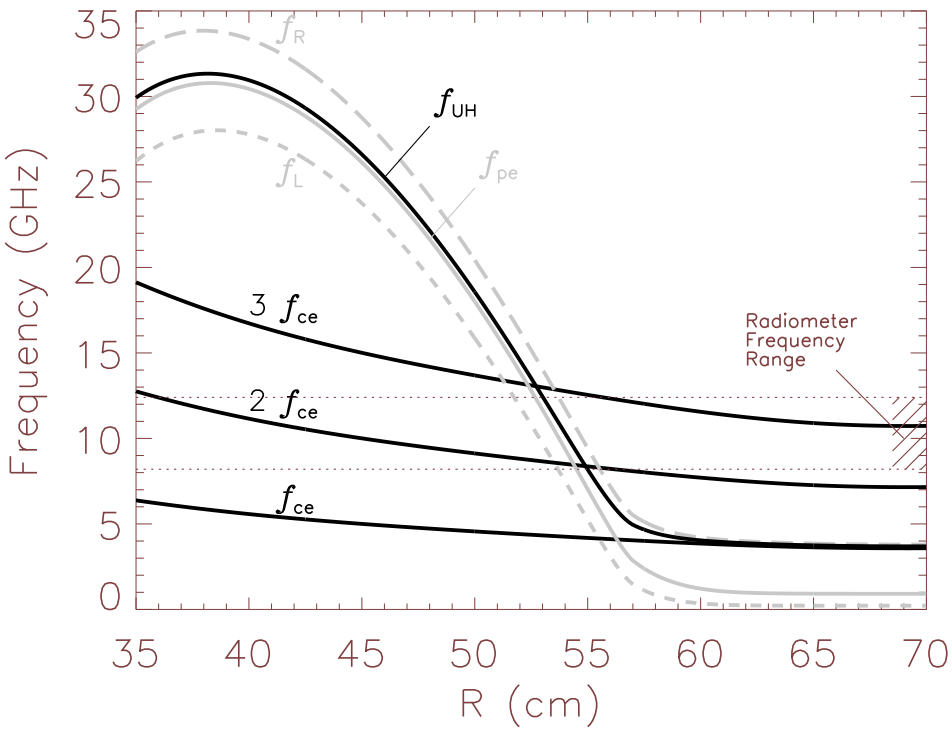

Figure 2.15: Characteristic frequencies in CDX-U, including the the upper and lower X-mode cutoff frequencies f_R and f_L, the upper-hybrid frequency f_{UH}, the plasma frequency f_{pe}, and the first three harmonics of the electron cyclotron frequency f_{ce}. The frequency range of the heterodyne radiometer is also indicated.

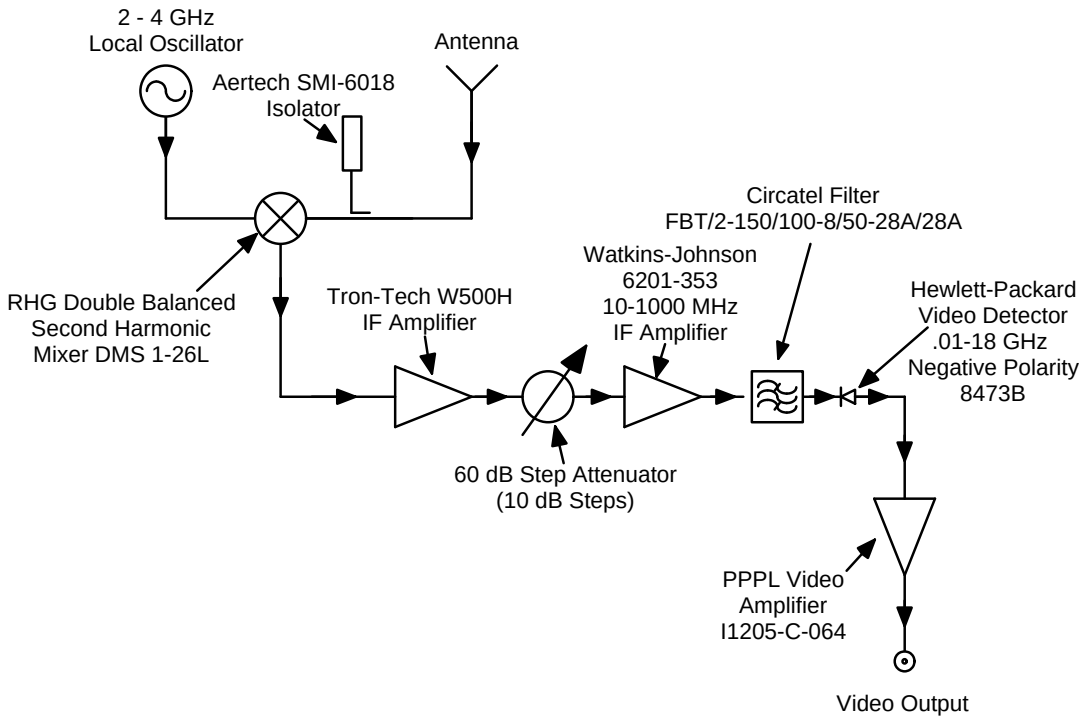

Figure 2.16: Schematic of the EBW radiometer.

absolute temperature calibration, it can serve as an effective diagnostic of temperature events, resolving temperature modulations as a function of time and plasma position.

2.4.7 Triple Langmuir Probe

A triple Langmuir probe, on loan from the PEGASUS group at the University of Wisconsin, was used to measure electron temperature and density at the plasma edge. The triple probe configuration is advantageous over a conventional Langmuir probe which requires a voltage sweep and I-V characteristic for each single measurement. The triple probe is comprised of three probe tips and provides instantaneous measurement of temperature and density, using a simple electronic circuit to bias and correlate the probe tips. The PEGASUS probe is actually comprised of four probe tips, providing simultaneous measurement of temperature (three tips) and density (one tip). An early description of the triple probe configuration is given in [Chen and Sekiguchi, 1965].

For a Maxwellian electron distribution at T_e, the electron current density at a probe tip held below the plasma potential, $V < \phi_P$ is given by

$$J_e \approx -J_e^{sat} \exp[\frac{e(V-\phi_P)}{k_B T_e}] \tag{2.7}$$

with

$$J_e^{sat} = n_e e \sqrt{\frac{k_B T_e}{2\pi m_e}} \tag{2.8}$$

For $\frac{e(V-\phi_P)}{k_B T_e} < -\frac{1}{2}$ (sheath formation) and $T_e \gg T_i$, the saturated ion current density (for ion species s) is roughly constant, given by

$$J_{is}^{sat} = n_{is} Z_{is} e \sqrt{\frac{k_B T_e}{m_{is}}} \tag{2.9}$$

The temperature ordering assumption is satisfied in CDX-U, since the ion-electron thermal equilibration time is comparable to the energy confinement time. (If $T_e \approx T_i$ then the value of J_{is} will increase by a factor of $\sqrt{2}$.)

A diagram of the triple probe circuit is shown in figure 2.17. Circles represent the

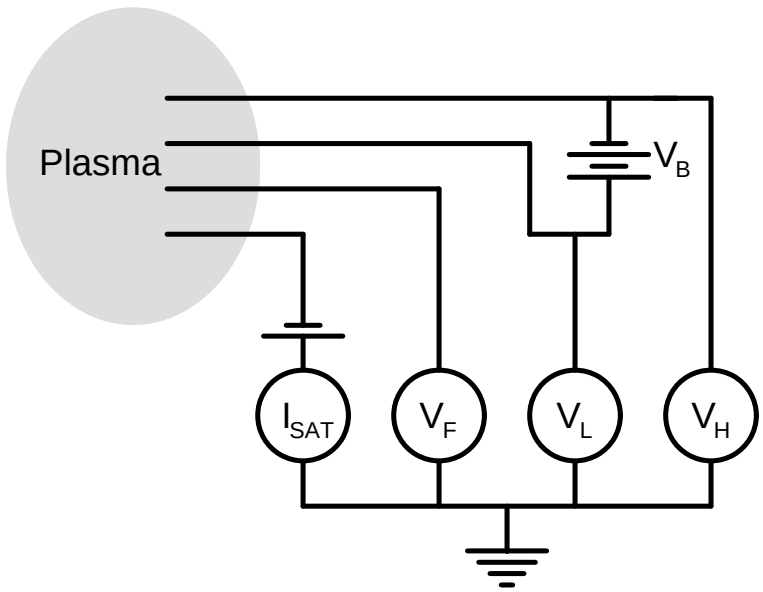

Figure 2.17: Biasing and metering circuit for the triple probe, indicating the battery, three voltmeters and one ammeter necessary to provide simultaneous measurement of electron temperature and density.

three voltmeters and one ammeter necessary for the measurement. The voltmeters, as is conventional, also represent high impedance circuit elements, allowing the probes to float.

Electron temperature is determined by the simultaneous solution of two equations, one provided by the floating probe potential V_F and one provided by the two probes biased at V_H and V_L. The voltage of the floating probe V_F must satisfy the condition that no net current is drawn, i.e.

$$I_e^{sat} + I_i^{sat} = 0 \tag{2.10}$$

where

$$I_e^{sat} = A_e J_e^{sat} \qquad \text{and} \qquad I_i^{sat} = \sum_s A_{is} J_{is}^{sat} \tag{2.11}$$

Defining $\alpha = I_e^{sat}/I_i^{sat}$, the floating potential satisfies

$$V_F = \phi_P - \frac{k_B T_e}{e} \ln \alpha \tag{2.12}$$

The two probes at V_H and V_L are biased with respect to each other by $V_B = V_H - V_L$, done in practice with a set of stacked 9V batteries. The probe pair $V_{H,L}$ is floating, so that both tips draw I_i^{sat}. The total electron current to the floating probe-pair must therefore balance $2I_i^{sat}$, leading to the equation

$$\left[\exp\left(\frac{eV_H}{k_B T_e}\right) + \exp\left(\frac{eV_L}{k_B T_e}\right)\right] = \frac{2}{\alpha}\exp\left(\frac{e\phi_P}{k_B T_e}\right) \tag{2.13}$$

Using equation 2.12 to substitute in the right-hand side of equation 2.13,

$$\left[\exp\left(\frac{eV_H}{k_B T_e}\right) + \exp\left(\frac{eV_L}{k_B T_e}\right)\right] = 2\exp\left(\frac{eV_F}{k_B T_e}\right) \tag{2.14}$$

or

$$\exp\left(\frac{e(V_H - V_F)}{k_B T_e}\right)\left[1 + \exp\left(\frac{-eV_B}{k_B T_e}\right)\right] = 2 \tag{2.15}$$

When $\frac{eV_B}{k_B T_e} \gg 1$, equation 2.15 is approximately solved by

$$T_e(eV) \approx \frac{V_H - V_F}{\ln 2} \tag{2.16}$$

A much more accurate approximate solution to equation 2.15, valid for all $\frac{eV_B}{k_B T_e}$ was derived in [Menard, 1998] and is used as the working equation to quickly derive the temperature at the CDX-U triple probe:

$$T_e(eV) \approx \frac{V_H - V_F}{\ln 2 - \ln\left(1 + 11.888(\frac{V_H - V_F}{V_B})^{3.57}\right)} \tag{2.17}$$

A working formula for the determination of electron density is based on equations 2.9 and 2.11, and is derived in [Menard, 1998], taking into account sheath effects and finite Larmor-radius effects:

$$n_e \approx \left(\frac{I_i^{sat}}{A_p e}\right)\left(\frac{m_p}{k_B T_e}\right)^{\frac{1}{2}}\frac{\bar{Z}}{\bar{Z}_\mu}\exp\left(\frac{1}{2}\right) \tag{2.18}$$

with the effective charge state $\bar{Z} = \sum_s \alpha_{is} Z_{is}$, $\bar{Z}_\mu = \sum_s \left(\frac{\alpha_{is} Z_{is}}{\mu_{is}}\right)$, the ion density fractions α_{is} satisfy $n_{is} = \alpha_{is} n_i$, and $\mu_{is} = m_{is}/m_{proton}$.

The CDX-U triple probe tips were replaced in January 2000 with a set machined by D. Cylinder. Figure 2.18 is a diagram of one tip and insulating sleeve. The effective probe area is computed to be $A_p = 10^{-5}$ m^2.

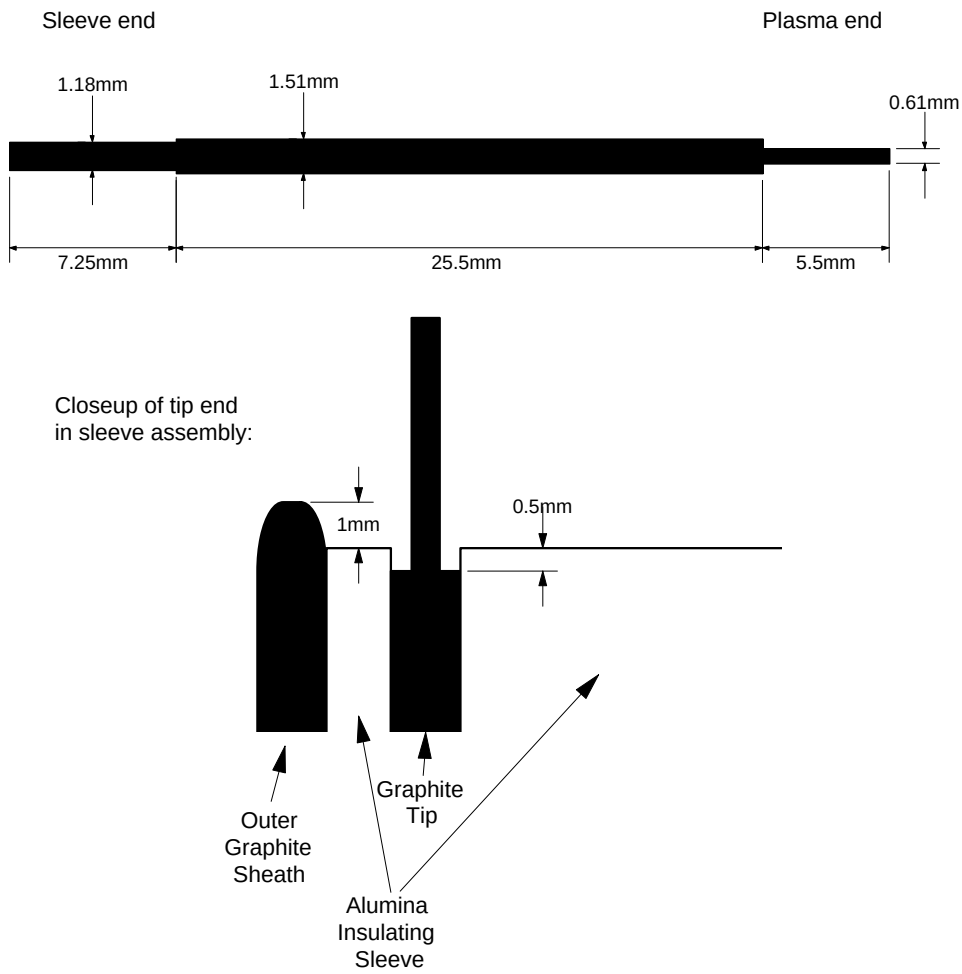

Figure 2.18: Diagram of triple probe tip and insulating sleeve, installed January 2000. Each probe tip is a single piece of machined graphite, and the four tips are held in a single insulating alumina sleeve. The entire assembly is surrounded by an outer graphite sleeve.

2.4.8 AXUV diode and Bolometer Array

Radiated power from CDX-U has been shown by spectral surveys to be almost exclusively composed of line emission from Oxygen and Carbon impurities. Although

CDX-U has a steel vessel and small areas of graphite, the limiting surfaces are B_4C, and thus the carbon impurity level is quite low. As a result, the bulk of the radiated power loss from CDX-U plasmas is from OIV, OV, and OVI ions emitting photons in the range 50-100 eV.

In order to provide a quick assessment of the relative radiated power level from CDX-U plasmas, a single AXUV diode is mounted on an extension tube attached to the the upper vessel flange, with a vertically viewing chord at R=34.2 cm. This diode is sensitive to a broad range of photon energies which includes the bulk of the radiated power spectrum for CDX-U, has quite uniform responsivity over this range, and has a fast response time. A typical trace from this diode is shown in figure 2.2.

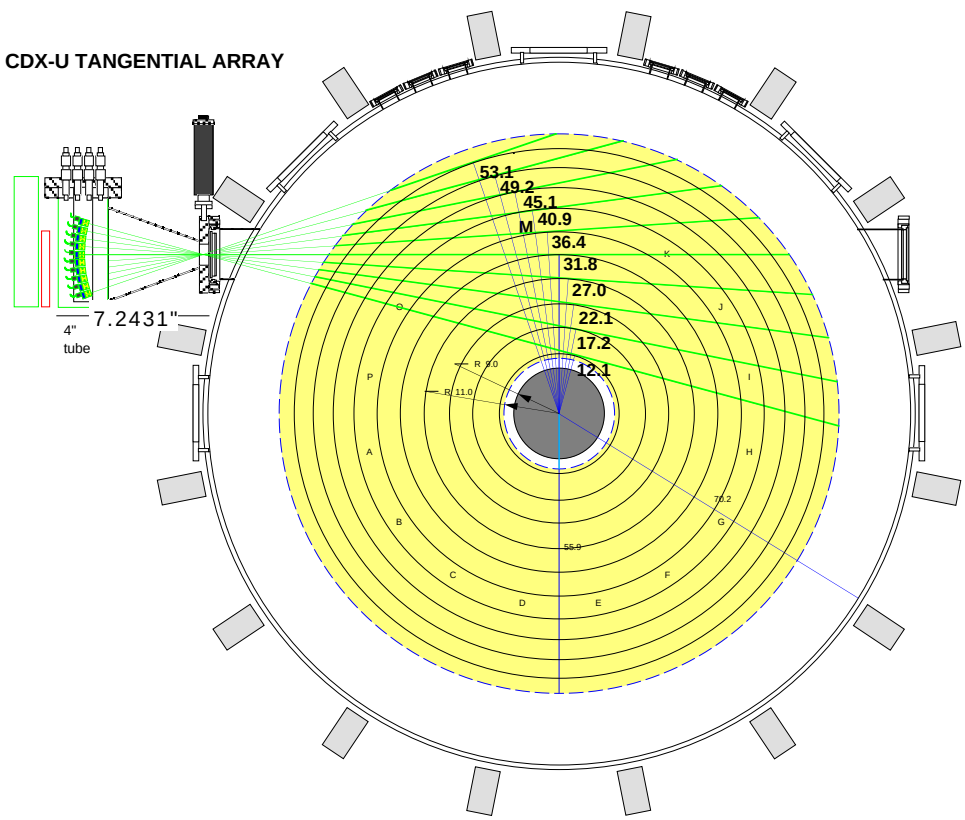

Figure 2.19: Diagram of the CDX-U bolometer array.

In addition to this single diode, CDX-U is equipped with a 10-channel AXUV photodiode array, looking at a series of collimated tangential sightlines arranged horizontally across the plasma midplane. The array uses a movable foil-filter set

at the entrance aperture to select the accepted energy range, including one setting with no filter (bolometer mode). Two filters that have been used on CDX-U are a 0.3 μm Ti foil for acceptance of CV light and a 0.5 μm Be filter for acceptance of AXUV OVI lines. This array is discussed in detail in [Soukhanovskii *et al.*, 2001], and is shown in figure 2.19.

2.4.9 Soft X-ray Array

CDX-U is equipped with a horizontally viewing soft X-ray (SXR) array which views 30 radial chords arranged vertically through the plasma core and edge. The SXR array layout is shown in figure 2.20. The detectors are biased surface-barrier diodes, and metal-foils are used at the entrance aperture as x-ray filters.

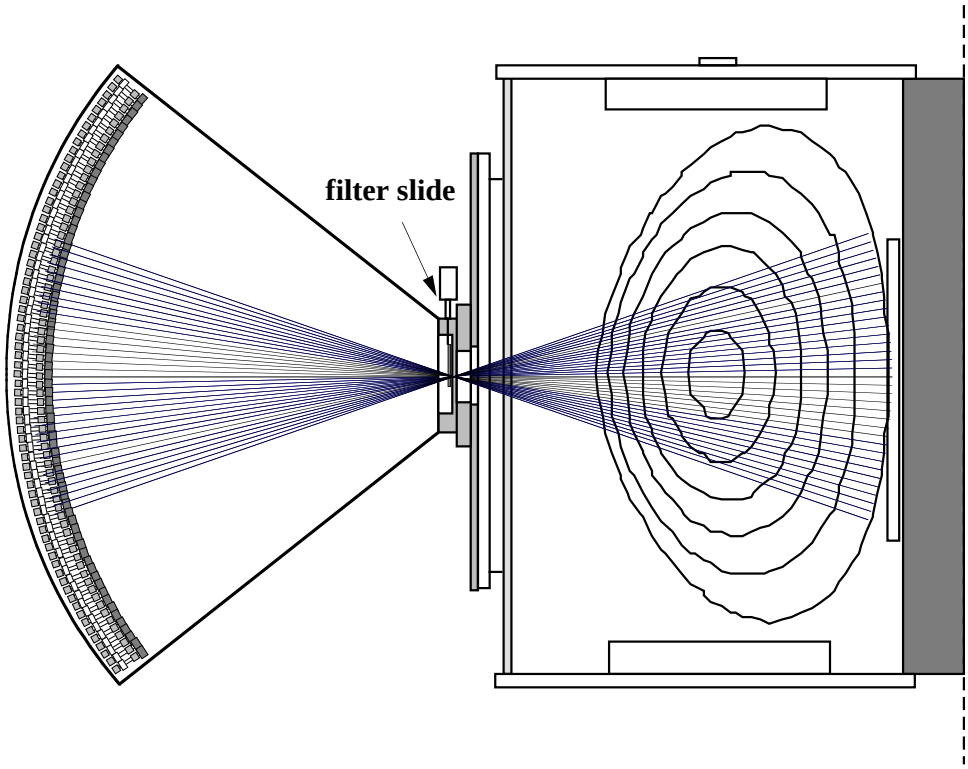

Figure 2.20: Diagram of the CDX-U soft x-ray array.

This array was used to track the spatial and temporal evolution of heat-pulses produced by sawteeth, as described in section 4.3. This was done using a 0.3 μm

Ti foil filter, which blocks out nearly all of the oxygen emission while admitting CV and CVI lines, which are highly T_e dependent.

This array has also been very effective for the observation of MHD activity, based on the accumulation of carbon in rotating magnetic islands [Stutman *et al.*, 1999]. The SXR array is also equipped with a 0.4 μm beryllium foil filter which isolates CVI emission lines, though this filter is rarely used due to the lack of CVI ($E_{ionization}$ = 490 eV) emission in CDX-U.

2.4.10 Multilayer Mirror Array

CDX-U is also equipped with a 10-channel array of multilayer mirror (MLM) based detectors, with collimated radial sightlines arranged vertically, similar to the SXR array. It has been shown that extreme ultraviolet multilayer mirrors can act as "mini-monochromators" with a very narrow accepted spectral range and fast time response, and can provide chord-integrated data for use in tomographic reconstruction of plasma emission profiles [Stutman *et al.*, 1997a]. The MLM array has been used with a mirror set tuned to OVI emission at 150 Å , and a mirror set tuned to LiIII emission at 130 Å. A diagram of the MLM array is shown in figure 2.21.

The development of the three spectroscopic arrays is a result of the collaboration with the Johns Hopkins University, and is primarily a result of the work of D. Stutman, with recent assistance from V. Soukhanovskii.

2.4.11 Fast Visible Camera

In order to observe visible emission at fast record rates, CDX-U uses a Kodak SR-Ultra Motion Corder fast framing camera. This camera is capable of recording up to 10,000 frames per second, though at a reduced resolution (128x34 pixels). Typically the camera is used at 1000 frames per second and 256x240 pixels resolution.

2.5 Data Acquisition and Storage

CDX-U uses a collection of integrated LabView software routines, CAMAC based timing modules and digitizers, and Iotech digital-to-analog converters to remotely control tokamak operation and data acquisition from two Sun workstations. The

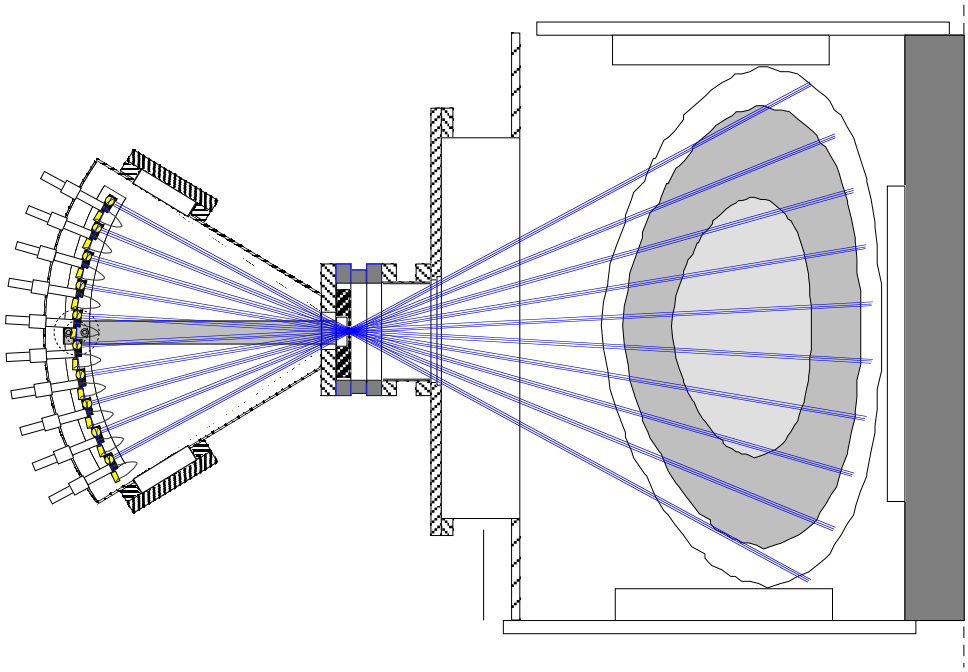

Figure 2.21: Diagram of the CDX-U multilayer mirror array.

control system, data acquisition system, and data file system were reconfigured and rewritten over the summer of 1998, and a description of the present system is described here.

2.5.1 Tokamak Control and Data Acquisition

As part of the 1998 CDX-U upgrade, a control room was developed to allow remote control of all aspects of tokamak operation and data handling from outside the locked test-cell. In the new configuration, CDX-U is remotely controlled using LabView software routines running on a pair of Sun workstations. Communication from the workstations to all other hardware is through GPIB connections, utilizing a set of fiber-optic GPIB extenders for each of three lines. This includes control commands sent from the workstations, and all data collection from the CAMAC-based waveform recorders. Triggering pulses for firing of capacitor banks, triggering of diagnostics and data acquisition waveform recorders is performed with a pair of Jorway 221/222 timing modules and several LeCroy 8501 timing units, which can be pre-programmed before each shot. The Robicon power supplies and the two

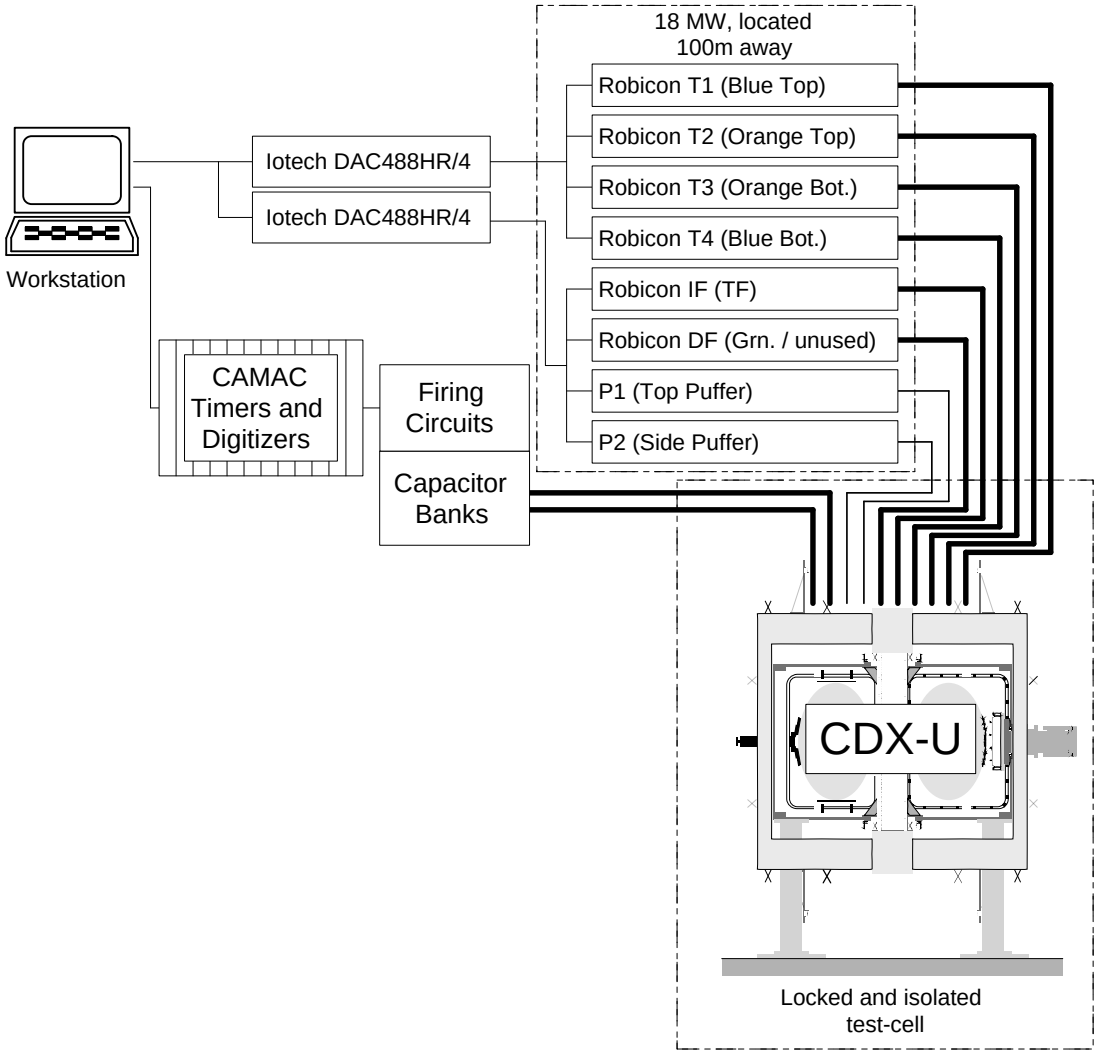

Figure 2.22: Schematic of the CDX-U control system, showing the path of data flow to the power systems, and the high-current cabling from the power systems to the tokamak.

Veeco PV-10 gas puffers used for fueling are controlled using waveforms from a pair of Iotech DAC488HR/4 four-channel digital-to-analog converters. The waveforms are produced, edited, and sent to the DAC's using a combination of IDL and LabView software routines. A schematic of the control system is shown in figure 2.22, indicating the flow of firing commands to the power supplies and capacitor banks, and the high-current cabling from the power systems to the magnetic field coils.

The shot-to-shot time delay is set in the software, and is counted down between shots. During this time, the timing settings of all triggered events can be independently entered from any of several control or diagnostic LabView sessions. The new triggering times are written to a set of files containing the timepoint data. Also during this time all digitizers are programmed and "armed". At t=-16 seconds, the timepoint files are read into the control program (this takes 2-3 seconds). At t=-11 seconds, the Jorway timing modules are programmed with the timing data. At t=0, a software trigger is sent to Jorway module 1, which then triggers the second Jorway module and the remaining diagnostics, waveform recorders and capacitor firing circuits. In this way, there are no software-induced delays in the triggering sequence.

Signals from all of the diagnostics are recorded on CAMAC based digitizing waveform recorders. CDX-U primarily uses LeCroy model 8210, 8212, and 6810 waveform recorders, and model 8100 amplifiers. Programming of the recorders is done through independent LabView routines for each diagnostic, and information is passed to the CAMAC modules through a GPIB interface. The contents of the three CAMAC crates is presented in tables 2.9 and 2.10. Note that CAMAC modules are used for both triggering and waveform recording, and indeed the timing units supply the stop trigger to the waveform recording modules.

Because of limited memory in each module and a long delay between t=0 (initial firing time) and plasma formation due to the ∼200 ms TF ramp-up time, each diagnostic is provided independent control over its recording window. For the main plasma data such as coil currents and basic plasma parameters, these are programmed from the main LabView module. For other diagnostics, the digitizers are pre-programmed independently, the triggering timepoint is written to a file, and the main LabView module reads this file and programs the triggering times accordingly. A table listing the digitization rates and time windows for each diagnostic is

Rack Layout (GPIB 1)			
Slot	**Module**	**Ch.**	**Waveform**
1	Jorway 221 (#1)	1	Ti-ball relay
		2	t_0: Jorway 222 (#2)
		3	t_0: Spectroscopy Racks
		4	t_0: DAC's
		5	t_0: I_P integrator
		6	Main DAQ
		7	OH1
		8	OH2
		9	Yellow
		10	Green
		11	Extra #1
		12	Extra #2
4	8210 (Probe)	1	V_H
		2	V_F
		3	V_L
		4	V_{SAT}
8	8212/8 (Coil waveforms)	1	TF
		2	Blue 1
		3	Blue 2
		4	Orange 1
		5	Orange 2
		6	Green
		7	OH
		8	Yellow
12	8212/32 (Main waveforms)	1	(unused)
		2	V_{loop}
		3	Fast ion gauge
		4	Top bolometer
		5	Limiter: Top
		6	Limiter: Bottom
		7	Limiter: Outer Upper
		8	Limiter: Outer Lower
16	8210 (I_P, n_e, RF2)	1	I_P
		2	Interferometer
		3	RF2
		4	RF2
20	8212/32 (RF1)	1-16	RF data
24/25	8901a GPIB Interface		

Table 2.9: Layout of the CDX-U diagnostic channels.

Rack Layout (GPIB 2)			
Slot	**Module**	**Ch.**	**Waveform**
2	8210	1-4	Magnetics
6	8210	1-4	Magnetics
10	8210	1-4	Magnetics
14	8210	1-4	Magnetics
22/23	Jorway 221/22 (#2)	1 3 5	Magnetics EBW Kodak camera
24/25	8901a GPIB Interface		

Rack Layout (GPIB 3)			
Slot	**Module**	**Ch.**	**Waveform**
2	8210	1-4	Magnetics
6	8210	1-4	Magnetics
10	8210	1-4	Magnetics
14	8210	1-4	Magnetics
19	6810 (EBW)	1-4	EBW Data
21	BNC adapter (EBW)		EBW voltage settings
22	3112 (EBW)		EBW output voltages

Table 2.10: Layout of the CDX-U diagnostic channels, crates 2 and 3.

presented in table 2.11.

Diagnostic	**Digitizer**	**# Ch.**	**Samp.**	**# Pts.**	Δt_{record}
Main waveforms	8212	8	20 kHz	1000	50 ms
Coil currents	8212	8	5 kHz	1500	300 ms
I_P, n_e, RF2	8210	4	100 kHz	5000	50 ms
Triple probe	8210	4	100 kHz	5000	50 ms
Magnetics, ψ loops	8210	30,11	250 kHz	7000	28 ms
SXR	8210	30	250 kHz	7000	28 ms
MLM, Bolo. arrays	8210	20	250 kHz	7000	28 ms
EBW	6810	4	200/1000 kHz	8k/32k	40/32 ms
RF1	8212	16	10 kHz	500	50 ms

Table 2.11: Digitization rates and recording windows for all CDX-U diagnostics.

2.5.2 File Storage

In order to facilitate the automation of data analysis and the combined use of several datasets from different diagnostics, a uniform data storage format was adopted in the summer of 1998. A directory tree based on experiment date and shotname is set up on the two large storage disks `/cdxdata` and `/cdxdata2`, physically located at the main workstation console, accessible from the entire PPPL Unix cluster.

During an experiment, data is stored in the directory structure

`/cdxdata/DIRECTORYNAME/data/recent/SHOTNAME.SUFFIX`

where `DIRECTORYNAME` is the directory name corresponding to each diagnostic. The CDX-U diagnostics and directory names are listed in table 2.12. `SHOTNAME` is the CDX-U shotname, which is simply composed of the date and time of the shot in the format MMDDYYHHMM, where hours (HH) are listed in 24-hour format. `SUFFIX` is a three letter suffix associated with each file type. Generally this is associated with each diagnostic, but in the case of a single diagnostic producing several datafiles, this suffix is used to identify each. The CDX-U suffixes are listed in table 2.12.

For example, a datafile from the magnetics array from a shot fired at 2:30 p.m.

Diagnostic	Directory	Suffix
Main waveforms	maindata	.MDT
I_P, interferometer	maindata	.IPN
Coil currents	maindata	.CCT
DAC waveforms	dac	.WFS
Magnetics	magnetics	.MAG
ψ loops	magnetics	.PSI
Triple probe	probe	.PRB
SXR array	sxr	.SXR
MLM, bolometer arrays	mlm_bolo	.mlm_bolo
EBW	ebw	.EBW
RF waveforms	rf	.RF1
RF scattering data	rf	.RF2
TVTS images	tvts	.SPE
TVTS profiles	tvts	.TTS
LIF	lif	.LIF
MOSS spectrometer	moss	.MOS
STRS spectrometer	strs	.strs

Table 2.12: Data directories and file suffixes for all CDX-U datafile types.

on May 31, 2000 (shotname 0531001430) would be stored as

`/cdxdata/magnetics/data/recent/0531001430.MAG`

Datafiles are periodically archived to conserve disk space on the `/cdxdata` and `/cdxdata2` disks. Archived data is compressed using the GZIP utility and is stored in an archival directory tree

`/cdxdata/DIRECTORYNAME/data/storage/SHOTDATE/SHOTNAME.SUFFIX.gz`

where `DIRECTORYNAME`, `SHOTNAME` and `SUFFIX` are just as described for "recent" data, and `SHOTDATE` is simply the first six characters of `SHOTNAME`, corresponding to the shot date.

To facilitate automated file retrieval, CDX-U has adopted a standardized file format. The format includes comment lines, in an attempt to encourage the creation of self-describing datafiles. Also included is a section for data constants that may be

relevant to the dataset, but not part of the recorded waveform arrays (i.e. a relevant gain setting or position measurement). Table 2.13 lists a CDX-U "`.IPN`" datafile example, demonstrating the CDX-U standard datafile format for a file containing waveforms from the I_P Rogowski coil and the microwave interferometer. Lines 1-6 are comment lines describing the data arrays, line 7-9 are available for data constants (in this case $R_{interferometer}$), line 10 contains the data array dimensions, and the data array begins on line 11. The file ends with a line containing "`end`".

```
c  CDX-U Plasma current and interferometer traces
c  Three columns: time (s), Ip, interferometer trace.  Ip is 35.4 kA/V
c  Line 7 contains the radial location of the interferometer (cm)
c  Line 10 contains the dimensions of the bulk data
c  Output arrays begin on line 11, with time (s) in first column
c
35.000000


5000.000000  3.000000
0.200000  0.029297  -0.390625
0.200010  0.029297  -0.390625
0.200020  0.029297  -0.390625
0.200030  0.029297  -0.380859
0.200040  0.029297  -0.380859
⋮
0.249950  -0.019531  -0.068359
0.249960  -0.019531  -0.068359
0.249970  -0.019531  -0.068359
0.249980  -0.019531  -0.078125
0.249990  -0.019531  -0.068359
end
```

Table 2.13: CDX-U "`.IPN`" datafile example, demonstrating the CDX-U standard datafile format. Lines 1-6 are comment lines, line 7-9 are available for data constants (in this case $R_{interferometer}$), line 10 contains the data array dimensions, and the data array begins on line 11. The file ends with a line containing "`end`".

Chapter 3

The CDX-U Multichannel Thomson Scattering System

Thomson scattering from electrons was first observed in 1963 by Fiocco and Thompson, using a 20 Joule ruby laser to scatter light from an electron beam with density $n_e \approx 5 \times 10^9$ cm^{-3} [Fiocco and Thompson, 1963]. Thomson scattering from a plasma was observed in the same year by two independent teams. Füfner, et al. scattered ruby light from a θ-pinch plasma at IPP Garching, and Schwarz scattered ruby light from a helium hollow-cathode discharge at CalTech [Füfner *et al.*, 1963; Schwarz, 1963]. Since that time Thomson scattering has become a widely established and commonly used electron temperature diagnostic on all major fusion plasma experiments.

As fusion experiments became larger and more complex, single-point measurements were found to be insufficient, and multichannel systems were developed to provide simultaneous measurements of multiple scattering volumes. The first multichannel system was developed for the PLT tokamak at PPPL [Bretz *et al.*, 1978], and since that time multichannel systems have become a standard electron temperature diagnostic on large fusion experiments.

Due to performance and cost limitations, multichannel Thomson scattering systems have not generally been feasible for smaller plasma physics experiments such as CDX-U. As smaller experiments have become more sophisticated, though, profile information is increasingly valuable, while at the same time technological advances and component availability have made multichannel systems much more affordable

and manageable. In particular, multichannel temperature and density information is critical for any kind of transport assessment in CDX-U. This chapter describes the major components and innovative aspects of the CDX-U TVTS system [Munsat and LeBlanc, 1999], one of the most advanced multipoint Thomson scattering systems for a machine this size, and a major portion of this thesis work.

3.1 Introduction

Two excellent reviews of the Thomson scattering process are given in [Hughes, 1975] and [Sheffield, 1975]. A brief general review of Thomson scattering from plasmas is presented here, followed by an application of the theory to the CDX-U TVTS configuration.

If an electromagnetic wave scatters from a moving particle, the particle will oscillate in response to the wave fields at a Doppler shifted frequency

$$\omega_d = \omega_i - \mathbf{k}_i \cdot \mathbf{v} \tag{3.1}$$

where ω_d is the Doppler-shifted frequency, ω_i is the incident wave frequency, $\mathbf{k}_i$ is the incident wave vector, and $\mathbf{v}$ is the particle velocity.

Light re-emitted (scattered) from the particle will also have frequency ω_d, in the frame of the moving particle. To a stationary external observer, the scattered light undergoes a second Doppler shift, resulting in an observed frequency

$$\omega_s = \omega_d + \mathbf{k}_s \cdot \mathbf{v} \tag{3.2}$$

where ω_s is the scattered wave frequency and $\mathbf{k}_s$ is the scattered wave vector. Setting $\mathbf{k} = \mathbf{k}_s - \mathbf{k}_i$, the overall Doppler shifted frequency is given by

$$\omega_s = \omega_i + \mathbf{k} \cdot \mathbf{v} \tag{3.3}$$

One can imagine that given a fixed-frequency source, an ensemble of particles with velocities $\mathbf{v}_j$ would scatter a collection of photons with a spectrum of frequencies $\omega_{s,j}$, and that the frequencies $\omega_{s,j}$ could then be detected and used to infer the velocities $\mathbf{v}_j$. This is precisely what is done in Thomson scattering systems.

By looking closely at the scattered wave fields, one can quantitatively calculate the power in each region of the scattered spectrum. In practice, it is also important to carefully consider the effects of scattering angle, collection solid angle, photon energy, and detection optics to determine the expected scattered photon spectrum.

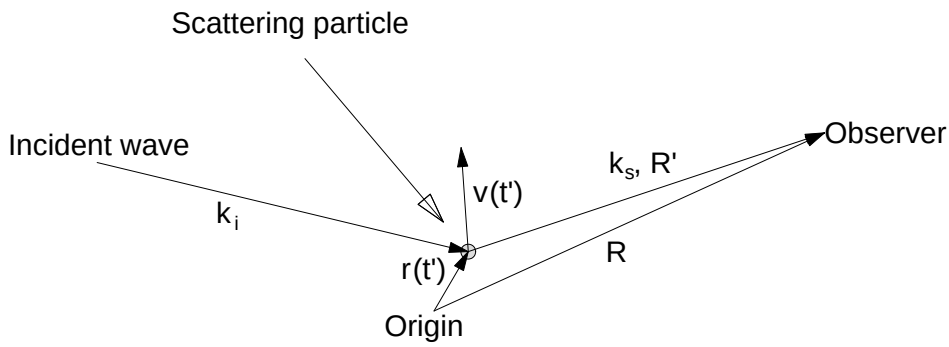

Figure 3.1: Scattering geometry for electromagnetic wave scattered from a moving particle.

Consider the geometry shown in figure 3.1, with an incident wave given by

$$\mathbf{E}_i(\mathbf{r},t) = \mathbf{E}_{i0}\cos(\mathbf{k}_i\cdot\mathbf{r}-\omega_i\,t) \qquad \mathbf{B}_i(\mathbf{r},t) = \frac{1}{c}\left(\hat{i}\times\mathbf{E}_i(\mathbf{r},t)\right) \tag{3.4}$$

where $\hat{i}$ is the incident wave direction $(\mathbf{k_i}/k_i)$ and $\mathbf{E}_{i0}$ is the time-independent electric field component of the incident wave.

For scattering from a non-relativistic electron $\left(\frac{v}{c}\ll 1\right)$ the scattered electric field at an observation point $\mathbf{R}$ will be

$$\mathbf{E}_s(\mathbf{R},t) = \left(\frac{e^2}{4\,\pi\,\epsilon_0\,m_e\,c^2\,R}\right)[\hat{\mathbf{s}}\times(\hat{\mathbf{s}}\times\mathbf{E}_{i0})]\cos(\mathbf{k}_i\cdot\mathbf{r}(t')-\omega_i t') \tag{3.5}$$

or

$$\mathbf{E}_s(\mathbf{R},t) = \frac{r_{e0}}{R}[\hat{\mathbf{s}}\times(\hat{\mathbf{s}}\times\mathbf{E}_{i0})]\cos(\mathbf{k}_i\cdot\mathbf{r}(t')-\omega_i t') \tag{3.6}$$

where $r_{e0}=\frac{e^2}{4\pi\epsilon_0 m_e c^2}$ is the classical electron radius. Here t' is the "retarded time", allowing for the time lag between the scattering and the observation of the wave

$$t' = t - \frac{R}{c} - \frac{\hat{\mathbf{s}}\cdot\mathbf{r}(0)}{c} \tag{3.7}$$

and the position of the particle at the retarded time is

$$\mathbf{r}(t') = \mathbf{r}(0) + \mathbf{v}t' \tag{3.8}$$

With the substitution of equations 3.7 and 3.8 into 3.6, the cosine term becomes

$$\cos\left(\mathbf{k}_i \cdot \mathbf{r}(0) + \left[k_i - \frac{\mathbf{k}_i \cdot \mathbf{v}}{c}\right][R - ct - \hat{\mathbf{s}} \cdot \mathbf{r}(0)]\right) \tag{3.9}$$

Noting that $\left(\frac{v}{c} \ll 1\right)$ and $|\mathbf{k}_i| \approx |\mathbf{k}_s|$, equation 3.6 then becomes

$$\mathbf{E}_s(\mathbf{R}, t) = \frac{r_{e0}}{R}\left[\hat{\mathbf{s}} \times (\hat{\mathbf{s}} \times \mathbf{E}_{i0})\right]\cos(k_s R - \omega_s t - \mathbf{k} \cdot \mathbf{r}(0)) \tag{3.10}$$

The time-averaged power scattered at $\mathbf{R}$ into frequency ω_s (assuming that the scattering is done by an electron having velocity that satisfies $\omega_s = \omega_i + \mathbf{k} \cdot \mathbf{v}$) is given by the scattered Poynting flux $\mathbf{S}_s = \frac{1}{\mu_0}(\mathbf{E}_s \times \mathbf{B}_s)$

$$P_s(\mathbf{R}, \omega_s)d\Omega = R^2\,\mathbf{S}_s\,d\Omega = \frac{R^2}{\mu_0}(\mathbf{E}_s \times \mathbf{B}_s)d\Omega \tag{3.11}$$

which in this case reduces to

$$P_s(\mathbf{R}, \omega_s)d\Omega = \frac{R^2}{\mu_0\,c}E_s^2\,d\Omega \tag{3.12}$$

Considering a random ensemble of electrons (though still calculating the amount of power scattered per single electron), the phase factor $\mathbf{k} \cdot \mathbf{r}(0)$ will drop out of equation 3.10, which combines with equation 3.12 to give

$$P_s(\mathbf{R}, \omega_s)d\Omega = \frac{{r_{e0}}^2 {E_{i0}}^2}{\mu_0\,c}\left[\hat{\mathbf{s}} \times (\hat{\mathbf{s}} \times \hat{\mathbf{E}}_{i0})\right]^2 \cos^2(k_s R - \omega_s t)d\Omega \tag{3.13}$$

Noting that $\cos^2(k_s R - \omega_s t)$ averages to $\approx 1/2$, the average scattered power is given by

$$P_s(\mathbf{R}, \omega_s)d\Omega = \frac{P_i\,{r_{e0}}^2}{A}\left[\hat{\mathbf{s}} \times (\hat{\mathbf{s}} \times \hat{\mathbf{E}}_{i0})\right]^2 d\Omega \tag{3.14}$$

where the average incident power is defined as $P_i = \frac{{E_{i0}}^2 A}{2\mu_0 c}$ and A is the beam area.

For a plasma with a distribution of electron velocities, we take an ensemble integral over the velocity distribution, which includes a delta function relating the electron velocity to the proper scattered frequency.

$$P_s(\mathbf{R},\omega_s)d\omega_s d\Omega = \frac{N_e\, P_i\, {r_{e0}}^2\, d\Omega}{A}\left[\hat{\mathbf{s}}\times(\hat{\mathbf{s}}\times\hat{\mathbf{E}}_{i0})\right]^2 \iiint_{-\infty}^{\infty} d\mathbf{v}\,[f(\mathbf{v})\delta(\omega_s-\omega_i-\mathbf{k}\cdot\mathbf{v})] \tag{3.15}$$

where N_e is the total number of scattering centers.

By choosing a coordinate system with $dv_x dv_y dv_z \longrightarrow dv_k dv_{\perp k1} dv_{\perp k2}$, the integral reduces to a single dimension

$$P_s(\mathbf{R},\omega_s)d\omega_s d\Omega = \frac{N_e\, P_i\, {r_{e0}}^2\, d\Omega}{A}\left[\hat{\mathbf{s}}\times(\hat{\mathbf{s}}\times\hat{\mathbf{E}}_{i0})\right]^2 \int_{-\infty}^{\infty} dv_k\,[f(v_k)\delta(\omega_s-\omega_i-kv_k)] \tag{3.16}$$

Again, $\left(\frac{v}{c}\ll 1\right)$, so that $k\approx$ constant, and the integral simplifies to $\frac{1}{k}f\left(\frac{\omega}{k}\right)$. Also $N_e = n_e V = n_e AL$, where V is the scattering volume, A and L are the beam area and scattering length.

$$P_s(\mathbf{R},\omega_s)\, d\omega_s\, d\Omega = P_i\, {r_{e0}}^2\, d\Omega\, n_e\, L\left[\hat{\mathbf{s}}\times(\hat{\mathbf{s}}\times\hat{\mathbf{E}}_{i0})\right]^2 f\left(\frac{\omega}{k}\right)\frac{d\omega_s}{k} \tag{3.17}$$

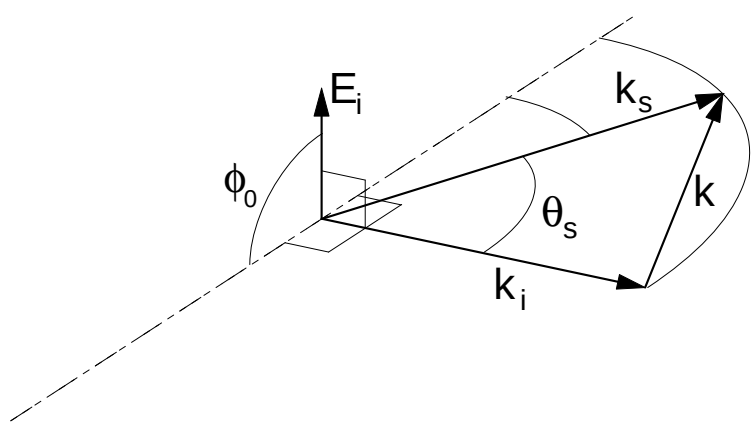

Figure 3.2: Scattering geometry indicating scattering angle relative to wave polarization direction

Note that $\int_{-\infty}^{\infty} f\left(\frac{\omega}{k}\right)\frac{d\omega_s}{k} = 1$. $\left[\hat{\mathbf{s}} \times (\hat{\mathbf{s}} \times \hat{\mathbf{E}}_{i0})\right]^2 = 1 - \cos^2(\phi_0)[1 - \cos^2(\theta_s)]$, where θ_s is the angle between $\hat{\mathbf{s}}$ and $\hat{\mathbf{i}}$ and ϕ_0 is the angle between $\hat{\mathbf{E}}_{\mathbf{i}}$ and the plane formed by $\hat{\mathbf{s}}$ and $\hat{\mathbf{i}}$ (see figure 3.2). For polarized incident light with detection geometry such that $\phi_0 = 90°$, $\left[\hat{\mathbf{s}} \times (\hat{\mathbf{s}} \times \hat{\mathbf{E}}_{i0})\right]^2 = 1$. The total scattered power into a detector covering $d\Omega$ steradians is then

$$P_s(\mathbf{R})\, d\Omega = P_i\, {r_{e0}}^2\, d\Omega\, n_e\, L \tag{3.18}$$

For realistic estimates of $n_e = 5 \times 10^{13}$ cm^{-3}, $d\Omega = .01$ sr, and $L = 1$ cm,

$$\frac{P_s}{P_i} = 4 \times 10^{-14} \tag{3.19}$$

which obviously puts very stringent requirements on both the input power and the detection efficiency.

Equation 3.17 can now be applied to a distribution of electrons in a thermal plasma to calculate the scattered spectrum. Consider a non-relativistic electron velocity distribution

$$f(\mathbf{v}) = \left(\pi {v_{te}}^2\right)^{-\frac{3}{2}} \exp\left(-\frac{{v_k}^2 + {v_{\perp k}}^2 + {v_{\perp k}}^2}{{v_{te}}^2}\right) \tag{3.20}$$

where the thermal velocity $v_{te} = \sqrt{\frac{2\kappa T_e}{m_e}}$.

Inserting this distribution function into equation 3.17 immediately leads to an expression for the frequency spectrum of scattered power

$$P_s(\mathbf{R}, \omega_s)\, d\omega_s\, d\Omega = \frac{P_i\, {r_{e0}}^2\, d\Omega\, n_e\, L}{k\, v_{te}\, \sqrt{\pi}} \left[\hat{\mathbf{s}} \times (\hat{\mathbf{s}} \times \hat{\mathbf{E}}_{i0})\right]^2 \exp\left[-\left(\frac{\omega_s - \omega_i}{k v_{te}}\right)^2\right] d\omega_s \tag{3.21}$$

where $k = 2k_i \sin(\frac{\theta}{2})$ (see figure 3.1).

It is also convenient to express the scattered spectrum in terms of the incident, scattered wavelengths λ_i, λ_s by using

$$\frac{\omega_s}{k_s} = \frac{\omega_i}{k_i} = c \tag{3.22}$$

$$\left(\frac{\omega_s - \omega_i}{k v_{te}}\right)^2 = \frac{(\lambda_s - \lambda_i)^2 c^2}{4 {v_{te}}^2 {\lambda_i}^2 \sin^2(\frac{\theta}{2})} \tag{3.23}$$

$$d\omega_s = \left(\frac{2\pi c}{{\lambda_i}^2}\right) d\lambda_s \tag{3.24}$$

and the simplifying substitution $\delta = (2v_{te}/c)\sin(\frac{\theta}{2})$.

Now the power scattered into solid angle $d\Omega$ and spectral range λ_s to $\lambda_s + \delta\lambda_s$ is given by

$$P_s(\mathbf{R}, \lambda_s)\, d\Omega\, d\lambda_s = \frac{P_i\, {r_{e0}}^2\, n_e\, L\, d\Omega\, d\lambda_s}{\lambda_i\, \delta\, \sqrt{\pi}} \left[\hat{\mathbf{s}} \times (\hat{\mathbf{s}} \times \hat{\mathbf{E}}_{i0})\right]^2 \exp\left[-\frac{(\lambda_s - \lambda_i)^2}{{\lambda_i}^2\, \delta^2}\right] \tag{3.25}$$

Because the scattered power is so low (see eq. 3.19), it is useful to put this in terms of a rate of scattered photons, so that photon-noise based statistical analysis can be applied. With $\frac{v_{te}}{c} \ll 1$, the energy per scattered photon is well approximated by $h\nu_i$, so that the photon expression is only slightly different than the scattered power expression.

$$N_s(\mathbf{R}, \lambda_s)\, d\Omega\, d\lambda_s = \frac{N_i\, {r_{e0}}^2\, n_e\, L\, d\Omega\, d\lambda_s}{\lambda_i\, \delta\, \sqrt{\pi}} \left[\hat{\mathbf{s}} \times (\hat{\mathbf{s}} \times \hat{\mathbf{E}}_{i0})\right]^2 \exp\left[-\frac{(\lambda_s - \lambda_i)^2}{{\lambda_i}^2\, \delta^2}\right] \tag{3.26}$$

where N_s is the number of scattered photons into the appropriate solid angle and spectral range, and N_i is the number of incident photons.

When considering an actual experimental diagnostic, it is important to also consider the two additional attenuating factors of detector quantum-efficiency (η) and finite optical transmission (T). Taking these into account, and assuming properly polarized incident light so that $\left[\hat{\mathbf{s}} \times (\hat{\mathbf{s}} \times \hat{\mathbf{E}}_{i0})\right]^2 = 1$, one can produce a compact working expression for scattered photoelectrons at the detector, also presented in [Bretz *et al.*, 1978].

$$N_{pe}(\mathbf{R}, \lambda_s) = \frac{N_i\, (\eta\, T)\, {r_{e0}}^2\, n_e\, L\, d\Omega\, d\lambda_s}{\lambda_i\, \delta\, \sqrt{\pi}} \exp\left[-\frac{(\lambda_s - \lambda_i)^2}{{\lambda_i}^2\, \delta^2}\right] \tag{3.27}$$

Applications of this equation to the CDX-U Thomson scattering system are

presented in section 3.5.

3.2 The TVTS Ruby Laser System

3.2.1 Beam Path and Optics

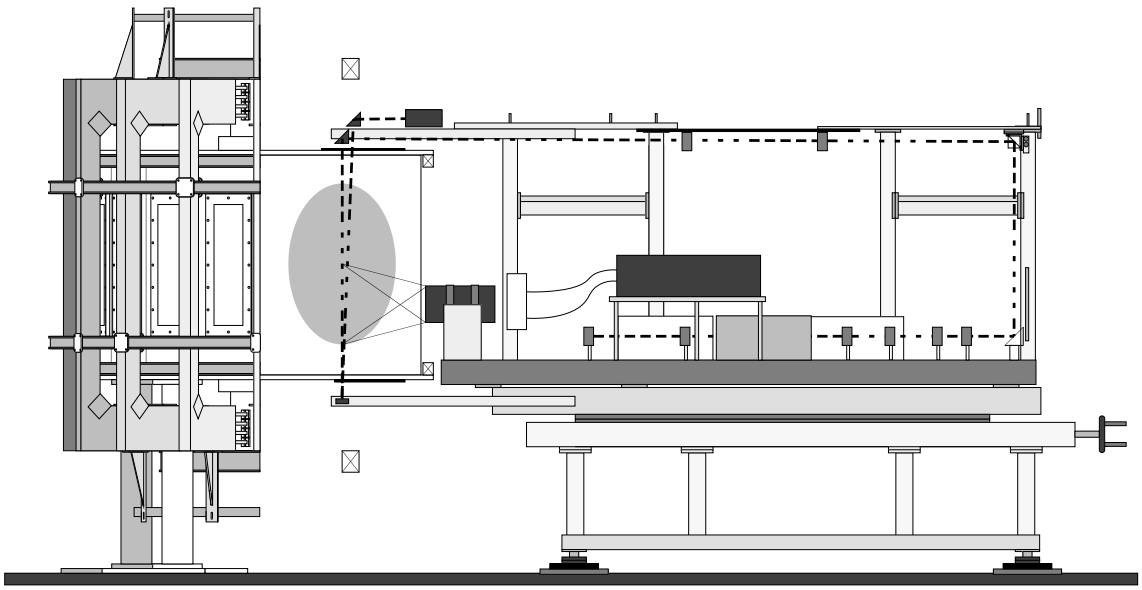

Figure 3.3: Cutaway view of CDX-U vessel and TVTS system

The CDX-U TVTS system uses a 5-Joule ruby laser, housed on a sliding framework which is movable in the major-radial direction (figure 3.3). The beam passes vertically down through the plasma, is reflected by a spherical mirror below the vacuum vessel, and passes back through the plasma, to be steered out to an external beam dump. The steering optics and beam dump are located outside of the field of view of the collecting optics, which minimizes the amount of stray light scattered from these surfaces.

The beam enters and exits the vacuum vessel through two matching windows mounted at the top and bottom of the vacuum vessel. The windows are anti-reflection coated on the outer surface, and are mounted with a 7° tilt to avoid window cavity modes and/or reflections back into the laser cavity. Dimensions of the beam entrance and exit windows are shown in figures 3.4 and 3.5.

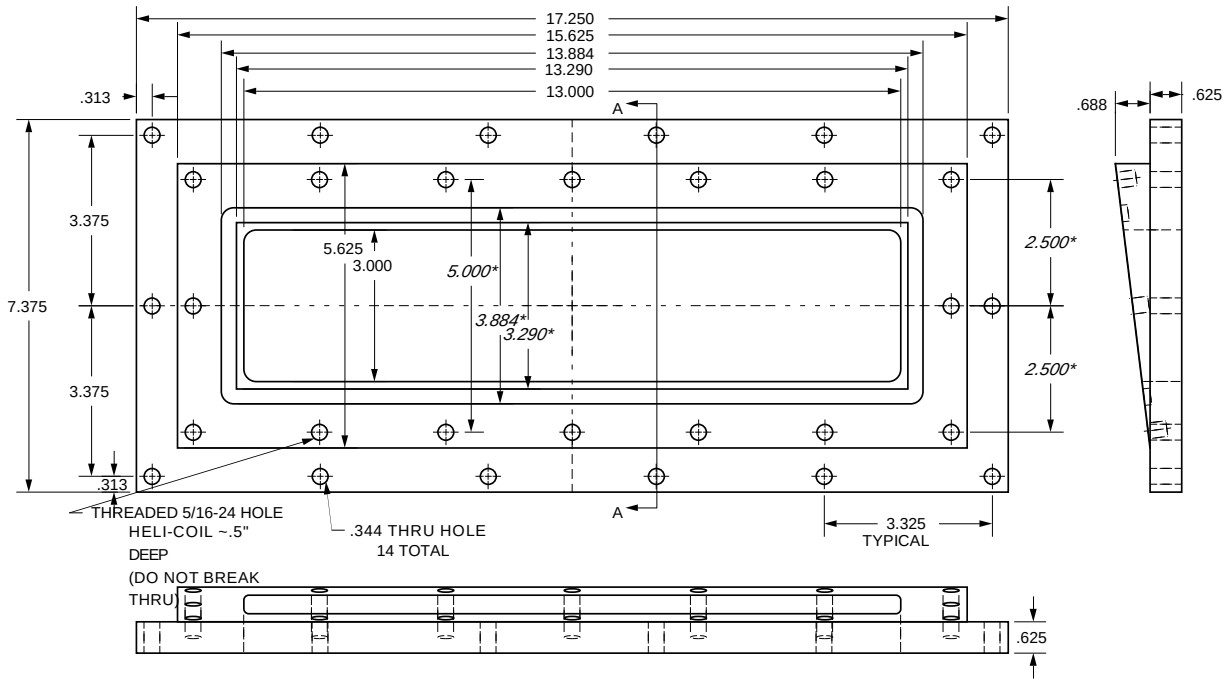

Figure 3.4: TVTS laser window flange, full view

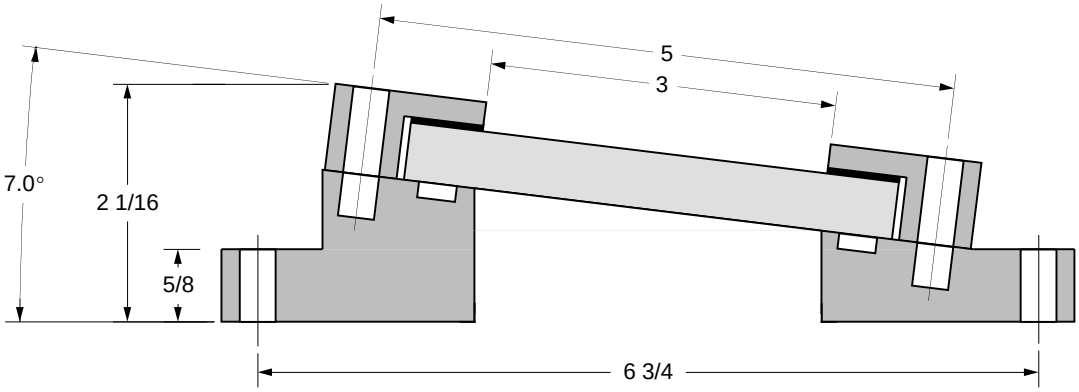

Figure 3.5: TVTS laser window, cross-sectional view

The original windows were made from BK7, a common inexpensive optical glass. During early testing of the laser system, the lower window was damaged by the laser beam, probably during a shot where the optics were improperly focused and the beam was very narrow at the window surface. The window was replaced with a spare BK7 window, and the problem has not recurred. A set of fused-silica replacement windows were obtained as spares, which have higher damage threshold rating than BK7.

The damaged window was posthumously tested to determine the damage threshold of the surface coating and the BK7 itself. The glass material was found to tolerate up to 10 Joules/cm^2 in a 50 ns laser pulse. At this level a small damage spot would form after several shots, which would grow in diameter and depth with repeated laser shots. After 10 shots (each at 10 Joules/cm^2) through the same spot, the damage depth reached halfway through the 0.5" glass plate. Damage to the antireflection coating occurred at lower laser energy, but did not spread to produce cracks in the glass. Interestingly, the glass damage always occurred on the beam-exit side, i.e. where the beam was traveling from glass to air. This is consistent with the geometry of the window that was damaged while mounted on the vacuum vessel.

The laser windows have 30.3 cm clear-aperture in the major-radial direction, allowing for coverage of nearly 70% of the major-radial plasma extent, as shown in figure 3.6. The movable optical table allows for sampling vertical chords at different major-radii, which insures measurement of the plasma center and can allow for 2-D scanning of the plasma cross-section.

The laser itself was previously used in the TFTR TVTS system [Johnson *et al.*, 1985]. The CDX-U system uses a modified version of the TFTR laser, eliminating the final amplification head and expanding the oscillator cavity. The laser layout is shown in figure 3.7. The CDX-U system uses three ruby heads and a longer cavity to expand the pulse length to 50 ns (compared to 15-20 ns pulse from a compressed cavity in the TFTR configuration).

A HeNe laser (λ = 6328 Å) is collinear with the ruby beam and is used for alignment of all optics. Mirrors 2 and 3 provide adjustability to steer the HeNe beam through the laser cavity. Mirror 4 is the back-reflector of the laser cavity, which fully reflects the ruby beam while passing the HeNe beam. The cavity is

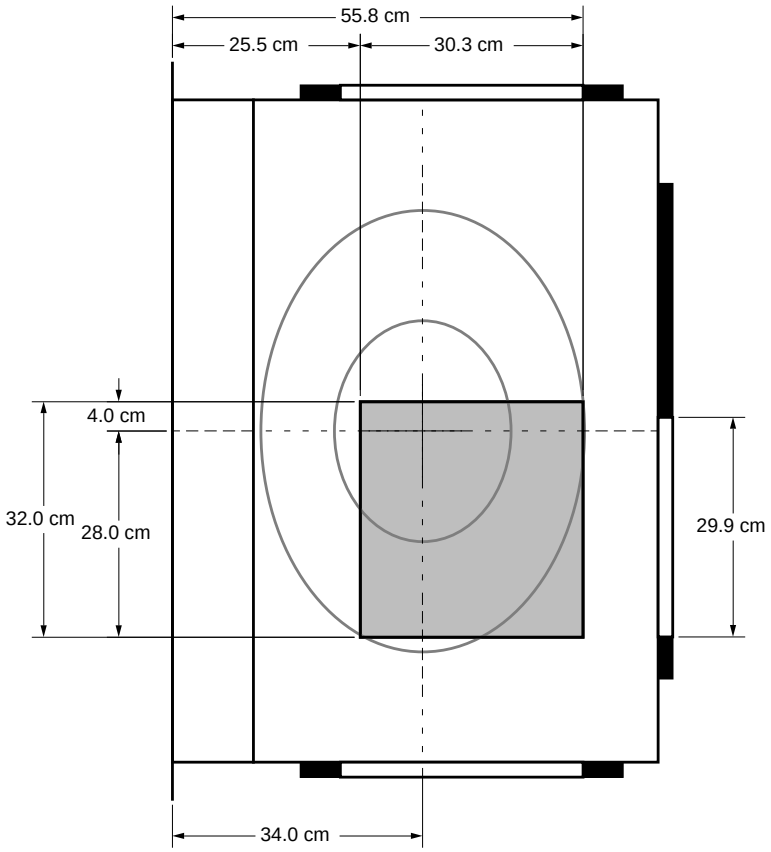

Figure 3.6: TVTS coverage in CDX-U; shaded area indicates area covered by TVTS diagnostic

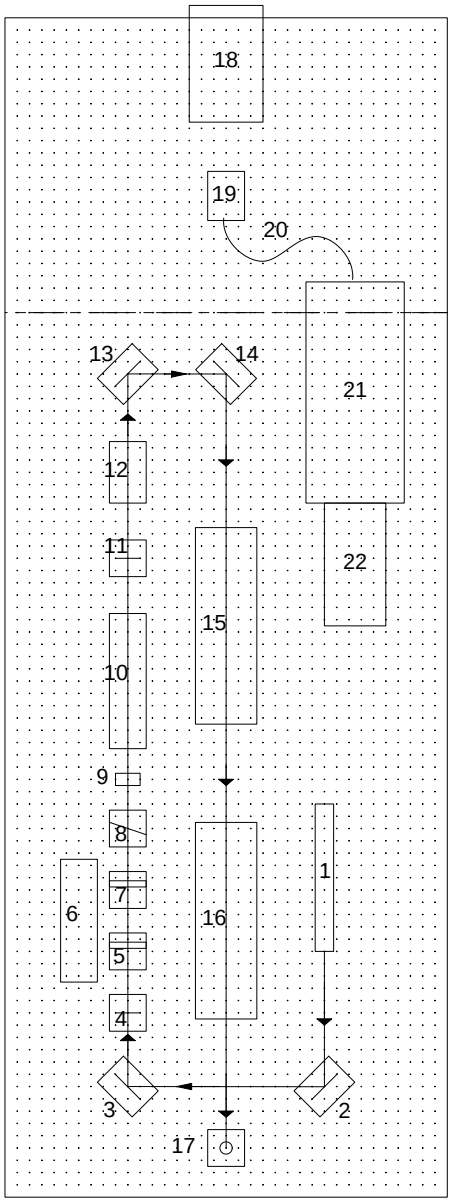

1. HeNe laser
2. 45° mirror
3. 45° mirror
4. HeNe passing mirror
5. Pockels cell
6. Pockels cell controller
7. Quarter-wave plate
8. Glan prism
9. Pinhole
10. 6 mm ruby rod
11. HeNe passing mirror
12. Beam expander
13. 45° mirror
14. 45° mirror
15. 18 mm ruby rod
16. 18 mm ruby rod
17. Steering mirror
18. Collecting objective lens
19. Fiber holders
20. Plastic fibers
21. Holospec Spectrometer
22. ICCD camera

Figure 3.7: TVTS laser optical table layout

actively Q-switched (see, for example [Koechner, 1996]) via a Pockels cell, in combination with a quarter-wave plate and a linear polarizer. The Pockels cell is a birefringent crystal, with a varying level of birefringence based on a voltage applied longitudinally along the crystal. During each round-trip within the laser cavity, the linearly-polarized beam traverses the Pockels cell and the $\lambda/4$ plate twice each. When no voltage is applied to the Pockels cell, the two passes through the $\lambda/4$ plate produce a combined rotation of the polarization by 90°, and the beam is absorbed by the polarizer. When the laser is to be fired, a high-voltage pulse is applied to the Pockels cell, sufficient to induce a $\lambda/4$ rotation of the beam polarization (2.6 kV). In this case, the combined effect of the $\lambda/4$ plate and the Pockels cell, each traversed twice, introduce a polarization rotation of 180°, which passes through the polarizer, and thus the laser beam power is allowed to multiply in the resonant laser cavity. The electronics for firing the Pockels cell are described in section 3.2.2.

The cavity output is 100 mJ, which is then sent through a beam-expander and two amplifying heads, bringing the final output energy to ∼5 J.

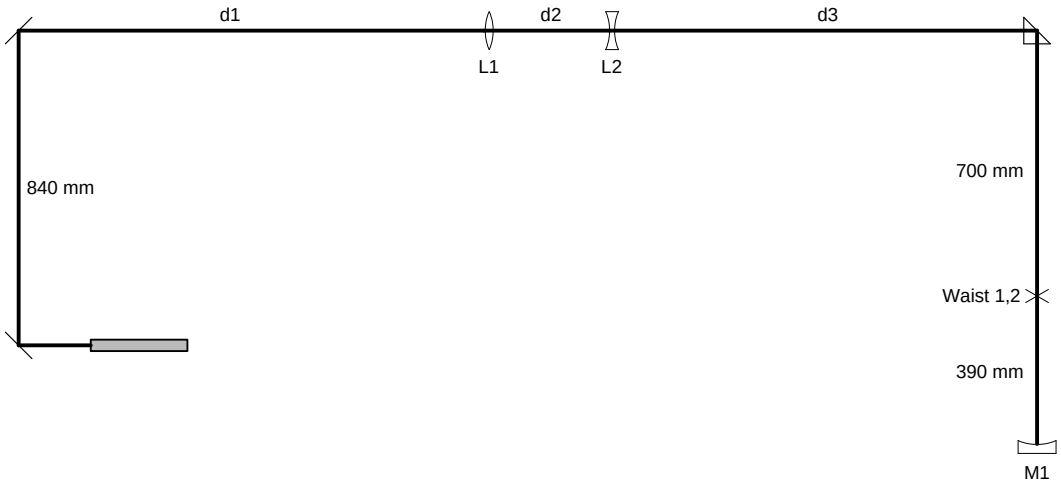

Figure 3.8: TVTS laser beam layout

A schematic of the laser beam path is shown in figure 3.8. Distances and focal lengths of the optics are described in table 3.1. Lenses L1 and L2 are mounted on movable mounts on an upside-down optical rail mounted inside the TVTS aluminum

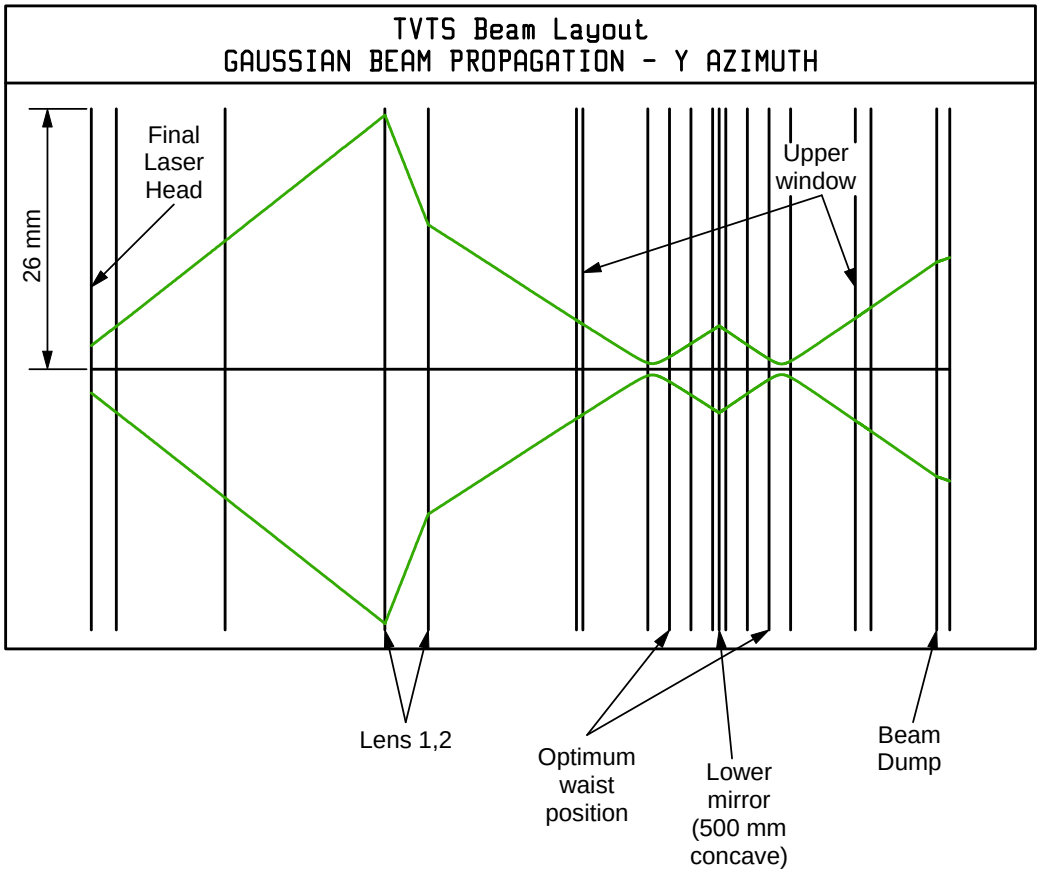

Figure 3.9: TVTS laser Gaussian-beam trace

framework. The focal lengths of L1, L2, and M1 were chose to place the down-going and up-going beam waists as close to the center of the TVTS viewing area as possible, and also keep the beam narrow enough within the scattering volume to be fully imaged while keeping it wide enough at the optical surfaces to avoid damage.

Results from a Gaussian-beam trace using the OSLO optical design program [Sinclair Optics, Inc., 1997] are shown in figure 3.9 and table 3.1. All optical surfaces are represented in the figure, as well as some dummy surfaces to represent important points in the laser path (such as the boundary of the scattering volume). Critical surfaces are indicated in the figure. Note that in both figure 3.9 and table 3.1 the beam path is represented linearly, so that any surfaces contacted in both the down-going pass and the up-going pass (pass 1, 2 respectively) are listed twice.

Although the Gaussian-beam trace is the result of a design study, the actual measured beam parameters match the values in the table. Most importantly, the actual beam is fully imaged by the collecting optics while not damaging the beam optics.

Because the radiated power from CDX-U consists almost exclusively of line radiation (i.e. very low Bremsstrahlung at CDX-U temperatures), background plasma light was not expected to affect the scattered spectrum over the 75 ns camera gate duration (which contains the 50 ns laser pulse). Unfortunately two weak CII lines fall within the collected spectrum, and required subtraction. The effect of these lines is covered in section 3.5.

The two-pass system doubles the number of scattered photons per joule of laser energy, thus lessening the laser energy requirements. Technical limitations inherent to the CDX-U machine geometry make this an essential feature of the system. Port availability precludes the use of a beam-path along the midplane, leaving a vertical path as the only feasible option. In order to avoid the CDX-U poloidal field coils with a vertical beam path, it is necessary to place steering optics very close to the plasma scattering volume (i.e. between the plasma shaping coils and the vacuum vessel). Damage threshold (power-density) limits on the optical coatings of these elements, along with optical (aspect-ratio) requirements of the plasma scattering volume itself, place lower and upper limits on the width of the beam as it comes in contact with the optics and passes through the plasma.

With a two-pass system, the design requirements on beam power-density can

Description		**Distance / Focal Length (mm)**
d1		1221
L1		585
d2		327
L2		-585
d3		1127
M1		251
Surface	**Pass**	**Gaussian beam radius (mm)**
Ruby rod face	1	7.0
L1	1	24.5
L2	1	14.0
Upper window	1	6.4
Plasma midplane	1	0.5
Center of TVTS view	1	1.5
Bottom of TVTS view	1	3.5
Lower window	1	5.5
Lower mirror	1	6.1
Lower window	2	5.5
Bottom of TVTS view	2	3.5
Center of TVTS view	2	1.4
Plasma midplane	2	0.6
Upper window	2	6.7
Beam dump	2	14.8

Table 3.1: TVTS laser beam-path and Gaussian-beam trace values

be met while retaining sufficient photons for measurements. The beam is > 8 mm in diameter at all optical surfaces, resulting in power density on the optics of ≤ 200 MW/cm^2 for a uniform (top-hat) beam profile, or twice this at the center of a Gaussian profile. This is below the damage threshold specifications from the window manufacturer, though only by a factor of 2-3. Damage testing (as described in section 3.2.1) has demonstrated that the windows can survive typical laser shots without damage. The beam is also ≤ 5 mm in diameter over the entire plasma scattering volume, which allows for full imaging by the collection optics.

Because of the requirement of radial-movability of the beam line and the desire to cover as much of the high-field side of the plasma as possible, it was necessary to fit the extension arms that hold the final upper turning mirror and lower spherical mirror between the laser windows and the return-legs of the toroidal-field coils. Although this space is only 2" tall, it was possible to fit a set of low-profile optical mounts with sufficient clearance to avoid contact with the vessel or the coils.

The original extension arm set was made from aluminum C-channel, but it was found that due to the fast swing of the vertical field, large eddy-currents were induced in the aluminum. These currents interacted with the toroidal field to produce a twisting force on the extension arm, which misaligned the beam during the plasma shot. The aluminum set was replaced with a set made from machined G-11 fiberglass, which eliminated the eddy-current misalignment.

Other Thomson scattering systems have incorporated even more than two passes [Kantor and Kouprienko, 1999; Campos and Machida, 2000], but these generally require one of two undesirable design features: either a substantially more complex series of beam optics can steer the beam through several passes and eventually to a beam dump, or a single set of confocal mirrors can send the beam through a high number of passes and then back into the laser cavity. The first option was judged to be too complicated for the photon gain achieved, and the second option introduced too high a risk of laser damage, due to the possibility of forming a focal spot in the return beam as it passes through one of the laser heads, which would result in damage or destruction of the ruby rod. An earlier, single-point Thomson scattering system on CDX-U employed this second technique, and several ruby rods were damaged.

3.2.2 Control Electronics

The layout of the TVTS triggering scheme is shown in figure 3.10. About 10 seconds before the CDX-U shot a trigger is sent to the charging supplies for the laser capacitor bank set, which pre-charge the banks that supply power to the flashlamps in the laser heads. Typical settings for the capacitor banks are presented in table 3.2.

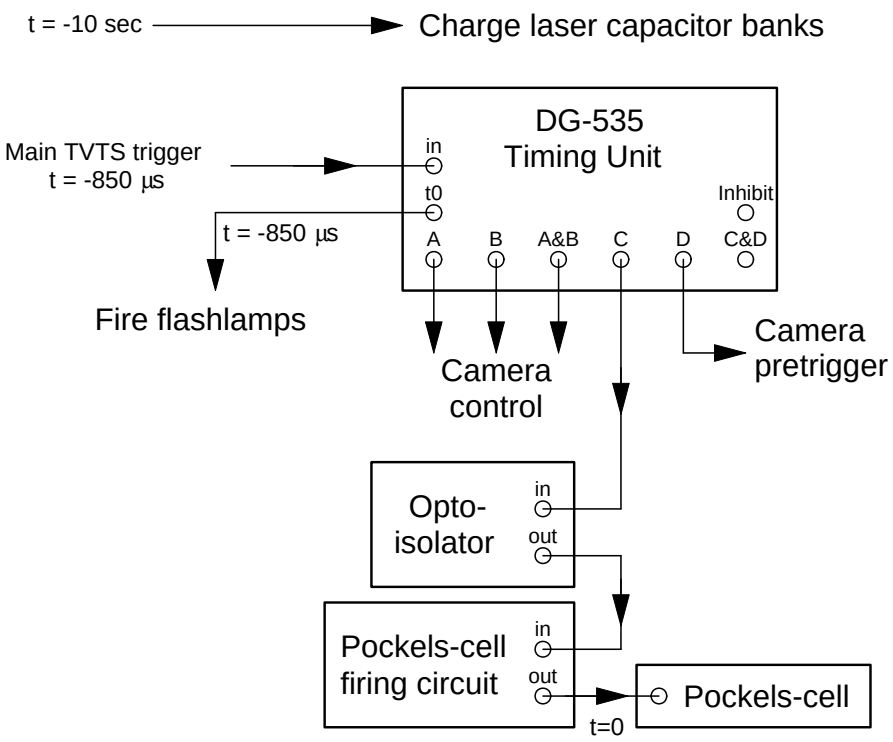

Figure 3.10: TVTS laser triggering layout

Head	C	banks	V(typ.)	t_{delay}	V(max)	E(max)
OSC	600 μF	1	1860 V	325 μs	2500 V	1.9 kJ
PRE	600 μF	1	2100 V	225 μs	2500 V	1.9 kJ
	640 μF	2	2100 V	225 μs	2500 V	4.0 kJ
AMP	640 μF	3	1950 V	250 μs	2500 V	6.0 kJ

Table 3.2: TVTS capacitor bank information

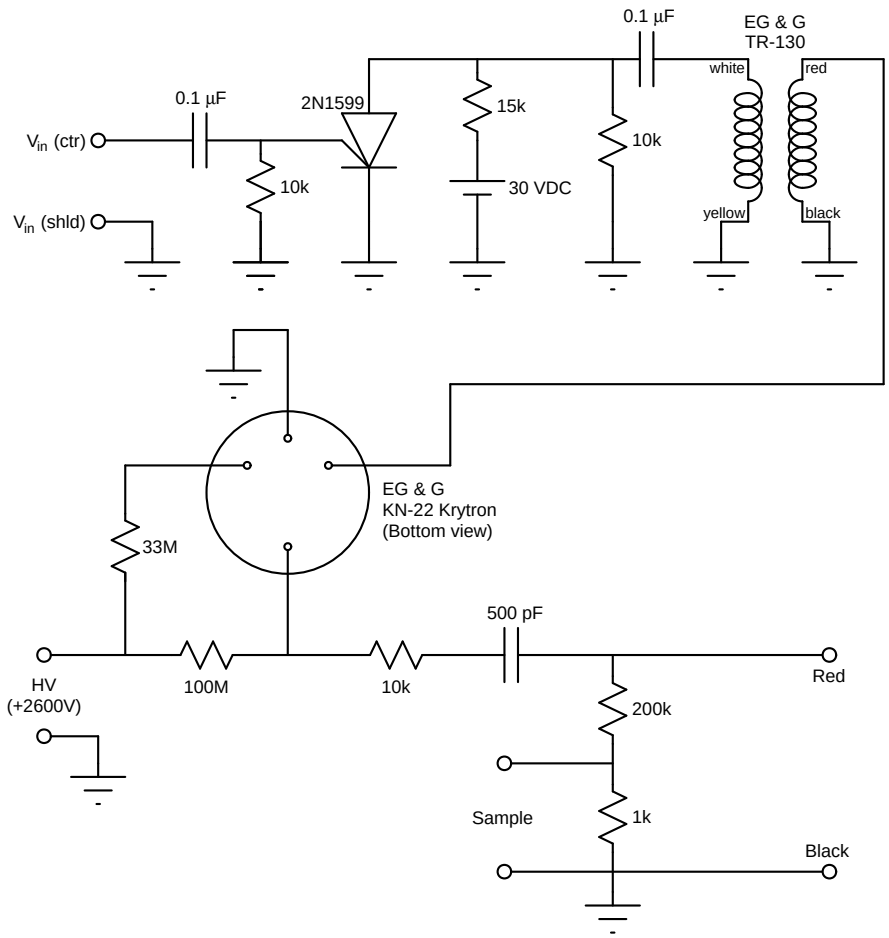

Figure 3.11: TVTS Pockels cell driver circuit

The remainder of the fine-scale timing is done with a Stanford Research Systems DG-535 timing unit, capable of triggering with jitter < 60 ps [Stanford Research Systems, Inc., 1999]. At t = −850 μs, a trigger pulse is sent to fire the flashlamps. After 850 μs the number of photons in the laser cavity is maximized, and a trigger pulse is sent to fire the Pockels cell, which actively Q-switches the laser and induces the laser output pulse. The Pockels cell receives a short high-voltage pulse of 2.6 kV from a firing circuit described in figure 3.11. To protect the (expensive) DG-535 timing unit, the triggering pulse to the Pockels cell driver is sent through an optoisolator circuit, shown in figure 3.12. This introduces a delay of a fraction of a μs, but with jitter < 5 ns. This delay is accommodated in the flashlamp-warmup time (850 μs), which was empirically derived to maximize the cavity energy output.

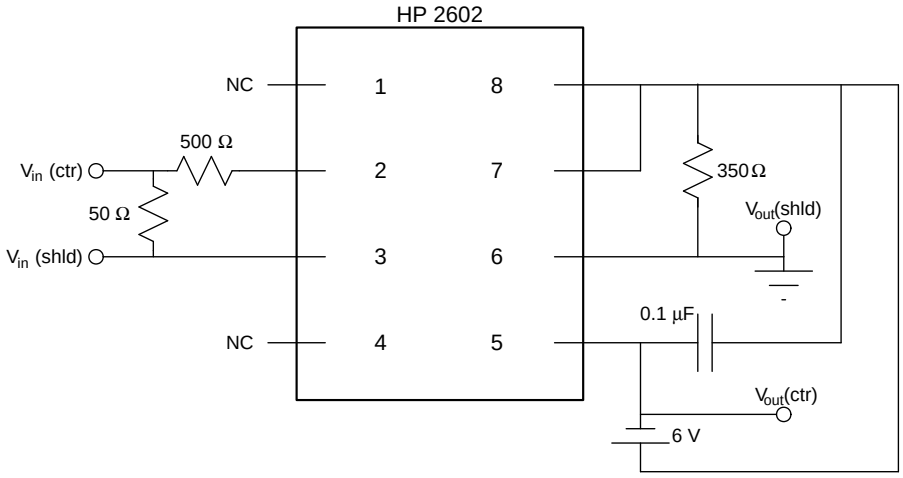

Figure 3.12: TVTS Pockels-cell optoisolator circuit

The optoisolator circuit (figure 3.12) is triggered with a positive-going voltage slope, from 0 V to +5 V. The output is held at -6 V (provided by a set of 4 AA batteries for isolation purposes) before the input pulse, and shorted to 0 V upon triggering. Thus the pulse sent to the Pockels cell driver is a positive-going pulse from -6 V to 0 V.

3.2.3 Multi-Pulse Calculations

One of the fundamental noise limitations of the TVTS system comes from the limited number of scattered photons, which is a direct result of the limitations

on ruby laser power imposed by the damage threshold of the beam optics. The consequence of this is that usable TVTS data is necessarily composed of multiple averaged shots, and signal levels from the outer half of the plasma are typically too low to produce reliable temperature measurements. This limitation could be avoided if the laser could be pulsed several times in rapid succession, within the duration of a single flashlamp pulse. In this case, the damage threshold of the optics would only limit the per-pulse energy, which could be multiplied by the number of pulses. The camera would need to be gated accordingly, to accept the scattered photons while rejecting the stray-light between pulses. On this time scale ($\sim$100 μs), the plasma is assumed stationary, so that the scattered light pulses could be summed to produce a single timepoint measurement. This improvement could lead to the availability of single-shot measurements in the plasma core and extension of useful channels further into the plasma edge, which may be particularly useful for plasma-edge studies in CDX-U.

Repetetive pulsing of ruby lasers has been previously demonstrated [Huntley, 1994; Grace *et al.*, 1998], though in these experiments the objective was to achieve tens of pulses with a high degree of pulse-to-pulse energy uniformity, even if at lower power. In the TVTS case, the objective would be to maximize the power output from a few pulses. Uniformity in output energy between the pulses is not critical, but keeping the per-pulse energy as high as possible is important, since each pulse of scattered photons includes a background level of stray light.

In order to explore the possibility of multiple-pulsing of the TVTS ruby laser, a numerical simulation was set up based on the differential equations used to describe Q-switching of a laser cavity [Koechner, 1996; Huntley, 1994]. First the model was set up to mimic the observed behavior of the existing single-pulse cavity, and the model was then extended to explore multiple pulsing.

The inversion population in the lasing medium and the number of photons in the laser cavity can be described by a pair of coupled differential equations:

$$\begin{aligned} \frac{dN}{dt} &= W_p\,(N_t - N) - 2\,B\,q\,N - \left(\frac{N_t - N}{\tau}\right) \\ \frac{dq}{dt} &= q\left(V_{rod}\,B\,N - \frac{1}{\tau_c}\right) \end{aligned} \tag{3.28}$$

where N is the inversion population of the lasing material, q is the photon population in the cavity. W_p is the pump rate of the cavity, and N_t is the number of active atoms per unit volume in the ruby rod. B is given by

$$B = \frac{\sigma\, l\, c}{V_{rod}\, d} \tag{3.29}$$

where V_{rod} and l are the volume and length of the active region of the lasing medium, d is the cavity length, c is the speed of light, and σ is the absorption coefficient per atom. τ_c is the cavity lifetime, given by

$$\tau_c = \frac{d}{\gamma c} \tag{3.30}$$

where γ is the total logarithmic loss per pass in the cavity, defined as follows:

$$\begin{aligned} \gamma &= \gamma_i + \frac{\gamma_1 + \gamma_2}{2} \\ \gamma_1 &= -\ln(1 - T_1) \\ \gamma_2 &= -\ln(1 - T_2) \\ \gamma_i &= -\ln(1 - T_i) \end{aligned} \tag{3.31}$$

where T_1 and T_2 are the transmission of the front coupler and back reflector (cavity mirrors), respectively, and T_i is the fractional internal loss per pass.

The pair of differential equations 3.28 were converted to difference equations for the simulation, as follows:

$$\begin{aligned} N_i &= N_{i-1} + \Delta t \left[W_p \left(N_t - N_{i-1} \right) - 2\, B\, q_{i-1}\, N_{i-1} - \left(\frac{N_t - N_{i-1}}{\tau} \right) \right] \\ q_i &= q_{i-1} + \Delta t \left[q_{i-1} \left(V_{rod}\, B\, N_{i-1} - \frac{1}{\tau_c} \right) \right] \end{aligned} \tag{3.32}$$

where $\Delta t = t_i - t_{i-1}$ is the timestep, taken as 1 ns in the simulations.

All parameters are either physical constants corresponding to material properties, or are geometrical parameters which were taken to be as close as possible to the values in the CDX-U laser. The single free parameter was the absolute magnitude of W_p, which was difficult to measure in the laboratory. The evolution of W_p was given a functional form which matches the measured evolution of the flashlamp

intensity (see figure 3.13):

$$W_p(t) = \frac{W_{p0}\, t}{300\ \mu s} \exp\left(1 - \frac{t}{300\ \mu s}\right) \tag{3.33}$$

W_{p0} was adjusted in the single-pulse case so that the integrated modeled output pulse energy matched the actual CDX-U cavity output (i.e. 100 mJ), and was then scaled appropriately for the proposed multiple-pulse case. $W_{p0} = 1700\ \mathrm{s}^{-1}$ for the single-pulse case and $2800\ \mathrm{s}^{-1}$ for the multi-pulse case. Values of the other parameters are given in table 3.3.

Parameter	**Value**
l	6 in.
d	30 in.
V_{rod}	$\pi\, l\, (1\,\mathrm{mm})^2$
σ	$1.2 \times 10^{-20}\ \mathrm{cm}^2$
T_i (low Q)	0.5
T_i (high Q)	0.01
T_1	0.4
T_2	0.005

Table 3.3: Parameters used in the multi-pulsed Q-switch simulation

The laser energy produced by each pulse is given by integrating equation 3.28, with the appropriate substitutions. Defining N_i and N_f as the inversion population before and after Q-switching, respectively, the output energy is given by

$$E_{out} = \left(\frac{\gamma_1 + \gamma_2}{4\,\gamma}\right) \frac{h\,\omega}{2\,\pi}\, V_{rod}\, (N_i - N_f) \tag{3.34}$$

Results of the single-pulse simulation are shown in figure 3.13(a-d), which contains several notable features. Figure 3.13a shows the evolution of the flashlamp pump rate W_p. Figures 3.13b and 3.13c show the inversion population N and photon population q, evolved from the difference equations 3.32. Figure 3.13d shows an expanded view of the photon population at the laser pulse, plotted against $\mathrm{t\text{-}t}_{(\mathrm{Q-switch})}$.

Though W_{p0} was adjusted to force E_{out} to match the experimental value of ∼100 mJ, the evolution of the modeled W_p matches the experimentally measured

flashlamp intensity evolution. Experimentally, it was found that the maximum energy could be extracted with a Q-switch delay of 850 μs from the flashlamp firing time, which is considerably later than the peak of the flashlamp light (at ~300 μs). This is reproduced in the simulation, with the peak of the inversion population occurring at t= 850 μs. Intuitively, the inversion peak occurs when the cavity loss rate equals the flashlamp pump rate.

Figure 3.13d shows an expanded view of the photon population at the laser pulse, which roughly matches the experimentally measured cavity output pulse. The modeled laser pulse is ~30 ns FWHM, while the measured laser pulse is 50-70 ns FWHM.

It is interesting to note that the output pulse appears ~150 ns after the Q-switching time. The rapid non-linear growth of the photon population in the cavity upon Q-switching is sensitive to the small number of photons in the cavity during the inversion buildup. A consequence of this is that the timing of the output pulse contains a "jitter" that is on the order of the pulse width. This is indeed seen in the laboratory, and is addressed in section 3.3.6.

Even without Q-switching, if the inversion population is allowed to build up indefinitely, the cavity will spontaneously produce a laser pulse. This can be seen in equations 3.28 when N reaches a value

$$N_{crit} = \frac{1}{B\, V_{rod}\, \tau_c} \tag{3.35}$$

in which case dq/dt becomes positive, q begins to grow, and a "relaxation" pulse is emitted. If W_p is maintained, N will oscillate about N_{crit}, and multiple low-energy pulses will be emitted. Active Q-switching simply forces N_{crit} downward (through τ_c) after an appreciable buildup of inversion population, causing a precipitous drop in N and an associated large spike in q. The second plot in figures 3.13 and 3.14 shows N_{crit}, in both low-Q and high-Q states.

A second set of plots corresponding to the multi-pulse simulation is shown in figure 3.14. For this simulation, the pump rate W_p was scaled up by ~1.7, corresponding to an achievable level with the present oscillator capacitor bank. The Q-switching times for three pulses were determined by N reaching N_{crit}, which also corresponds to $E \sim 100$ mJ cavity output. It is important that the cavity output

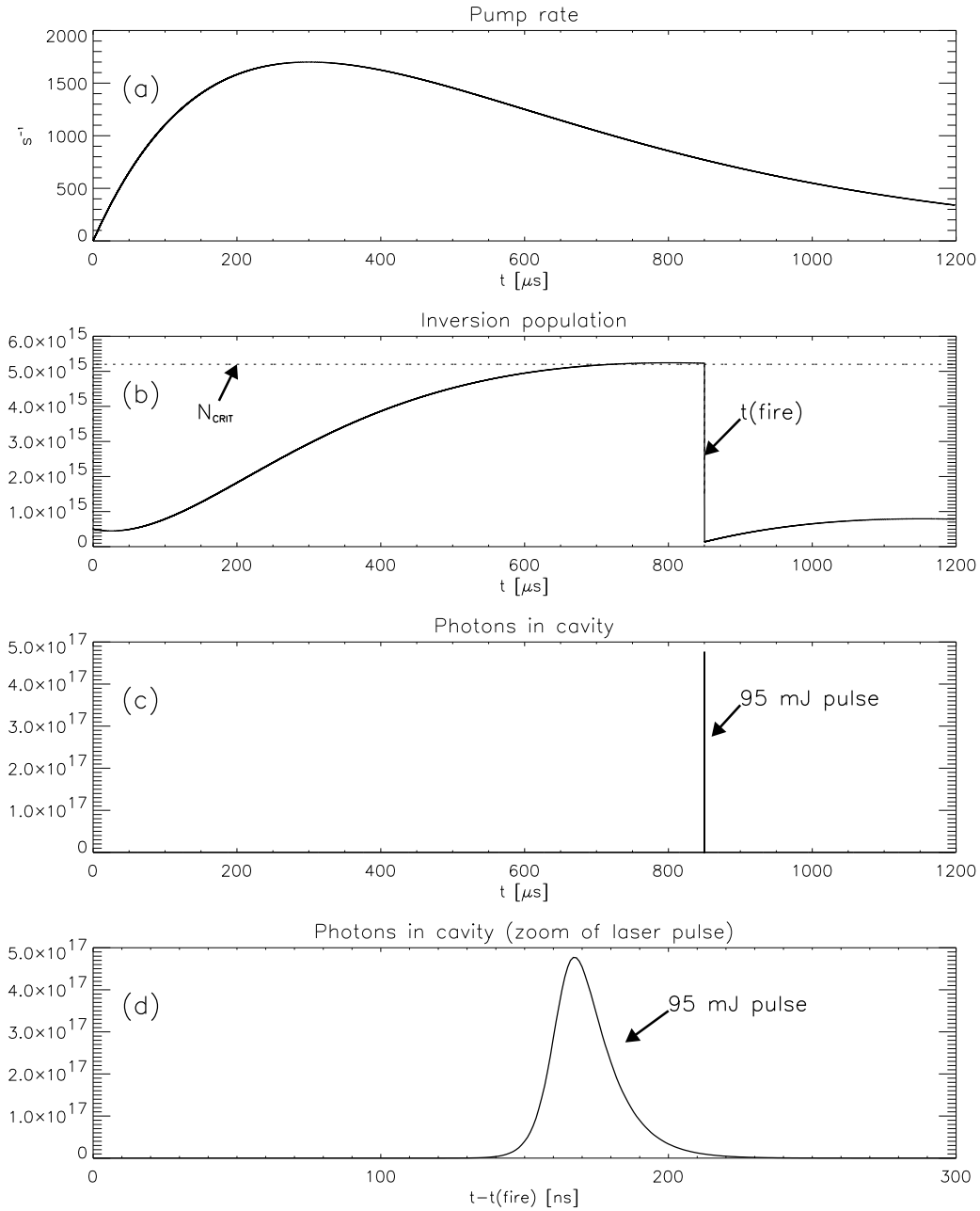

Figure 3.13: Modeled behavior of TVTS laser cavity with single Q-switched pulse. The laser is fired 850 μs after the flashlamps are fired, and the output pulse is 95 mJ.

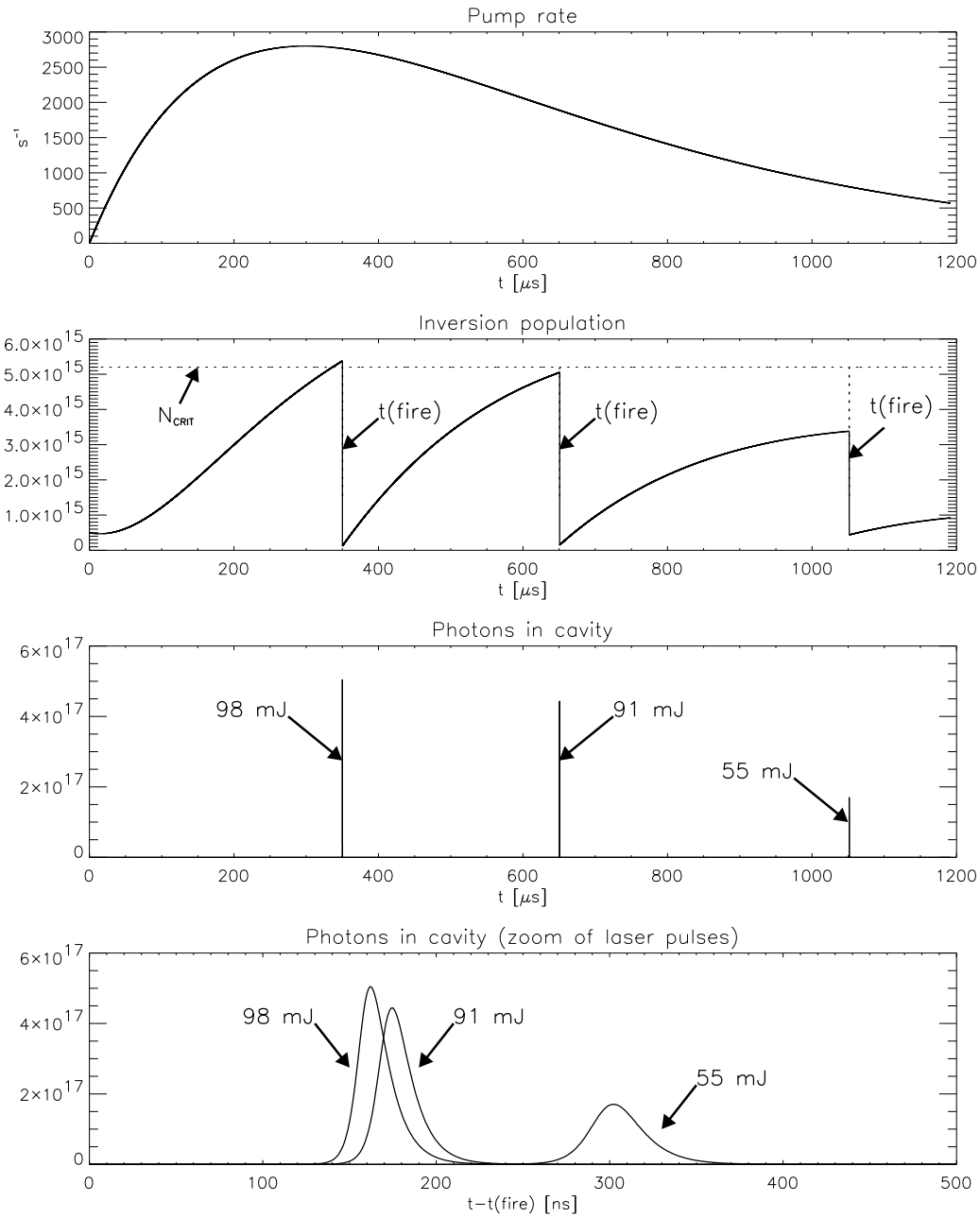

Figure 3.14: Modeled behavior of TVTS laser cavity with increased flashlamp pumping and three Q-switched pulses. The laser is fired 350 μs, 650 μs, and 1050 μs after the flashlamps are fired, producing pulses of 98 mJ, 91 mJ, and 55 mJ. The per-pulse power is similar to the single-pulse case, though the total energy is $\sim$ 2.5 times higher.

be kept at or below 100 mJ, since this level has been established to provide roughly 5 J of amplified output while not damaging the beam optics.

The significant result from the multi-pulse simulation is the achievement of ∼250 mJ total cavity output while keeping the per-pulse output at or below 100 mJ.

In order to realize the multi-pulsing scheme in the laboratory, several technical considerations must be addressed. First, the Pockels cell must be fired three times in rapid succession. (The present Pockels cell driver, shown in figure 3.11, is only capable of a single high-voltage pulse.) To provide the multiple pulsing, a high-voltage pulse amplifier (model GRX-3.0K-H) was purchased from Directed Energy, Inc. It is driven by a DC high-voltage supply (2.6 kV) and a TTL-level input pulse, and is capable of pulse bursts in excess of 50 kHz. A second consideration is the synchronization of the camera to the laser pulses. The Princeton Instruments ICCD camera (described in section 3.3.5) can be pre-programmed to accept and sum multiple exposures, and the triggering circuit (see section 3.3.6) is capable of firing several times in rapid succession. Though there is typically a limit of ∼1 ms between distinct CCD exposures due to download time of the pixel information, this limit does not apply to multiple exposures that are summed on the CCD chip and then downloaded. Lastly, in order for each of the pulses from the laser cavity to translate into a fully amplified laser pulse, it is necessary that the amplifier heads are not depleted before the completion of the pulse sequence. Though it is expected that the amplifier heads are far from depletion with each pulse, this would have to be verified in the laboratory.

3.3 Light Collection

The optical system for light collection is in some sense the most complicated part of the TVTS system. It consists of a main collection lens, an array of plastic fiber-optic bundles, a high-dispersion spectrometer, and an intensified CCD (ICCD) camera with GaAs photocathode. All components were chosen to be simple, cost-effective, and modular; a critical combination to be able to construct the system on a small machine such as CDX-U.

3.3.1 Collecting Lens

The main collecting lens is shown in figures 3.15 and 3.16. It was designed specifically for CDX-U using the OSLO optical design software [Sinclair Optics, Inc., 1997]. The requirements for the collection lens on the CDX-U TVTS system are several-fold. Maximum throughput is necessary on any Thomson scattering diagnostic, based on the low Thomson scattering cross-section of the electrons. For the CDX-U geometry there is also a requirement of high acceptance angle, based on the plasma elongation and close proximity of the lens to the plasma. Any imaging system requires sharp focus (i.e. focal spot size $\ll$ fiber size), and it is generally important to minimize the component cost. Because the lens is used to image a narrow line rather than a full two-dimensional object, the macroscopic image quality (i.e. the existence or lack of barrel-type or pincushion-type distortions) is unimportant. Also, since the image plane is matched with configurable fiber bundles rather than a flat film plate or ccd chip, the image plane does not need to be flat.

Property	**Value**
Full field of view	39°
Magnification	0.23
Image-side f/#	f/2.0
Object-side f/#	f/8.6
Focal length	10.5 cm
Front lens diameter	15 cm
Vignetted beam diam.	5.2 cm (axis)
	4.0 cm (edge)
Collection solid angle	.01 sr
Transmission	94%

Table 3.4: TVTS collection lens specifications

The CDX-U collecting lens is a 5-element, 10.5 cm focal-length lens covering 39° at f/8.6, with magnification of 0.23. The lens is 45 cm from the beamline, and images 32 cm of the scattering volume onto an array of plastic optical-fibers arranged onto the curved focal plane. An overview of the collection lens specifications is presented in table 3.4

Figure 3.15 shows the basic lens layout, including ray-fans traced from the center and edges of the object (i.e. the scattering volume) through the limiting aperture

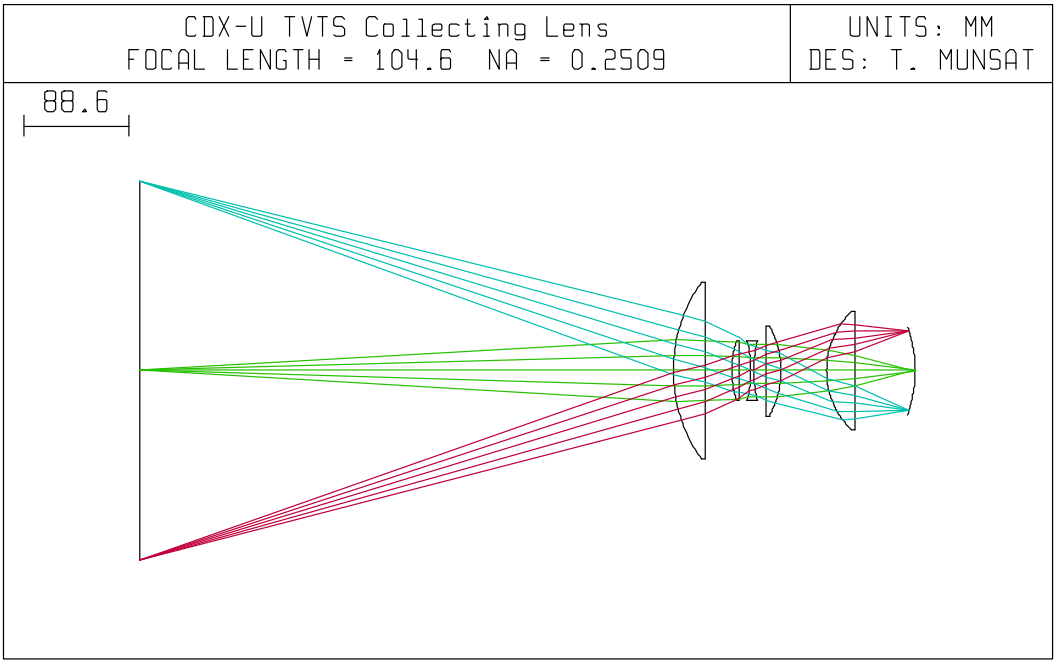

Figure 3.15: TVTS collection lens layout, including ray-fans traced from the center and edges of the scattering volume, through the limiting aperture in the center of the lens, to the curved image plane.

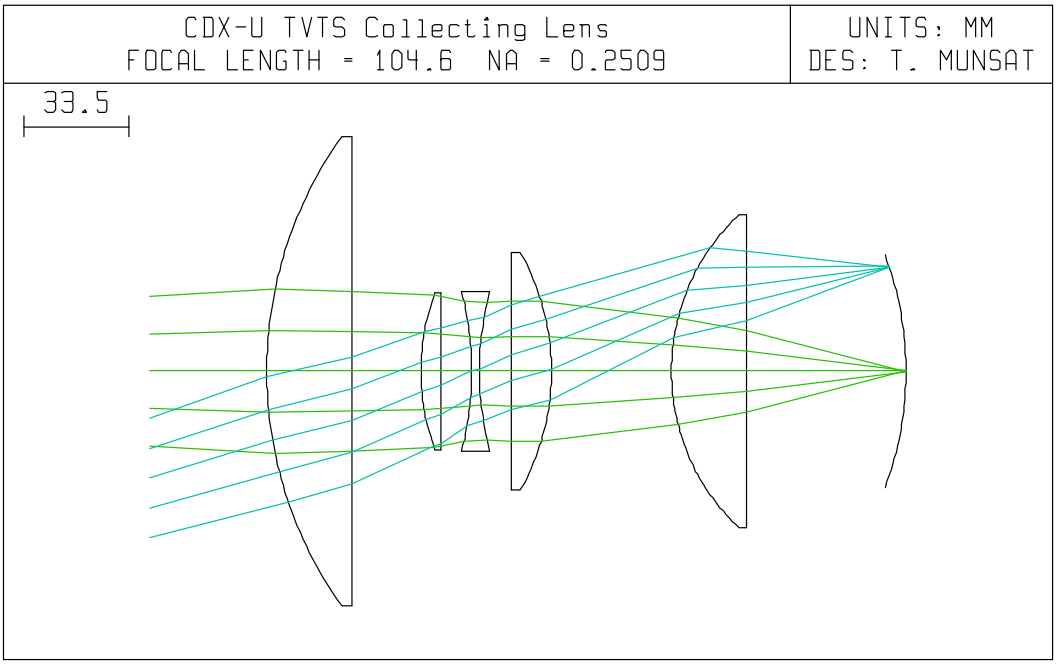

Figure 3.16: TVTS collection lens, closeup

in the center of the lens, to the curved image plane. A closeup diagram of the lens is shown in figure 3.15. Though the front lens element is 15 cm in diameter, it is clear that the full area is not filled by rays from any given object point. The second (plano-convex) lens element acts as the limiting aperture for the lens system, so that the non-vignetted collection area at the front element is 5.2 (4.0) cm in diameter for rays originating at the center (edge). This provides collection solid-angle of $\Delta\Omega = .01$ at the optical axis, .008 at the edge of field. Despite the fact that the collection area is smaller than on other TVTS systems, close plasma access allows for a collection solid-angle comparable to other systems [Johnson *et al.*, 1986].

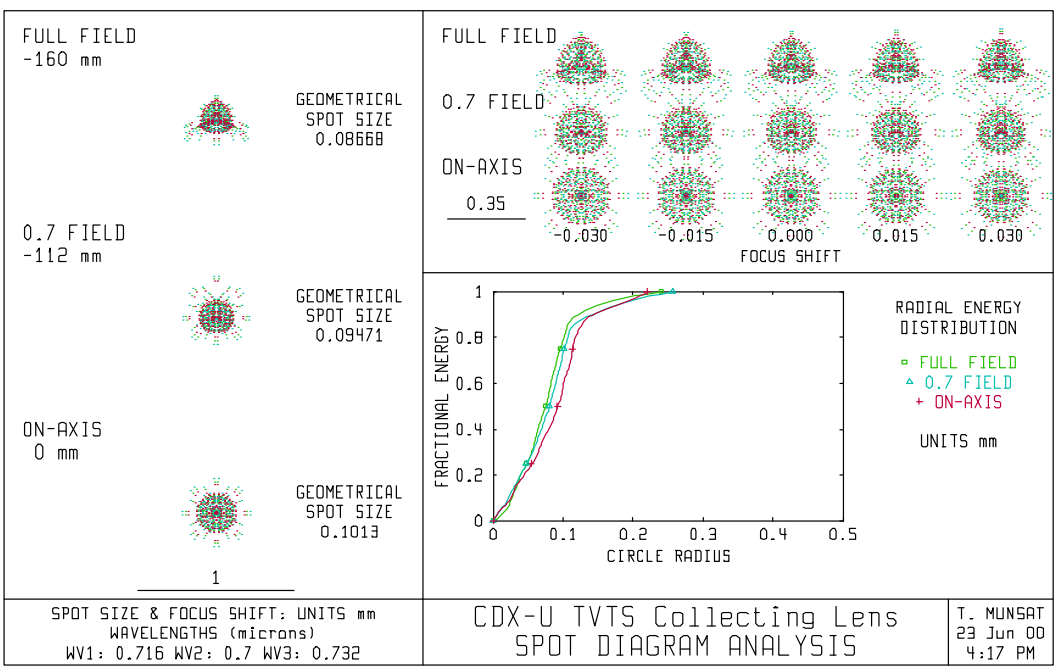

Figure 3.17: Collection lens spot-size analysis. Focal spot size is ∼0.1 mm over the full image field.

The focal spot size was analyzed using OSLO, with the results shown in figure 3.17. Ray fans originating at three representative points (on the optical axis, at 70% of the way to the edge of the object 112 mm from the axis, and at the very edge of the object 160 mm from the axis) were traced through the full lens system to the focal plane. Several hundred rays were traced through the system, chosen to fill the limiting aperture with an even distribution. The clusters of arrival points of the three ray fans at the image plane are shown at the far left of figure 3.17.

The focal spot-size is defined as the r.m.s. distance of the ray arrival points from the center of the cluster. In practice, the requirement of sharp focus translates into achieving a small spot size over the full image, and results from the OSLO spot-size analysis indicate a ∼0.1 mm spot size over the entire field of view, clearly sufficient for the fibers (figure 3.18).

Also shown in figure 3.17 are spot size clusters corresponding to small focal shifts of the image plane, indicating the robustness of the focal distance. This is used as a check for whether a theoretically optimized lens configuration is unusable in practice due to oversensitivity to small misplacement of the image plane. Lastly, a plot of relative energy distribution is shown, again indicating the sharpness of the focusing and the consistency of focusing across the full image plane.

The cost of the collection lens was kept low by designing around "off the shelf" glass elements, so that no custom glass grinding was required. The specifications of the lens elements are presented in table 3.5, including manufacturer, catalog number, and material used for each glass element. All lens elements are anti-reflection coated for 6943 Å, and the combined price of all five coated glass elements roughly equals the cost of the custom lens-mount that holds them.

3.3.2 Fiber-Optic Bundles

An array of custom-made fiber bundles consisting of square plastic fibers is used to re-arrange the image of the beam into the entrance slit of the spectrometer (figure 3.18). Plastic fibers are much less expensive than custom quartz fiber bundles, and are not overly lossy for short transmission distances. The fiber used is Bicron BCF-98 [Bicron Corporation, 1998], which is produced in a variety of sizes. The spectral attenuation curve for BCF-98 is shown in figure 3.19. Though there is a loss peak exactly in the wavelength region of interest (700-750 nm), even at worst the loss is only 1.8 dB/m. For the 20 cm fiber length used in this system, this translates to over 90% transmission. By comparison, quartz fiber bundles can be extremely transmissive over long distances, but are subject to finite packing and cladding fractions which typically limit transmission to ∼60%. Plastic fibers, though much lossier over long distances, can be produced with square cross-section, increasing the packing fraction to essentially 1. Fiber cladding takes up ∼15% of the cross-sectional area. As shown in figure 3.18, standard fiber sizes have been arranged to

Element 1:	**Spindler-Hoyer**	**312364 (BK7)**
Surface 1	R=129.57 mm	
Surface 2	R=∞	
Thickness	27.0 mm	
Focal length	252.3 mm	
Diameter	150.0 mm	
Air space	22.3 mm	
Element 2:	**Spindler-Hoyer**	**312243 (Fused Silica)**
Surface 1	R=75.53 mm	
Surface 2	R=∞	
Thickness	6.1 mm	
Focal length	165.6 mm	
Diameter	50.0 mm	
Air space	10.0 mm	
Element 3:	**Newport Optics**	**KBC082 (BK7)**
Surface 1	R=-103.57 mm	
Surface 2	R=-103.57 mm	
Thickness	2.5 mm	
Focal length	-100.8 mm	
Diameter	50.8 mm	
Air space	10.0 mm	
Element 4:	**Newport Optics**	**KPX226 (BK7)**
Surface 1	R=∞	
Surface 2	R=77.44 mm	
Thickness	13.0 mm	
Focal length	150.0 mm	
Diameter	76.2 mm	
Air space	38.2 mm	
Element 5:	**Spindler-Hoyer**	**312390 (BK7)**
Surface 1	R=68.79 mm	
Surface 2	R=∞	
Thickness	24.0 mm	
Focal length	133.9 mm	
Diameter	100.1 mm	
Air space	51.0 mm	

Table 3.5: TVTS collection lens specifications, including manufacturer, stock number, and material for all elements.

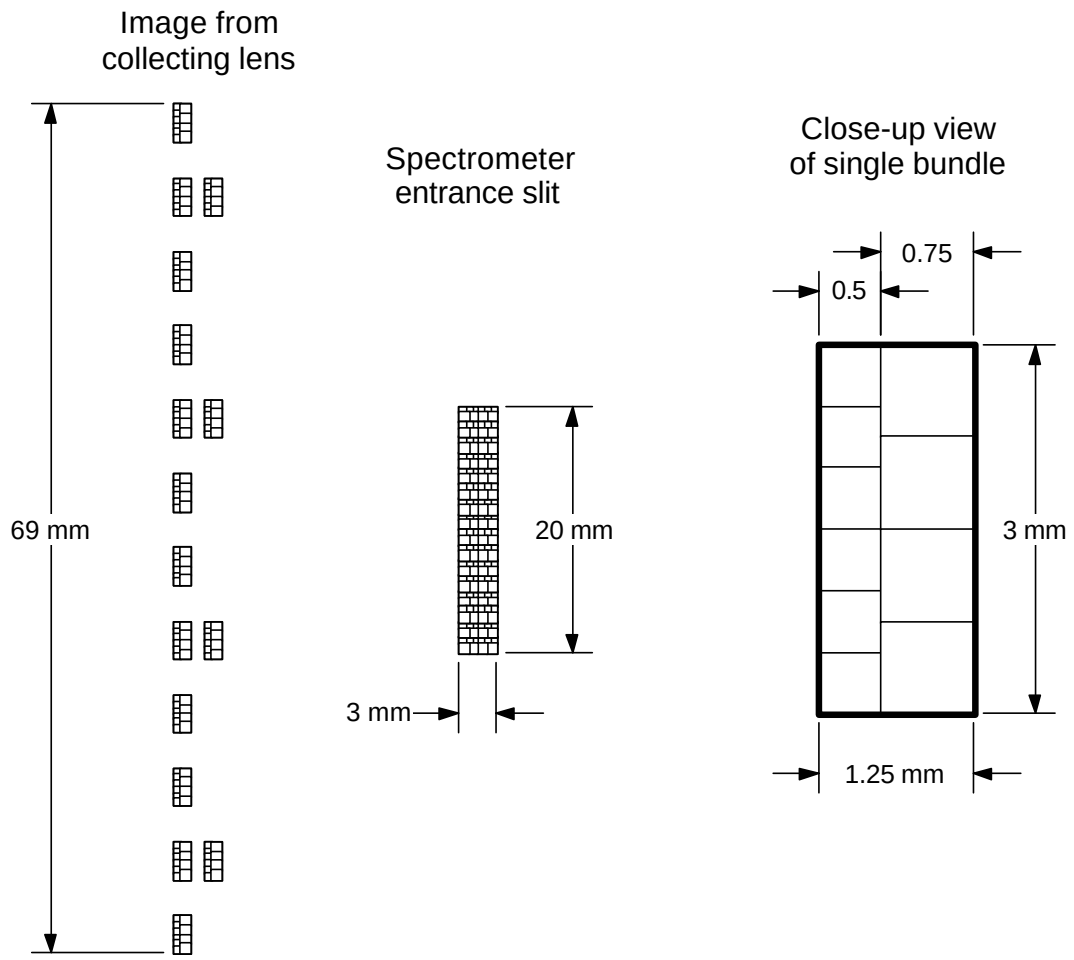

Figure 3.18: Plastic fiber-optic bundles, end view. Shown are the arrangement at the end facing the collection lens (including the "blanks" and the background channels beside the beamline channels), the end facing the spectrometer entrance slit (note the geometrical rearrangment), and a detail of a single bundle, demonstrating the construction of a custom-sized bundle from factory square-fiber stock.

provide custom bundle dimensions.

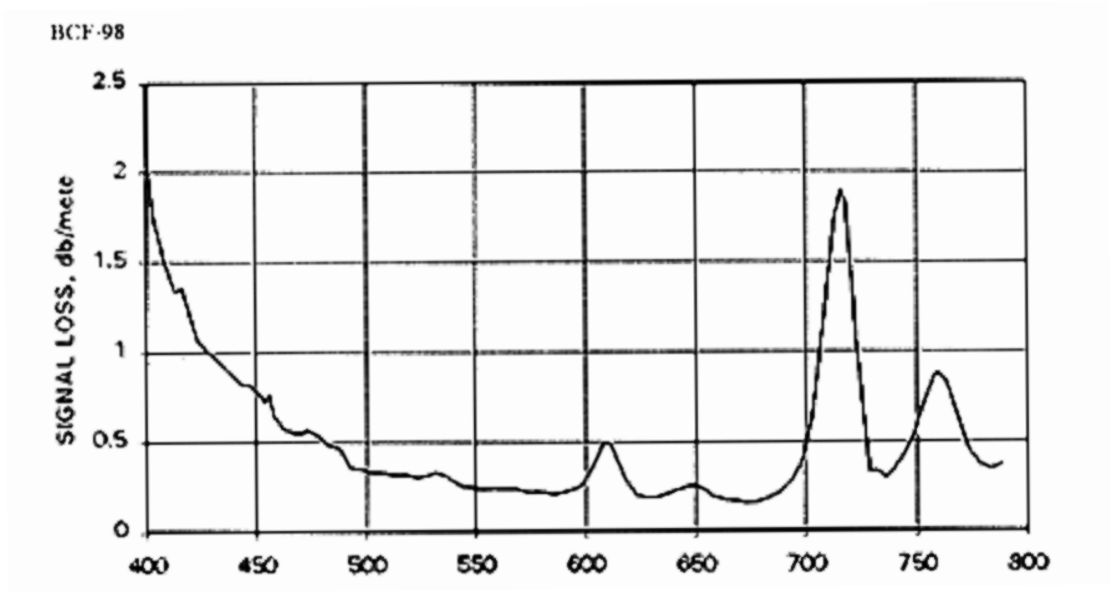

Figure 3.19: Attenuation spectrum of Bicron BCF-98 plastic optical fiber

In order to cover the full plasma half-height while still fitting all of the fibers into the 20 mm entrance-slit of the spectrometer, the fiber bundles are arranged with gaps between them, so that the fibers sample the entire beam length but only image 50% of the scattering volume (see figure 3.18). The fiber tips are mounted in a modular holder, shown in figure 3.20. The holder is made with two rows of 23 grooves each, with the full set of 23 mapping to the full imaged beamline. The spectrometer entrance slit height can accept 16 bundles, which can be arranged in any desired configuration within the 46 grooves of the fiber mount. Presently, 12 bundles are arranged with 11 empty grooves in one row, which maps to the beam line. 4 bundles are distributed across the second row of grooves to sample the background light beside the beamline. This arrangement is shown in figure 3.18.

The modular holder provides the option of sampling a smaller region of the plasma at higher resolution, merely by rearranging the front end of the fiber bundles into a different set of grooves in the fiber holder. Also, the optical system can be upgraded to double the resolution across the full beamline by simply filling the blank grooves with fibers that lead to a second spectrometer and camera.

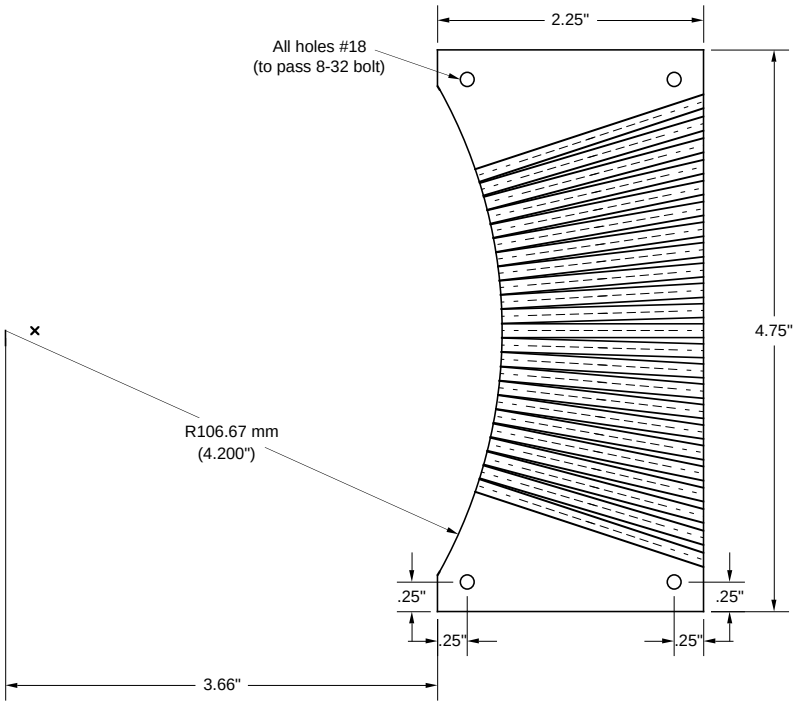

Angles of groove centerlines:

Groove #	Angle (deg.)
1	18.17
2	16.52
3	14.87
4	13.22
5	11.57
6	9.91
7	8.26
8	6.61
9	4.96
10	3.30
11	1.65
12	0
13	-1.65
14	-3.30
15	-4.96
16	-6.61
17	-8.26
18	-9.91
19	-11.57
20	-13.22
21	-14.87
22	-16.52
23	-18.17

Figure 3.20: TVTS fiber bundle holder. The machined holder includes two rows of 23 grooves each, any 16 of which can be used (per spectrometer).

3.3.3 Viewing Dump

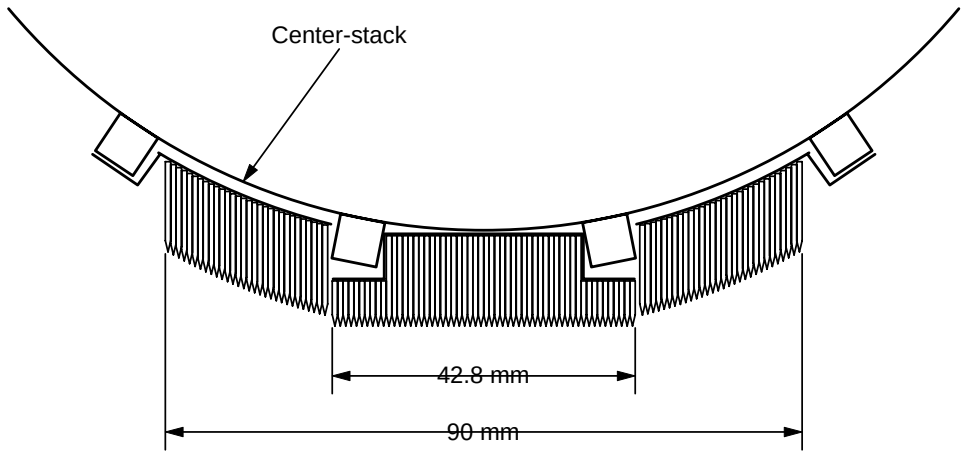

Figure 3.21: TVTS viewing dump, top view (shown mounted on CDX-U center-stack)

In order to reduce the stray light reflecting from the center-stack into the collection optics, a viewing dump constructed of razor blade stock is mounted on the CDX-U center stack. A diagram of the top-view of the view dump is shown in figure 3.21. The CDX-U center-stack features vertical 1/4" nut-plates welded to the inner vessel wall, which proved ideal for mounting the viewing dump to. Although the reflectivity of the CDX-U viewing dump was not measured, other experiments have measured similar viewing dumps and found them to have 0.5%-3% reflectivity, compared with 30%-60% for a typical steel surface [Johnson *et al.*, 1986]. Fortunately, the center-stack is wide enough so that no other part of the vacuum vessel is imaged onto the fiber tips, and a more extensive dump on the outer vessel wall is unnecessary.

The razor-blade stock is machined from non-magnetic stainless steel, and welded together into modules which comprise the viewing dump. Unfortunately the razor-blade stock has a non-correctable "bow" in it, along the direction from the sharp side to the back side of the blade. This precludes the construction of a long vertical module, which would be bowed so much that the middle of the module would be

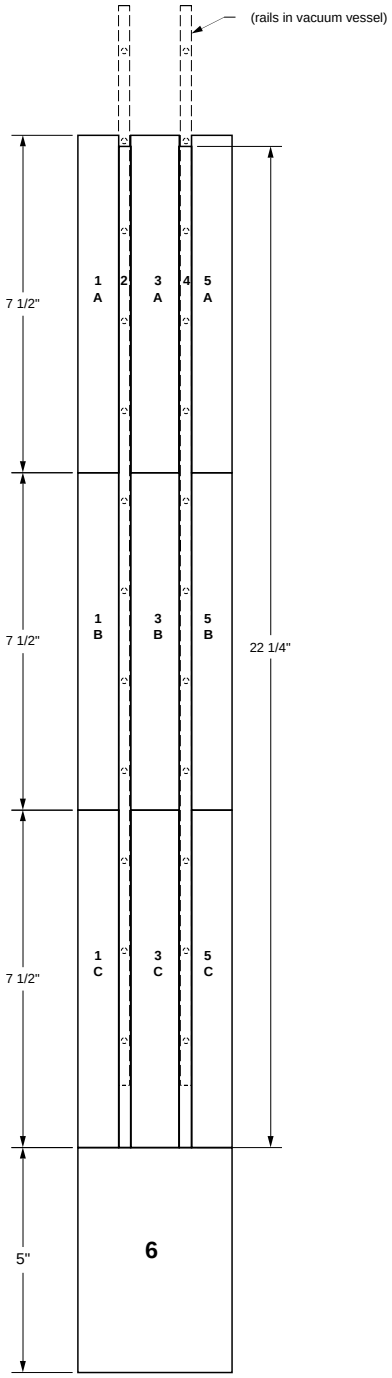

Figure 3.22: TVTS viewing dump, as seen from collecting optics. The whole unit is made up of 12 modules, in order to accommodate the curvature of the center-stack and the bowing of the razor blade stock.

separated from the center-stack by 1" or more. This problem was circumvented by breaking the modules up into smaller parts, so that the effect of the bowing was reduced to tolerable levels. A diagram of the 12 modules, arranged to cover the center-stack, is shown in figure 3.22. The modules labeled 1, 3, and 5 (3 of each, arranged vertically) are mounted first, with mounting tabs and bolts on both sides of each module. After all nine of these are installed, the long strips labeled 2 and 4 are installed, with mounting tabs above and below the razor material. Lastly, module 6 is installed below the other 11 modules, covering the lower mounting tabs on modules 2 and 4, and the gussets at the base of the center-stack.

3.3.4 High-Dispersion Spectrometer

Light from the fibers is dispersed with a Holospec f/1.8 spectrometer which uses a volume-holographic transmission grating sandwiched between two prisms for dispersion [Kaiser Optical Systems, Inc., 1998]. This spectrometer was chosen for its combination of high light throughput and compactness. The input light is pre-filtered with a holographic rejection filter tuned to the 6943 Å ruby line. Wavelengths in the range 680 nm $< \lambda <$ 700 nm are rejected by 10^6. A detail of the attenuation spectrum of the notch filter is shown in figure 3.23. Note that the wavelength region of interest in this system for temperature measurements is 703 nm $< \lambda <$ 732 nm.

The dispersive element is a volume-holographic transmission grating sandwiched between two prisms, as shown in figure 3.24. The use of a holographic transmission grating allows for very high throughput in a compact instrument. In a traditional ruled grating, the surface is cut with alternating high and low regions, or cut with a blaze angle. In either case, the edges of each groove are sharp, which lead to multiple diffraction orders. Because of this, there is a finite distribution of the diffracted light into the m=1,2,3,... diffraction orders, resulting in a loss of energy into the m=1 order at the detector. A volume-holographic grating, on the other hand, uses a medium with a sinusoidally varying index of refraction along one direction, leading to an extremely efficient direction of diffracted light into the first order. A more detailed overview of volume-holographic optics and a description of applications are given in [Tedesco *et al.*, 1993; Owen *et al.*, 1995].

As shown in figure 3.24, light enters the grating through one prism, is diffracted into first order, and is subsequently reflected back through the grating, with the

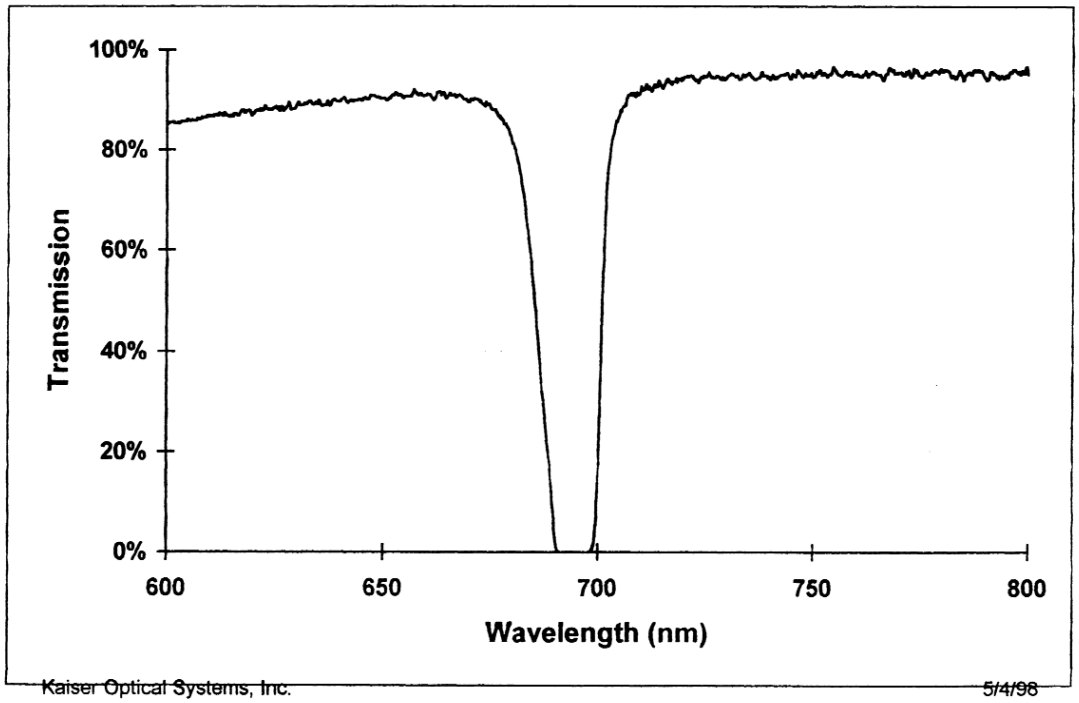

Figure 3.23: Transmission spectrum of holographic notch-filter

zero-order light from the second pass detected at the spectrometer output. The Holospec is a fixed-grating spectrometer, and the input and output optics constrain the angle from input to output to a fixed 90°. The complex prism geometry is necessary to achieve the desired dispersion and central wavelength for the TVTS system within the constraints of the fixed-grating spectrometer.

Although the steepness of the angle between the ray and the grating on the second pass directs most of the light into the zero order, there is a finite energy loss due to this second pass. Despite this, the grating efficiency is ∼80% at the center of the spectrum, and ∼40% at the edge. An overview of the Holospec specifications is presented in table 3.6. Note that the standard 85 mm camera lens on the spectrometer output has been replaced with a 58 mm lens to achieve the desired spectral dispersion.

In order to properly analyze the collected spectra, it is critical to calculate a detailed ray-trace through the spectrometer, which maps a ray of any wavelength from any point on the input plane to its corresponding point on the output plane [Bell, 1998]. We begin with the following definitions (for reference, see figure

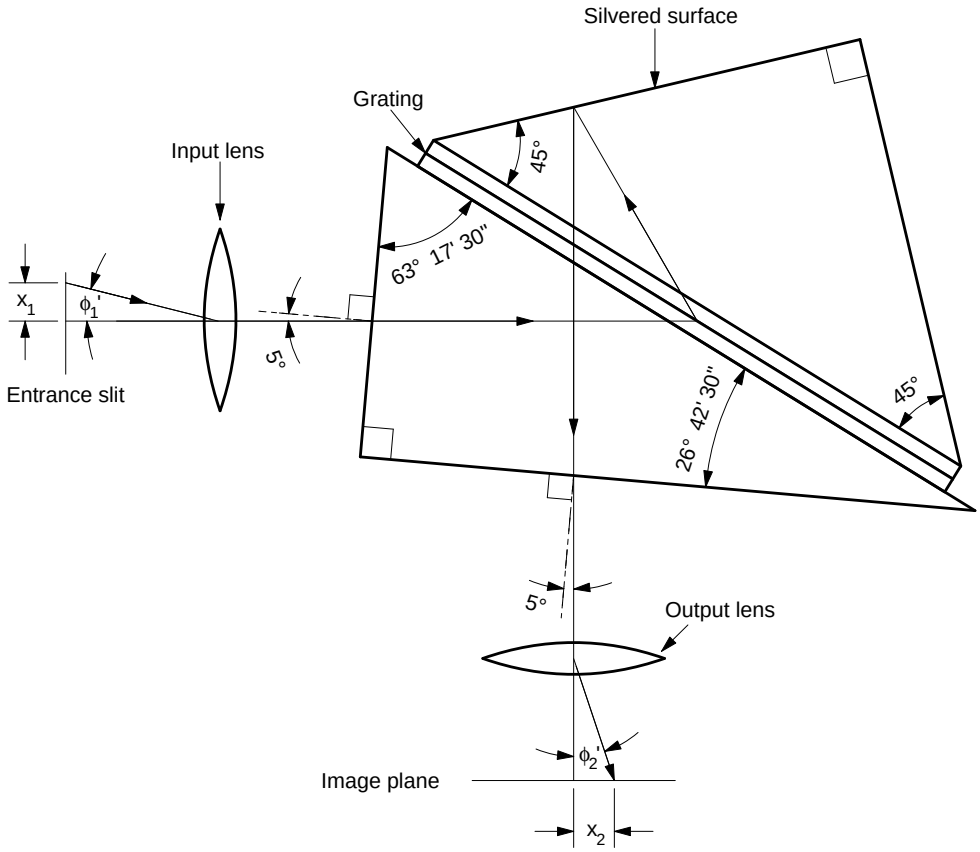

Figure 3.24: Holographic transmission grating for TVTS spectrometer. The combination of dispersion and central wavelength are achieved with custom grating line density and a double-prism arrangement as shown. Optical parameters are described in table 3.6.

Property	**Value**
f/#	f/1.8
Line density	2405.29 mm^{-1}
Entrance focal length	85 mm
Exit focal length	58 mm
Maximum slit height	20 mm
Maximum image plane height	13.7 mm
Grating efficiency (716 nm)	∼80%
Grating efficiency (700 nm, 732 nm)	∼40%

Table 3.6: Holographic spectrometer specifications

	λ	=	wavelength
	λ_0	=	central wavelength
	$n(\lambda)$	=	index of refraction of BK7
	n_0	=	index of refraction at $\lambda = \lambda_0$
	d	=	line separation (= 2405.29 mm^{-1})
	θ_P	=	internal prism angle (= $63°17'30''$)
	α_1	=	angle of prism normal (= $5°$)
	θ_1	=	incidence angle of λ_0 at grating
	θ_2	=	refraction angle of λ_0 at grating
	x_1	=	entrance slit ray position (horizontal)
	z_1	=	entrance slit ray position (vertical)
3.24):	x_2	=	image plane ray position (horizontal)
	z_2	=	image plane ray position (vertical)
	${\phi_1}'$	=	external ray entrance angle (horizontal)
	γ'	=	external ray entrance angle (vertical)
	ϕ_1	=	internal ray entrance angle (horizontal)
	γ	=	internal ray entrance angle (vertical)
	${\phi_2}'$	=	external ray exit angle (horizontal)
	ϕ_2	=	internal ray exit angle (horizontal)
	f_1	=	focal length of input lens (= 85 mm)
	f_2	=	focal length of output lens (= 58 mm)

The index of refraction of BK7 is given by [Schott Corporation, 1999]:

$$n(\lambda) = \sqrt{a_0 + a_1\lambda^2 + a_2\lambda^{-2} + a_3\lambda^{-4} + a_4\lambda^{-6} + a_5\lambda^{-8}}$$

where

$$
\begin{aligned}
a_0 &= 2.2718929 \\
a_1 &= -1.0108077 \times 10^{-2} \\
a_2 &= 1.0592509 \times 10^{-2} \\
a_3 &= 2.0816965 \times 10^{-4} \\
a_4 &= -7.6472538 \times 10^{-6} \\
a_5 &= 4.9240991 \times 10^{-7}
\end{aligned}
$$

Starting with the grating equation

$$\frac{\lambda}{d\ \cos(\gamma)} = \sin(\theta_1 + \phi_1) + \sin(\theta_2 + \phi_2) \tag{3.36}$$

we can use Snell's law and simple geometric relations to form the following relations between the unknown variables and the external angles.

$$\theta_1 = \theta_2 = \theta_P - \sin^{-1}\left(\frac{\sin(\alpha_1)}{n_0}\right) \tag{3.37}$$

$$\phi_1 = \sin^{-1}\left(\frac{\sin(\alpha_1)}{n_0}\right) - \sin^{-1}\left(\frac{\sin(\alpha_1 - \phi_1{}')}{n}\right) \tag{3.38}$$

$$\phi_2 = \sin^{-1}\left(\frac{\sin(\alpha_1)}{n_0}\right) - \sin^{-1}\left(\frac{\sin(\alpha_1 - \phi_2{}')}{n}\right) \tag{3.39}$$

$$\gamma = \sin^{-1}\left(\frac{\sin(\gamma')}{n}\right) \tag{3.40}$$

$$\tan(\gamma') = \frac{z_1}{f_1} = \frac{z_2}{f_2} \tag{3.41}$$

$$\tan(\phi_1{}') = \frac{x_1}{f_1} \tag{3.42}$$

$$\tan(\phi_2{}') = \frac{x_2}{f_2} \tag{3.43}$$

Equations 3.36-3.43 now form a system of 11 equations in the 11 variables θ_1, θ_2, ϕ_1, $\phi_1{}'$, ϕ_2, $\phi_2{}'$, γ, γ', λ_0, x_2, and z_2. The line spacing, focal lengths, and angles d, f_1, f_2, θ_P, and α_1 are constants, and λ, x_1, and z_1 are input quantities. Although it appears that equations 3.36-3.43 comprise only 10 equations, the definition of λ_0 as the ray that enters and exits at $\phi_1 = 0$ and $\phi_2 = 0$ (with no vertical displacement, so that $\gamma = 0$ as well), provides a second, special case of equation 3.36.

In practice, λ_0 can be solved by combining equations 3.36 and 3.37 with $\lambda = \lambda_0$ and $\phi_1 = \phi_2 = \gamma = 0$, and is found to be 7200 Å. This determines n_0 and immediately provides θ_1 and θ_2 through equation 3.37. Given λ and z_1, equations 3.41 and 3.40 provide γ', γ, and z_2. Equations 3.42 and 3.38 provide $\phi_1{}'$ and ϕ_1. ϕ_2 is found by inverting equation 3.36, then $\phi_2{}'$ can be found by inverting equation 3.39. Finally, the position of the output ray x_2 is given by equation 3.43.

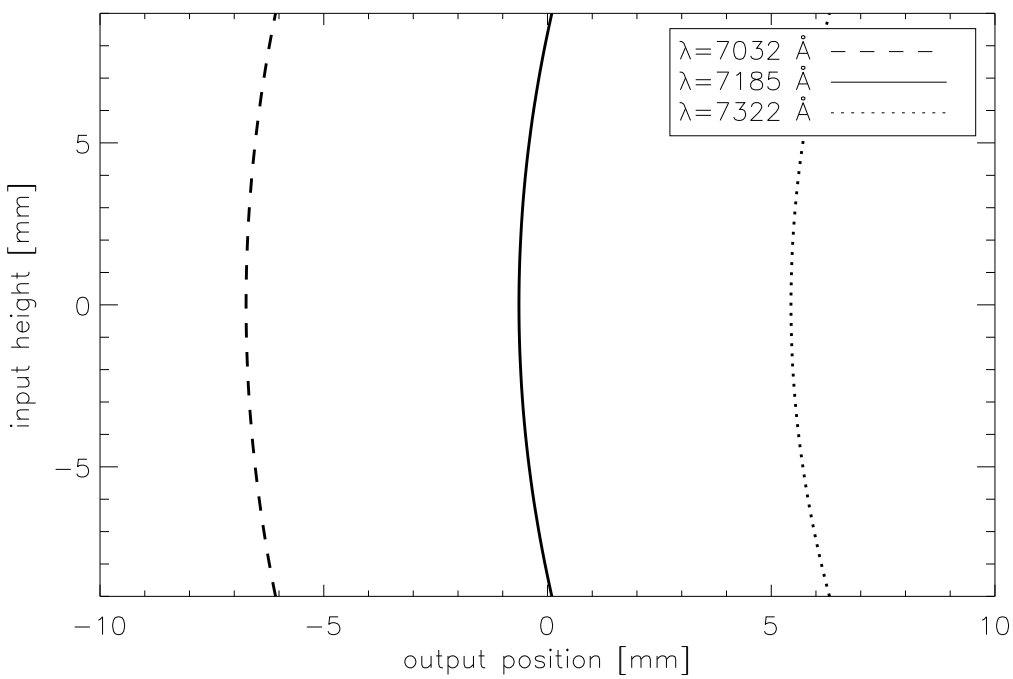

Figure 3.25: Spectrometer output image position vs. ray input height, calculated for a straight entrance slit. Shown are maps for $\lambda = 7032$ Å, $\lambda = 7185$ Å, and $\lambda = 7322$ Å.

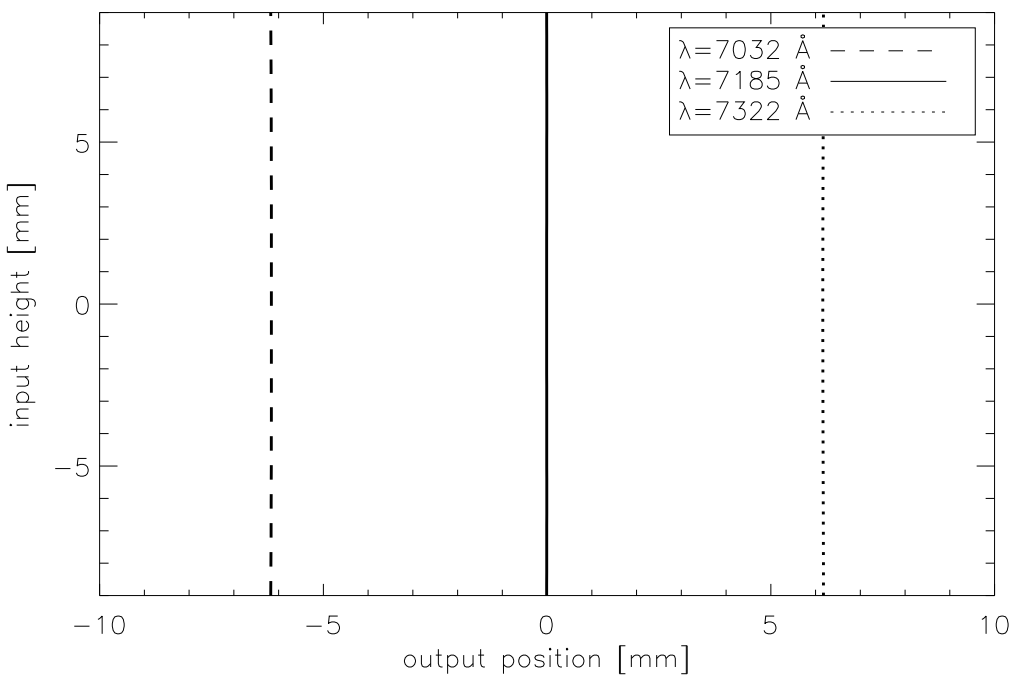

Figure 3.26: Spectrometer output image position vs. ray input height, calculated for a curved entrance slit (see figure 3.27). Shown are maps for $\lambda = 7032$ Å, $\lambda = 7185$ Å, and $\lambda = 7322$ Å.

One consequence of having a finite entrance-slit height is that rays arriving at the grating from different slit positions have different angles of incidence, and thus diffract to different positions on the image plane. An illustration of this is shown in figure 3.25, which shows a map of the position of the 7032 Å, 7185 Å, and 7322 Å lines on the image plane, calculated as a function of slit-height for a straight entrance slit.

In order to simplify analysis of the spectra from all positions along the entrance slit, the output can be "straightened" by curving the entrance slit in the opposite direction so as to negate this effect. This correction is illustrated in figure 3.26, which shows a map of the same three lines as figure 3.25, but this time calculated for a properly curved entrance slit, now producing straight lines at the image plane. A detail of the entrance-slit that produces this mapping is shown in figure 3.27.

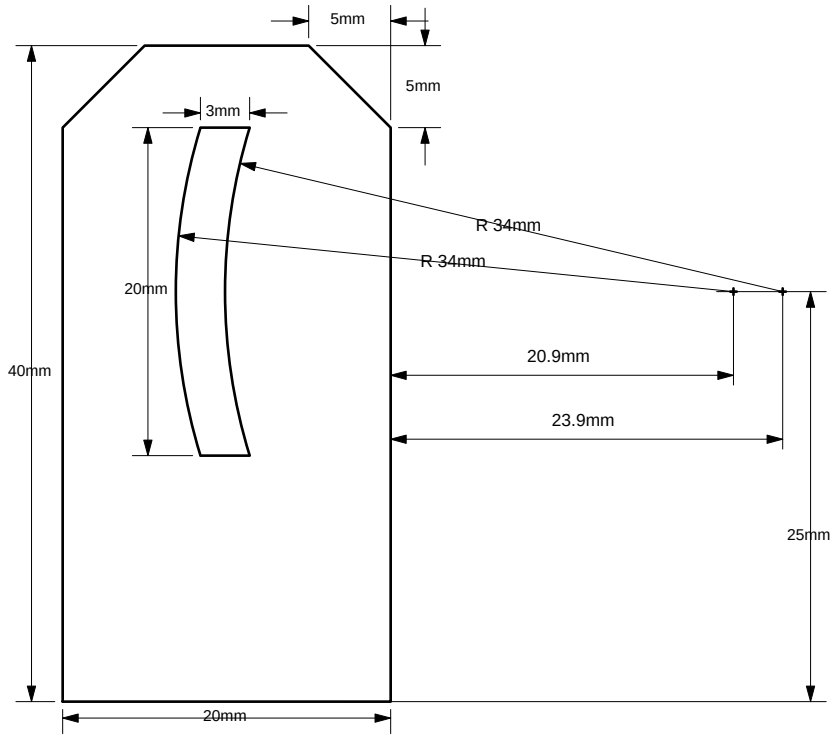

Figure 3.27: Curved entrance-slit designed for TVTS spectrometer

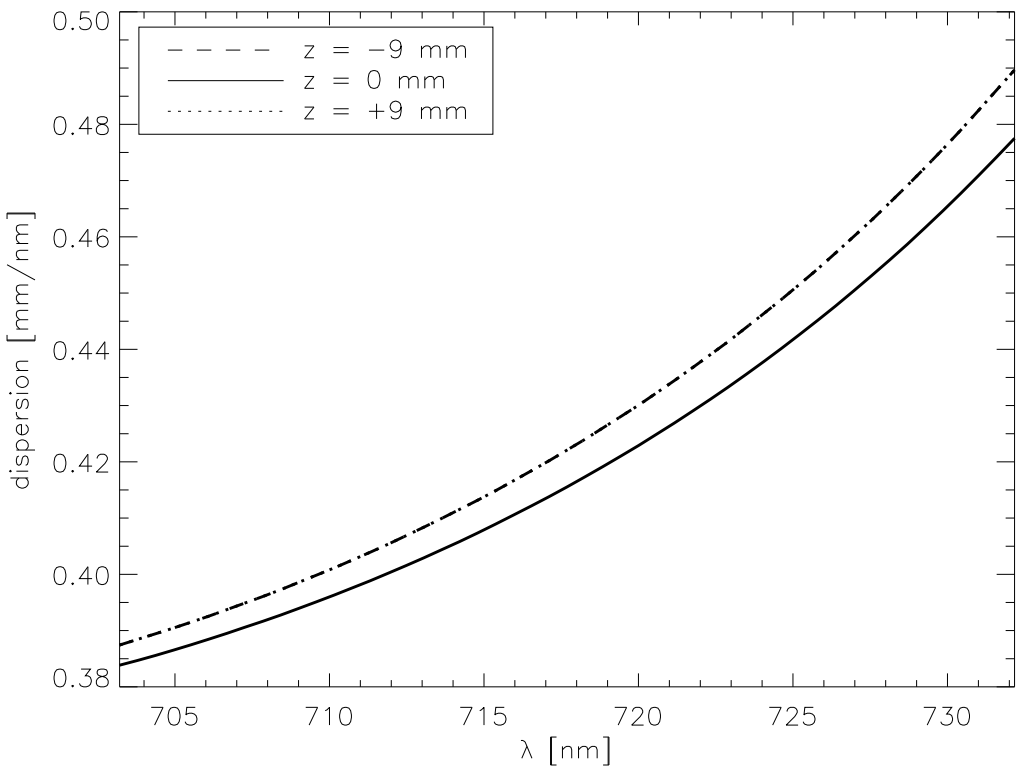

Figure 3.28: Spectrometer dispersion vs. λ, calculated for slit entrance heights of -9 mm, 0 mm, and +9 mm. Note that the dispersion curves at z=±9 mm overlap, but are distinct from the curve at z=0 mm.

In practice, after using the curved entrance-slit shown in figure 3.27, it was found that the largest source of error in the interpretation of the spectra was the position of the fibers at the entrance slit. The rectangular fiber bundles were fit into the curved entrance slit, but even the variation (relative to the slit edge) from the top to the bottom of each bundle caused considerable uncertainty in the fiber position. Since the spectral fitting is automated via computer, it was decided that it would be easier and more reliable to return to a straight entrance slit, and accommodate the exit-plane curvature in the detailed spectral fitting routines.

An additional consequence of having an entrance slit with finite height (without curved-slit correction) is that the dispersion curves vary slightly as a function of slit height. This is illustrated in figure 3.28, which shows the dispersion curves at the optical axis, and at the ends of a straight entrance slit at ±9 mm. Note that the dispersion curves at z=±9 mm overlap, but are distinct from the curve at z=0 mm. This variation in dispersion is automatically taken into account by the spectral fitting routines.

Another factor that must be considered is the effect of the finite slit width on the detected spectrum. Even if the slit is curved as a function of z, the width is constant. Defining $\Delta\lambda_S$ as the slit-width mapped onto the spectrometer image plane, the 'slit function' $s(\lambda)$ can be defined as as follows:

$$s(\lambda) = \begin{cases} 1 & : \quad \frac{-\Delta\lambda_S}{2} < \lambda < \frac{\Delta\lambda_S}{2} \\ 0 & : \quad \text{otherwise} \end{cases} \tag{3.44}$$

The spectrum reaching the CCD is the convolution of the slit function with the un-convolved intensity spectrum $I(\lambda)_{raw}$, given by

$$I(\lambda)_{convolved} = \frac{1}{\Delta\lambda_S} \int_{\lambda-\frac{\Delta\lambda_S}{2}}^{\lambda-\frac{\Delta\lambda_S}{2}} I(\lambda')_{raw} \quad \mathrm{d}\lambda' \tag{3.45}$$

3.3.5 Intensified CCD Camera

The detector used is an IMAX intensified CCD made by Princeton Instruments [Princeton Instruments, 1998]. The intensifier uses an 18 mm GaAs Gen IV photocathode which provides ∼30% quantum efficiency in the 700 nm range. Noise

which is implicit to signal amplification and digitization leads to a usable "detective quantum efficiency" of ∼15% (see section 3.4).

The intensifier is fiber-optically coupled to a 512×512 pixel CCD through a tapered fiber bundle with taper ratio of 1.27:1. The 512×512 pixels, each 19 μm × 19 μm cover an effective image area of 12.35 mm × 12.35 mm. The ∼1 kV, 100 ns pulse which gates the image intensifier is provided by an internal high-voltage pulser, so that the camera unit requires only TTL-level input signals.

The camera is thermoelectrically cooled, typically to -15° C, though no external water or air lines are required. The camera is controlled via a PCI-bus computer interface card mounted in a dedicated PC, located in the CDX-U control room. The PC is used to set up the camera for an upcoming exposure, the camera is triggered by a branch of the tokamak triggering chain, and the image is then retrieved and stored to disk.

Timing of the camera in relation to the tokamak pulse and laser pulse is controlled by a Stanford Research Systems DG-535 timing unit. A number of relative delays are set in the DG-535, which are listed in table 3.7 as a reference for future modifications. Also, relevant software settings for the "WinView" software package, used for camera control, are listed in table 3.8.

Delay	**Setting**	**Description**
A	T_0 + 850 μs	Delay from flashlamp firing to Pockels-cell firing
B	A + 100 ns	Duration of intensifier gating
C	A - 1100 ns	Pre-trigger delay required by Pockels-cell HV pulse-forming circuit
D	A - 50 μs	Pre-trigger delay to clear CCD

Table 3.7: DG-535 delay generator settings for TVTS ICCD control

3.3.6 Laser Timing Jitter

Because the timing of both the laser pulse and the camera gate are controlled by a master clock, i.e. the DG-535 delay generator, any jitter in the delay from the Pockels-cell trigger to the laser pulse results in a relative mistiming of the camera gate. In practice, this jitter was found to be on the order of 50-100 ns, the same

Option	**Setting**
Exposure time	100 μs
Number of images	1
Number of accumulations	1
Intensifier mode	Gate mode
Intensifier gain	255
Data corrections	None
ADC type	Slow
Timing mode	External Sync
Continuous cleans	On
Shutter control	Normal
Pre-open	On
Sync/Async	Full speed (sync)
Wait for TTL	Off
Thresholding	None
Controller	ST133, version 3
Camera type	TH 512×512
Shutter type	Electronic
Readout mode	Full frame
RS170 type	NTSC
Interface	High speed PCI
Number of cleans	0
Number of strips per clean	4
Minimum skip block size	16
Number of blocks	32

Table 3.8: WinView software settings for TVTS ICCD control

as the duration of the gate itself. It was therefore necessary to devise a different timing scheme, which involved synchronizing the camera gate to the actual laser pulse, rather than to the Pockels cell trigger.

Other TVTS systems have traditionally used a triggering scheme in which a fraction of the light emitted from the oscillator cavity is sent through a fiber-optic to a photodiode which triggers the camera gate. A positive delay is inserted into this line to match the delay experienced by the laser light as it travels through the laser amplification stages, through any beam transport to the scattering volume, and from the scattering volume through the collection optics to the camera, so that when the light arrives at the camera, the gate is open. This delay is on the order of nanoseconds, and is often in practice introduced by a length of fiber-optic between the oscillator- sampling optic and the photodiode. This scheme relies on the fact that the delay introduced by the laser path length is longer than the switching delay of the photodiode and gating circuit, which is just barely the case with the compact CDX-U system.

A triggering circuit was built for the CDX-U system which applies the scheme described above, replacing the gate-pulse camera inputs previously from the DG-535. The switching delays in this circuit were kept to an absolute minimum, on the order of 35 ns. It was found that by using the shortest fiber-optic possible and by triggering off of the very early buildup of oscillator output, the camera gate led the arrival of scattered light by $\sim$12 ns. The camera gate was delayed to the proper timing by the introduction of attenuating filters in front of the sampling fiber optic, so that the camera gate was triggered by a higher level of oscillator light. This also led to more stable synchronization of the laser and camera gate.

3.4 Calibration

Calibration of the TVTS system involved the verification of factory specifications for many of the constituent components, calibration of subsystems, and final calibration of the full integrated diagnostic. Each of these steps is outlined in the following sections.

3.4.1 Spectral Calibration of Spectrometer

The determination of temperature from the measured spectra is critically dependent on the known dispersion of the spectrometer. A careful calibration, comparing the expected dispersion to the measured values was thus necessary. The calibration was performed using the combination of spectrometer and camera, a set of Helium, Neon, and Argon discharge tubes, and a 50 μm centered entrance slit. 15 known emission lines were bright enough to analyze, and are listed in table 3.9, along with the pixel location of the best-fit Gaussian for each line. A quadratic function was then best-fit to the 15 coordinate pairs (wavelength, pixel mapping) to provide a simple formula describing the measured spectrometer dispersion. Plots of the three spectra from Neon, Argon, and Helium, along with the best-fit dispersion curve, are shown in figure 3.29

Element	**Wavelength [Å]**	**Pixel**
Ne	7245.17	355.058
Ne	7173.94	225.031
Ne	7059.11	29.5230
Ne	7051.29	16.5144
Ar	7067.22	42.6094
Ar	7107.48	109.938
Ar	7206.98	284.438
Ar	7272.94	408.094
Ar	7125.83	141.234
Ar	7147.04	177.738
Ar	7158.83	198.473
Ar	7311.72	484.914
Ar	7316.01	493.375
He	7065.19	38.7344
He	7281.35	423.652

Table 3.9: Emission Lines for Spectrometer Calibration

The mapping of wavelength to CCD pixel (at the center of the entrance slit) is provided by the fitting routine, and is:

$$\text{Pixel} = 23637.7 - 8.31136\,\lambda + 7.03628 \times 10^{-4}\,\lambda^2 \tag{3.46}$$

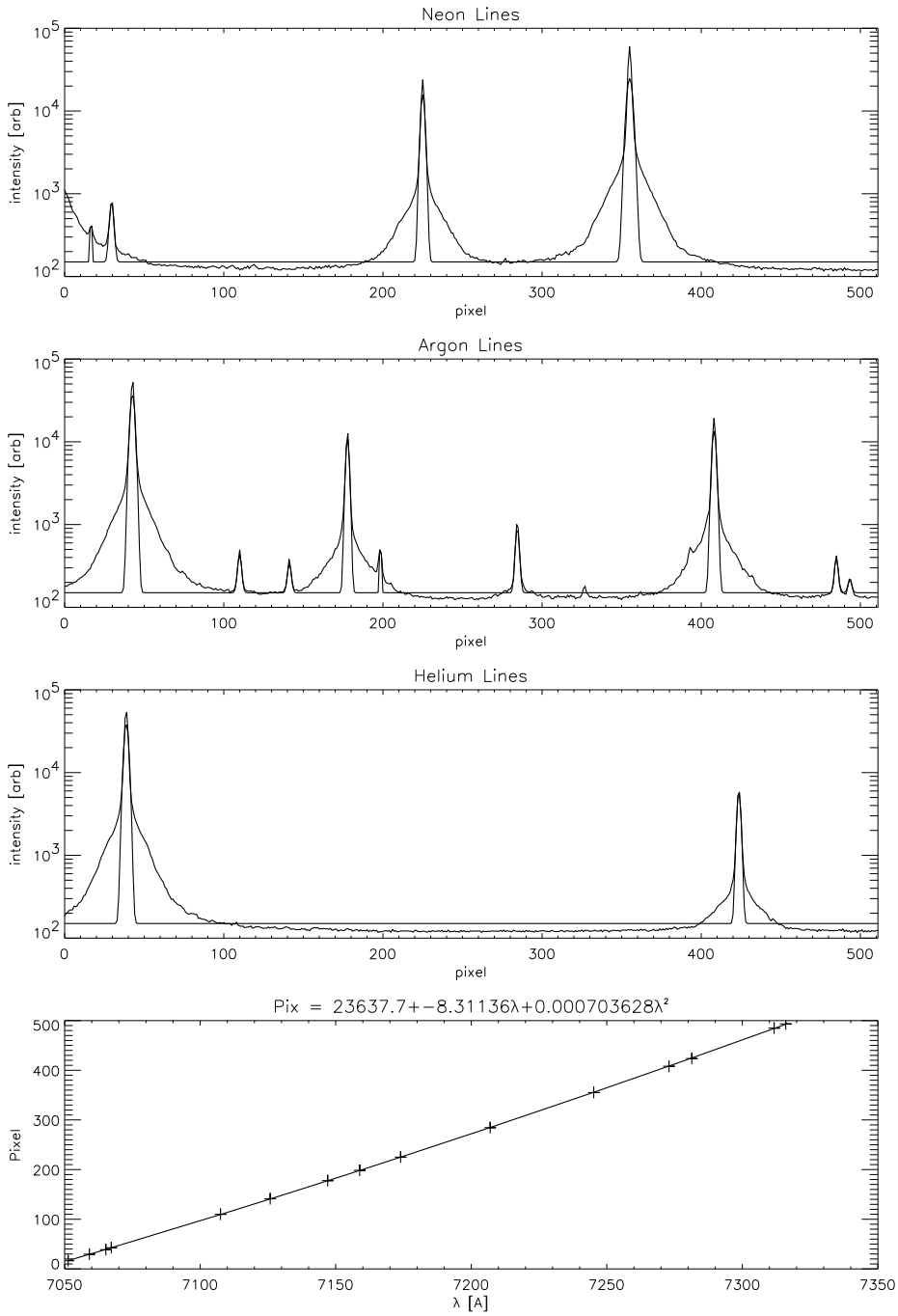

Figure 3.29: Spectral calibration of TVTS spectrometer using 15 known emission lines from Ne, Ar, and He discharge lamps.

where λ is in Å. This represents a 3% magnification over the modeled ray-trace, which was verified by measuring the height of the entrance slit and comparing it to the height of the image on the detector plane.

3.4.2 Determination of ICCD Quantum-Efficiency

Though the stated quantum-efficiency of the GaAs intensifier is ∼30%, the usable quantum efficiency of the camera unit is reduced from this figure due to amplification and digitization noise. The figure of merit for a detector of this kind is the "Detective Quantum Efficiency" (DQE), which is typically ∼ 50% of the rated quantum-efficiency for intensified CCD detectors. DQE can be determined by the signal-to-noise formula

$$SNR_{out} = \frac{\langle S \rangle}{\sigma_S} = \frac{\langle N \rangle}{\sqrt{\frac{{\sigma_N}^2}{DQE} + 2{\sigma_d}^2}} \tag{3.47}$$

where S is the number of output counts, N is the number of input photons, and $\sigma_{S,N}$ are the standard-deviation of these quantities. σ_d is the "dark" noise, intrinsic to the digitization and readout of the CCD signals. This can be measured in practice by exposing the camera to a dark room, and taking shot-to-shot statistics of the pixel counts. In the case of the Princeton Instruments camera, σ_d was found to be negligible compared to the other noise sources, and in this case the SNR formula can be simplified and inverted to provide a formula for DQE:

$$DQE = \frac{\langle S \rangle^2}{{\sigma_S}^2} \cdot \frac{{\sigma_N}^2}{\langle N \rangle^2} = \frac{SNR_{out}}{SNR_{in}} \tag{3.48}$$

The DQE was determined for the Princeton Instruments ICCD by taking 20 exposures each of an Optronics calibrated light source at 9 different intensity settings and exposure times, covering nearly four orders of magnitude in total photons collected. The light source was filtered by a narrow bandpass filter centered at 7000 Å, representative of the wavelength range expected from Thomson scattering. The range of integrated photon intensity was also chosen to correspond to levels expected from Thomson scattering.

Results of this study are shown in figure 3.30. The first plot shows the response

of the detector at each light/exposure setting. The response was found to be extremely linear over the full range, with a measured sensitivity of 55.8 counts per photon. Error bars are shown, and represent shot-to-shot variation over the 20 exposures. The second plot shows the signal-to-noise ratio of the input photons (estimated as the square-root of the number of incident photons) and camera response (calculated from measured shot-to-shot statistics). Error bars for SNR of the output counts are presented, and represent pixel-to-pixel variation across the CCD. DQE is determined to be ∼17%.

3.4.3 Whiteplate Calibration of Collection Optics and Detector

It is necessary to spectrally calibrate the full system of collection optics, from the front lens through the fiber optics, spectrometer, to the CCD. This is important not only to firmly calibrate the total throughput of the optical system, but to be able to calibrate any spectral variation implicit to the system. In particular this can be due to antireflection coatings on the elements of the collecting lens, the spectral variation in the attenuation in the plastic fibers, the notch filter at the entrance to the spectrometer, and the variation across the surface of the CCD and intensifier. The attenuation curve for the fibers is shown in figure 3.19, and the notch-filter characteristic is shown in figure 3.23. Center-to-edge variation in ICCD response is typically up to 50%.

The system was tested using a LabSphere calibrated light source with known spectral radiance. This spectrum was fed through the ray-tracing routines for the spectrometer to produce an "ideal" response at the CCD, which was then compared to the measured response, which is shown in figure 3.31.

The most visible characteristic in figure 3.31 is the center-to-edge variation from the image intensifier, found to be ∼55%. 11 spatial channels are readable, though strong response is only visible in the inner 9 channels. The top edge of the CCD is unused because of vertical mis-placement of the entrance slit, which can be straightforwardly corrected in future work.

The quotient of the measured response divided by the ideal response provides the spectral attenuation through the full system of collection optics, which is then

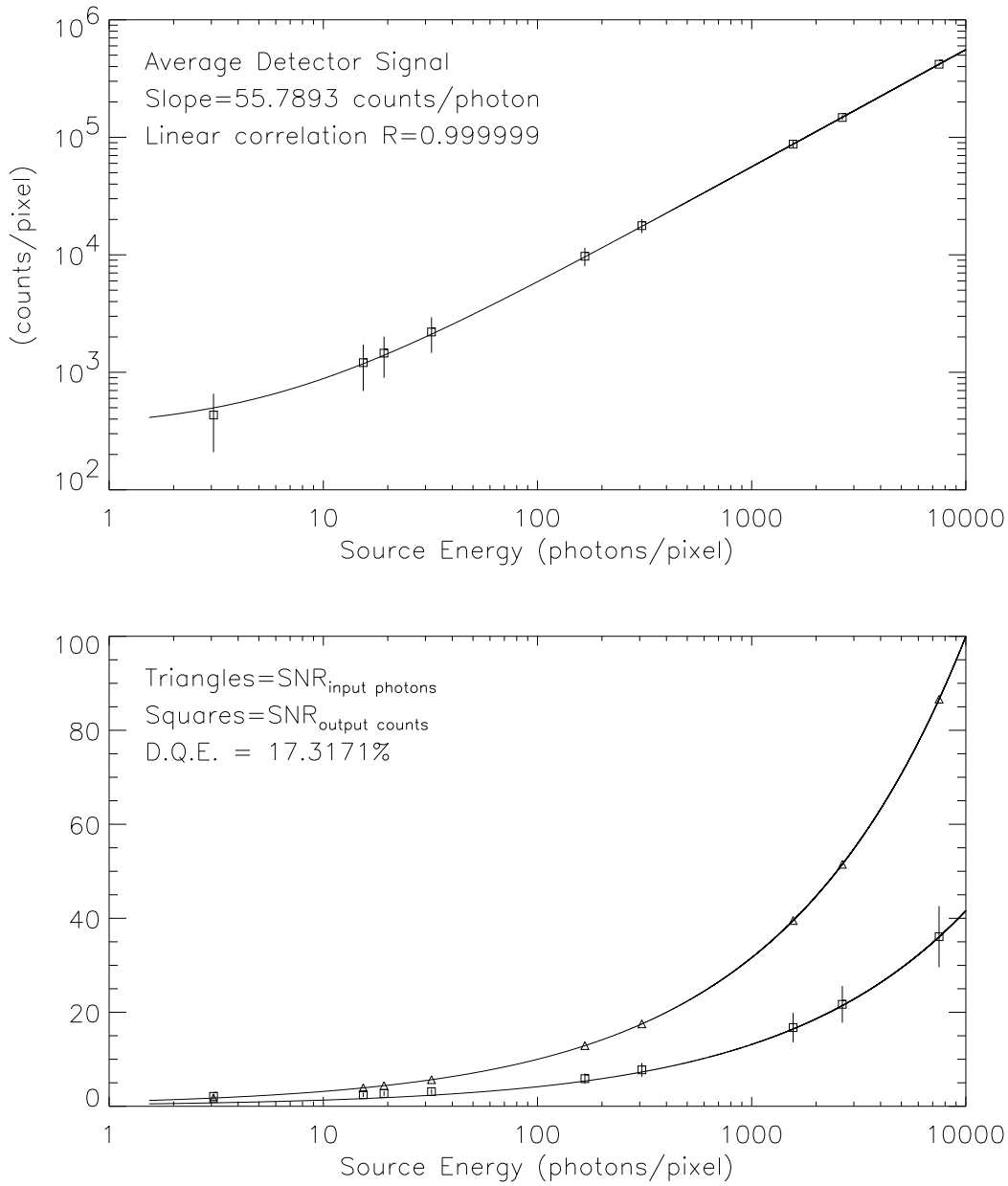

Figure 3.30: DQE calculation for the ICCD camera. The first plot shows the response of the detector, linear over nearly four orders of magnitude. Error bars represent shot-to-shot variation over 20 exposures. The second plot shows the signal-to-noise ratio of the input photons (estimated) and camera response (calculated). Error bars represent pixel-to-pixel variation. DQE is determined to be ∼17%.

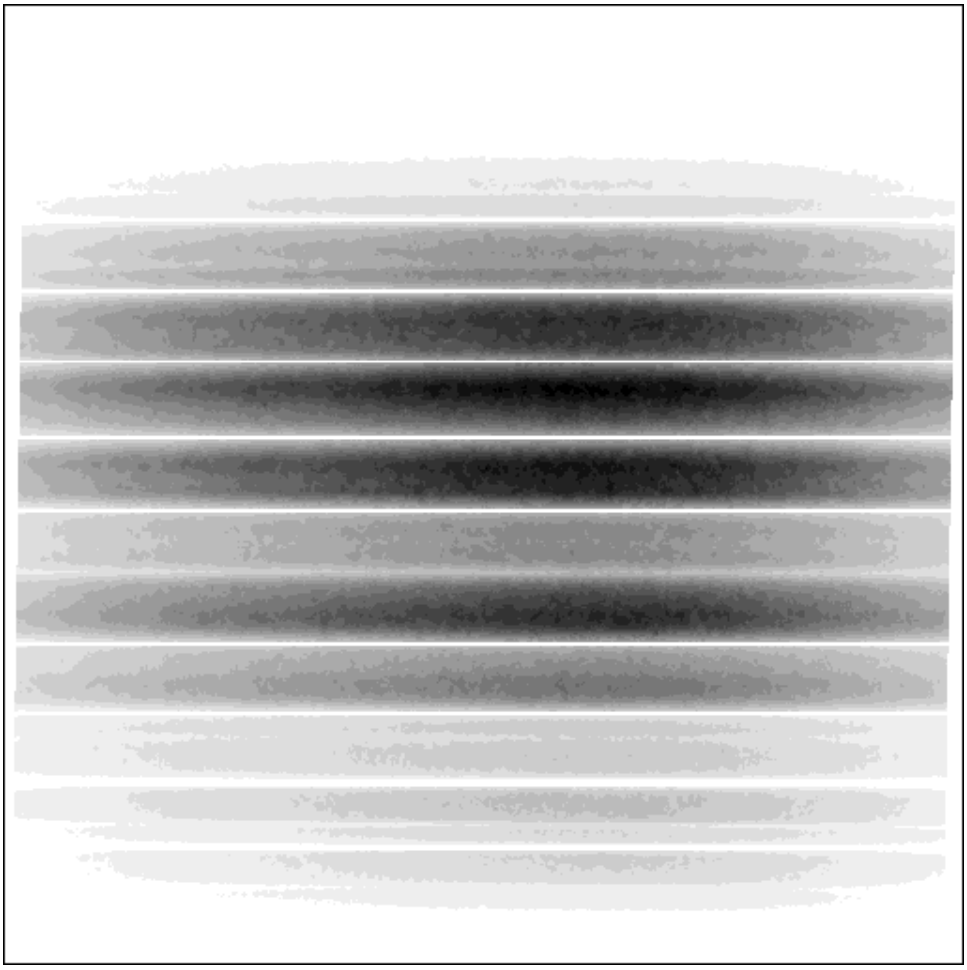

Figure 3.31: Whiteplate response at the CCD. X-axis corresponds to wavelength, y-axis corresponds to spatial channel. Strongest response is shown as darkest. 11 spatial channels are readable, though strong response is only visible in the inner 9 channels. The top edge of the CCD is unused because of vertical mis-placement of the entrance slit.

used to correct all measured spectra.

3.4.4 Full System Calibration Using Raman Scattering

Though each component of the TVTS system can be effectively calibrated using the methods described above, it is extremely useful to have an integrated test and calibration of the full working system, including the laser. This provides an absolute calibration for electron density measurements, provides a final check of the timing synchronization between the laser and the detectors, and verifies the alignment of the collection fibers. Often Rayleigh scattering from neutral Helium or Argon is used for this purpose.

In the CDX-U system, the plasma temperatures are such that the spectrum is quite compressed, and the Thomson scattered spectrum lies very close in wavelength to the ruby laser line. Because of this, the notch-filter which blocks the laser line is an essential part of the system. Rayleigh scattering, in which the scattered light has the same wavelength as the laser beam, is therefore not possible in the CDX-U system.

An alternative method is to use Raman scattering from diatomic molecules, in which the scattered spectrum is shifted due to rotational resonances of the molecule. This method has been used in several Thomson scattering systems [Rohr, 1981; Howard *et al.*, 1979; McCool *et al.*, 1981]. A brief overview is provided here following [McCool *et al.*, 1981], including application to the CDX-U system.

Raman scattering is a process by which a molecule gains or loses rotational or vibrational energy during a photon scattering event. The rule for rotational Raman scattering is that $\Delta J = \pm 2$, where J is the rotational quantum number of the molecule. If $\Delta J = +2$, the molecule gains energy from the photon, and the scattered photon wavelength increases. This is termed Stokes scattering, and the $\Delta J = -2$ case is termed anti-Stokes scattering.

A Raman scattered spectrum consists of a series of discrete lines centered around the incident laser wavelength. The intensity of each scattered line is dictated by the scattering cross-section relevant to that line and the number of molecules in an initial state appropriate to that transition energy.

The Raman line wavelengths are given by the formula [Herzberg, 1939]:

$$\lambda_{J\to J'} = \frac{1}{\tilde{\nu}_0 + \Delta\tilde{\nu}} \tag{3.49}$$

where $J' = J \pm 2$, $\tilde{\nu}_0 = (6943\ \text{Å})^{-1} = 14402\ \text{cm}^{-1}$, and $\Delta\tilde{\nu} = (E_J - E_{J'})/hc$.

For the ground vibrational state [Weber, 1979]:

$$\frac{E_J}{hc} = B_0[J(J+1)] - D_0[J(J+1)]^2 + H_0[J(J+1)]^3 \tag{3.50}$$

For Hydrogen, $B_0 = 59.3392\ \text{cm}^{-1}$, $D_0 = 0.04599\ \text{cm}^{-1}$, and $H_0 = 5.21\times10^{-5}\ \text{cm}^{-1}$. For Nitrogen, $B_0 = 1.989548\ \text{cm}^{-1}$, $D_0 = 5.72 \times 10^{-6}\ \text{cm}^{-1}$, and $H_0 = 3.7 \times 10^{-10}\ \text{cm}^{-1}$.

The cross section for Raman scattering from a linearly polarized source is given by [Penney *et al.*, 1974]:

$$\sigma_{J\to J'} = \frac{7\,(2\pi)^4\,S(J)\,\gamma^2}{45\,(\lambda_{J\to J'})^4} \tag{3.51}$$

where

$$S(J) = \frac{3(J+1)(J+2)}{2(2J+1)(2J+3)} \quad \text{for} \quad J \to J+2$$

$$S(J) = \frac{3J(J-1)}{2(2J+1)(2J-1)} \quad \text{for} \quad J \to J-2 \tag{3.52}$$

The constant γ^2 is $9.28\times10^{-50}\ \text{cm}^6$ for ruby light scattered from H_2, and $0.45\times10^{-48}\ \text{cm}^6$ for ruby light scattered from N_2 [McCool *et al.*, 1981].

The intensity calculated for each Raman line is proportional to the number of molecules in an initial state susceptible to that particular transition. For a gas in thermal equilibrium (Boltzman distribution of rotational states), the fraction of molecules in state J is given by [Penney *et al.*, 1974]:

$$F_J = \frac{g_J\,(2J+1)}{Q}\exp\left(-\frac{E_J}{k_B T}\right) \tag{3.53}$$

where the degeneracy g_J is as follows: for H_2, $g_{J=even} = 1$ and $g_{J=odd} = 3$; for N_2, $g_{J=even} = 6$ and $g_{J=odd} = 3$. Q is the normalization constant such that

$$\sum F_J = 1$$

i.e.

$$Q = \sum g_J \, (2J+1) \, \exp\left(-\frac{E_J}{k_B T}\right) \tag{3.54}$$

The relative intensity of each Stokes or anti-Stokes line ($J' = J \pm 2$) is then given by

$$I_{J \to J'} = F_J \cdot \sigma_{J \to J'} \tag{3.55}$$

Figure 3.32 shows the relative intensity of the first 38 Stokes and anti-Stokes lines for Raman scattering from N_2. Figure 3.33 shows a similar plot for H_2, though only they first 9 lines are shown, and the wavelength scale is considerably expanded. Recalling that the CDX-U TVTS wavelength range is from 7000-7320 Å, one sees that quite a number of N_2 lines fall within the detector range, though only on the low-λ edge of the detector. Alternatively, only two H_2 lines fall within the detector range, though they fall squarely in the center of the detector.

In order to model the expected signal from Raman scattering, it is first necessary to bin the relative-intensity plot into the spectral mapping of each detector pixel, then convolve this response with the mapping of the finite slit width onto the CCD, as described in section 3.3.4. Defining the function $\rho_i(\lambda)$ to be 1 where λ falls within the mapping of $pixel_i$ and 0 otherwise,

$$\sigma_{Raman,i} = \sum_{J=0}^{\infty} (F_J)(\sigma_{J \to J+2})(\rho_i(\lambda_{J \to J+2})) + \sum_{J=2}^{\infty} (F_J)(\sigma_{J \to J-2})(\rho_i(\lambda_{J \to J-2})) \tag{3.56}$$

The signal reaching the entrance slit will of course be dependent on the density of scattering molecules, the scattering volume, the number of incident photons, and the optical collection efficiency. The scattered signal at each pixel from an infinitely

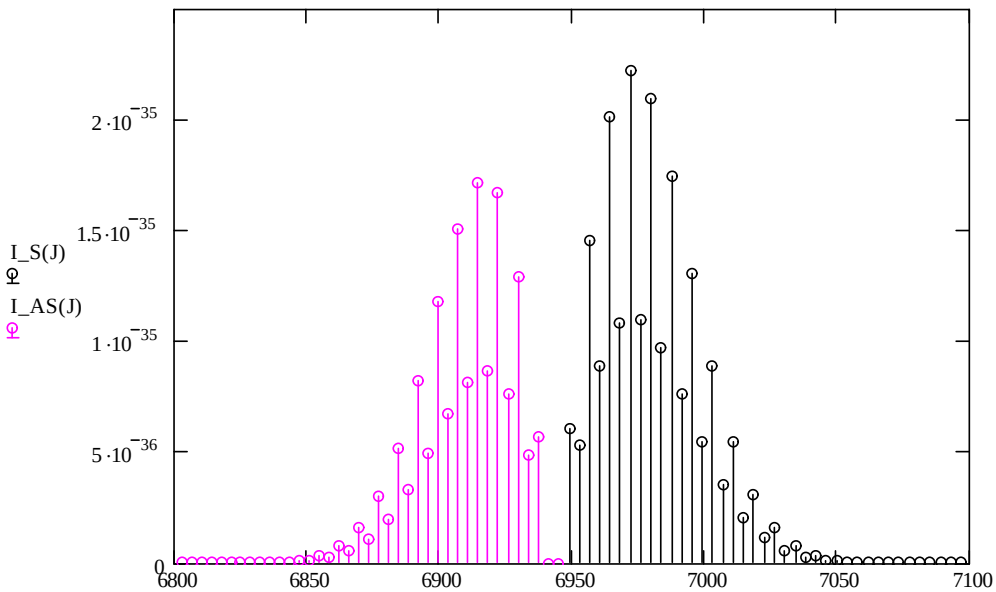

Figure 3.32: Relative intensity of Stokes (black) and anti-Stokes (gray) Raman lines vs. λ [Å], as given by equation 3.55 for scattering from N_2.

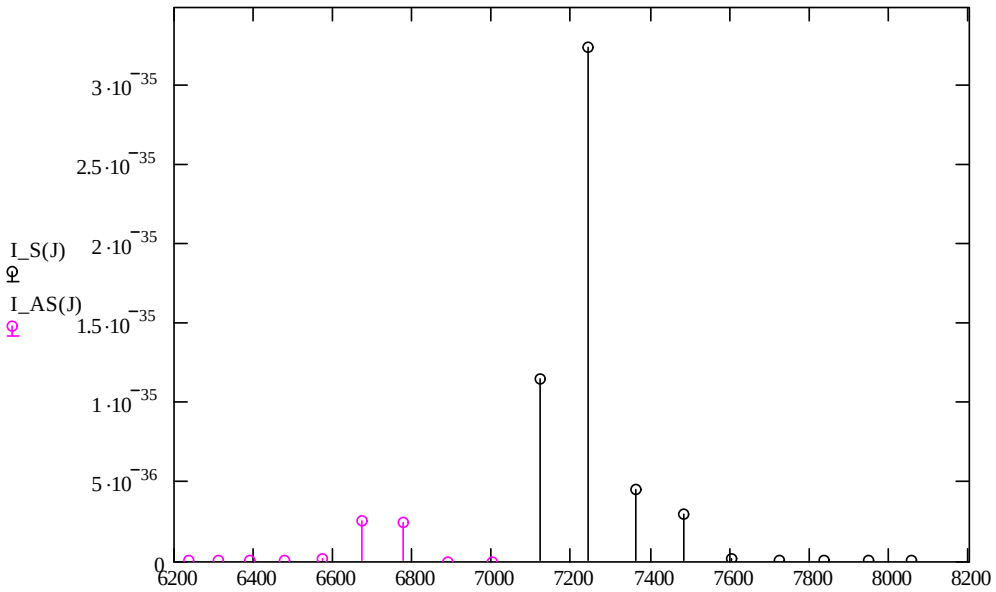

Figure 3.33: Relative intensity of Stokes (black) and anti-Stokes (gray) Raman lines vs. λ [Å], as given by equation 3.55 for scattering from H_2.

thin entrance slit is given by

$$S_{Raman,i} = \sigma_{Raman,i} \times \left(\frac{n_n \; L \; \Delta\Omega \; T \; \eta \; N_i}{LPC} \right) \tag{3.57}$$

where n_n is the density of neutral molecules, L is the scattering volume, $\Delta\Omega$ is the collection solid angle, T is the optical transmission, η is the detector quantum-efficiency, N_i is the number of incident photons, and LPC is the number of CCD lines per spatial channel (38 for the CDX-U system).

Finally, the signal is convolved with the finite slit width. Defining Δpix as the mapping of the slit-width to the image plane of the spectrometer (measured in pixels), the convolved signal at $pixel_i$ is given by

$$S_{Raman,i}(convolved) = \frac{1}{\Delta pix} \sum_{j=i-\frac{\Delta pix}{2}}^{i+\frac{\Delta pix}{2}} S_{Raman,j} \tag{3.58}$$

Due to the difficulty of filling CDX-U with relatively high pressure (10's of torr necessary) H_2, it was decided to calibrate the CDX-U system with N_2. Because the entire TVTS system is housed on a moving support structure, it is possible to move the beam-path behind the CDX-U vacuum vessel and vertical field coils, so that Raman scattering can be performed through ambient air (78% N_2). This turned out to be a simple way to periodically perform a system check of the TVTS diagnostic whenever there was a question as to whether any of the components were working properly.

Figure 3.34 shows a comparison of the measured Raman scattering signals, taken in air at atmospheric pressure, and expected signals, calculated using equation 3.58 for the fully convolved case. Comparisons are shown for the 9 readable TVTS channels and one "background" channel imaging beside the beamline. Ideally the background channel would show no response, though there is a readable signal of ∼5-10% of the level seen by the channels imaging the beam. This can be due either to light reaching the background fiber bundle or to crosstalk in the imaging optics and detector.

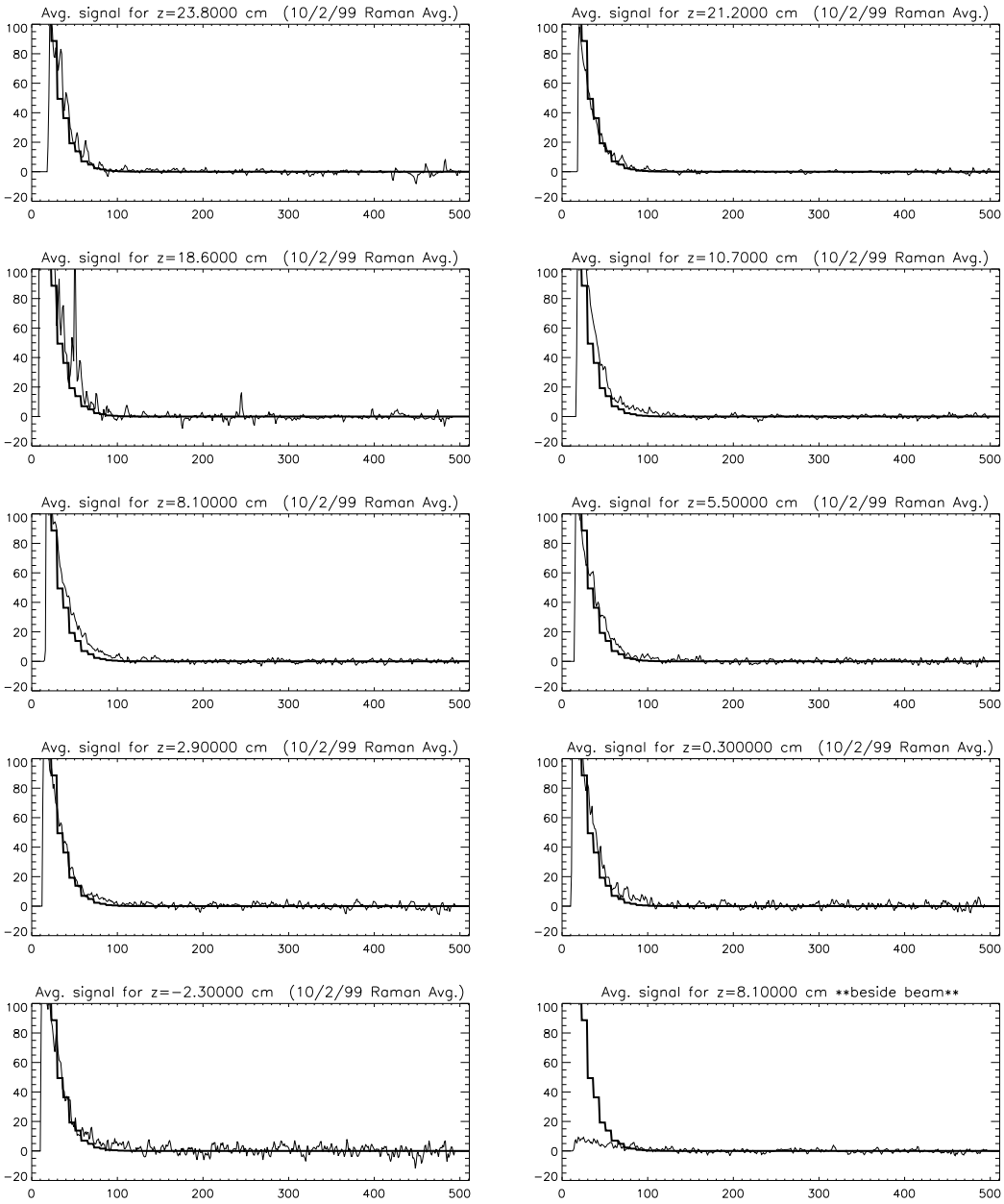

Figure 3.34: Comparison of measured and expected Raman scattering signals, shown for the 9 readable TVTS channels and one "background" channel imaging beside the beamline.

3.5 System Performance Calculations

The quality of scattered spectra at any particular location in the plasma is critically dependent on both n_e and T_e at that location. In order to accurately model system performance, sample n_e and T_e profiles were used to predict the performance of the TVTS system. Model parameters included $n_e(0) = 2 \times 10^{13}$ cm^{-3}, $n_e(z_{max}) = 2 \times 10^{12}$ cm^{-3}, $T_e(0) = 100$ eV, $T_e(z_{max}) = 10$ eV. Here $z_{max} = \kappa\, a = 33$ cm. Profiles are given by the functions

$$\begin{aligned} n_e(z) &= n_e(z_{max}) + (n_e(0) - n_e(z_{max}))\left(1 - \left(\frac{z}{z_{max}}\right)^2\right)^2 \\ T_e(z) &= T_e(z_{max}) + (T_e(0) - T_e(z_{max}))\left(1 - \left(\frac{z}{z_{max}}\right)^2\right)^2 \end{aligned} \tag{3.59}$$

Additional parameters used in the model are 8 Joule total laser energy (4 Joules x 2 passes), $\eta = 0.15$, and 30% optical transmission. Also the actual CDX-U optical geometry is used, which includes 12 sampling fibers each with a scattering length in the plasma of $L = 1.25$ cm, collection solid angle of $\Delta\Omega = 0.01$ sr, spectral-width per pixel of $\Delta\lambda = 0.56$ Å, and scattering angle ranging from 71.6° to 108.4°.

The number of photoelectrons produced per pixel by scattered light is given by equation 3.27, repeated here for convenience:

$$N_{pe}(z, \lambda_s) = \frac{N_i\,(\eta\, T)\, {r_{e0}}^2\, n_e\, L\, \Delta\Omega\, \Delta\lambda_s}{\lambda_i\, \delta\, \sqrt{\pi}} \exp\left[-\frac{(\lambda_s - \lambda_i)^2}{{\lambda_i}^2\, \delta^2}\right]$$

Here

$$\delta = \frac{2 v_{te}}{c}\left(f_1 \sin\left(\frac{\theta_{s1}}{2}\right) + f_1 \sin\left(\frac{\theta_{s1}}{2}\right)\right) \tag{3.60}$$

which differs from the definition used in equation 3.27, because of the double-pass beam path through the plasma. Light will be scattered from both the down-going and up-going beams, and the two resulting scattering angles must be accounted for. Thus f_1 and f_2 are the relative fractions of down-going and up-going beam power ($f_1 \approx 0.6$, $f_2 \approx 0.4$), and θ_{s1} and θ_{s2} are the angles between the down-going and up-going beam and the scattering direction.

Although the actual spectra are fit using the full 512-pixel spectrum, and are fit to a simulated spectrum based on a detailed ray-trace through the spectrometer optics (see section 3.3.4), the overall optical design was based on a performance specification derived from simulated spectra from model plasma profiles. In this simulation, the spectrum was binned into five spectral channels, the width of which corresponds to the mapping of the entrance slit onto the image plane. Taking 50 photoelectrons per channel as the noise floor, the model T_e and n_e profiles provided a full 5-point spectra over spatial channels 1-7 (of 12), 4-point spectra over channels 8-9, a 3-point spectrum in channel 10, and a 2-point spectrum in channel 11. Channel 12 (corresponding to the edge values of n_e and T_e) only exceeded the noise floor in the first spectral channel. Note that this does not explicitly rule out measuring T_e down to the edge value, but either higher n_e or higher photon statistics from other system improvements is required to produce a readable signal in the outer spectral channels. As described in section 3.3.2, the fiber bundles are designed so that they can be rearranged to cover different regions of the plasma as needed.

3.5.1 Statistical Error Bars

Since the quality of the data fit which determines T_e and n_e depends on a finite number of collected photons, it is important to determine the error-bars which result from the photon statistics.

The collected spectrum is given by (see equation 3.27)

$$N_{pe}(\mathbf{R}, \lambda_s) = \frac{K_1\, n_e}{\sqrt{T_e}} \exp\left[-\frac{(\lambda_s - \lambda_{ruby})^2}{K_2\, T_e}\right] \tag{3.61}$$

where

$$K_1 = \frac{N_i\,(\eta\, T)\, {r_{e0}}^2\, L\, d\Omega\, d\lambda_s}{\sqrt{K_2}\,\sqrt{\pi}} \tag{3.62}$$

$$K_2 = \frac{8{\lambda_{ruby}}^2}{m_e c^2}\left(f_1 \sin\left(\frac{\theta_{s1}}{2}\right) + f_2 \sin\left(\frac{\theta_{s2}}{2}\right)\right)^2 \tag{3.63}$$

By substituting

$$X = \lambda_s - \lambda_{ruby} \qquad Y = \ln(N_{pe}) \tag{3.64}$$

the data analysis becomes a least-squares fit to the curve

$$Y = A + CX^2 \tag{3.65}$$

which produces the quantities

$$A = \ln\left(\frac{K_1\, n_e}{\sqrt{T_e}}\right) \tag{3.66}$$

and

$$C = \frac{-1}{K_2\, T_e} \tag{3.67}$$

The least-squares coefficients A and C are given by the following "normal equations" (extension of equations 8.10-8.12 in [Taylor, 1982]):

$$A = \frac{\left(\sum {x_i}^4\right)\left(\sum y_i\right) - \left(\sum {x_i}^2 y_i\right)\left(\sum {x_i}^2\right)}{\Delta} \tag{3.68}$$

$$C = \frac{N\left(\sum {x_i}^2 y_i\right) - \left(\sum y_i\right)\left(\sum {x_i}^2\right)}{\Delta} \tag{3.69}$$

$$\Delta = N\left(\sum {x_i}^4\right) - \left(\sum {x_i}^2\right)^2 \tag{3.70}$$

where x_i are the $\lambda_s - \lambda_{ruby}$ values for each pixel, y_i are the values $\ln(N_{pe})$, the natural log of the photon count at each pixel, $N = 512$, and all sums are over the 512 pixels in each spectrum (already summed over the ~38 pixels per spatial channel).

We are now interested in the error in the T_e and n_e values derived from the coefficients A and C. Since T_e and n_e depend on the derived values A and C, the calculation of σ_{T_e} and σ_{n_e} will first require a calculation of σ_A and σ_C, which will

in turn begin with a calculation of σ_y. Deviations of the y_i from the curve given by equation 3.65 will be given by $y_i - (A + C{x_i}^2)$, leading to a standard deviation given by

$$ {\sigma_y}^2 = \frac{1}{N-2} \sum (y_i - A - C{x_i}^2)^2 \tag{3.71} $$

Using standard error-propagation, σ_A and σ_C can be calculated using

$$ {\sigma_A}^2 = {\sigma_y}^2 \sum \left(\frac{dA}{dy_i} \right)^2 \qquad {\sigma_C}^2 = {\sigma_y}^2 \sum \left(\frac{dC}{dy_i} \right)^2 \tag{3.72} $$

Differentiating equation 3.68 leads to

$$ \frac{dA}{dy_i} = \frac{\left(\sum {x_i}^4\right) - \left({x_i}^2\right)\left(\sum {x_i}^2\right)}{\Delta} \tag{3.73} $$

$$ \left(\frac{dA}{dy_i} \right)^2 = \frac{\left(\sum {x_i}^4\right)^2 + \left({x_i}^4\right)\left(\sum {x_i}^2\right)^2 - 2\left({x_i}^2\right)\left(\sum {x_i}^2\right)\left(\sum {x_i}^4\right)}{\Delta^2} \tag{3.74} $$

$$ \sum \left(\frac{dA}{dy_i} \right)^2 = \frac{N\left(\sum {x_i}^4\right)^2 + \left(\sum {x_i}^4\right)\left(\sum {x_i}^2\right)^2 - 2\left(\sum {x_i}^2\right)^2\left(\sum {x_i}^4\right)}{\Delta^2} \tag{3.75} $$

$$ \sum \left(\frac{dA}{dy_i} \right)^2 = \frac{\left(\sum {x_i}^4\right)}{\Delta} \left[\frac{N\left(\sum {x_i}^4\right) - \left(\sum {x_i}^2\right)^2}{\Delta} \right] \tag{3.76} $$

$$ \sum \left(\frac{dA}{dy_i} \right)^2 = \frac{\left(\sum {x_i}^4\right)}{\Delta} \tag{3.77} $$

with Δ defined in equation 3.70.

Inserting this result into equation 3.72 leads to

$$ {\sigma_A}^2 = {\sigma_y}^2 \frac{\left(\sum {x_i}^4\right)}{\Delta} \tag{3.78} $$

The same calculation can be performed for σ_C, beginning with equation 3.72 and the differentiation of equation 3.69:

$$\frac{dC}{dy_i} = \frac{N\left({x_i}^2\right) - \left(\sum {x_i}^2\right)}{\Delta} \tag{3.79}$$

$$\left(\frac{dC}{dy_i}\right)^2 = \frac{N^2\left({x_i}^4\right) + \left(\sum {x_i}^2\right)^2 - 2N\left({x_i}^2\right)\left(\sum {x_i}^2\right)}{\Delta^2} \tag{3.80}$$

$$\sum\left(\frac{dC}{dy_i}\right)^2 = \frac{N^2\left(\sum {x_i}^4\right) + N\left(\sum {x_i}^2\right)^2 - 2N\left(\sum {x_i}^2\right)^2}{\Delta^2} \tag{3.81}$$

$$\sum\left(\frac{dC}{dy_i}\right)^2 = \frac{N}{\Delta}\left[\frac{N\left(\sum {x_i}^4\right) - \left(\sum {x_i}^2\right)^2}{\Delta}\right] \tag{3.82}$$

$$\sum\left(\frac{dC}{dy_i}\right)^2 = \frac{N}{\Delta} \tag{3.83}$$

with Δ defined as before in equation 3.70.

Inserting this result into equation 3.72 leads to

$${\sigma_C}^2 = {\sigma_y}^2\,\frac{N}{\Delta} \tag{3.84}$$

We can now use error-propagation with equations 3.66 and 3.67 to determine the error in T_e and n_e using

$$\sigma_{T_e} = \sigma_C\left|\frac{dT_e}{dC}\right| = \frac{\sigma_C}{K_2\,C^2} \tag{3.85}$$

$$\sigma_{n_e} = \left[\left(\left|\frac{dn_e}{dA}\right|\sigma_A\right)^2 + \left(\left|\frac{dn_e}{dT_e}\right|\sigma_{T_e}\right)^2\right]^{1/2} \tag{3.86}$$

$$\sigma_{n_e} = \frac{exp(A)}{2\,K_1\,\sqrt{T_e}}\sqrt{4\,{T_e}^2\,{\sigma_A}^2 + {\sigma_{T_e}}^2} \tag{3.87}$$

Error bars can thus be generated for each dataset from the raw spectra. Using the model profiles from equation 3.59 in the CDX-U TVTS optical geometry, T_e error bars of 5%(center), 10%(edge), and n_e error bars of 10%(center), 35%(edge) were calculated.

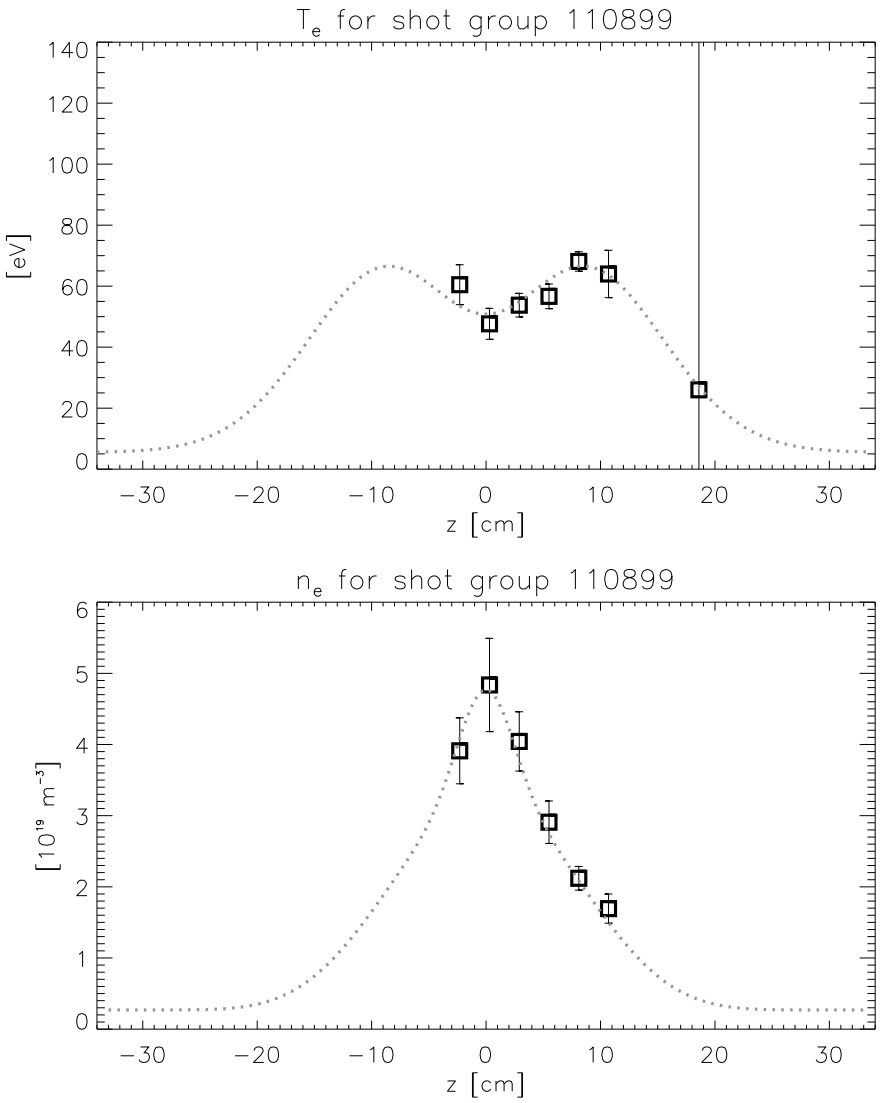

Figure 3.35: Typical CDX-U T_e and n_e profiles, plotted vs. z. A 7-point central profile demonstrates standard CDX-U discharge parameters.

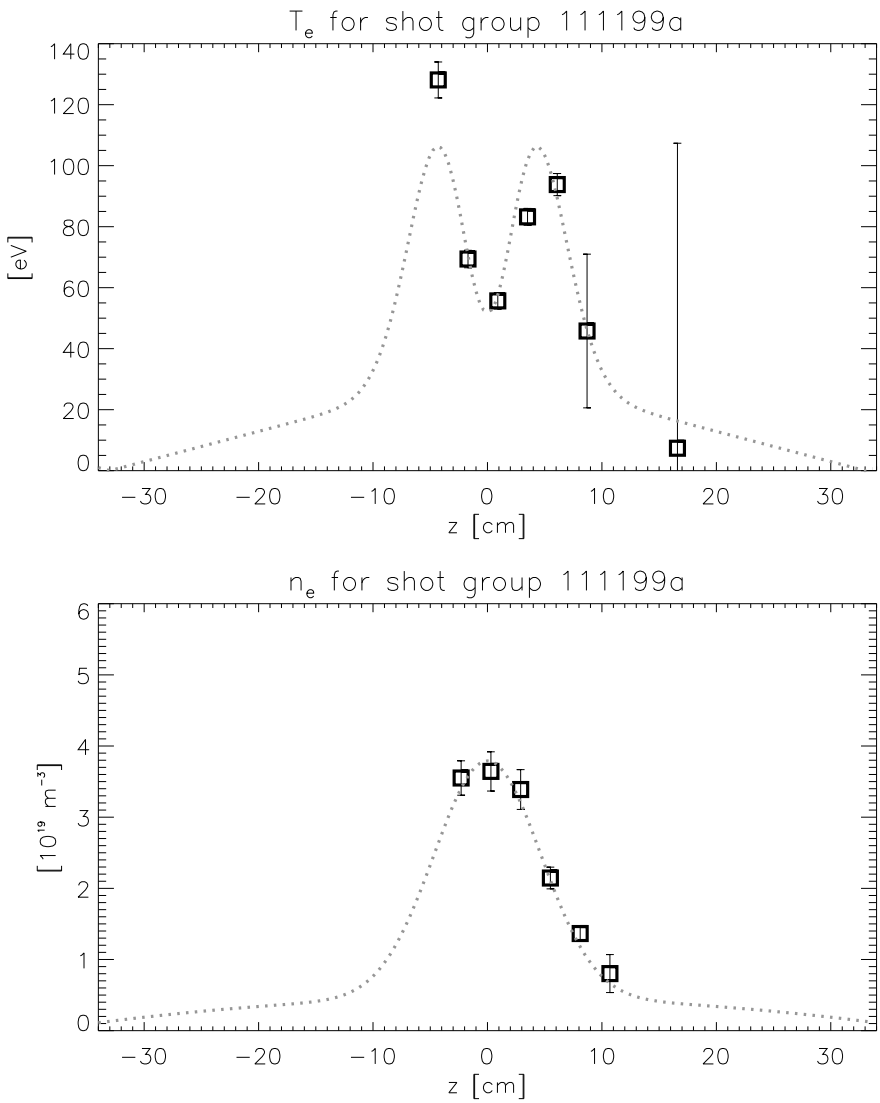

Figure 3.36: Typical CDX-U T_e and n_e profiles, plotted vs. z. A 7-point central profile demonstrates profiles with reduced fueling and thus lower n_e. The hollowness of the T_e profile is exaggerated, with higher T_e just off-axis than achieved with higher fueling and n_e conditions.

Once the TVTS system was operational, it was discovered that the density profiles achieved in CDX-U are often quite peaked, so that the terms "center" and "edge" must be revised to reflect the radii of high and low relative electron density. Furthermore, it was found that two carbon impurity emission lines (7326.19 Å and 7119.45 Å) fall within the spectral range of the detector, and must be subtracted from the raw signal. This quite straightforward, provided the Thomson scattered intensity is sufficient to differentiate between it and the emission lines (recall that an infinitely narrow emission line, once convolved with the wide entrance slit, spans ∼20% of the spectral range of the detector). The requirement that the CII lines be clearly discernible from the Thomson scattered spectrum provided the most stringent limit on photon statistics, and because of this, the best data was taken by averaging together exposures taken from several (5-10) similar discharges.

Acceptable TVTS spectra are generally recorded within r/a∼0.5. Edge temperature and density values are regularly recorded with the triple Langmuir probe, so that a fairly complete profile can be recorded. TVTS profiles (plotted vs. z) for typical CDX-U conditions are shown in figures 3.35 and 3.36. Error-bars are computed as described in section 3.5.1. Highly peaked n_e profiles and hollow T_e profiles with steep edge gradients are typical. Figure 3.36 shows profiles with reduced fueling and thus relatively lower central n_e. In this case the hollowness of the T_e profile is exaggerated, with higher temperatures achieved just off-axis than in the case shown in figure 3.36.

Chapter 4

Determination of χ_e Using Temperature Perturbations

The study of cross-field transport in toroidal magnetic confinement systems has been ongoing for several decades, and by now is a well-studied subject, both with regard to theoretical models and experimental results. The application of theoretical models to ST's, however, and indeed the attainment of experimental results from ST's, has only occurred in the past few years, and therefore provides only a limited collection of results. The following section introduces the two subjects of ST transport and perturbative transport measurements, and covers the experimental and theoretical results of the temperature perturbation experiments in CDX-U.

The CDX-U study includes two separate experiments, in which temperature perturbations were introduced both by gas puffing at the plasma edge and by sawteeth at the q=1 radius. Although both of these techniques have been extensively used in conventional tokamaks, the perturbative study of χ_e in CDX-U is the first of this type in an ST.

4.1 Introduction

One of the fundamental outstanding challenges in developing a fusion reactor is the understanding of cross-field transport. This includes energy transport, particle transport of all plasma species, and angular momentum transport. Fundamental diffusion coefficients for all of these can be derived based on Coulomb collisions in

a realistic toroidal magnetic geometry (neoclassical estimates), but unfortunately the experimentally observed values of transport coefficients consistently exceed neoclassical estimates by a wide margin.

Recent high performance discharges with tailored magnetic-shear profiles have produced plasmas with neoclassical ion thermal transport [Levinton *et al.*, 1995] and ion particle transport [Efthimion *et al.*, 1999a], and neoclassical ion thermal transport has also been observed in the START ST [Gates *et al.*, 1998]. Electron thermal transport remains far from neoclassical, though, and is the least understood of the plasma fluxes. One of the continuing challenges in fusion physics is the description and understanding of anomalous transport, and in particular electron thermal transport.

The global energy confinement time is defined as

$$\tau_E = \frac{W_P}{\sum P_{in}} = \frac{\int \frac{3}{2}\left(n_e\, T_e + \sum n_i\, T_i\right) \mathrm{d}^3\mathrm{x}}{\sum P_{in}} \tag{4.1}$$

where W_P is the stored kinetic energy in the plasma and $\sum P_{in}$ is the total input power. For a plasma with both ohmic and auxiliary heating,

$$\tau_E = \frac{\int \frac{3}{2}\left(n_e\, T_e + \sum n_i\, T_i\right) \mathrm{d}^3\mathrm{x}}{I_P\, V_{loop} - \frac{\partial}{\partial t}\left(\frac{1}{2} L\, I_P{}^2\right) + P_{aux}} \tag{4.2}$$

where I_P is the plasma current, L is the plasma inductance, and the denominator contains explicit terms for ohmic and auxiliary heating sources. Obvious simplification to this formula occurs in steady-state, when time derivatives are zero.

The derivation of local transport coefficients, both experimentally and theoretically, is typically reduced from a fully toroidal geometry to a 1-D problem, with the single direction taken normal to the magnetic flux surfaces. This reduction depends on the assumption that parallel transport exceeds cross-field transport by so much that measurable quantities are essentially constant on a flux surface. Given this assumption, the transport coefficients $\mathrm{D_{i,e}}$ (particle diffusivity for ions, electrons)

and $\chi_{\mathrm{i,e}}$ (thermal diffusivity for ions, electrons) are described by the Onsager matrix

$$\begin{bmatrix} \Gamma_i \\ q_e \\ q_i \end{bmatrix} = \begin{bmatrix} D_i & A_{12} & A_{13} \\ A_{21} & \chi_e & A_{23} \\ A_{31} & A_{32} & \chi_i \end{bmatrix} \begin{bmatrix} \frac{\partial n_e}{\partial \rho} \\ \frac{\partial T_e}{\partial \rho} \\ \frac{\partial T_i}{\partial \rho} \end{bmatrix} \tag{4.3}$$

where ρ is the flux-surface label. Here only one ion energy equation is retained despite the possibility of multiple ion species, due to the assumed strong collisional coupling between ion species. Also, only a single particle transport coefficient is shown, based on the assumption of a single ion species and the reduction of equations by one due to quasineutrality [Burrell *et al.*, 1990]. In practice, separate particle diffusivities for bulk and various impurity ions are often calculated. Often only the diagonal terms are considered in transport analyses, with the assumption that the off-diagonal terms will be small by comparison. Though this may not necessarily be the case, the lack of a complete and detailed dataset often necessitates this assumption in order to analyze the local transport at all.

In both theoretical and experimental transport studies, the objective is focused on the determination of the diffusion coefficients in equation 4.3.

4.1.1 Transport in Spherical Tori

The primary advantages behind the development of the ST concept have been the predicted MHD equilibria achievable in this geometry. MHD properties of ST's have been extensively studied and modeled, and stable equilibria with $\beta \sim 50\%$ and bootstrap-current fraction $f_{BS} \sim 100\%$ have been predicted for aspect ratio below 1.5 [Menard *et al.*, 1997; Miller *et al.*, 1997; Hender *et al.*, 1992].

Confinement predictions for the ST geometry have been more sparse, though, with most studies limited to the application of global confinement scalings originally developed for conventional tokamaks [Sykes *et al.*, 2000; Peng, 2000]. This is of course bound to change in the coming years, with the introduction of the large ST experiments NSTX (PPPL) and MAST (Culham). Confinement studies are of utmost importance to the development of the ST as a candidate fusion reactor, since many of the most interesting MHD phenomena depend on highly tailored pressure and current profiles. In general, it has been expected that the prevailing

factor to determine the confinement properties of ST's would be the low toroidal field (imposed by the technical limitations of a narrow center-stack), which could degrade confinement to far below that achievable in conventional tokamaks.

A notable exception is the prediction of microinstability stabilization at low aspect ratio [Rewoldt *et al.*, 1996; Stambaugh *et al.*, 1998]. In [Rewoldt *et al.*, 1996], the growth rate of the toroidal drift mode and the MHD ballooning mode were calculated as a function of aspect ratio, and it was found that as R/a fell below ∼1.5, both modes were completely stabilized. The stabilization was found to be primarily due to the reduction of "bad" magnetic field-line curvature over the length of the mode structure. This is consistent with the intuitive idea that the ST geometry naturally attains high edge-q values without resorting to the reduction of plasma current, which in general acts to destabilize low-n MHD instabilities.

Experimentally, the dependence of confinement on aspect ratio was studied at high R/a (2.8-8.0) in the TFTR tokamak [Grisham *et al.*, 1991]. This early study showed a strong positive scaling of confinement time with major radius ($\tau_E \sim R^{1.5-1.8}$) and a weakly negative dependence on minor radius. Interestingly, the dependence of the Lawson triple-product $\langle n\,T\rangle\tau_E$ on aspect ratio was extremely weak. Though the above results might imply that confinement would be worse at lower aspect ratio, it must be noted that this data was taken in a conventional tokamak configuration at low β without elongation or triangularity. Additionally, since transport may have been dominated by microinstabilities, it is unclear whether a simple extrapolation to very low aspect ratios provides a sufficient treatment of the transport question.

The entire collection of thermal transport data in ST's can be covered by summarizing the results from the START device ($I_P \sim 200$ kA, $B_T \sim$ 4-6 kG, $T_e \sim$ 300-500 eV, R/a=1.3-1.5) [Colchin *et al.*, 1993], including both ohmic and NBI-heated, and both L-mode and H-mode plasmas. In general these have been global τ_E derivations and χ_e calculations based on power-balance considerations.

Global τ_E estimates for ohmic START plasmas were performed at R/a∼1.3 over the range I_P = 50-250 kA [Walsh *et al.*, 1995]. It was found that measured confinement degraded weakly with plasma current, and $\tau_E \sim 0.5 - 1.2$ ms. Confinement modeling was subsequently performed, with reasonable agreement found with three semi-empirical scaling models, namely the T11 model, the Rebut-Lallia-Watkins

model, and a modified form of the Lackner-Gottardi model [Roach, 1996].

Later studies of τ_{E} in NBI-heated and high-performance ohmic L-mode discharges demonstrated confinement times up to 4 ms, which exceeded Neo-Alcator confinement scalings by up to a factor of 3. Interestingly, τ_{E} in the NBI-heated discharges showed reasonable agreement with scalings derived from the ITER database, developed from a collection of medium and large-scale high-aspect-ratio tokamaks. In the START parameter regime, there was little difference between the ITER L-mode scaling and the ITER H-mode scaling, and indeed some shots showed $\tau_{E,ITER97:H-mode} < \tau_{E,measured} < \tau_{E,ITER97:L-mode}$ [Sykes, 1999b; Sykes, 1999a].

Calculation of χ_{e} profiles from power-balance considerations, along with calculations of global τ_{E}, were also performed for high-performance NBI-heated START discharges [Gates *et al.*, 1998]. Again, τ_{E} was found to reasonably agree with the ITER database, despite limited applicability. $\chi_{\mathrm{e}} \sim 20$ m$^2/s$ and $\chi_{\mathrm{i}} \sim 5 - 10$ m$^2/s$ were derived using a detailed power-balance based transport code. Although the radial dependence of χ_{e} showed a poor match to all of the three empirical models which the data was compared to, the overall magnitude was in reasonable agreement with the modified Lackner-Gottardi model, as in the START ohmic experiments described previously. χ_i was found to be in reasonable agreement with Chang-Hinton neoclassical estimates, and neoclassical χ_{e} estimates were not performed.

4.1.2 Perturbation Experiments to Measure χ_{e}

Global confinement times and local diffusion coefficients have traditionally been calculated based on power-balance considerations, often with the steady-state simplification, as described in the opening paragraphs of section 4.1. A second technique to assess local coefficients is to follow the dynamic response of the state variables in response to an applied perturbation. In practice, perturbations have been in the form of sawtooth reconnections (temperature perturbations), localized/modulated ECRH heating (temperature perturbations), gas injection and impurity laser-blowoff (temperature/density perturbations), and modulated NBI heating (ion temperature/density perturbations).

Depending on the diagnostics available in a given experiment, perturbation analysis can lead to a much more precise measure of transport than power balance methods, which depend on precise measurement of local gradients (see equation

4.3). Additionally, transient transport analysis can provide a decoupling of density and temperature gradients from each other, and a decoupling of temperature and density from their gradients, with no essential degradation of the quality of the data. Perturbative techniques are insensitive to source and sink terms in the flux equations, and by explicitly using time dependence can ideally separate diffusive from convective transport terms [Cardozo, 1995].

One feature of transient analysis that is particularly relevant to the CDX-U experiments is that of diagnostic instrumentation. For power-balance analysis, one is required to know with great certainty the profiles of electron temperature, ion temperature, electron and ion density, and all power sources and sinks, including ohmic heating and radiative losses. Though it is not necessary to know the time dependence of these quantities, *all* quantities must be known in order to calculate *either* of χ_e or χ_i. The use of transient techniques, on the other hand, are critically dependent on time resolved data, but do not require absolute calibration, and only require a subset of the above measurements to measure the individual χ_e or χ_i values. This situation precisely describes CDX-U, which lacks T_i diagnostics and has only an uncalibrated estimate of radiated power, but is equipped with two uncalibrated yet spatially and temporally-resolved instruments. The EBW T_e diagnostic (section 2.4.6), while not absolutely calibrated, provides time-resolved temperature profiles, and the SXR array (section 2.4.9) provides time-resolved CV emission profiles.

It is important to point out the implicit difference in what is measured by perturbative techniques, as compared to steady-state power-balance. Figure 4.1, adapted from [Cardozo, 1995], illustrates how perturbative measurements can produce χ values that differ from those derived by power balance techniques. In the figure, the dark line describes χ as a function of ∇T, allowing χ to have some nonlinear dependence on temperature gradient. A steady-state power-balance measurement taken at the point shown would result in a measurement of $\chi^{\text{p.b.}}$, while a perturbative measurement taken as shown would result in a measurement of $\chi^{\text{pert.}}$.

Experimentally, perturbative experiments have been performed on nearly all major fusion experiments over the past decade, and by now this is a well established technique. Several representative examples are mentioned below. Quite often the χ_e value derived from perturbative techniques exceeds χ_e derived from power

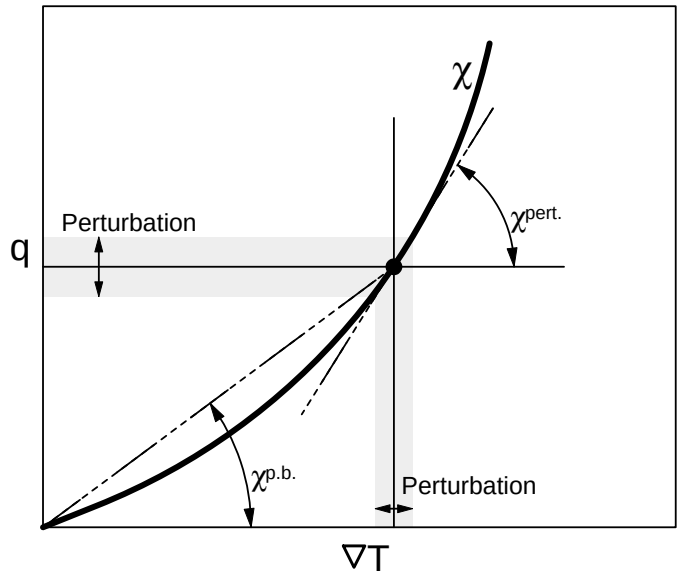

Figure 4.1: Measurement of χ from steady-state and perturbative methods (adapted from [Cardozo, 1995]). χ as a function of ∇T is shown as the dark solid line. A steady-state power-balance measurement taken at the point shown would result in a measurement of $\chi^{\text{p.b.}}$, while a perturbative measurement taken as shown would result in a measurement of $\chi^{\text{pert.}}$.

balance by a factor of 1-5 or more. Nonlinear gradient dependence (i.e. fig. 4.1) or fast nonlocal transport are cited as explanations for this, though recent work on sawteeth and fishbone oscillations in TFTR and DIII-D has demonstrated that transient MHD activity may dominate these effects by introducing weak stochasticity to the local field structure [Fredrickson *et al.*, 2000].

Perturbative techniques have also been used in conjunction with steady-state methods to distinguish between different theoretical models which would be indifferentiable with steady-state methods alone. This complementary approach was used in TFTR to demonstrate a strong dependence of D_e on T_e, consistent with electrostatic microinstability theory [Efthimion *et al.*, 1991]. A similar complementary approach was used for studies of helium, iron, and electron particle transport in TFTR, in which ratios of the particle diffusivities were found to agree with quasilinear electrostatic drift-wave calculations [Synakowski *et al.*, 1993].

On TFTR, sawtooth oscillations were used as a source of temperature perturbations both inside and outside the inversion radius. ${\chi_e}^{\text{pert.}}$ was found to exceed ${\chi_e}^{\text{p.b.}}$

by a factor of two to ten, which was later explained as the existence of a fast nonlocal redistribution of energy during the sawtooth crash. Analysis of the full extended temperature perturbation led to an estimate of ${\chi_e}^{\text{pert.}} \sim {\chi_e}^{\text{p.b.}}$ [Fredrickson *et al.*, 1986; Fredrickson *et al.*, 1990].

A similar study was performed on high-performance ohmic and ICRH plasmas on JET, again with ${\chi_e}^{\text{pert.}}$ derived from analysis of sawtooth temperature perturbations. It was found that in ohmically heated plasmas, ${\chi_e}^{\text{pert.}} \sim 2.5 \times {\chi_e}^{\text{p.b.}}$ while in ICRH heated plasmas ${\chi_e}^{\text{pert.}} \sim {\chi_e}^{\text{p.b.}}$ [Tubbing *et al.*, 1987].

A cold-pulse study was performed on TFTR by the injection of impurities, which radiated and cooled the plasma edge. Both laser-ablation of iron and gas-injection of helium were used, and both produced clear propagating cold-pulses with ${\chi_e}^{\text{pert.}} \sim 4 \times {\chi_e}^{\text{p.b.}}$ [Kissick *et al.*, 1994]. Evidence for nonlocal behavior in H-mode plasmas on TEXT was shown using this same technique, requiring some non-local behavior in the core to explain the pulse evolution [Gentle *et al.*, 1995a].

Transient transport experiments were carried out on the W7-AS stellarator, using both heat pulses (localized ECRH) and cold pulses (impurity injection). In both cases, ${\chi_e}^{\text{pert.}} \sim {\chi_e}^{\text{p.b.}}$ [Walter *et al.*, 1998; Giannone *et al.*, 1992; Gasparino *et al.*, 1998].

Clearly it is common that ${\chi_e}^{\text{pert.}}$ exceeds ${\chi_e}^{\text{p.b.}}$ by some factor, though often it is the initial perturbation which is found to act nonlocally to produce this discrepancy, with subsequent propagation consistent with power-balance estimates.

It should be reiterated that although most applications of transient transport analysis attempt to compare ${\chi_e}^{\text{pert.}}$ with ${\chi_e}^{\text{p.b.}}$, in CDX-U the diagnostic set is insufficient for a high-quality assessment of ${\chi_e}^{\text{p.b.}}$, and transient techniques were necessary to assess χ_e at all.

4.2 Cold-Pulse Experiments Using Edge Gas-Puffing

4.2.1 Experimental Setup

The experimental arrangement for the cold pulse experiments is shown in figure 4.2. The EBW radiometer is located on the midplane, outside the vacuum vessel looking radially in through a quartz window towards the centerstack. The frequency range

is 8.4-12.4 GHz, which corresponds to R=35.7-53.3 cm.

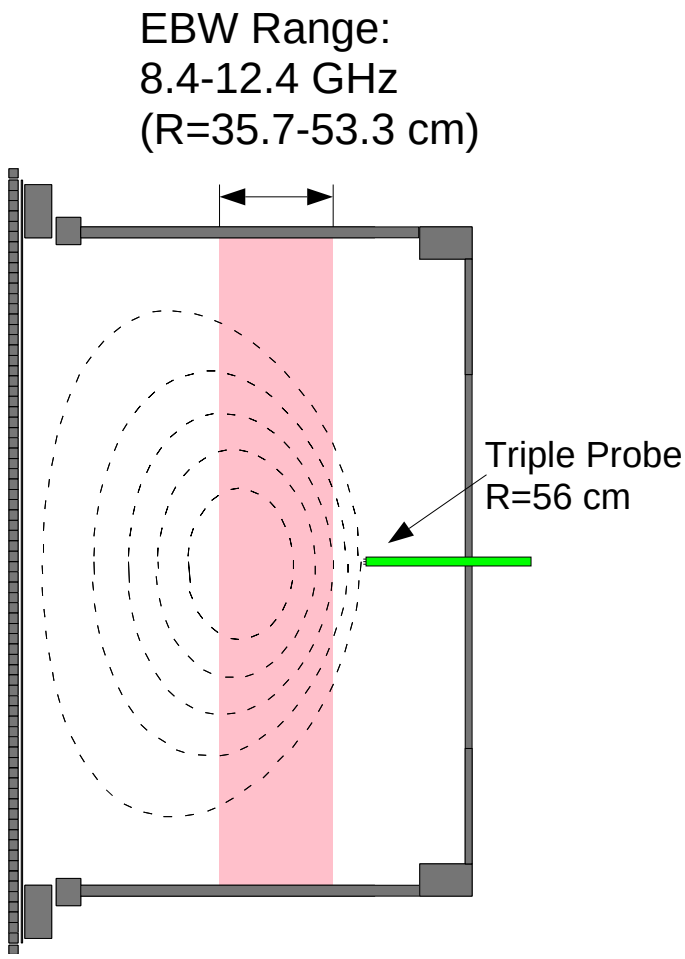

Figure 4.2: Experimental setup for CDX-U coldpulse experiments. The EBW temperature diagnostic covers a range of 8.4-12.4 GHz, corresponding to R=35.7-53.3 cm. The triple probe is fixed at R=56 cm.

Fueling for the plasma is provided by gas puffing through a Veeco PV-10 piezoelectric valve, controlled via computer with preprogrammed waveforms. In general, CDX-U plasmas exhibit a tradeoff between temperature and electron density, which is controlled with gas fueling. This has traditionally been used as a control to vary the background plasma equilibrium, providing plasmas which are varied by roughly a factor of two in temperature ($T_e(0) = 50 - 100$ eV) and a factor of five in central density ($n_e(0) = 1 - 5 \times 10^{19}$ m^{-3}). This control has been exploited for the temperature pulse experiments by modulating the gas puffing to produce a fast

pulse of gas injection at the plasma edge. This acts to locally cool the edge (on timescales shorter than the particle diffusion time) which then propagates to the plasma center as a cold-pulse.

In experiments such as these in which the temperature is perturbed through fueling modification, it is critical to investigate the possibility of coupling between the density and temperature perturbations, and the effect that it will have on the measured diffusion coefficients. A mathematical outline of the coupling between density and temperature perturbations and the effect of off-diagonal elements in the transport matrix (eq. 4.3) is given in [Gentle, 1988]. The primary finding of this work is an analytical treatment of the effect that gradient-dependent transport coefficients will have on perturbative measurements as compared to steady-state methods, as illustrated in figure 4.1. It is also found that coupling of the temperature and density perturbations can lead to a separate "fast" and "slow" eigenmode solution to the diffusion equation, with corresponding pulse propagation rates.

In practice, the coupling between temperature and density perturbations is maximized if the thermal and particle diffusion occurs on the same time scale, and is minimized if χ and D are very distinct. In CDX-U, as well as in START, it appears that electron thermal diffusion far exceeds electron and ion particle diffusion, though even in the case of $\chi_e >> D$, coupling of thermal and particle transport along with off-diagonal corrections to the transport matrix have been measured using perturbative techniques in JET [Hogeweij *et al.*, 1991].

In CDX-U, the measured core temperature perturbations (resulting from perturbations imposed at the edge) are interpreted as representative of the faster of the two diffusion rates, namely χ_e, with off-diagonal coupling terms assumed small. It is important to keep in mind, however, that without a full analysis of the particle diffusion coefficients in CDX-U the possibility of coupling between χ and D effects on the gas-puff measurements cannot be completely dismissed.

Representative waveforms of gas puffer actuation, line-integrated density (measured with the microwave interferometer), and temperature modulations measured with the EBW radiometer and the triple probe are shown in figure 4.3. The phase comparison of the last three plots demonstrates the opposite effect that the gas modulation has on the temperature and density. There is a delay between the applied voltage on the puffer and the density response, such that the "off" pulse from

220.3-221.3 ms corresponds to the density decrease observed on the interferometer trace at ∼221.6-222.6 ms.

For these experiments, gas-puffing modulations were introduced to a background plasma, and the temperature response was recorded by both the triple-probe and the EBW radiometer. A series of reproducible discharges were taken, with the EBW diagnostic either set to a different fixed frequency for each shot or quickly scanning the full frequency range within each shot. The triple probe was held at a fixed position for all shots. The EBW frequency range was 8.4-12.4 GHz, covering R=35.7-53.3 cm, or roughly the center to the outer edge of the plasma.

4.2.2 Modeling of Edge Perturbations

The evolution of heat perturbations in a plasma can be modeled by starting with the electron heat balance equation in cylindrical geometry

$$\frac{3}{2}\, n_e(r)\, \frac{\partial T_e(r,t)}{\partial t} = \frac{1}{r}\, \frac{\partial}{\partial r}\left[r\, n_e(r)\, \chi_e(r)\, \frac{\partial T_e(r,t)}{\partial r} \right] + \sum Q \tag{4.4}$$

where $\sum Q$ is the sum of all non-diffusive sources and sinks of electron thermal energy, which in the case of CDX-U consists of ohmic heating, heat transfer to ions, convection, and radiation. A temperature perturbation about the equilibrium state will then be described by the perturbed equation

$$\frac{3}{2}\, n_e\, \frac{\partial \tilde{T}_e(r,t)}{\partial t} = \frac{1}{r}\, \frac{\partial}{\partial r}\left[r\, n_e\, \chi_e\, \frac{\partial \tilde{T}_e(r,t)}{\partial r} \right] \tag{4.5}$$

Solutions to this equation, describing the relaxation of $\tilde{\mathrm{T}}_{\mathrm{e}}(\mathrm{r},\mathrm{t})$ from sawtooth-induced perturbations, have been derived in [Soler and Callen, 1979; Fredrickson *et al.*, 1986], and will be described in detail in section 4.3.2. In this case, the initial conditions for equation 4.5 were modeled as the sum of two opposing delta functions, and the subsequent relaxation was then solved analytically. One result of this treatment is that χ_{e} can be derived from the trajectory of the perturbation peak in space and time, governed by the relationship

$$\Delta t_{peak} \approx \frac{(\Delta r_{peak})^2}{9\, \chi_e} \tag{4.6}$$

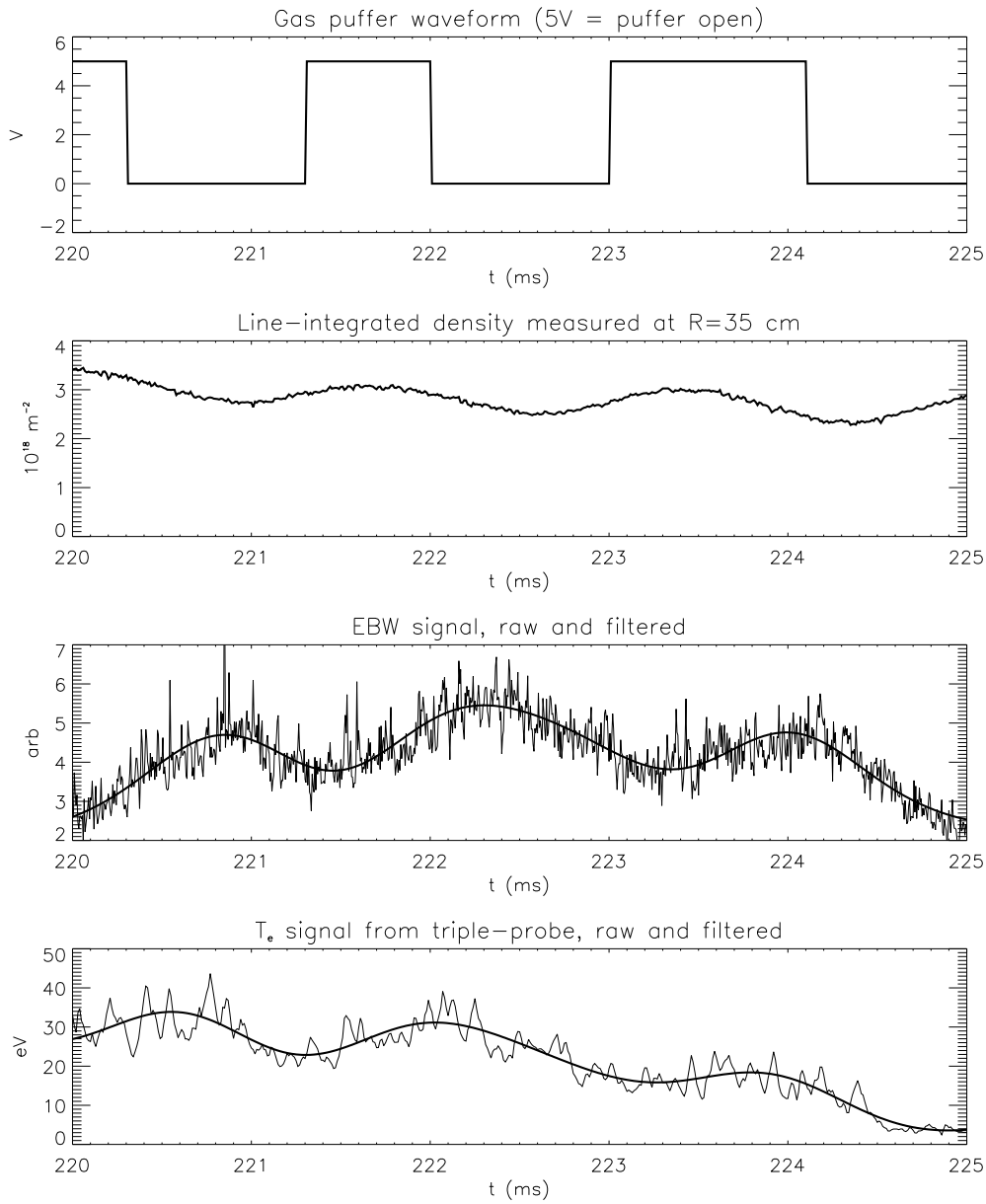

Figure 4.3: Representative waveforms of gas puffer actuation, line-integrated density (measured with the microwave interferometer), and temperature modulations measured with the EBW radiometer and the triple probe. The phase comparison of the last three plots demonstrates the opposite effect that the gas modulation has on the temperature and density. (An actuation delay in the gas puffer introduces a constant delay between the first plot and the other three, making a direct phase comparison misleading for this trace.)

where Δt_{peak} is the delay between the initial perturbation and the local measurement, and Δr_{peak} is the difference between the location of the local peak and the location of the initial perturbation. If the perturbation arrival time is then plotted against radial position, the result will be parabolic, with the quadratic term equal to $\frac{1}{(9\,\chi_e)}$.

In the case of cold-pulses induced by gas puffing at the plasma edge, the initial conditions from the sawtooth treatment (i.e. two opposing delta functions at the perturbation location) are not valid, and therefore the simple relationship 4.6 cannot be used. Instead, the cold-pulses were modeled by solving equation 4.5 numerically, based on more realistic boundary conditions. Rather than imposing an initial condition as a function of radius, a time-dependent perturbation was imposed at the edge, and the relaxation over the plasma profile was evolved in time. From this relaxation, the trajectory of the perturbation peak was plotted to provide a straightforward means of comparison to experiment.

The results of this simulation for various χ_{e} values and perturbation source locations are shown in figure 4.4. The trajectory of $\tilde{\mathrm{T}}_{\mathrm{e}}$ peak is shown starting at the perturbation source location, propagating to the tokamak center. The upper figure represents a perturbation imposed at r=7 cm, with representative χ_{e} values of 1, 2, and 5 m^2/s, and the lower figure represents a perturbation imposed at r=10 cm with the same χ_{e} values.

Interestingly, it was found that close to the perturbation source, the trajectory of the peak obeyed equation 4.6 quite closely, despite the use of very different constraints on the diffusion equation. As the perturbation approaches $r = 0$, the trajectory diverges from quadratic behavior, and the peak quickly 'fills in' the center of the plasma column.

Also note that figure 4.4 shows perturbations introduced at r=7 cm and r=10 cm, rather than at the full plasma edge (r=22 cm). This was done for purposes of comparison to experiment, and will be explained in the following section.

4.2.3 Experimental Results

Cold pulse experiments were performed using a fast-scanning EBW radiometer system, which provided 50 frequency sweeps per millisecond, covering 8.4-12.4 GHz (as described in section 4.2.1). Data was sampled at 1 MHz, providing 20 points

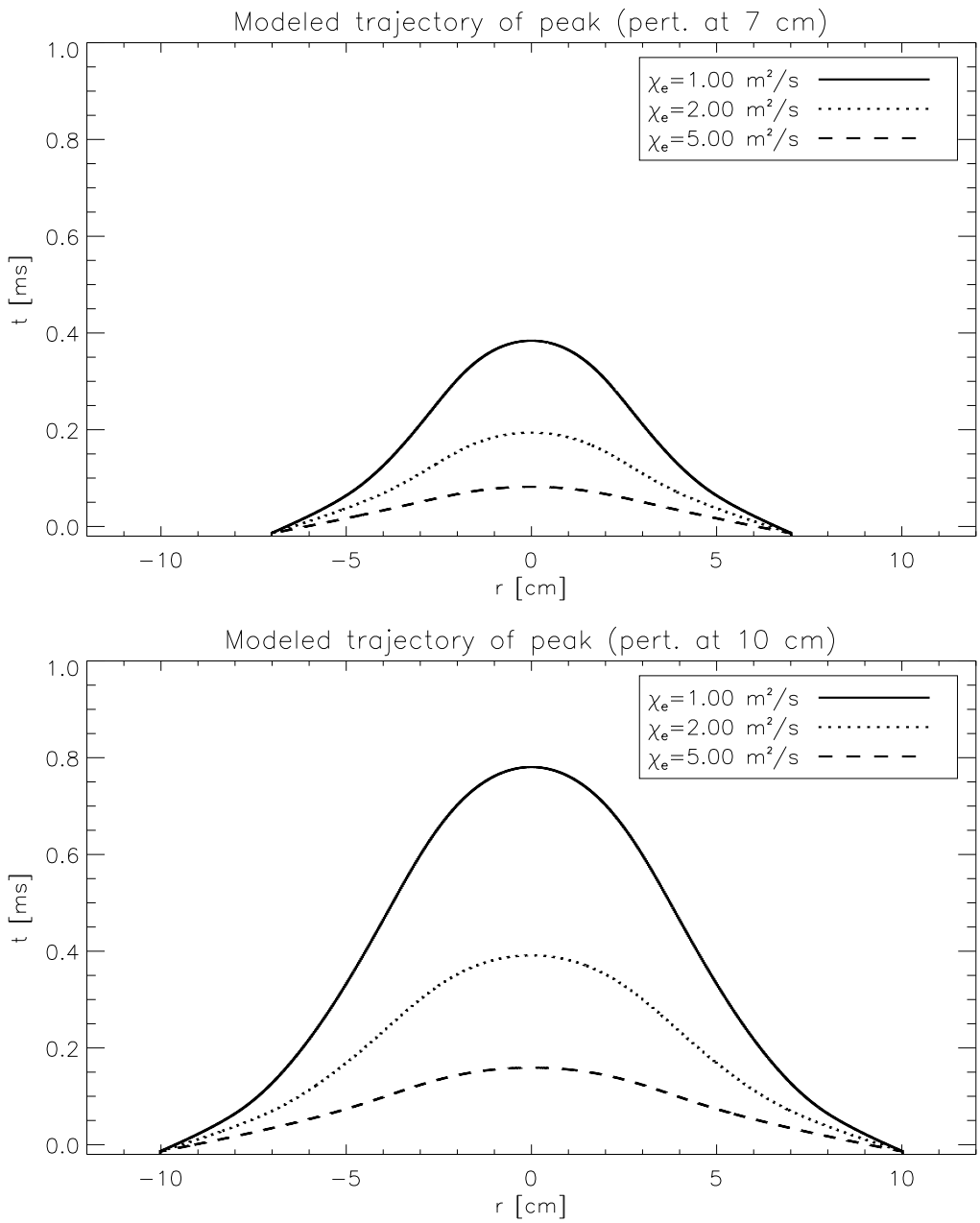

Figure 4.4: Modeled trajectory of $\tilde{T}_e$ peak from an edge perturbation, propagating to the tokamak center. The figure (a) represents a perturbation imposed at r=7 cm, with representative χ_e values of 1, 2, and 5 m^2/s. The figure (b) represents a perturbation imposed at r=10 cm with the same χ_e values.

per sweep, though the phase of the frequency sweep was uncorrelated with the phase of the sampling, so that the 20 frequencies sampled in one sweep were not necessarily the same 20 as in the next sweep. Of course the frequency was recorded simultaneously with the radiometer signal, so that the frequency for each data point is precisely known.

From this data, the trajectory of the peak of the cold-pulse perturbation was derived by plotting radiometer signal against frequency and time on an irregular grid (necessary because of the uncorrelated sweep phase and sampling phase). In order to improve the signal-to-noise to a level sufficient for deriving the location of the perturbation peaks, data from several identical shots were summed. The combined data was then interpolated and regridded to a regular grid and smoothed, to provide a set of distinct time traces at fixed frequency locations. The local minimum at the cold-pulse was then located for each frequency/radius. Because of the regridding process, interpolated time traces were produced at several hundred frequency/radius locations. In order to faithfully represent the original sampling rate (and not present misleadingly high resolution in the data points), the analyzed data was re-binned into 20 evenly spaced locations before plotting.

This dataset was taken in a set of CDX-U discharges with $\mathrm{T_e}(0) = 70$ eV and $\mathrm{n_e}(0) = 2.5 \times 10^{19}$ m^{-3}, which is the most typical operating regime for CDX-U. Data from the cold-pulse experiment with the fast-scanning radiometer is shown in figure 4.5. Plotted over the data is the result of the simulation described in section 4.2.2, with $\chi_\mathrm{e} = 2.2$ m^2/s and $r_{perturbation} = 7.5$ cm.

Error bars in R were produced by perturbing each of the quantities used to provide the mapping between frequency and radius (namely $\mathrm{B_T}$ and $\mathrm{I_P(r)}$) by their estimated error, and also taking into account the error introduced by the finite bandwidth of the radiometer electronics. Each contribution to the overall error in R was then added in quadrature, though in practice the radiometer bandwidth dominated the other effects [Jones, 2000]. Errors in t represent the scatter in the derived temperature peaks within each bin of over-gridded time traces.

The good fit between the data and model implies that thermal transport in the CDX-U core is well described by a diffusive process, with a diffusion coefficient of $\chi_\mathrm{e} = 2.2$ m^2/s. An additional important result comes from the fact that the data is well modeled by a perturbation originating at r=7.5 cm, corresponding to r/a=0.34.

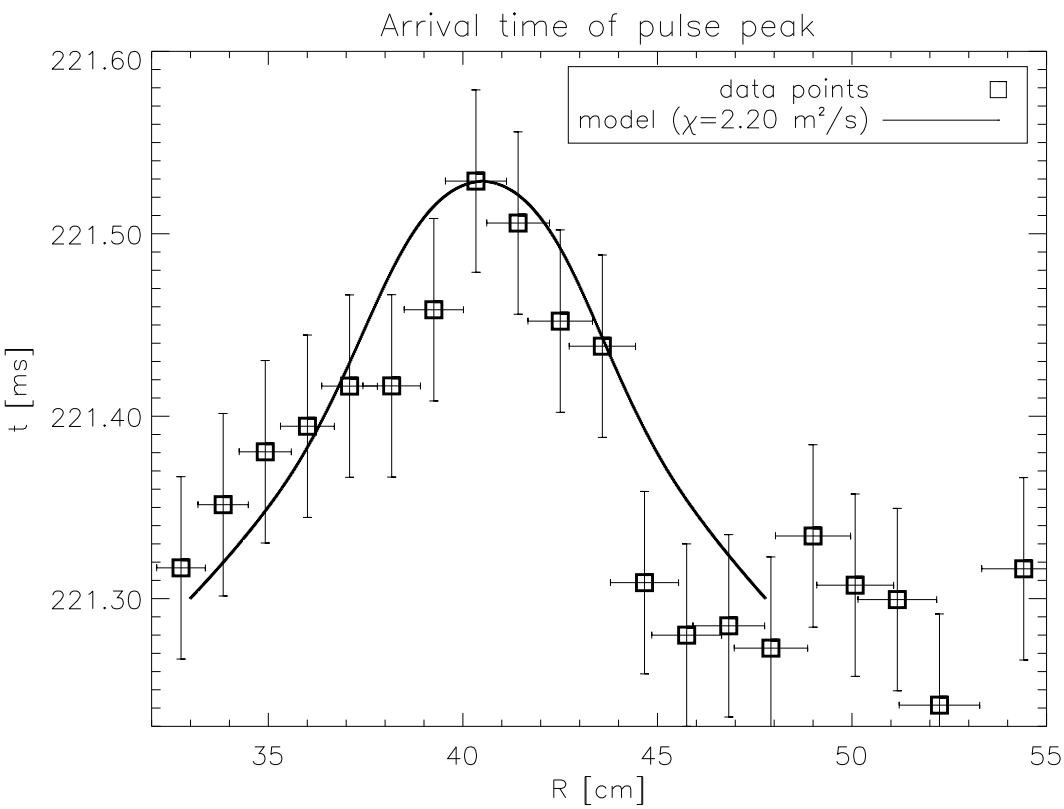

Figure 4.5: Comparison of χ_e model with data from fast-scanning EBW radiometer. Model parameters are $\chi_e = 2.2$ m^2/s and $r_{perturbation} = 7.5$ cm, corresponding to $r_{perturbation}/a = 0.34$.

Outside this region, the data points are quite flat, meaning that the perturbation is reaching the outer points at nearly the same time. This implies either that the diffusive transport is very fast beyond r=7.5 cm, or that the perturbation introduced by the cold-pulse is not diffusive outside the plasma core.

Although there have been many cases in which perturbations have been shown to produce ballistic or nonlocal responses (e.g. [Fredrickson *et al.*, 1990; Gentle *et al.*, 1995b]), the sawtooth heat-pulse analysis in section 4.3 points towards the other explanation, that thermal transport is much faster outside than inside the core in CDX-U.

A second data set was taken using a slightly different experimental arrangement. In this set, the EBW radiometer sampled a single frequency during each shot, and was scanned over the range 8.4-12.4 GHz over the course of several identical shots. This of course provided higher sampling rate at each frequency, but lacked single-shot profile information. In order to finely synchronize each shot, the triple probe was used to record the cold pulse at the plasma edge. Δt_{peak} was then taken as the difference between the perturbation peak location recorded at the EBW location and the triple-probe location. Plasma parameters for these discharges were $\mathrm{T_e}(0) = 50$ eV and $\mathrm{n_e}(0) = 2.5 \times 10^{19}$ m^{-3}. These results are shown in figure 4.6.

The results from this set are nearly identical to those from the set using the fast-scanning radiometer, with $\chi_\mathrm{e} = 2.3$ m^2/s and $r_{perturbation} = 7.2$ cm, corresponding to $r_{perturbation}/a = 0.33$. As in the previous set, the data fits the model very well inside the core, and flattens out beyond r/a $\sim 1/3$, indicating a rapid increase in transport level outside the core.

It should be noted that this set was taken with a lower total plasma current that in the previous set, but with the same vertical field setting, which is consistent with the 2 cm difference in R_0.

Finally, a data set was taken in a similar fashion to the previous set, but with one scanning and one fixed-frequency EBW radiometer. Again, Δt_{peak} is taken as the difference between the perturbation peak location recorded by the two diagnostics. This data was taken in a set of CDX-U discharges with lower density than the previous sets, $\mathrm{n_e}(0) = 1.5 \times 10^{19}$ m^{-3}. $\mathrm{T_e}(0)$ is estimated to be ~ 70 eV based on comparison with other datasets, though low photon statistics prevent a reliable $\mathrm{T_e}$

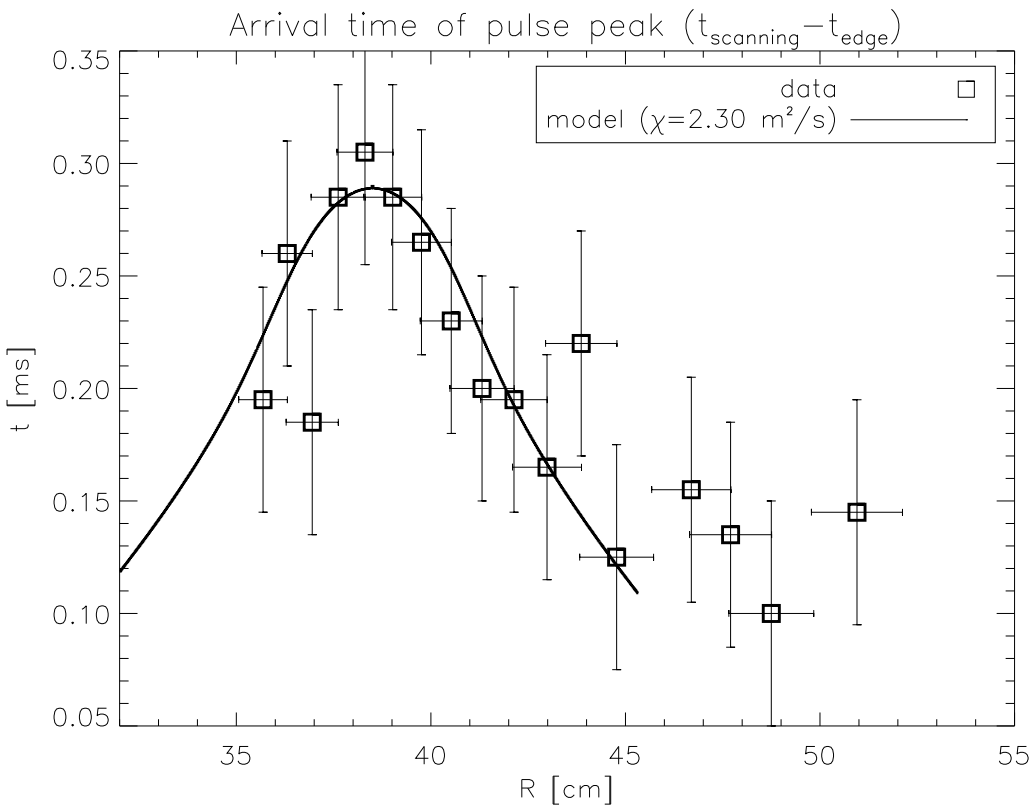

Figure 4.6: Comparison of χ_e model with data from a shot-to-shot scan using a variable-frequency EBW radiometer and a fixed triple-probe at the plasma edge. Plotted is the difference in arrival time of the perturbation peak, as measured by the two diagnostics. Model parameters are $\chi_e = 2.3$ m^2/s and $r_{perturbation} = 7.2$ cm, corresponding to $r_{perturbation}/a = 0.33$.

measurement in this set. Cold-pulse data from this set is shown in figure 4.7.

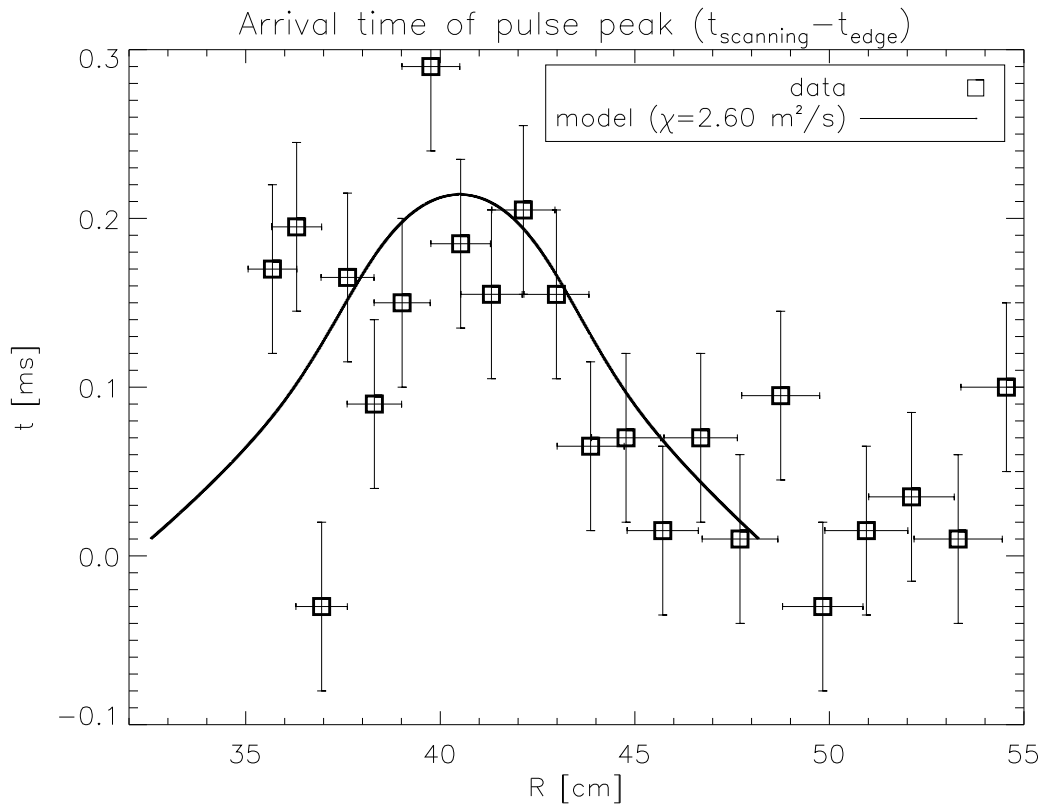

Figure 4.7: Comparison of χ_e model with data from a shot-to-shot scan using one variable-frequency EBW radiometer and one fixed-frequency radiometer. Plotted is the difference in arrival time of the perturbation peak, as measured by the two radiometers. Model parameters are $\chi_e = 2.6$ m^2/s and $r_{perturbation} = 8.0$ cm, corresponding to $r_{perturbation}/a = 0.36$.

Although this set is not as clean as the other two, it is clearly consistent with them. The data is best-fit with model parameters $\chi_e = 2.6$ m^2/s and $r_{perturbation} = 8.0$ cm, corresponding to $r_{perturbation}/a = 0.36$. Interestingly, even at lower density, the derived χ_e and $r_{perturbation}$ values are very close to that derived for the previous two datasets.

Despite the differences in measurement technique and even global plasma parameters among the three cold-pulse datasets, the results are quite consistent. Core transport is measured to be in the range 2.2 m^2/s $\leq \chi_e \leq$ 2.6 m^2/s, with χ_e increasing sharply outside $r/a \sim 1/3$.

4.3 Heat-Pulse Experiments Using Sawteeth

Electron thermal transport in CDX-U was also assessed by recording the spatial and temporal evolution of sawtooth-induced perturbations with the soft x-ray (SXR) array. This experiment is a particularly good complement to the edge cold-pulse experiments for four reasons: it utilizes a temperature perturbation produced by a completely different phenomenon (sawteeth rather than gas puffing), the perturbations are introduced in a different radial location (q=1 surface rather than plasma edge), the propagation is in the opposite direction (outward rather than inward), and the analysis was done using a different diagnostic (SXR rather than EBW). Because these two experiments are so independent from each other, each provides a very good cross-check of the physics results derived from the other.

4.3.1 Experimental Setup

The primary diagnostic used for the sawtooth analysis was the SXR array, described in section 2.4.9. A layout of the array, including the intersection of the viewing chords with the CDX-U flux-surfaces, is shown in figure 4.8. The r value for each viewing chord was calculated by taking the outermost flux surface that the chord intersects and mapping it back around to the midplane. This assumes that thermal energy is transported around a flux surface on a time scale much faster than the diffuse transport from one flux surface to the next along the shortest path (on the midplane). Since the array is vertically symmetric about the midplane, the 30 viewing chords correspond to 15 radial locations: r[cm]= 13.88, 13.00, 12.11, 11.20, 10.28, 9.35, 8.41, 7.45, 6.47, 5.48, 4.48, 3.47, 2.44, 1.40, 0.34.

A representative example of SXR sawtooth data is shown in figure 4.9. The normal "forward" sawtooth is visible inside the inversion radius, some fast oscillations associated with the reconnection layer are visible just at the inversion radius, and a sharp "reverse sawtooth" is visible immediately outside the inversion radius.

It is important to note that the SXR (CV line emission) data is not inverted for this experiment. The fact that the SXR intensity increases with all three parameters T_e, n_e, and n_C, all of which are peaked in CDX-U, means that each measurement will be heavily weighted by the innermost flux-surface intersected by the viewing chord. An additional potential problem with the use of integrated viewing chords is

that of pulse "pileup", if the sawtooth repetition time is shorter than the trajectory time to the edge of the plasma. This is not a problem in CDX-U, since the sawtooth repetition time is longer than the pulse trajectory time.

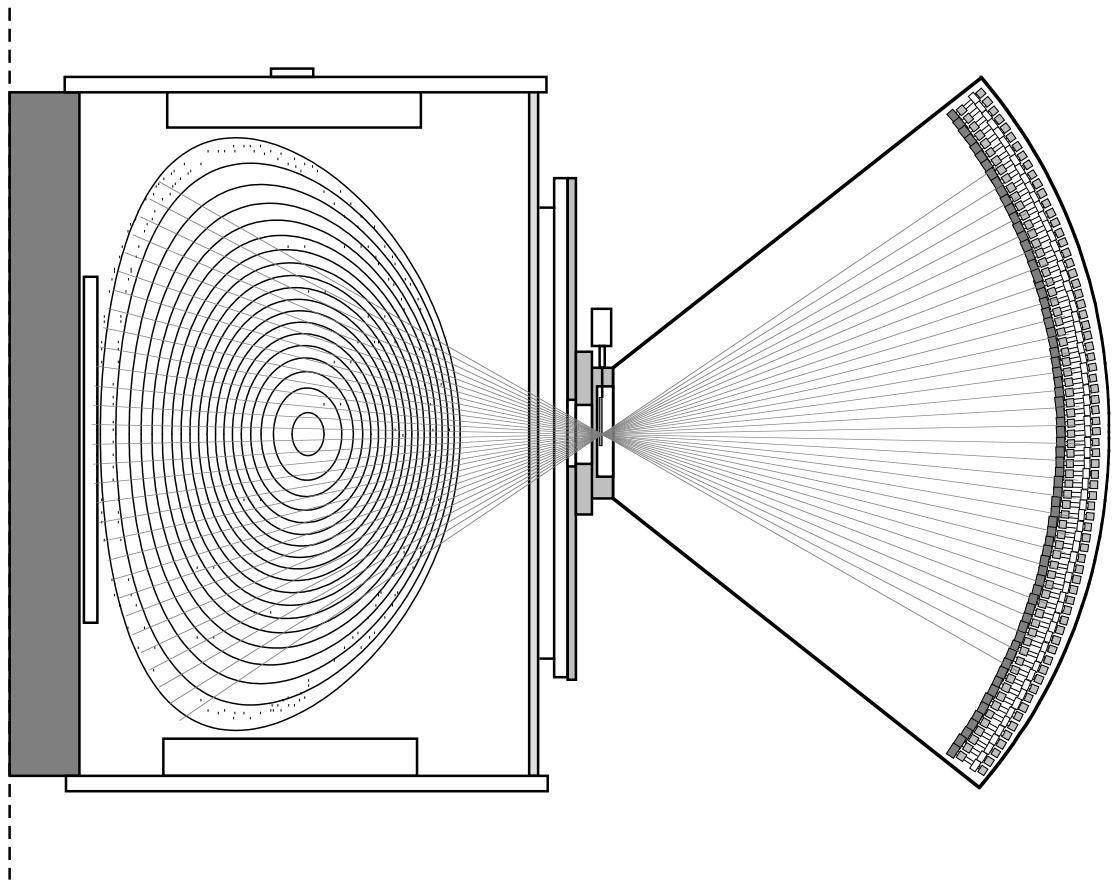

Figure 4.8: Layout of SXR array, including the intersection of the viewing chords with the CDX-U flux surfaces.

4.3.2 Modeling of Sawtooth Perturbations

As outlined in section 4.2.2, the evolution of a diffusion-dominated temperature perturbation will be governed by the equation

$$\frac{3}{2}\, n_e \, \frac{\partial \tilde{T}_e(r,t)}{\partial t} = \frac{1}{r}\, \frac{\partial}{\partial r} \left[r \, n_e \, \chi_e \, \frac{\partial \tilde{T}_e(r,t)}{\partial r} \right] \tag{4.7}$$

In the case of sawteeth-induced perturbations, the initial conditions for this

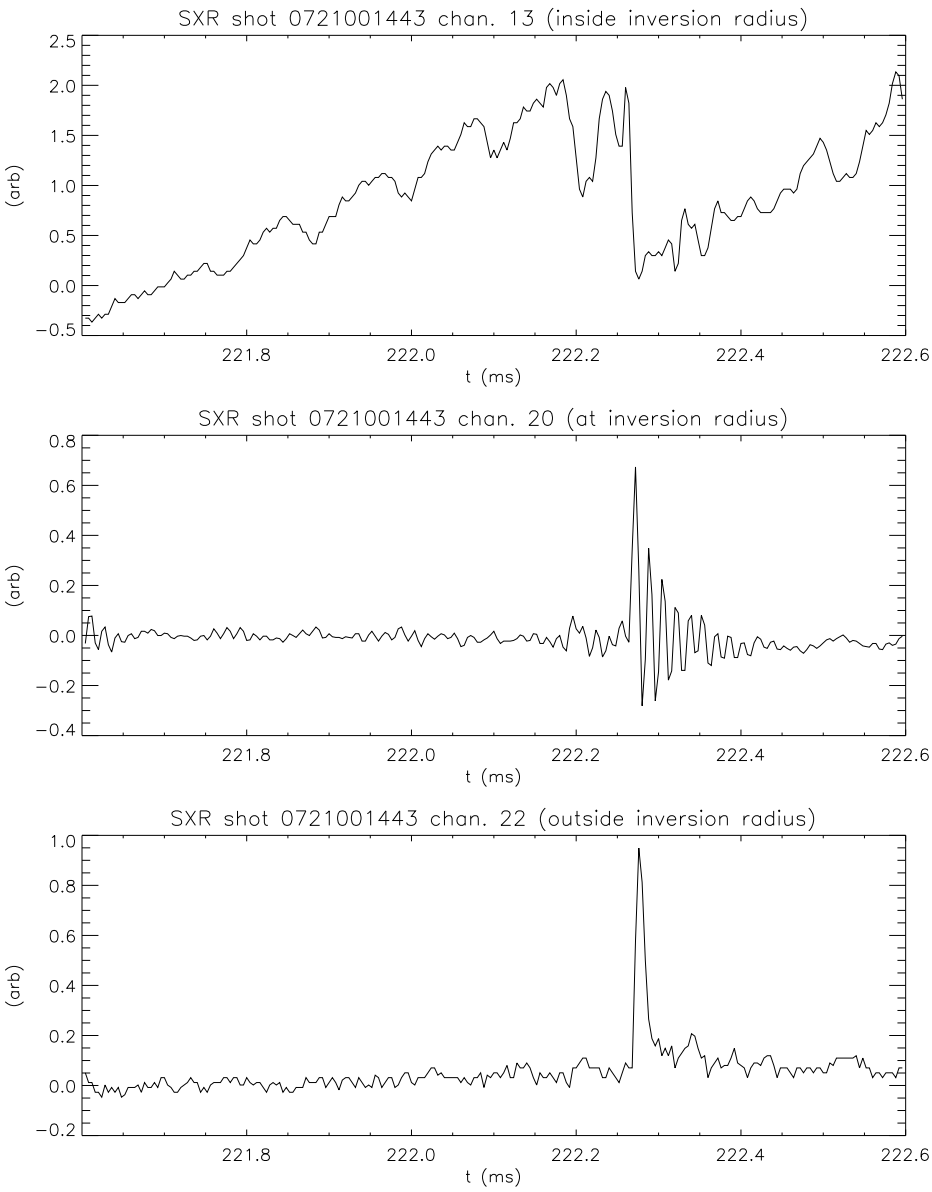

Figure 4.9: Typical sawtooth traces from SXR channels viewing inside, at, and immediately outside the sawtooth inversion radius.

equation are typically taken as a pair of opposing δ-functions. An analytical solution to this equation with δ-function initial conditions was obtained in [Soler and Callen, 1979] using a Green's function, and is given by

$$\begin{aligned}\tilde{T}_e(r,t) &= \frac{A^2\, r_1\, r_s\, \tilde{T}_{e0}}{2\,t} \exp\left(\frac{-A^2\, r^2}{4\,t}\right) \times \\ &\left[\exp\left(\frac{-A^2\, {r_2}^2}{4\,t}\right) \mathrm{I}_0\left(\frac{A^2\, r\, r_2}{2\,t}\right) - \exp\left(\frac{-A^2\, {r_1}^2}{4\,t}\right) \mathrm{I}_0\left(\frac{A^2\, r\, r_1}{2\,t}\right)\right] \end{aligned} \tag{4.8}$$

where t is the time measured from the sawtooth time t_0, $A = \sqrt{1.5/\chi_e}$, r_s is the sawtooth inversion radius, r_0 ($\leq \sqrt{2}\, r_s$) is the reconnection radius, and r_1 and r_2 are the positions of the assumed negative and positive delta functions, respectively (each of magnitude $\tilde{\mathrm{T}}_{\mathrm{e0}}$). A plot showing the shape of these solutions as a function of r and t, is given in figure 4.10.

A long-time (small Bessel-function argument) expansion of equation 4.8 was derived in [Soler and Callen, 1979], and is given by

$$\tilde{T}_e(r,t) \sim \frac{r^2}{t^3} \exp\left(\frac{-A^2\, r^2}{4\,t}\right) \tag{4.9}$$

which leads to a perturbation-peak trajectory given by

$$\Delta t_{peak} = \frac{A^2\, {r_{peak}}^2}{12} = \frac{{r_{peak}}^2}{8\,\chi_e} \tag{4.10}$$

It was subsequently shown in [Fredrickson *et al.*, 1986] that a more appropriate expansion of equation 4.8 is derived using a large, rather than small, Bessel-function argument, in order to be closest to the analytical solution near the peak in $\tilde{\mathrm{T}}_{\mathrm{e}}$. In this case, the approximate solution is given by

$$\tilde{T}_e(r,t) \approx \tilde{T}_{e0} \left[\frac{A^3\, r_s\, r_1\, (r_2 - r_1)}{4\,\sqrt{\pi}\,(r_1\, r_2)^{1/4}}\right] \left[\frac{\sqrt{r}\, \exp\left(\frac{-A^2\,(r-r_s)^2}{4\,t}\right)}{t^{3/2}}\right] \left[1 - \frac{t}{A^2\, r\, r_s}\right] \tag{4.11}$$

which leads to a perturbation-peak trajectory given by

$$\Delta t_{peak} \approx \frac{(\Delta r_{peak})^2}{13.5\, A^2} = \frac{(\Delta r_{peak})^2}{9\,\chi_e} \tag{4.12}$$

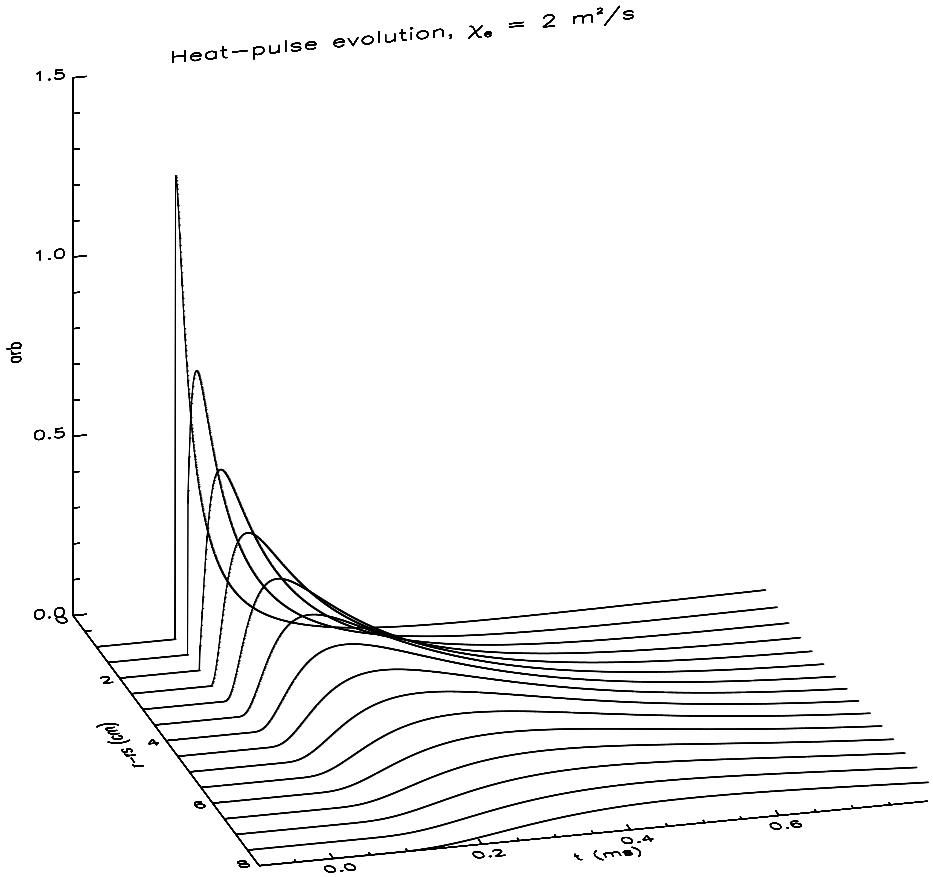

Figure 4.10: Modeled spatial and temporal evolution of temperature-perturbation produced from two opposing δ-functions. $\tilde{\mathrm{T}}_\mathrm{e}$ is plotted as a function of r and t, as the pulse propagates outward from $r_{perturbation}$.

only slightly different than that derived for the small Bessel-function argument expansion.

4.3.3 Experimental Results

Sawtoothing discharges in CDX-U are generally formed with relatively high density and an increased ohmic drive (loop-voltage) to keep the temperature in the typical CDX-U range of $50 - 100$ eV. For these discharges, $\mathrm{n_e}(0) = 5 \times 10^{19}$ m^{-3} and $\mathrm{T_e}(0) = 70$ eV.

The raw SXR data was best-fit to the evolved perturbation function given by equation 4.8, parameterized by χ_e, t_s, r_{obs}, and an arbitrary scalar magnitude. In the fitting routine, r_s and t_s were held fixed at the measured sawtooth location and time. χ_e was allowed to vary to produce a best-fit parameterized curve to the data at each measurement chord. A representative sample of SXR waveforms covering the full range of the SXR array, plotted with the best-fit solutions of equation 4.8 is shown in figure 4.11.

In this figure, it is important to notice the progression from one observation channel to the next as the pulse travels from the q=1 surface outward. Channels for $r - r_s < 5$ cm demonstrate a progression well represented by equation 4.8 and figure 4.10. The Δr covered between figure 4.11a and 4.11d is 3.9 cm, nearly identical to that covered between figure 4.11d and 4.11e (3.6 cm). The pulse shape, on the other hand, undergoes significant relaxation/delay over the first 3.9 cm, and nearly no change over the last 3.6 cm.

In order to illustrate this effect more clearly, the t_{peak} values for each channel were plotted against the observation radius for that channel. χ_e was then straightforwardly derived using equation 4.12.

Error in the χ_e estimate is dominated by error in the quadratic fit, which can be calculated using equation 3.65 and equations 3.72 - 3.84. This can then be straightforwardly propagated to produce an estimate for σ_{χ_e}. Error presented on χ_e plots is $\pm 2\,\sigma_{\chi_e}$.

The trajectory of the heat-pulse from figure 4.11 is shown in figure 4.12. Clearly a quadratic is not an accurate representation of the data over the full range of the SXR measurements, so equation 4.12 was only used in the region where it accurately represents the data. This corresponds to $r_s < r < 10.5$ cm, over which

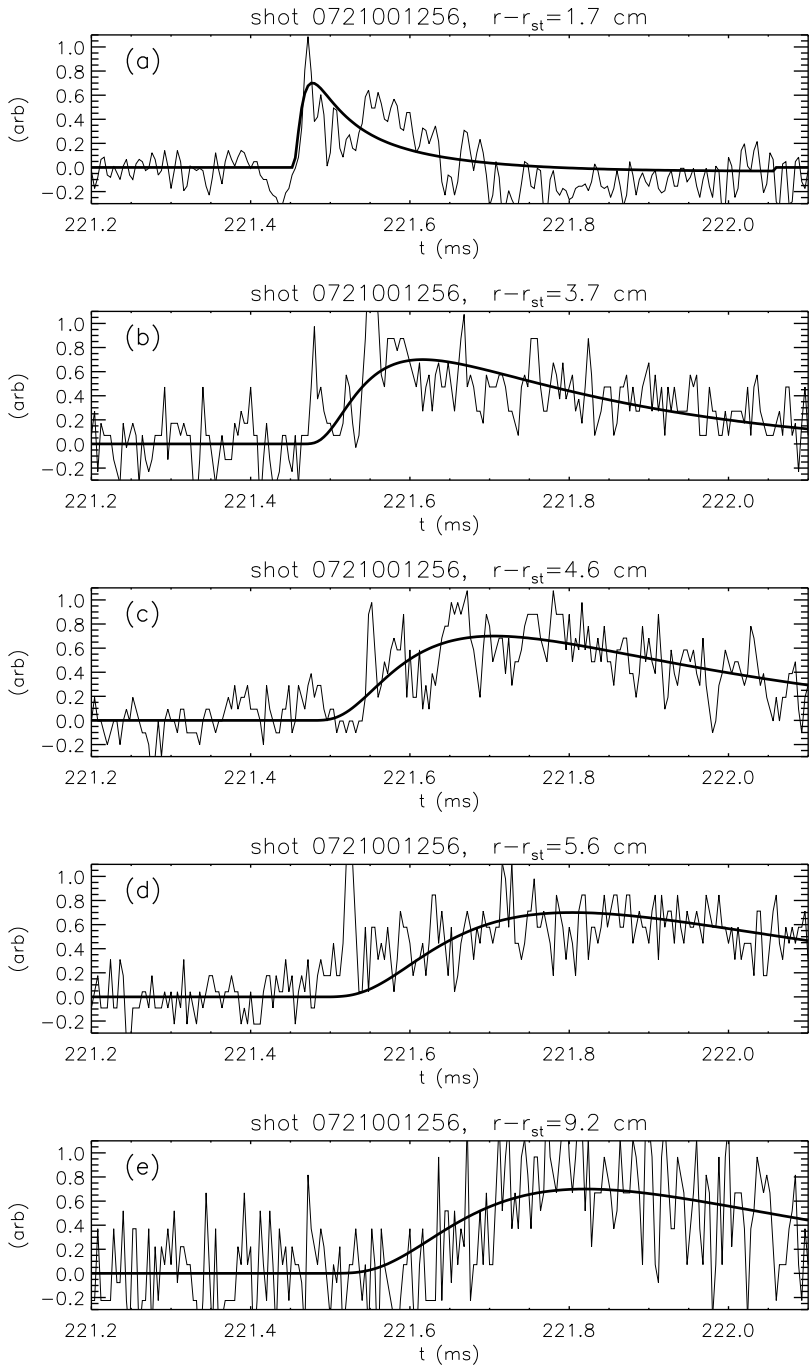

Figure 4.11: Data and best-fit curves based on equation 4.8 for heat-pulses observed around $t = t_{sawtooth}$ and at $r > r_{sawtooth}$, shot 0721001256. The radial excursion between plots (a) and (d) is nearly identical to that between plots (d) and (e), though the pulse shape evolves significantly in the former case, and is nearly identical in the latter.

$\chi_e = 1.1$ m^2/s The analysis of several similar sawtoothing discharges showed very uniform profile behavior, with derived χ_e values in the core ranging from 0.8 to 2.2 m^2/s.

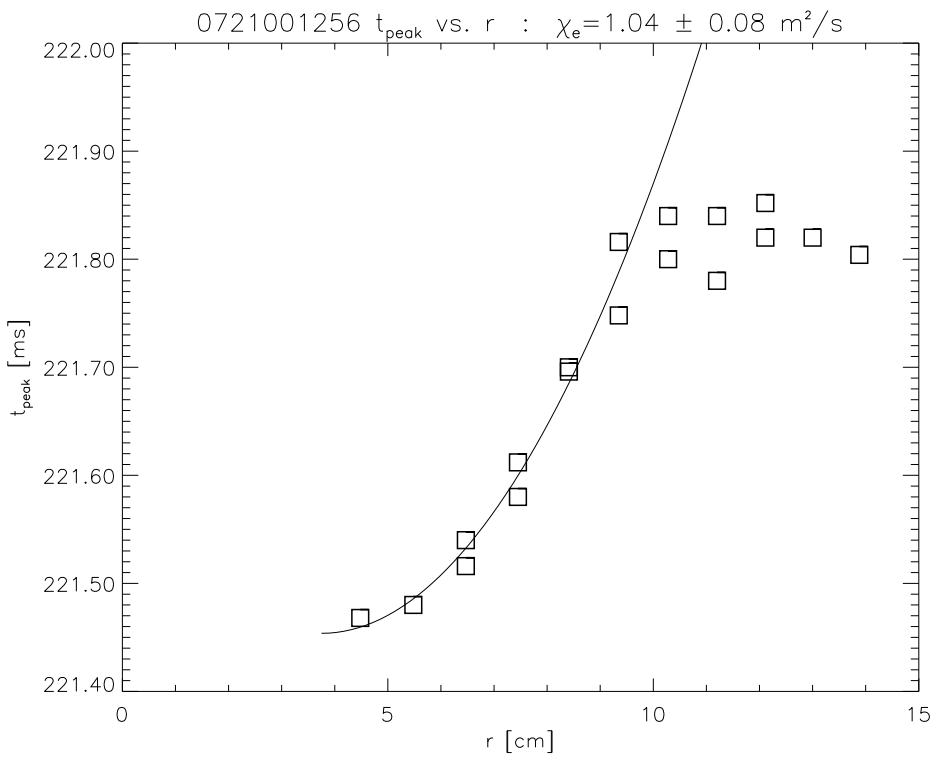

Figure 4.12: Heat-pulse trajectory, with quadratic best-fit curve to channels corresponding to $r_s < r < 10.5$ cm. $\chi_e = 1.1$ m^2/s in the core, increasing steeply outside r/a $\sim$ 1/3.

Clearly χ_e exhibits very different behavior in two distinct regions. χ_e is quite low and uniform in the measured region within r/a $\sim$ 1/3 - 1/2, and increases steeply outside this region. Although it is difficult to assess a χ_e value in the outer region with reasonable precision, it appears to exceed the core value by an order of magnitude or more. Both the derived χ_e values and profile behavior are in very good agreement with the edge cold-pulse study, despite the quite different experimental technique.

It is useful to compare the profile behavior of χ_e with the profiles of the fundamental electron parameters T_e and n_e. Figure 4.13 shows the heat-pulse trajectory plot from figure 4.12 plotted above T_e and n_e profiles from TVTS. Clearly the T_e

profile (fig. 4.13b) is consistent with the χ_e profile derived from the sawtooth analysis (fig. 4.13a). A sharp temperature gradient exists in the region of measured low χ_e (r/a$\sim$1/3), and a much flatter (and colder) region exists where χ_e is measured to be sharply higher.

The n_e profile (fig. 4.13c) also exhibits a steep central gradient and peak, though the n_e gradient appears at lower radius than the temperature gradient. The n_e peak, as well as the corresponding dip in T_e, appear within the q=1 radius, shown in fig. 4.13a as the source of the sawtooth perturbation.

In trying to determine whether the sharp change in χ_e represents a transport-barrier in CDX-U, it is important to consider the possibility that CDX-U simply exhibits good confinement which is degraded over some region due to a large magnetic island. In CDX-U, evidence for magnetic islands can be obtained with both the SXR array and the scanning interferometer, both of which sample nearly the full plasma radius and are highly time-resolved, though both are also line-integrated measurements. Additional information may be provided by the triple probe, located at r=22 cm.

The SXR array has been quite useful in CDX-U for the observation of MHD islands, regularly visible on the q=1 surface, and sometimes visible on the q=2 surface as well. Looking at the frequency and level of fluctuations in the SXR channels has been extensively used to identify and describe island formation in CDX-U. When using the SXR array as a monitor of fluctuation levels, it is crucial to normalize the measured fluctuation levels to the mean signal level for each channel to remove the explicit dependence on T_e and n_e, which are both quite peaked. Additionally, it is necessary to calculate the noise-floor for each channel, due to both x-ray photon statistics and amplification/digitization noise. The noise-floor calculation is particularly important for the channels outside of the core, which have the lowest signal levels.

The digitization bit-noise and amplifier noise levels are calculated by using signals from the SXR array recorded before the plasma shot. These 'background' signals are then run through the same analysis as the 'plasma' signals, and a noise level is established which takes into account all noise implicit to the data acquisition.

The spectral SXR photon-noise levels for each channel are calculated using the

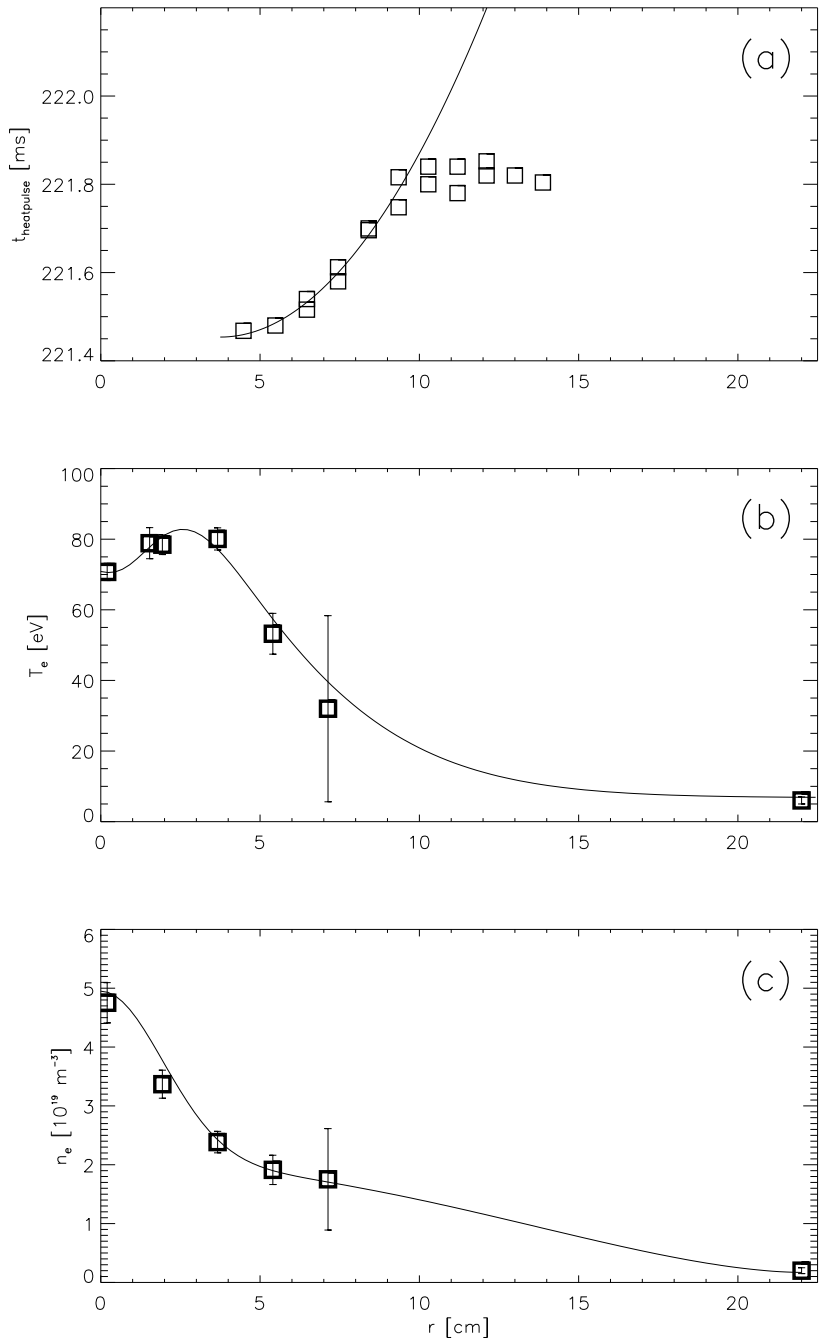

Figure 4.13: Comparison of χ_e behavior (a) with electron T_e and n_e profiles (b and c). The steep T_e gradient at r/a$\sim$1/3 matches the location of the low measured χ_e. The n_e profile also exhibits a steep central peak, though at lower r than the temperature gradient (i.e. within the q=1 sawtooth inversion radius)

expression

$$S_{PN} = \sqrt{2\ S_0\ \langle E_\nu \rangle\ \Delta f} \qquad \left[\frac{phot.}{sec}\right] \tag{4.13}$$

where S_0 is the average power [watts] incident on the detector, $\langle E_\nu \rangle$ is the average photon energy (CV line emission at $h\nu = 306$ eV), and Δf is the frequency bandwidth used in the Fourier analysis [Sesnic *et al.*, 1994]. Substituting

$$\Delta f = \frac{1}{N\ t_{samp}} \qquad \left[sec^{-1}\right]$$
$$S_0\ \langle E_\nu \rangle = C\ V_0 \qquad \left[\frac{phot.}{sec}\right] \tag{4.14}$$

where N is the total number of points in the time window, t_{samp} is the digitization sampling interval, V_0 is the mean signal level over the time window to be analyzed [volts], and C is the calibration constant of the detector $\left[\frac{phot./sec}{volt}\right]$, leads to

$$S_{PN} = \sqrt{\frac{2\ C\ V_0}{N\ t_{samp}}} \qquad \left[\frac{phot.}{sec}\right] \tag{4.15}$$

or

$$S_{PN} = \sqrt{\frac{2\ V_0}{C\ N\ t_{samp}}} \qquad [volt] \tag{4.16}$$

Figure 4.14 shows the fluctuation levels in the SXR signals, plotted against minor radius (as mapped for the sawtooth study). The fluctuation levels have been normalized to the mean signal level, as described above. Also shown are the noise-floors imposed by amplification/digitization noise and the x-ray photon noise. The frequency spectrum has been split into two frequency windows, from 1-75 kHz and from 75-125 kHz ($f_{Nyquist} = 125$kHz).

In the lower frequency range there is a fairly flat fluctuation level profile in the central channels, reaching a level that is indistinguishable from the noise floor in the outer channels (corresponding to the region of low overall SXR signals). The higher frequency range exhibits no levels above the noise floor. From the SXR signals, there is no visible evidence of a large island outside of r = 10 cm, though

this plot does not provide conclusive proof that an island is not there. Rather, the profile signature is dictated by the peakedness of the electron pressure profile, leading to signals in the outer channels that are too weak to demonstrate the presence or absence of an island.

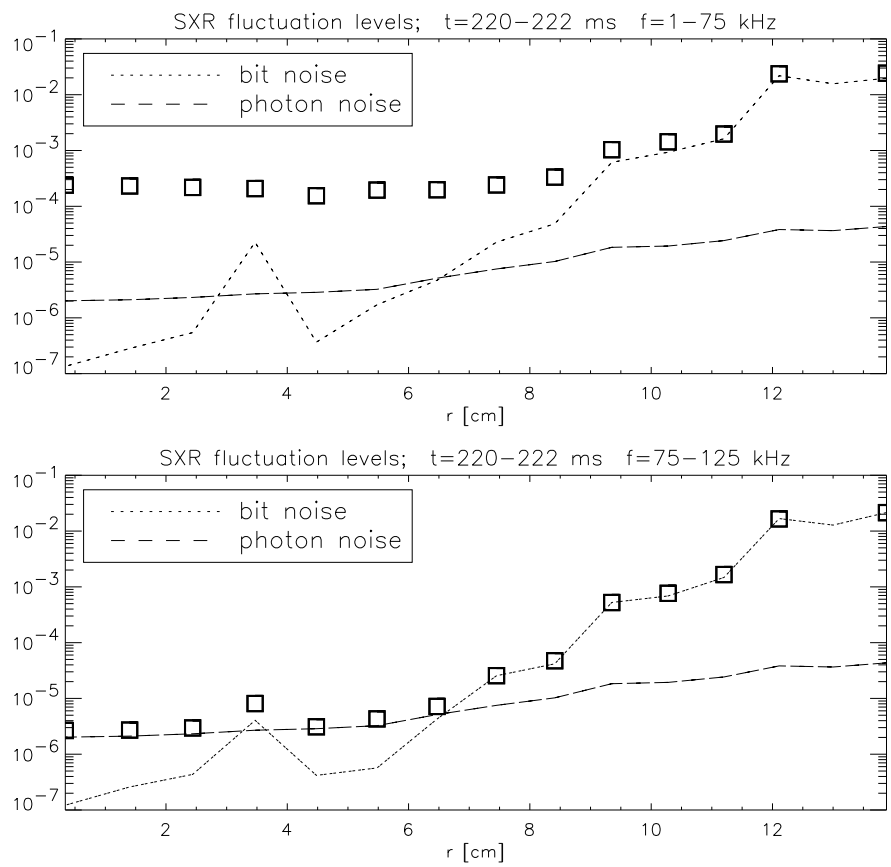

Figure 4.14: Fluctuation levels of the SXR signals, plotted against minor radius. The two plots correspond to frequency windows of 1-75 kHz and 75-125 kHz, respectively. No strong MHD signatures are visible on the SXR signals near the χ_e transition region, though for r > 10 cm the signal levels are so low as to be dominated by amplifier/digitizer or photon noise.

Representative spectra of the SXR signal fluctuations, taken at r = 4.8 cm and 10.2 cm (chosen to best represent the low and high χ_e regions), are shown in figure 4.15. Fluctuations at r = 4.48 cm show the q=1 island at ∼10-12 kHz and harmonics. Fluctuations at r = 10.2 cm exhibit nearly 'white' noise, reaching a noise floor at $\sim 10^{-7}$.

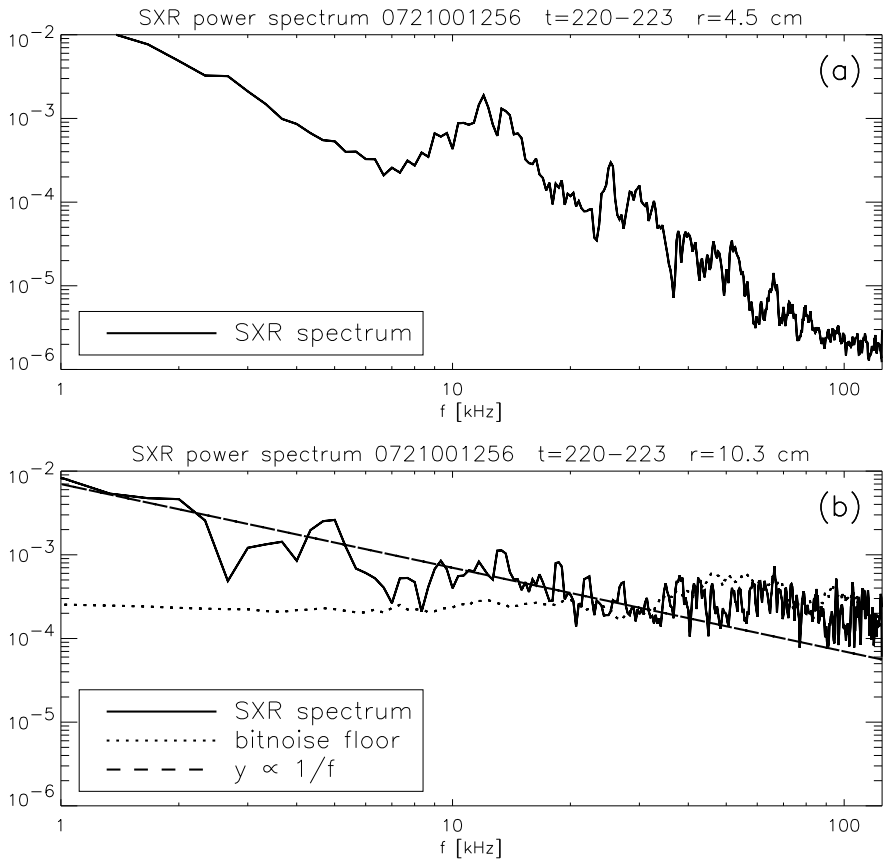

Figure 4.15: Fluctuation spectra of the SXR signals, taken at two representative radii; r = 4.8 cm and 10.2 cm represent the low and high χ_e regions, respectively. Fluctuations at r = 4.48 cm show the q=1 island at ∼10 kHz and harmonics. Fluctuations at r = 10.2 cm exhibit nearly 'white' noise, lower than the preceding plot by two orders of magnitude or more, and reaching a noise floor at $\sim 10^{-7}$. Fluctuation levels at r=10.3 cm, measurable above the noise floor for f < 20 kHz, are similar to or lower than the corresponding levels at r=4.5 cm.

Figure 4.15 provides additional evidence that a large island does not exist outside of the q=1 surface. Whereas figure 4.14 shows only the average fluctuation level, which is very close to the noise floor, figure 4.15 shows the lower frequency band $f < 20$kHz clearly above the noise floor, representing a meaningful measurement in this band. Comparing the plots 4.15a and 4.15b (r=4.5 cm and 10.3 cm, respectively), it appears that the relative fluctuation level in the high χ_e region is equal to or lower than that in the low χ_e region.

Figure 4.16 shows an analysis of the microwave interferometer signal, similar to plots 4.14 and 4.15. The interferometer was radially scanned over the course of the sawtooth study (one radial position per shot). This data was recorded at 100 kilosamples per second ($f_{Nyquist} = 50$kHz, and therefore only the single frequency window of 1-50 kHz is represented in the first figure.

The radial map does exhibit some degree of variation in the fluctuation level, though interestingly the regions with the highest fluctuation levels correspond to *both* the regions of high and low measured χ_e. The spatial variation can be seen in more detail in the second plot, which shows individual power spectra for r = 5, 11, and 15 cm. From this plot, it appears that the majority of the spatial variation is from fluctuations below 10 kHz. Again, it is notable that the fluctuation level is nearly identical in the two distinct regions of low and high measured χ_e, but is somewhat lower for $f < 20$kHz near r = 11 cm, at the χ_e transition region.

Figure 4.17 shows spectra of T_e and n_e fluctuations, measured at r=22 cm (plasma edge) with the triple probe. Although this measurement is taken well outside of the χ_e transition location, it is included for completeness. No strong peaks are visible corresponding to the q=1 island rotation peaks visible with the SXR array (f=10-12 kHz and harmonics), which would be the expected signature of an island near the plasma edge rotating in phase with the q=1 island.

The dominant MHD activity in CDX-U appears to be the q=1 magnetic island, located deep within the good confinement region. Given the magnitude of this island and the size of the high χ_e region, it would seem that any magnetic island capable of causing this transport transition would need to be quite significant. The spatial and spectral analysis of the SXR, interferometer, and triple-probe signals do not show any evidence of a magnetic island in the vicinity of the χ_e transition, and therefore the χ_e behavior appears to be due to a kind of transport barrier near

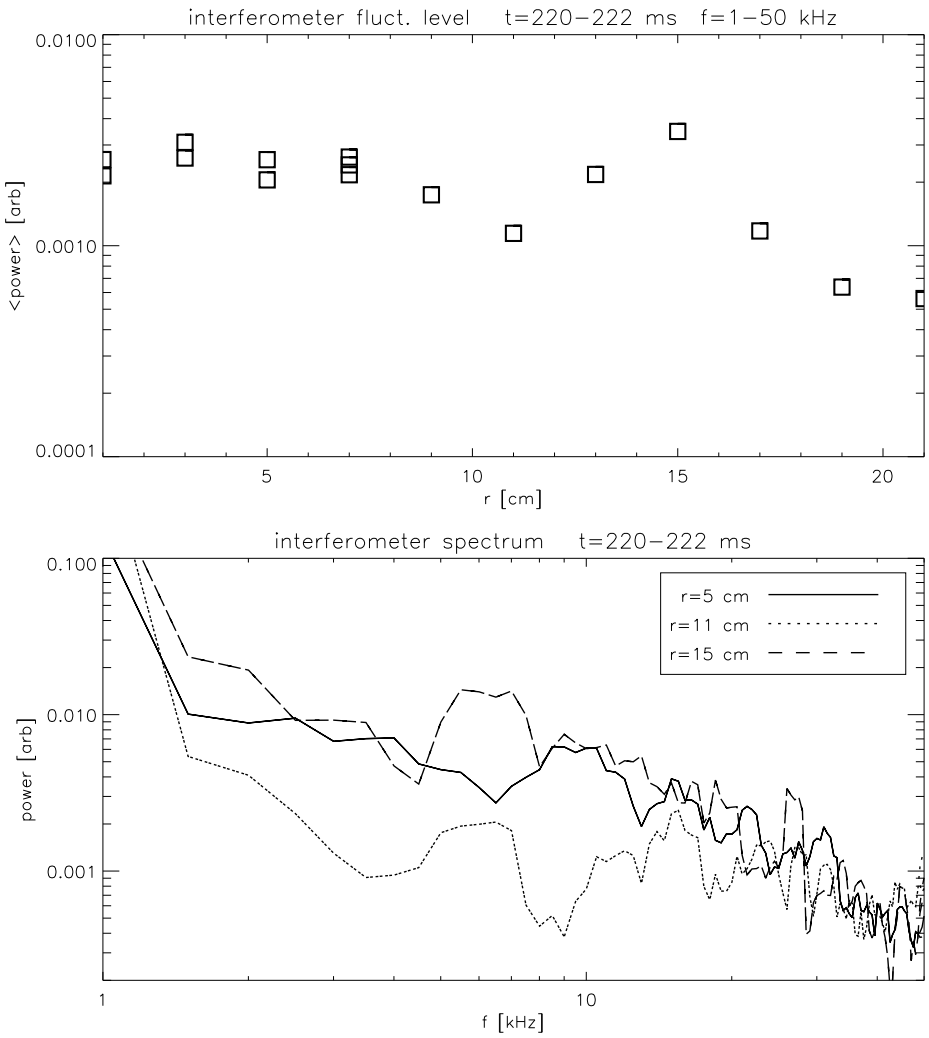

Figure 4.16: Fluctuation levels and spectra from the interferometer signals. The first plot shows a broad fluctuation spectrum, through both the low and high χ_e regions. The second plot shows three fluctuation spectra, taken at r = 5, 11, and 15 cm.

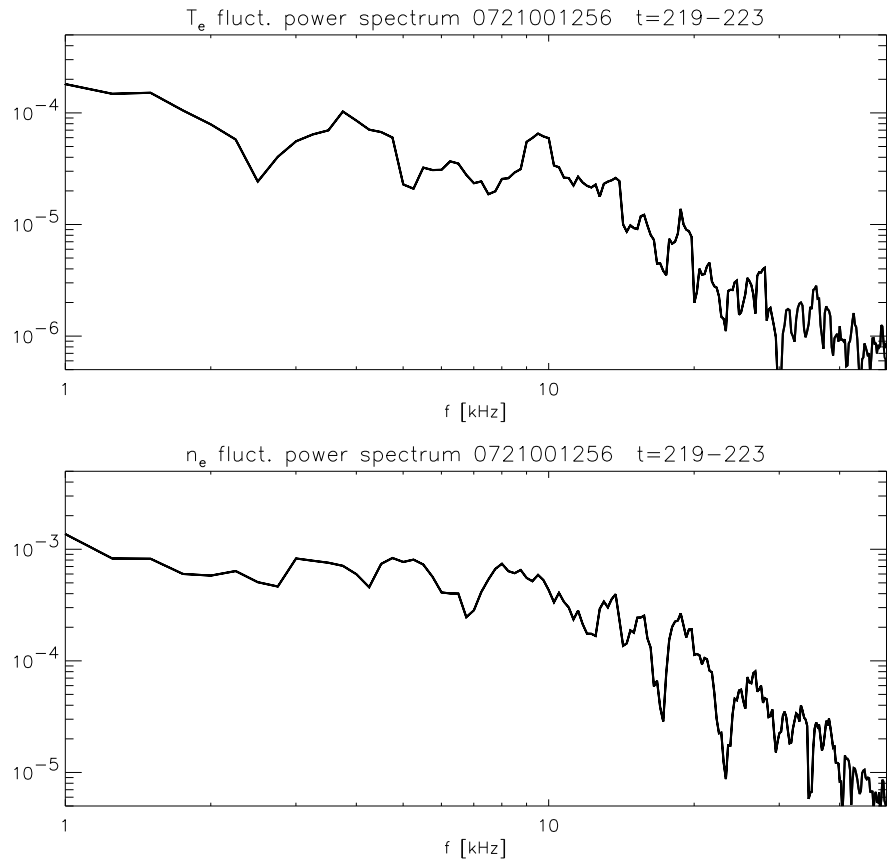

Figure 4.17: Fluctuation power spectra of T_e and n_e , measured with the triple probe located at r=22 cm (plasma edge). No strong peaks are visible corresponding to the q=1 island rotation peaks visible with the SXR array (f=10-12 kHz).

r/a=1/3.

4.4 Comparison With Neoclassical Estimates and Scaling Laws

Although it is widely believed that microturbulence of one form or another is the dominant mechanism leading to measured transport coefficients, it is nonetheless useful to maintain a comparison of any experimental data with neoclassical estimates. Although tokamak experiments have yet to achieve neoclassical electron confinement, many experiments have seen neoclassical-level ion confinement, as mentioned in the introduction to this chapter. Additionally, transport barriers have been seen on tokamaks with direct electron heating, though even in these cases electron thermal transport remains anomalously high [Greenfield *et al.*, 1999].

Neoclassical estimates of all transport coefficients have been well established for high aspect ratio geometry, often using inverse aspect-ratio as an expansion parameter in the derivation. A comprehensive review of neoclassical transport calculations is given in [Hirshman and Sigmar, 1981], and an abbreviated treatment can be found in [Wesson, 1997]. The commonly used "Chang-Hinton" expression for χ_i which incorporates finite aspect-ratio effects and interpolates between different collisionality regimes is given in [Chang and Hinton, 1986].

Neoclassical estimates for χ_e which include finite aspect-ratio effects and span all collisionality regimes have recently been developed in [Houlberg *et al.*, 1997], and incorporated into the NCLASS and FORCEBAL codes.

Figure 4.18 shows the χ_e estimates calculated by the FORCEBAL code, using the profiles shown in figure 4.13 and a magnetic equilibrium geometry produced from the EFIT code for these shots. The two curves shown represent $\chi_{e,nc}$ calculated using two different methods of gradient computation.

Clearly the $\chi_{e,nc}$ produced from FORCEBAL is a very poor match to the measured χ_e, both in magnitude and profile shape. The measured χ_e is 10 times higher than that predicted by FORCEBAL, and the profile shape of the data (i.e. fairly constant in the core, with a dramatic increase at r$\sim$10 cm) bears no resemblance to the FORCEBAL profile.

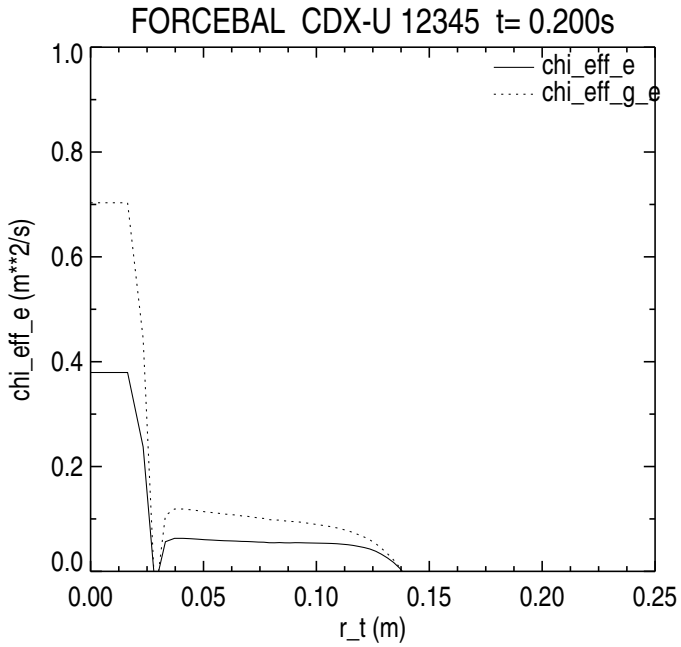

Figure 4.18: Neoclassical estimate of χ_e, calculated with the FORCEBAL code for CDX-U profiles taken from the temperature-pulse experiments.

Interestingly, if the Chang-Hinton expression for χ_i is modified for electrons, by replacing all ion quantities (ν_i, ρ_i, etc.) with the corresponding electron quantities, the resulting χ_e profile shape matches the CDX-U data much more closely. The result of this calculation is shown in figure 4.19 along with two other scalings (described below), all renormalized to $\chi_e = 1\text{m}^2/\text{s}$ at r=8 cm to facilitate profile comparison. $\chi_{e,nc}$ calculated by modifying the Chang-Hinton χ_i expression is 5 times lower than the measured CDX-U value, somewhat comparable to the result obtained using FORCEBAL. The profile, though, is clearly a much closer match to the CDX-U data, though the modified Chang-Hinton expression places the χ_e gradient at a larger r value than that measured in CDX-U.

Also shown in figure 4.19 are two semi-empirical χ_e scalings which have both been used in past comparisons to START transport data. χ_LAG represents the Lackner-Gottardi model, presented in [Lackner and Gottardi, 1990], modified by Connor for low aspect-ratio and presented in [Roach, 1996]. This is a model intended for ohmic and L-mode plasmas, based on a simple model in which trapped particles are displaced by a banana width with each bounce. The modified LAG

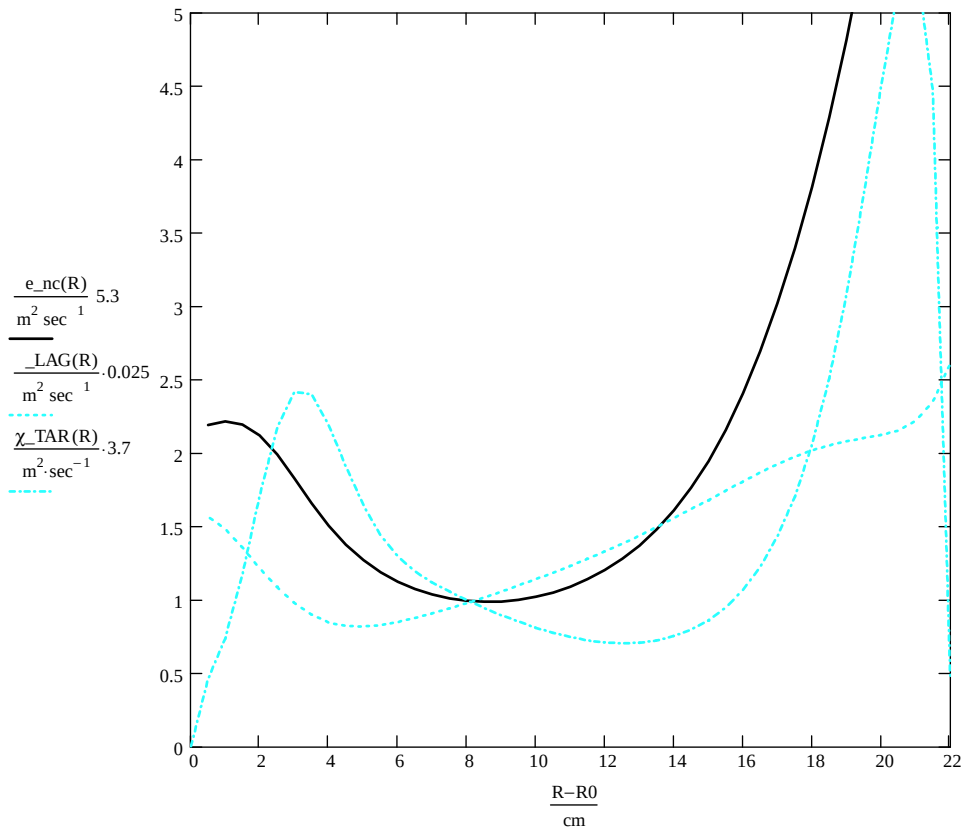

Figure 4.19: χ_e estimates from a modified Chang-Hinton χ_i expression (labeled χe_nc), along with the two semi-empirical estimates χ_LAG, and χ_TAR. Each estimate has been renormalized to match the measured CDX-U value of 1.0 m^2/s at r=8 cm, with the normalization constant indicated in the plot legend. (Chang-Hinton underestimates χ_e by a factor of 5.3, χ_LAG overestimates χ_e by a factor of 40, and χ_TAR underestimates χ_e by a factor of 3.7.)

model is given by

$$\chi_e{}^{LAG} = 0.33\,\nu_i \left(\frac{T_e}{T_i}\right)^{1.5} \left(\frac{\rho_i\,R_{max}}{R_0\,\epsilon}\right)^2 \frac{q}{k\,R_0}\,f_T{}^4 \tag{4.17}$$

where f_T is the trapped-particle fraction, R_{max} is the outermost major-radius of the given flux-surface, and all quantities are in SI units.

The LAG model reproduces the measured χ_e profile very poorly, and also overestimates the minimum χ_e by a factor of 40. Interestingly, this is the model that has produced the best agreement with START power-balance based χ_e data, in magnitude if not always in profile shape. It should also be noted that in the START high-performance NBI-heated discharges, the LAG estimates were very close to those calculated for CDX-U, though in that case χ_e from the START experiment was a much closer match to the LAG model [Gates *et al.*, 1998].

The third model shown in 4.19 is the χ_TAR model, a semi-empirical model based on JET data and presented in [Taroni *et al.*, 1994]. This scaling is given by

$$\chi_e{}^{TAR} = 3.3 \times 10^{-4}\,\frac{T_e\,q^2\,a}{B_T}\,\frac{\nabla p_e}{p_e} \tag{4.18}$$

where $\mathrm{T_e}$ is in eV, and all other units are SI. This scaling seems to be closest to the χ_e from the modified Chang-Hinton expression in magnitude, though the calculated location of $\nabla\chi_\mathrm{e}$ is even further out in radius, and thus further from the measured location in CDX-U.

In general, the comparisons to the two neoclassical and two semi-empirical χ_e estimates is quite unsatisfactory. Only one model seems to vaguely represent the measured χ_e behavior (modified Chang-Hinton expression), and even this is a factor of five too low. Interestingly, the models chosen both underestimate and overestimate the measured χ_e, though with the estimates covering such a wide range of predictions, it is difficult to draw concrete conclusions from the comparisons.

4.5 Conclusions

The electron transport profile has been measured in CDX-U using two independent perturbative methods, representing the first local measurements of χ_e in a spherical

torus. χ_e is found to be 1-2 m^2/s in the CDX-U core ($r/a \leq 1/3$), sharply increasing outside of this region by an order of magnitude or more. T_e profiles exhibit sharp gradients in the region of low measured χ_e, reaffirming the conclusion of distinct regions of high and low transport levels. Though it cannot be entirely ruled out, it appears from all available diagnostics that the profile behavior is not caused by a degradation of confinement due to the presence of a magnetic island, and is indeed a kind of transport barrier. Though D_e was not measured explicitly in these experiments, the n_e profiles also exhibit very sharp gradients in the core region, though at a measurably different radius than the thermal transport barrier. Specifically, the n_e peak appears inside the q=1 radius, and the T_e gradient region appears outside of q=1. The location of other rational q surfaces has not been measured in these plasmas.

The measured χ_e level is a factor of 5-10 higher than neoclassical estimates, and the profile shape is a poor match to the experimental data. Likewise, two semi-empirical χ_e scalings which have shown somewhat favorable comparison to START electron transport data show poor agreement with the CDX-U experimental results.

Chapter 5

Conclusions and Future Work

5.1 Electron transport in ST's

Though the experiments presented here represent the first localized χ_e measurement in an ST and the first electron profile information from CDX-U, the subject of electron transport in CDX-U and ST's in general is by no means exhausted. In particular, electron tranport studies can continue on CDX-U as the machine program and diagnostic set continue to evolve, and the results from CDX-U can be compared with other ST's at PPPL and elsewhere.

It is important to remember that several studies have been performed on other tokamaks which indicate that χ_e measured by by perturbative techniques can be several times higher than that determined by power-balance techniques, due to nonlinearities in the dependence of χ on ∇T, local MHD perturbations, or coupled n_e and T_e diffusion. Comparison with neoclassical χ_e calculations indicate that the experimental values in CDX-U are 5-10$\times$ higher than neoclassical estimates, though the steady-state experimental value may be closer than this.

The edge cold-pulse experiment is likely the most susceptible to coupling between n_e and T_e diffusion, since the T_e perturbation is a direct consequence of an induced n_e perturbation. Indeed, the χ_e values from the edge cold-pulses were consistently higher than those determined from sawtooth analysis.

CDX-U is presently embarking on a campaign of lithium-limiter experiments, which will undoubtedly affect the plasma conditions and possibly the transport. Also, as the EBW temperature diagnostic continues to evolve, there will be many

opportunities for continued exploration of electron transport in CDX-U. Additionally, measurements of other thermal and particle fluxes may be measured to determine χ_{i} and $\mathrm{D}_{\mathrm{e,i}}$ so that the different transport coefficients can be compared.

Both NSTX and MAST will be maturing to the level necessary to make χ_{e} measurements during the coming years, and undoubtedly the subject of electron transport in spherical tori will be extensively studied on these two major experiments. In addition to repeating the cold-pulse and heat-pulse experiments presented here in the larger machines, the diagnostic capabilities of NSTX and MAST will be sufficient to make detailed comparisons with power-balance based transport measurements.

5.2 TVTS system

The CDX-U Thomson scattering system will be an invaluable tool for future experiments in CDX-U, and will benefit from continued improvement. As with other Thomson scattering systems, the most critical limitation is the total collected photons, and several improvements can be made to increase this number.

As covered in section 3.2.3, there is a possibility that the laser cavity can be converted from a single-pulse system to a multiple (2-3) pulse system, with a predicted power gain of 2.5×. Additionally, there are a number of straightforward improvements that can be made to the optical system to improve total system performance.

One difficulty of placing the TVTS system adjacent to the vacuum vessel (rather than isolated in a separate laser room, for example) is that local heat-sources such as vacuum pumps can cause temperature gradients in the optical table, which lead to some flexing of the table surface. Although the optical table is quite stiff, a small degree of flexing can have a compound effect on the TVTS system performance. Firstly, the oscillator cavity can go out of alignment very easily, which results in a reduction in output power and a slight redirection of the output beam. Since the camera gate is triggered on the rise-phase of the oscillator pulse, the synchronization of the laser and camera is critically dependent on the uniformity of the output power from the cavity, so that if the output power drops, the camera gate can suffer some mistiming with respect to the scattered light pulse. Additionally, small deviations

in the output beam direction, propagated over the ∼10 m laser beam path, can degrade the alignment of the fibers to the beamline.

The optical table is presently cooled only as a consequence of the contact of the laser heads with the table surface. This is quite a small area of contact, and while the laser heads themselves are kept at a quite steady 65°F, the bulk of the optical table is susceptible to temperature gradients. This can be vastly improved with the installation of cooling lines over the periphery of the table, fed from the same chiller that feeds the ruby heads.

With these fairly straightforward improvements, the TVTS system should work reliably and consistently, and provide high quality data for future experiments on CDX-U.

Bibliography

Bekefi, G. (1966). *Radiation Processes in Plasmas.* Wiley, NY.

Bell, R. (1998). Private communication.

Bicron Corporation (1998). 3379 Monika Circle, Orlando, FL 32812.

Bornatici, M., Cano, R., Debarbieri, O., and Engelmann, F. (1983). Electron-Cyclotron Emission and Absorption in Fusion Plasmas. *Nucl. Fus.* **23**, 1153.

Bretz, N., Dimock, D., Foote, V., Johnson, D., Long, D., and Tolnas, E. (1978). Multichannel Thomson scattering apparatus. *Applied Optics* **17**, 192.

Burrell, K., Gentle, K., Luhmann, N., Marmar, E., Murakami, M., Schoenberg, K., Tang, W., and Zarnstorff, M. (1990). Status of local transport measurements and analysis in toroidal devices. *Phys. Fluids B* **2**, 2904.

Campos, D. and Machida, M. (2000). A multipass system for Thomson scattering diagnostic with multipulse-lasing. *Contributions to Plasma Physics* **40**, 86.

Cardozo, N. L. (1995). Perturbative Transport Studies in Fusion Plasmas. *Plasma Phys. and Contr. Fus.* **37**, 799.

Chang, C. and Hinton, F. (1986). Effect of impurity particles on the finite aspect-ratio neoclassical ion thermal conductivity in a tokamak. *Phys. Fluids* **29**, 3314.

Chen, S.-L. and Sekiguchi, T. (1965). Instantaneous direct-display of plasma parameters by means of triple probe. *J. Appl. Phys.* **36**, 2363.

Choe, W. (1996). *Feasibility study of electron injection for tokamak transport control*. PhD thesis, Princeton University.

Choe, W., Ono, M., and Chang, C. (1996). Study of Electron Ripple Injection Concept for Radial Electric Field Control in a Tokamak. *Nucl. Fus.* **36**, 1703.

Choe, W., Ono, M., Hwang, Y., and Chang, C. (1998). Feasibility Experiments for Electron Ripple Injection on Current Drive Experiment-Upgrade. *Phys. Plasmas* **5**, 966.

Colchin, R., Carolan, P., Duck, R., Edlington, T., Fielding, S., Gibson, K., Goodall, D., Gryaznevich, M., Hender, T., Hugill, J., Jenkins, I., Li, J., Manhood, S., Parham, B., Robinson, D., Singleton, M., Sykes, A., Todd, T., Turner, M., Valovic, M., Walsh, M., and Wilson, H. (1993). The Small Tight Aspect Ratio Tokamak experiment. *Phys. Fluids B* **5**, 2481.

Darrow, D. (1988). *DC Helicity Injection Studies on the Current Drive Experiment*. PhD thesis, Princeton University.

Darrow, D., Ono, M., Forest, C., Greene, G., Hwang, Y., Park, H., Taylor, R., Pribyl, P., Evans, J., Lai, K., and Liberati, J. (1990). Properties of DC Helicity Injected Tokamak Plasmas. *Phys. Fluids B* **2**, 1415.

Edmonds, J. and Reilly, J. (1985). *Global Energy: Assessing the Future*. Oxford University Press, New York.

Efthimion, P., Barnes, C., Bell, M., Biglari, H., Bretz, N., Diamond, P., Hammett, G., Heidbrink, W., Hulse, R., Johnson, D., Kusama, Y., Mansfield, D., Medley, S., Nazikian, R., Park, H., Ramsey, A., Rewoldt, G., Scott, S., Stratton, B., Synakowski, E., Tang, W., Taylor, G., Zarnstorff, M., and Zweben, S. (1991). Comparison of steady-state and perturbative transport coefficients in TFTR. *Phys. Fluids B* **3**, 2315.

Efthimion, P., Goeler, S. V., Houlberg, W., Synakowski, E., Zarnstorff, M., Batha, S., Bell, R., Bitter, M., Bush, C., Levinton, F., Mazzucato, E., McCune, D., Mueller, D., Park, H., Ramsey, A., Roquemore, A., and Taylor, G. (1999a). Observation of Neoclassical Transport in Reverse Shear Plasmas on TFTR. *Nucl. Fus.* **39**, 1905.

Efthimion, P., Hosea, J., Kaita, R., Majeski, R., and Taylor, G. (1999b). New electron cyclotron emission diagnostic for measurement of temperature based upon the electron Bernstein wave. *Rev. Sci. Instrum.* **70**, 1018.

Fiocco, G. and Thompson, E. (1963). Thomson Scattering of Optical Radiation from an Electron Beam. *Phys. Rev. Lett.* **10**, 89.

Forest, C. (1992). *Pressure driven currents in the CDX-U trapped particle configuration*. PhD thesis, Princeton University.

Forest, C., Greene, G., and Ono, M. (1990). CDX-U two-dimensional scanning microwave system. *Rev. Sci. Instrum.* **61**, 2888.

Forest, C., Hwang, Y., Ono, M., and Darrow, D. (1992). Internally generated currents in a small-aspect-ratio tokamak geometry. *Phys. Rev. Lett.* **68**, 3559.

Forest, C., Hwang, Y., Ono, M., Greene, G., Jones, T., Choe, W., Schaffer, M., Hyatt, A., Osborne, T., Pinsker, R., Petty, C., Lohr, J., and Lippmann, S. (1994). Investigation of the formation of a fully pressure-driven tokamak. *Phys. Plasmas* **1**, 1568.

Fredrickson, E., Austin, M., and Groebner, R. (2000). Heat pulse propagation studies on DIII-D and the Tokamak Fusion Test Reactor. *Phys. Plasmas* **7**.

Fredrickson, E., Callen, J., K.McGuire, Bell, J., Colchin, R., Efthimion, P., Hill, K., Izzo, R., Mikkelsen, D., Monticello, D., Pare, V., Taylor, G., and Zarnstorff, M. (1986). Heat Pulse Propagation Studies in TFTR. *Nucl. Fus.* **26**, 849.

Fredrickson, E., McGuire, K., Cavallo, A., Budny, R., Janos, A., Monticello, D., Nagayama, Y., Park, W., Taylor, G., and Zarnstorff, M. (1990). Ballistic Contributions to Heat-Pulse Propagation in the TFTR Tokamak. *Phys. Rev. Lett.* **65**, 2869.

Füfner, E., Kronast, B., and Kunze, H. (1963). Experimental results on light scattering by a θ-pinch plasma using a ruby laser. *Physics Letters* **5**, 125.

Gasparino, U., Erckmann, V., Hartfuss, H., Maassberg, H., and Rome, M. (1998). Transient analysis through heat waves driven at different radial positions. *Plasma Phys. and Contr. Fus.* **40**, 233.

Gates, D., Akers, R., Appel, L., Carolan, P., Conway, N., Dowling, J., Gryaznevich, M., Hender, T., Kwon, O., Martin, R., Nightingale, M., Price, M., Roach, C., Sykes, A., Tournianski, M., M.Walsh, C.D.Warrick, team, S., and team, N. (1998). High-performance discharges in the Small Tight Aspect Ratio Tokamak (START). *Phys. Plasmas* **5**, 1775.

Gentle, K. (1988). Dependence of heat pulse propagation on transport mechanisms: Consequences of nonconstant transport coefficients. *Phys. Fluids* **31**, 1105.

Gentle, K., Cima, G., Gasquet, H., Hallock, G., Phillips, P., Rowan, W., Watts, C., and Gehre, O. (1995a). Characteristics of Equilibrium and Perturbed Transport Coefficients in Tokamaks. *Physica Scripta* **52**, 411.

Gentle, K., Rowan, W., Bravenec, R., Cima, G., Crowley, T., Gasquet, H., Hallock, G., Heard, J., Ouroua, A., Phillips, P., Ross, D., Schoch, P., and Watts, C. (1995b). Strong Nonlocal Effects in a Tokamak Perturbative Transport Experiment. *Phys. Rev. Lett.* **74**, 3620.

Giannone, L., Erckmann, V., Gasparino, U., Hartfuss, H., Kuhner, G., Maassberg, H., Stroth, U., Tutter, M., Kasparek, W., Muller, G., Schuller, P., Dammertz, G., Gantenbein, G., Geist, T., Kuntze, M., Nickel, H., Piosczyk, B., and Thumm, M. (1992). Electron Thermal Conductivity from Heat-Wave Propagation in Wendelstein 7-AS. *Nucl. Fus.* **32**, 1985.

Grace, J., Nebolsine, P., and Goldey, C. (1998). Repetitively pulsed ruby lasers as light sources for high- speed photography. *Opt. Eng.* **37**, 2205.

Greenfield, C., Rettig, C., Staebler, G., Stallard, B., Austin, M., Burrell, K., DeBoo, J., deGrassie, J., Doyle, E., Gohil, P., Groebner, R., Lohr, J., McKee, G., Peebles, W., Petty, C., Pinsker, R., Rice, B., Rhodes, T., E.J.Synakowski, Waltz, R., and Zeng, L. (1999). Behaviour of electron and ion transport in discharges with an internal transport barrier in the DIII-D tokamak. *Nucl. Fus.* **39**, 1723.

Grisham, L., Scott, S., Goldston, R., Bell, M., Bell, R., Bretz, N., Bush, C., Grek, B., Hammett, G., Hill, K., Jobes, F., Johnson, D., Kaye, S., Mansfield, D., Mueller, D., Park, H., Ramsey, A., Schivell, J., Stratton, B., Synakowski, E., Taylor, G., and Towner, H. (1991). Scaling of Confinement with Major and Minor Radius in the Tokamak Fusion Test Reactor. *Phys. Rev. Lett.* **67**, 66.

Gryaznevich, M., Akers, R., Carolan, P., Conway, N., Gates, D., Field, A., Hender, T., Jenkins, I., Martin, R., Nightingale, M., Ribeiro, C., Robinson, D., Sykes, A., Tournianski, M., Valovi, M., and Walsh, M. (1998). Achievement of Record β in the START Spherical Tokamak. *Phys. Rev. Lett.* **80**, 3972.

Hender, T., Baker, L., Hancox, R., Hicks, J., Knight, P., Robinson, D., and Wilson, H. (1992). Tight aspect ratio tokamak reactors. *in Plasma Physics and Controlled Nuclear Fusion Research 1992 (Proc. 14th Int. Conf. Wurzburg, 1992) Vol. 3, IAEA, Vienna* , 339.

Herzberg, G. (1939). *Molecular Spectra and Molecular Structure*, volume 1: Diatomic Molecules. Prentice Hall, New York.

Hirshman, S. and Sigmar, D. (1981). Neoclassical transport of impurities in tokamak plasmas (review paper). *Nucl. Fus.* **21**, 1079.

Hogeweij, G., O'Rourke, J., and Sips, A. (1991). Evidence of Coupling of Thermal and Particle Transport from Heat and Density Pulse Measurements on JET. *Plasma Phys. and Contr. Fus.* **33**, 189.

Holdren, J. (1990). Energy in Transition. *Scientific American* **263**, 156.

Holdren, J. (1991). Safety and Environmental Aspects of Fusion Energy. *Annu. Rev. Energy Environ.* **16**, 235.

Hosea, J., Arunasalam, V., and Cano, R. (1977). Electron Cyclotron Emission from the Princeton Large Tokamak. *Phys. Rev. Lett.* **39**, 408.

Houghton, J., Jenkins, G., and Ephraums, J., editors (1990). *Climate change: The IPCC scientific assessment*, Cambridge. Intergovernmental Panel on Climate Change, Cambridge University Press.

Houlberg, W., Shaing, K., Hirshman, S., and Zarnstorff, M. (1997). Bootstrap current and neoclassical transport in tokamaks of arbitrary collisionality and aspect ratio. *Phys. Plasmas* **4**, 3230.

Howard, J., James, B., and Smith, W. (1979). Rotational Raman calibration of Thomson scattering. *J. Phys. D: Appl. Phys.* **12**, 1435.

Huba, J. (1994). *NRL Plasma Formulary.* Naval Research Laboratory, Washington, D.C.

Hughes, T. (1975). *Plasmas and Laser Light.* Adam Hilger Ltd, London.

Huntley, J. (1994). High-speed laser speckle photography. Part 1: repetitively Q-switched ruby laser light source. *Opt. Eng.* **33**, 1692.

Hutchinson, I. (1987). *Principles of plasma diagnostics.* Cambridge University Press.

Hwang, Y., Forest, C., and Ono, M. (1996). Observation of nonclassical radial current diffusion in a fully bootstrap current driven tokamak. *Phys. Rev. Lett.* **77**, 3811.

Hwang, Y.-S. (1993). *Studies of non-inductive current drive in the CDX-U tokamak.* PhD thesis, Princeton University.

Johannson, T., Kelly, H., Reddy, A., and Williams, R., editors (1992). *Renewable Energy: Sources for Fuels and Electricity.* Island Press, Washington DC.

Johnson, D., Bretz, N., Dimock, D., Grek, B., Long, D., Palladino, R., and Tolnas, E. (1986). Multichannel Thomson scattering systems with high spatial- resolution. *Rev. Sci. Instrum.* **57**, 1856.

Johnson, D., Dimock, D., Grek, B., Long, D., McNeill, D., Palladino, R., Robinson, J., and Tolnas, E. (1985). TFTR Thomson Scattering System. *Rev. Sci. Instrum.* **56**, 1015.

Jones, B. (2000). Private communication.

Jones, T. (1992). CDX-U New Center Stack with Ohmic Heating Solenoid. Technical Report PPPL-TM-396, Princeton Plasma Physics Laboratory.

Jones, T. (1995). *Low-aspect-ratio tokamak start-up and operational current limits in CDX-U.* PhD thesis, Princeton University.

J.P. Holdren, e. a. (1997). Report to the President on Federal Energy Research and Development for the Challenges of the Twenty-first Century. *PCAST report* .

Kaiser Optical Systems, Inc. (1998). P.O. Box 983, 371 Parkland Plaza, Ann Arbor, MI 48106.

Kantor, M. and Kouprienko, D. (1999). High repetition rate probing laser for Thomson scattering diagnostics. *Rev. Sci. Instrum.* **70**, 780.

Keilhacker, M., Gibson, A., Gormezano, C., Lomas, P., Thomas, P., Watkins, M., Andrew, P., Balet, B., Borba, D., Challis, C., Coffey, I., Cottrell, G., Esch, H. D., Deliyanakis, N., Fasoli, A., Gowers, C., Guo, H., Huysmans, G., Jones, T., Kerner, W., Konig, R., Loughlin, M., Maas, A., Marcus, F., Nave, M., Rimini, F., Sadler, G., Sharapov, S., Sips, G., Smeulders, P., Soldner, F., Taroni, A., Tubbing, B., von Hellerman, M., Ward, D., and Team, J. (1999). High fusion performance from deuterium-tritium plasmas in JET. *Nucl. Fus.* **39**, 209.

Kissick, M., Fredrickson, E., Callen, J., Bush, C., Chang, Z., Efthimion, P., Hulse, R., Mansfield, D., Park, H., Schivell, J., Scott, S., Synakowski,

E., Taylor, G., and Zarnstorff, M. (1994). Transient Electron Heat Diffusivity Obtained from Trace Impurity Injection on TFTR. *Nucl. Fus.* **34**, 349.

Koechner, W. (1996). *Solid-State Laser Engineering.* Springer Series in Optical Sciences. Springer, New York, fourth edition.

Lackner, K. and Gottardi, N. (1990). Tokamak confinement in relation to plateau scaling. *Nucl. Fus.* **30**, 767.

Laqua, H., Erckmann, V., Hartfuss, H., and Laqua, H. (1997). Resonant and nonresonant electron cyclotron heating at densities above the plasma cutoff by O-X-B mode conversion at the W7-As stellarator. *Phys. Rev. Lett.* **78**, 3467.

Laqua, H. and Hartfuss, H. (1998). Electron Bernstein wave emission from an overdense plasma at the W7-AS stellarator. *Phys. Rev. Lett.* **81**, 2060.

Lawson, J. (1957). Some criteria for a power producing thermonuclear reactor. *Proc. of the Phys. Soc. B* **70**, 6.

Levinton, F., Zarnstorff, M., Batha, S., Bell, M., Bell, R., Budny, R., Bush, C., Chang, Z., Fredrickson, E., Janos, A., Manickam, J., Ramsey, A., Sabbagh, S., Schmidt, G., Synakowski, E., and Taylor, G. (1995). Improved Confinement with Reversed Magnetic Shear in TFTR. *Phys. Rev. Lett.* **75**, 4417.

Livingston, R., Anderson, T., Besmann, T., Olszewski, M., Perry, A., and West, C. (1982). *A Desirable Energy Future: A National Perspective.* The Franklin Institute Press, Philadelphia.

Lo, E. (1997). *Tangential phase contrast imaging diagnostic for density fluctuation measurement on CDX-U.* PhD thesis, Princeton University.

Lo, E., Wright, J., and Nazikian, R. (1995). Linear-Systems Description of the CO2 Laser-Based Tangential Imaging-System. *Rev. Sci. Instrum.* **66**, 1180.

McCool, S., McCool, I., Bengtson, R., and Phillips, P. (1981). Calibration of Thomson Scattering Density Measurements. Technical Report DOE-ET-53042-7, University of Texas.

Menard, J. (1998). *High-Harmonic Fast Wave Coupling and Heating Experiments in the CDX-U Spherical Tokamak*. PhD thesis, Princeton University.

Menard, J., Jardin, S., Kaye, S., Kessel, C., and Manickam, J. (1997). Ideal MHD stability limits of low aspect ratio tokamak plasmas. *Nucl. Fus.* **37**, 595.

Menard, J., Majeski, R., Kaita, R., Ono, M., Munsat, T., Stutman, D., and Finkenthal, M. (1999). High-harmonic fast magnetosonic wave coupling, propagation, and heating in a spherical torus plasma. *Phys. Plasmas* **6**, 2002.

Miller, R., Lin-Liu, Y., Turnbull, A., Chan, V., Perlstein, L., Sauter, O., and Villard, L. (1997). Stable equilibria for bootstrap-current-driven low aspect ratio tokamaks. *Phys. Plasmas* **4**, 1062.

Munsat, T. and LeBlanc, B. (1999). A low-cost TVTS system for CDX-U. *Rev. Sci. Instrum.* **70**, 755.

Ono, M., Forest, C., Hwang, Y.-S., Armstrong, R., Choe, W., Darrow, D., Greene, G., Jones, T., Jarboe, T., Martin, A., Nelson, B., Orvis, D., Painter, C., Zhou, L., Rogers, J., Schafer, M., Hyatt, A., Pinsker, R., Staebler, G., Stambaugh, R., Strait, E., Greene, K., Leuer, J., and Lohr, J. (1992). Novel current drive experiments on the CDX-U, HIT, and DIII-D tokamaks. In *Plasma Physics and Controlled Nuclear Fusion Research 1992*, volume 1 of *Fourteenth conference proceedings*, page 693, Würzburg, Germany. IAEA, Vienna.

Ono, M., Greene, G., Darrow, D., Forest, C., Park, H., and Stix, T. (1987). Steady-state tokamak discharge via DC helicity injection. *Phys. Rev. Lett.* **59**, 2165.

Ono, M. and The CDX Group (1988). Current Drive Experiment - an upgrade proposal (CDX-U). Princeton Plasma Physics Laboratory. Submitted to the Experimental Research Branch of the Division of Applied Plasma Physics in the Office of Fusion Energy in the U.S. Department of Energy.

Owen, H., Battey, D., Pelletier, M., and Slater, J. (1995). New spectroscopic instrument based on volume holographic optical elements. In Benton, S., editor, *Practical Holography IX*, volume 2406, page 260. SPIE.

Peacock, N., Robinson, D., Forrest, M., Wilcock, P., and Sannikov, V. (1969). Measurement of the electron temperature by Thomson scattering in Tokamak T3. *Nature* **224**, 488.

Peng, Y.-K. (2000). The Physics of Spherical Torus Plasmas. *Phys. Plasmas* **7**, 1681.

Peng, Y.-K. and Strickler, D. (1986). Features of spherical torus plasmas. *Nucl. Fus.* **26**, 769.

Penney, C., St.Peters, R., and Lapp, M. (1974). Absolute rotational Raman cross sections for N_2, O_2, and CO_2. *J. Opt. Soc. Am.* **64**, 712.

Princeton Instruments (1998). 3660 Quakerbridge Rd., Trenton, NJ 08619.

Rewoldt, G., Tang, W., Kaye, S., and Menard, J. (1996). Microinstability properties of small-aspect-ratio tokamaks. *Phys. Plasmas* **3**, 1667.

Roach, C. (1996). Modelling ohmic confinement experiments on the START tokamak. *Plasma Phys. and Contr. Fus.* **38**, 2187.

Rohr, H. (1981). Rotational Raman Scattering of Hydrogen and Deuterium for Calibrating Thomson Scattering Devices. *Phys. Lett.* **81A**, 451.

Sakharov, A. and Tamm, I. (1959). *Plasma Physics and the Problem of Controlled Thermonuclear Reactors*. Pergamon, New York.

Schott Corporation (1999). 3 Odell Plaza, Yonkers, NY 10701.

Schwarz, S. (1963). Scattering of Optical Pulses from a Noequilibrium Plasma. *Proceedings of the IEEE* **51**, 1362.

Sesnic, S., Kaita, R., Kaye, S., Okabayashi, M., Powers, E., Bell, R., Gammel, G., Holland, A., Im, S., Kugel, H., LeBlanc, B., Levinton, F., and Takahashi, T. (1994). Non-Linear Coupling of Low n Modes in PBX-M. *Nucl. Fus.* **34**, 1365.

Sheffield, J. (1975). *Plasma Scattering of Electromagnetic Radiation.* Academic Press, New York.

Sinclair Optics, Inc. (1997). 6780 Palmyra Road, Fairport, NY 14450.

Soler, M. and Callen, J. (1979). On Measuring the Electron Heat Diffusion Coefficient in a Tokamak from Sawtooth Oscillation Observations. *Nucl. Fus.* **19**, 703.

Soukhanovskii, V., Stutman, D., Iovea, M., Finkenthal, M., Moos, H., Munsat, T., Jones, B., Hoffman, D., Kaita, R., and Majeski, R. (2001). Multilayer mirror and foil filter AXUV diode arrays on CDX-U spherical torus. *Rev. Sci. Instrum.* **72**.

Stambaugh, R., Chan, V., Miller, R., and Schaffer, M. (1998). The spherical tokamak path to fusion power. *Fus. Technol.* **33**, 1.

Stanford Research Systems, Inc. (1999). 1290-D Reamwood Avenue, Sunnyvale, CA 94089.

Stix, T. (1962). *The Theory of Plasma Waves.* McGraw-Hill, New York.

Stutman, D., Finkenthal, M., Soukhanovskii, V., Menard, J., Munsat, T., Kaita, R., and Majeski, R. (1999). Spectroscopic Evidence for High-Harmonic Fast Wave Heating in the CDX-U Spherical Torus. *Plasma Phys. and Contr. Fus.* **41**, 867.

Stutman, D., Hwang, Y., Menard, J., Choe, W., Ono, M., Finkenthal, M., May, M., Regan, S., Soukhanovskii, V., and Moos, H. (1997a). Multilayer Mirror Based Line Emission Tomography for Spherical Tokamaks. *Rev. Sci. Instrum.* **68**, 1055. Part II.

Stutman, D., Hwang, Y., Ono, M., Finkenthal, M., and Moos, H. (1996). Spectroscopic Diagnostics on Low Aspect-Ratio Tokamaks. *J. Electron. Spectr.* **80**, 249.

Stutman, D., Menard, J., Hwang, Y.-S., Choe, W., and Ono, M. (1997b). Line emission tomography for CDX-U using filtered diodes. *Rev. Sci. Instrum.* **68**, 1059. Part II.

Sykes, A. (1999a). Physics of Spherical Tokamaks. *Tech. Phys.* **44**, 1047.

Sykes, A. (1999b). The Spherical Tokamak Programme at Culham. *Nucl. Fus.* **39**, 1271.

Sykes, A., Akers, R., Appel, L., Carolan, P., Connor, J., Conway, N., Counsell, G., Dnestrovskij, A., Dnestrovskij, Y., Gryaznevich, M., Helander, P., Nightingale, M., Ribeiro, C., Roach, C., Tournianski, M., Walsh, M., Wilson, H., Team, S., and Team, N. (2000). H-Mode Operation in the START Spherical Tokamak. *Phys. Rev. Lett.* **84**, 495.

Synakowski, E., Efthimion, P., Rewoldt, G., Stratton, B., Tang, W., Grek, B., Hill, K., Hulse, R., Johnson, D., Kissick, M., Mansfield, D., McCune, D., Mikkelsen, D., Park, H., Ramsey, A., Redi, M., Scott, S., Taylor, G., Timberlake, J., and Zarnstorff, M. (1993). Helium, Iron, and electron particle transport and energy transport studies on the Tokamak Fusion Test Reactor. *Phys. Fluids B* **5**, 2215.

Taroni, A., Erba, M., Springmann, E., and Tibone, F. (1994). Global and local energy confinement properties of simple transport coefficients of the Bohm type. *Plasma Phys. and Contr. Fus.* **36**, 1629.

Taylor, G., Efthimion, P., Jones, B., and the CDX-U team (2001). Further advances in the EBW diagnostic, or something similar. *Rev. Sci. Instrum.* **00**, 0000.

Taylor, J. R. (1982). *An Introduction to Error Analysis.* University Science Books. Oxford University Press.

Tedesco, J., Owen, H., Pallister, D., and Morris, M. (1993). Principles and Spectroscopic Applications of Volume Holographic Optics. *Anal. Chem.* **65**, 441A.

Tubbing, B., Cardozo, N. L., and Wiel, M. V. D. (1987). Tokamak Heat Transport – A Study of Heat Pulse Propagation in JET. *Nucl. Fus.* **27**, 1843.

Walsh, M., Bamford, R., Carolan, P., Connor, J., Ferreira, J., Goodall, D., Gryaznevich, M., Hugill, J., Jenkins, I., Martin, R.,

Manhood, S., Ribeiro, C., Roach, C., Robinson, D., Shevchenko, V., Sykes, A., Todd, T., Tomas, J., and Wilson, H. (1995). Confinement at Tight Aspect Ratio in START. In *Proceedings of the 22nd European Physical Society Conference*, volume 3, page 33, Bournemouth, U.K.

Walter, H., Stroth, U., Bleuel, J., Burhenn, R., Geist, T., Giannone, L., Hartfuss, H., Koponen, J., Ledl, L., Pereverzev, G., Group, E., and Team, W.-A. (1998). Transient transport phenomena induced by cold pulses in W7-AS. *Plasma Phys. and Contr. Fus.* **40**, 1661.

Weber, A., editor (1979). *Raman Spectroscopy of Gases and Liquids*, volume 11 of *Topics in Current Physics*. Springer-Verlag, Berlin.

Wesson, J. (1997). *Tokamaks*. Oxford University Press, New York.

Wu, K., Ram, A., and Bers, A. (1996). Electron Bernstein wave studies... In *Proceedings of the American Physical Society*, volume 41, page 1425.